Printed electronics prototyping of flexible optoelectronic methylammonium trihalide perovskite-based devices

by

Charles TRUDEAU

THESIS PRESENTED TO ECOLE DE TECHNOLOGIE SUPÉRIEURE
IN PARTIAL FULFILLEMENT FOR THE DEGREE OF
DOCTOR OF PHILOSOPHY
Ph.D.

MONTREAL, 11 JANUARY 2021

ÉCOLE DE TECHNOLOGIE SUPÉRIEURE
UNIVERSITÉ DU QUÉBEC

BOARD OF EXAMINERS (THESIS PH.D.)

THIS THESIS HAS BEEN EVALUATED

BY THE FOLLOWING BOARD OF EXAMINERS

Mr. Sylvain G. Cloutier, Thesis Supervisor
Department of Electrical Engineering, École de technologie supérieure

Mr. Martin Bolduc, Thesis Co-supervisor
Department of Electrical Engineering, École de technologie supérieure

Mr. Jean-François Boland, President of the Board of Examiners
Department of Electrical Engineering, École de technologie supérieure

Mr. François Blanchard, Member of the jury
Department of Electrical Engineering, École de technologie supérieure

Mr. Lawrence R. Chen, External Evaluator
Department of Electrical and Computer Engineering, McGill University

THIS THESIS WAS PRENSENTED AND DEFENDED

IN THE PRESENCE OF A BOARD OF EXAMINERS AND PUBLIC

4 NOVEMBER 2020

AT ÉCOLE DE TECHNOLOGIE SUPÉRIEURE

ACKNOWLEDGMENT

The work presented in this thesis could not be possible without the help and support of many of my colleagues, my professors, my friends and my family.

First, I would like to thank my supervisor Sylvain Cloutier and co-supervisor Martin Bolduc for their continued mentorship, their patience and support throughout my professional and personal life. They have helped me grow as a person and as a researcher in the years that I have known them.

I would also like to thank INO for supporting this research and providing the environment necessary for its success. I would like to give a special thank you to Patrick Beaupré who has helped me immensely with the training and troubleshooting of the Ceradrop printer and the other equipments used in this work. He has also helped with the some of the printing test plans and has proved to be idispensable for this research.

Likewise, I would like to thank my colleagues and friends at ETS who have helped in numerous ways. Thank you, Jaime, Felipe, FX, Debika, Xiohang, Soraya, Paul, Ivy, Dawit, Ibrahima and Somaiieh! You have made my time at ETS a truly positive one and have brought joy even during the dark winter months.

Lastly, I would like to thank my parents, Alain and Renée. Your ongoing support and love are always appreciated. Your food and spiced coffee have also been great motivators during the writing of this thesis!

Prototypage en électronique imprimable de dispositifs flexibles optoélectroniques à base de pérovskite de trihalogénure de méthylammonium

Charles TRUDEAU

RÉSUMÉ

Le domaine de l'électronique imprimable est devenu très étendu ces dernières années, avec des applications allant de la fabrication de dispositifs photovoltaïques à grand volume aux transistors à effet de champ organiques en passant par les diodes électroluminescentes organiques. Les technologies de l'électronique imprimable existantes, telles que l'impression à jet d'encre, l'impression héliogravure et l'impression par jet d'aérosol, sont utilisées dans l'impression conventionnelle depuis des décennies. Ce sont les progrès récents des matériaux fonctionnels et des formulations d'encre qui ont permis à ces technologies d'être utilisées pour la fabrication de dispositifs électroniques. L'un des principaux avantages de l'électronique imprimable par rapport aux techniques classiques de fabrication de dispositifs est son coût relativement bas et son débit élevé pour un dépôt en grande surface. L'un des principaux marchés d'applications des dispositifs flexibles à faible coût est celui de l'internet des objets, à des fins de communication et d'acquisition de données à grande échelle. En outre, il existe un réel besoin de passer des sources d'énergie non renouvelables actuelles aux sources d'énergie renouvelables et plus écologiques, telles que l'énergie solaire, éolienne et nucléaire. La production massive de dispositifs photovoltaïques flexibles à faible coût pourrait être une réponse partielle à ce besoin, car la fabrication sur des substrats flexibles réduit non seulement le poids de l'appareil et les coûts de transport, mais augmente également la facilité d'installation.

Les pérovskites constituent un matériau d'intérêt courant pour les applications photovoltaïques. Elles peuvent être traitées en solution et offrent une gamme de propriétés adaptées en fonction de leur composition et se sont révélées particulièrement efficaces pour la conversion de l'énergie solaire. Ces matériaux sont généralement fabriqués en laboratoire à des fins de recherche et de développement, mais certaines formulations commerciales peuvent maintenant être trouvées. Le développement commercial de ces matériaux est l'un des éléments moteurs du travail réalisé dans cette thèse. Dans ce travail, une étude de faisabilité de la fabrication de dispositifs actifs avec ces formulations commerciales de pérovskite, en utilisant des méthodes de l'électronique imprimée, est proposée. Plus spécifiquement, l'impression à jet d'encre est utilisée pour imprimer des dispositifs optoélectroniques actifs et flexibles à l'aide de formulations de pérovskite commerciales. Plusieurs architectures de dispositifs sont étudiées pour leur faisabilité de fabrication à l'aide de méthodes d'impression à jet d'encre. Une fois que les architectures les mieux adaptées pour l'impression de dispositifs sont identifiées, des matrices de dispositifs sont imprimées pour évaluer la faisabilité de la fabrication à grande échelle. Deux types de dispositifs à base de pérovskite sont fabriqués; un bolomètre pour les applications de bâtiments intelligents et des dispositifs photovoltaïques flexibles. Les bolomètres offrent de grandes capacités de détection de température, avec une

valeur de TCR jusqu'à 100%/°C, dans une plage de détection de température limitée de 17 ° C à 36 °C, et indiquent également le comportement de commutation de la lumière. Les performances des dispositifs photovoltaïques flexibles sont plutôt limitées, avec un rendement de conversion de puissance maximal obtenu de 0,11%. Cependant, cette étude a prouvé la faisabilité de la fabrication de ces dispositifs et propose des voies d'optimisation pour améliorer encore les performances. Des rendements de dispositifs photovoltaïques jusqu'à 80% sont trouvés pour certaines voies de fabrication et d'architectures, démontrant ainsi que des méthodes de fabrication de l'électronique imprimées peuvent être utilisées pour la fabrication de dispositifs flexibles à grande échelle.

Mots-clés: Électronique imprimable, pérovskite, dispositifs flexibles, couches minces

Printed electronics prototyping of flexible optoelectronic methylammonium trihalide perovskite-based devices

Charles TRUDEAU

ABSTRACT

The field of printable electronics has become very extensive in recent years, with applications ranging from high volume photovoltaic device fabrication to organic field-effect transistors and organic light-emitting diodes. Existing printed electronics technologies, such as inkjet printing, gravure printing, and aerosol jet printing have been used in conventional printing for decades. It is recent advances in functional materials and ink formulations which have allowed these technologies to be used for electronic device fabrication. One of the main advantages of printable electronics when compared to conventional device fabrication techniques is the relatively low cost and high throughput for large surface deposition. One of the main application markets for low-cost flexible devices is for the internet of things, in which there is a growing need for these devices, for communication and data acquisition purposes at a massive scale. Moreover, there is a real need to switch from current non-renewable energy sources to more renewable and ecological sources of energy such as solar, wind and nuclear energy. The massive production of flexible low-cost photovoltaic devices could be a partial answer to this need, as fabrication on flexible substrates not only lowers device weight and transport costs but also increases the ease of solar cell installation.

One material of current interest for photovoltaic applications are perovskites, which can be solution processed, offer a range of adapted properties depending on their composition and have been shown to be especially efficient in harvesting solar energy. These materials are typically made in lab for research and development purposes, however, some formulations can now be found commercially. The commercial development of these materials is one of the driving forces for the work performed in this thesis. In this work, a study of the feasibility of fabricating active devices with these commercial perovskite formulations, using printed electronic methods, is proposed. More specifically, inkjet printing is used to print flexible active optoelectronic devices using commercially available perovskite formulations. Multiple device architectures are studied for their fabrication feasibility using inkjet printing methods. Once the best suited architectures for device printing are identified, arrays of devices are printed to evaluate the feasibility of large-scale device fabrication. Two types of perovskite-based devices are fabricated; bolometers for smart building applications and flexible photovoltaic devices. The flexible bolometers offer great temperature sensing capabilities, with a TCR of up to 100 %/°C, within a limited temperature sensing range of 17 °C to 36 °C, these also show light switching behavior. The photovoltaic devices performances are rather limited, with an obtained maximum power conversion efficiency of 0.11 %, however this study proved their fabrication feasibility and offers optimization pathways to further enhance performances. Working photovoltaic device yields of up to 80 % are found, further demonstrating that printed electronic fabrication methods may be used for large scale flexible device fabrication.

Keywords: Printed electronics, perovskite, flexible devices, thin films

TABLE OF CONTENTS

LIST OF TABLES

Page

LIST OF FIGURES

Page

LIST OF ABREVIATIONS

3D	Three dimensional
ANP	Advanced Nano Products
BL	Blocking layer
CB	Chlorobenzene
CNT	Carbon nanotube
DCB	1,2-Dichlorobenzene
DMF	Dimethylformamide
DSSC	Dye sensitized solar cell
EQE	External quantum efficiency
ETL	Electron transport layer
EtOH	Ethanol
ETS	École de Technologie Supérieure
FEM	Finite element method
FF	Fill factor
FTO	Fluorine tin oxide
FWHM	Full width at half maximum
FWTM	Full width at one tenth maximum
Hex Fab	Hexagonal centered lattice
Hex Shift	Hexagonal shifted lattice
HTL	Hole transport layer
IC	Integrated circuit
INO	Institut National d'Optique

IoT	Internet of things
IPA	Isopropyl alcohol
IQE	Internal quantum efficiency
IR	Infrared
IS	Impedance spectroscopy
ITO	Indium tin oxide
I-V	Current – voltage
KPFM	Kelvin probe force microscopy
LCP	Liquid crystal polymer
LIDT	Laser-induced damage temperature
LiTFSI	Lithium bis(brifluoromethanesulfonyl)imide
MA	Methylammonium
MEMS	Microelectromechanical systems
MALH	Methylammonium lead halide
MOPAW	Master oscillator pulsed arbitrary waveform
MPP	Maximum power point
MWCNT	Multi-walled carbon nanotube
NEP	Noise-equivalent power
NIR	Near infrared
NP	Nanoparticle
NS	Nanostructured
NTC	Negative temperature coefficient
OA	Oleic acid

OFET	Organic field effect transistor
OLED	Organic light-emitting diode
OTFT	Organic thin film transistor
$PC_{60}BM$	[6,6]-phenyl-C61-butyric acid methyl ester
PCB	Printed circuit board
PCE	Power conversion efficiency
PDMS	Polydimethylsiloxane
PE	Printed electronics
PEDOT:PSS	Poly(3,4-ethylenedioxythiophene) polystyrene sulfonate
PET	Polyethylene terephthalate
PTFE	Polytetrafluoroethylene
PMMA	Poly(methyl methacrylate)
PS	Perovskite
PTC	Positive temperature coefficient
PV	Photovoltaic
QD	Quantum dot
R&D	Research and development
RFID	Radio-frequency identification
RH	Relative humidity
RMS	Root mean square
SEM	Scanning electron microscope
SWAP	Size, weight and power
TBP	4-tert-butylpyridine

TCO	Transparent conducting oxide
TCR	Temperature coefficient of resistance
TE	Thermal explosion
TF	Thin film
TFT	Thin film transistor
TGME	Triethylene glycol monomethyl ether
THz	Terahertz
UV	Ultraviolet
VPP	Vortex phase plate
XRD	X-ray diffraction

LIST OF SYMBOLS

$	US Dollar
%	Percentage
□	Square
°	Degree
°C	Degree Celsius
A	Amps
a	Steinhart-Hart coefficient
A(T)	Temperature dependent absorption coefficient
$A_{cross\text{-}section}$	Cross-sectional Area
A_{device}	Device area
Ag	Silver
Au	Gold
b	Steinhart-Hart coefficient
Beam(x,y,t)	Spatial and time dependent beam parameter
Br	Bromine
c	Steinhart-Hart coefficient
CdS	Cadmium sulfide
$CH_3NH_3^+$	Methylammonium cation
$CH_3NH_3PbX_3$	Methylammonium lead Trihalide
Cl	Chlorine
cm	Centimeter
cP	Centipoise

C_{PL}	Lattice drop packing constant
C_{PT}	Post treatment effect constant
Cu	Copper
D	Designed distance between interdigitated electrodes
D*	Specific detectivity
D_D	Drop diameter
dR	Change in resistance
dT	Change in temperature
dt	Change in time
e	Elementary charge of an electron
EF	Fermi level
eV	Electron volt
e_ϕ	Electrostatic potential
f	Frequency
G	Interdigitated electrode gap
hv	Photon energy
Hz	Hertz
I	Current
I_{sc}	Short circuit current
$I_{\%}$	Drop interpenetration
K	Kelvin
kg	Kilogram
kHz	Kilohertz

kJ	Kilojoule
L	Nozzle diameter
L_d	Diffusion length
ln	Natural logarithmic
m	Meter
mA	Milliampere
MACl	Methylammonium chloride
MAI	Methylammonium iodide
$MAPbCl_3$	Methylammonium lead chloride
$MAPbI_3$	Methylammonium lead iodide
$MAPbI_{3-x}Cl_x$	Methylammonium lead iodide chloride
$MAPbI_{3-x}(SCN)_x$	Methylammonium lead thiocyanate
$MAPbX_3$	Methylammonium lead Trihalide
mbar	Millibar
mg	Milligram
mJ	Millijoule
ml	Milliliter
mm	Millimeter
ms	Millisecond
mW	Milliwatt
MΩ	Mega Ohm
n	Density of charge carrier
nA	Nanoampere

N_L	Number of printed layers
nm	Nanometer
Oh	Ohnesorge number
P	Laser power constant
PbI_2	Lead iodide
PbS	Lead sulfide
P_G	Gaussian-pulse shape laser power constant
pL	Picoliter
ppm	Parts per million
P_S	Square-pulse shape laser power constant
PulseTrain(t)	Time dependent pulse train function
Q1	First quartile
Q3	Third quartile
R	Resistance
$\mathbb{R}$	Reflection coefficient
r_∞	Resistance coefficient
R_0	Resistance at 298 K
Re	Reynold's number
rpm	Rotations per minute
s	Second
SCN	Thiocyanate
$S_d(T)$	Temperature dependent splat diameter
SiO_2	Silicon dioxide

Sn	Noise RMS
T	Temperature
t	Time
T_0	Room temperature
TiO_2	Titanium dioxide
THK	Thickness
t_P	Pulse time width
T_{peak}	Peak temperature
$T_{residual}$	Residual temperature
uA	microampere
uJ	Microjoule
uL	Microliter
um	Micrometer
us	Microsecond
uΩ	Micro Ohm
ν	Jet Velocity
V	Volt
V_D	Jetted drop volume
v_{drift}	Drift velocity
V_b	Bias voltage
V_{oc}	Open circuit voltage
vol%	Volume percentage
V_R	Ink's active material volume ratio

V_y	Beam velocity in y direction
W	Watt
$W_{function}$	Work function
W_{IE}	Interdigitated electrode width
We	Webber number
W_I	Waveform intensity
wt%	Weight Percentage
w_x	Laser beam half width in x dimension
w_y	Laser beam half width in y dimention
y_0	Starting beam y position
ZnS	Zinc sulfide
α	Temperature coefficient
β	β parameter temperature coefficient
η	Viscosity
θ	Contact angle
θ_{Water}	Water contact angle
ρ	Density
σ	Conductivity
σL	Surface Tension
σLD	Dispersive component of the surface tension
σLP	Polar component of the surface tension
σS	Solid surface energy
σSD	Dispersive component of the solid surface energy

σ^{SP}	Polar component of the solid surface energy
Ω	Ohm
$\mathfrak{R}$	Responsivity

INTRODUCTION

The field of printable electronics has become very extensive in the recent years, with applications ranging from high volume photovoltaic (PV) device fabrication (Hubler et al., 2011, p. 1018-1022) to organic field-effect transistors (OTFTs) (Talapin & Murray, 2005, p.86-89) and organic light-emitting diodes (OLEDs) (Bale et al., 2006, p.453-459) Existing printed electronics (PE) technologies, such as inkjet, gravure printing, and aerosol jet printing have been used in conventional printing for decades. It is the recent advances in functional materials and ink formulations which have allowed these technologies to be used for electronic device fabrication. One of the main advantages of printable electronics when compared to conventional device fabrication techniques is the relatively low cost and high throughput for large surface deposition. Another advantage is its compatibility with low temperature processes which allow for flexible, temperature sensitive substrates to be used, giving rise to flexible electronics. One of the main application markets for low-cost flexible devices is for the internet of things (IoT) in which there is a growing need for these devices for communication and data acquisition purposes at a massive scale. Moreover, there is a real need to switch from current non-renewable energy sources to more renewable and ecological sources of energy such as solar, wind and nuclear energy. The massive production of flexible low-cost PV devices could be a partial answer to this need, as fabrication on flexible substrates not only lowers device weight and therefore transport costs but also increases the ease of PV installation.

However, what printable electronics gains in terms of cost and speed, it loses in terms of precision and resolution. As such, it is expected that simple, robust device designs with less constraints in terms of feature sizes and precision will be favored for device fabrication. A major part of the research and development (R&D) efforts are being expended to improve these lacking aspects of the PE field. Indeed, pre-printing and post-printing treatments are often utilised to optimize and control printing process dynamics, as well as the properties of the printed functional materials (Park & Kwon, 2007, p.188-192); (Ko et al., 2007, p.345202); (Laakso, Ruotsalainen, Halonen, Mantysalo & Kemppainen, 2009, p.1360-1366). Some of

these pre-printing and post-printing treatments have been developed to address the comparatively low resolutions achieved with PE (Tobjork et al., 2012, p.2949-2855); (Kim, Dhage, Shim & Hahn, 2009, p.791-798); (Chung, Hwang, Lee & Kim, 2012, p.035202); (Eun, Chon, Yoo, Song & Choa, 2015, p. 838-845); (Kwon et al., 2014, p.1137-1145); (Yeo et al., 2014, p.562-568).

Advances in material science is the main driving force behind the feasibility of device fabrication using printing methods. Solution processable materials such as inks and pastes are required for device fabrication using these methods. Furthermore, as with any technology, high quality materials with highly adapted properties are wanted to achieve high performance devices. This is especially true for PE, as device performances are currently lacking and any help to increase these performances are welcome. One material of current interest for PV applications are perovskites (PSs), which can be solution processed, offer a range of adapted properties depending on their composition and have been shown to be especially efficient in harvesting solar energy. These materials are typically made in lab for R&D purposes, however, some formulations can now be found commercially. The commercial development of these materials is one of the driving forces for the work performed in this thesis. In this work, the feasibility of fabricating active devices with these commercial PS formulations using PE methods is studied. More specifically, inkjet printing is used to print active optoelectronic flexible devices using commercially available methylammonium lead halide (MALH) PS formulations (e.g., $CH_3NH_3PbA_{3-x}B_x$, where A and B are I, Cl or Br).

Different device architectures are studied for their fabrication feasibility using inkjet printing methods. To achieve this, first, device architectures fabricated using conventional solution processed or other fabrication methods are studied. Solution processable materials are then identified and tested for inkjet printing using a Ceradrop F-series printer. A large part of this work is dedicated to optimizing the jetting and printing processes of these materials and their interactions with flexible substrates. Pre- and post-printing processes are also identified and tested for printing the various identified materials. The pre-printing, jetting, printing and post-printing processes are combined to form a complete layer fabrication process for each material.

Multilayered passive device prototypes can then be printed using the identified materials and the developped layer fabrication processes to acquire a technical expertise with the inkjet printing process, its limitations and the problems associated with this fabrication process. Latter, active rigid PS based devices are printed using the expertise acquired with passive device printing. The whole PE fabrication process is then transferred to flexible substrates while adapting the device architecture and the various layer fabrication processes to improve flexible device performances.

Throughout this work, optical annealing post-processes are given special consideration as they provide added advantages for PE when compared to other annealing processes. As such, a full chapter of this work is dedicated to furthering our understanding of one such process. Optical laser sintering processes for metallic ink annealing are studied using FEM simulations supported by experimental results.

CHAPITRE 1

STATE OF THE ART – PRINTED ELECTRONICS

In this chapter, an overlook of the different printing technologies and how they apply to the PE field is presented. State of the art digital inkjet printing technologies and printers are looked at in more detail as they are more pertinent to the research topic of this work. The state of commercially available inks commonly used in PE are equally explored.

1.1 Printing Technologies

In the following section, the state of the art of the regarding different printing technologies is explored. Namely, digital inkjet printing, aerosol printing and roll-to-roll printing processes, with extra attention being given to the digital inkjet printing process as it is more pertinent to the research topic of this work. An overview of the different printing processes with their limitations are included as well as an exploration of the different printing equipment associated with each printing technique.

The focus on digital inkjet printing techniques is driven by two (2) main factors;

1. The freedom of designs associated with digital printing techniques which allows for a faster design iteration process and therefore faster development cycles.
2. The tremendous waste of expensive and environmentally harmful materials associated with non-digital printing techniques due to their complex material handling procedures.

Both factors are beneficial to the emerging high-volume manufacturing sector where inkjet printing techniques can be explored as a potential way to boost profit margins, reach higher manufacturing volumes and open entirely new markets.

1.1.1 Digital Inkjet Printing

Inkjet printing is one of the printing techniques which is most familiar to the general public. Indeed, desktop inkjet printers are used in the day to day lives of millions of people for their home, school and office printing needs. Inkjet printers are the most commonly used type of printers, ranging from small inexpensive consumer models to large and expensive professional machines used for large scale production or R&D purposes. In inkjet printing, drops of inks are ejected or "jetted" from an ink reservoir in a controlled fashion through a series of nozzles onto paper, plastic or other substrates. Figure 1.1 illustrates the inkjet printing process. By controlling the jetting of the ink drops and the positioning of the nozzles with respect to the printing substrate, a digital image comprising of a series of ink dots can be transferred onto said substrate.

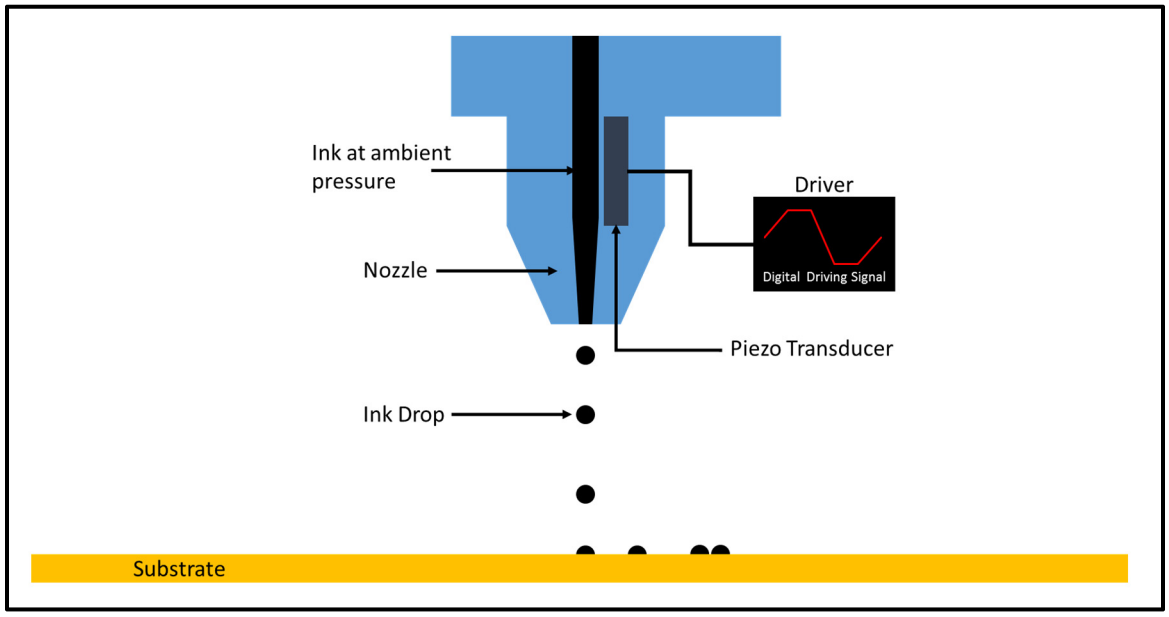

Figure 1.1 Schematic representation of the inkjet printing process

There exist two main technologies when it comes to ink jetting, namely, thermal inkjet and piezoelectric inkjet. These two processes differ in the method used for ejecting the ink droplet

from the nozzles. In both cases, the print cartridges consist of a series of tiny chambers, each containing a piezoelectric transducer or a heating element. To eject a drop from the chamber, a pulse of current is passed through either the piezoelectric transducer or the heating element. In the case of piezoelectric inkjet, the current in the piezoelectric transducer induces a deformation of the chamber, causing a pressure increase which propels the ink drop from the chamber through the nozzle. An opposing deformation of the chamber is then induced with an opposing current which causes a pressure decrease, filling the chamber with more ink for the next jetting cycle. For thermal inkjet, the current in the heating element cause the ink to heat inside the chamber and eventually the ink undergoes rapid vaporization. This event forms a gas bubble which propels a drop of ink from chamber through the nozzle. Once the ink cools, the gas can be reabsorbed in the ink and allows more ink into the chamber for the next jetting cycle. These two jetting mechanisms are illustrated in Figure 1.2. Typically, piezoelectric inkjet is preferred since the thermal cycling of the ink in thermal inkjet is often detrimental to the ink jetting process as it can affect the physical properties of the ink. This aspect is especially true for active ink compositions employed for PE purposes.

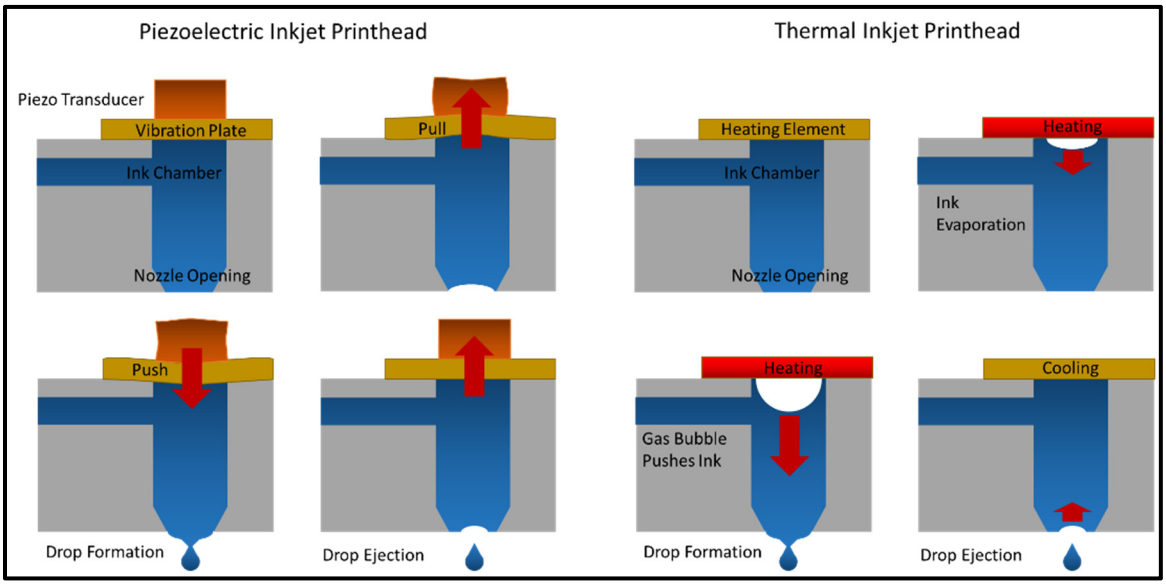

Figure 1.2 Schematic representation of the jetting sequence in a piezoelectric and thermal inkjet printhead

Inkjet printing is still used predominantly in the graphics industry and in the consumer printing markets. The digital drop-on-demand capabilities of inkjet printing make it a very flexible printing technique and allow for altering print designs rapidly and cheaply. This aspect of inkjet printing along with the relatively low cost of the entry level consumer printers are the main reasons why inkjet printing is the most used printing method. There exists a wide range of inkjet printers, printheads and nozzles commercially available to suit most printing needs, from benchtop document printing to large scale industrial printing and for R&D purposes.

Inkjet printhead and nozzle technologies can be split into three categories which are suited for different needs. The least complex inkjet printhead technologies are inkjet single nozzle technologies. Single nozzle inkjet printheads are typically constructed from a glass or quartz tube with a piezoelectric transducer for jetting purposes, as illustrated in Figure 1.3. Typical commercially available single nozzle inkjet printheads orifice (nozzle opening diameter) sizes range from 10 µm to 80 µm. These inkjet printheads need to be connected to a separate ink reservoir which is not restricted in size. A separate ink reservoir can be an advantage since it can be adapted to be suited for a wide array of ink materials including harsh solvent components. It can also be adapted to be suited to a wide array of ink volumes which is especially beneficial when working with expensive ink formulations or when a large range of ink formulations are tested for jetting. The large range in orifice sizes is also advantageous since it allows for a wider range in ink viscosities and/or particle loading and particle size in the jetted ink (Alaman, Alicante, Pena & Sanchez-Somolinos, 2016, p.910). The wide range of available orifice sizes and the separate ink reservoir make the single nozzle inkjet printheads very well suited for R&D purposes as it allows for a wider array of materials to be jetted while keeping costs down and avoiding complications that can come with jetting using multiple nozzles. The inkjet single nozzle is therefore optimal for ink jetting process optimization and for novel ink formulations.

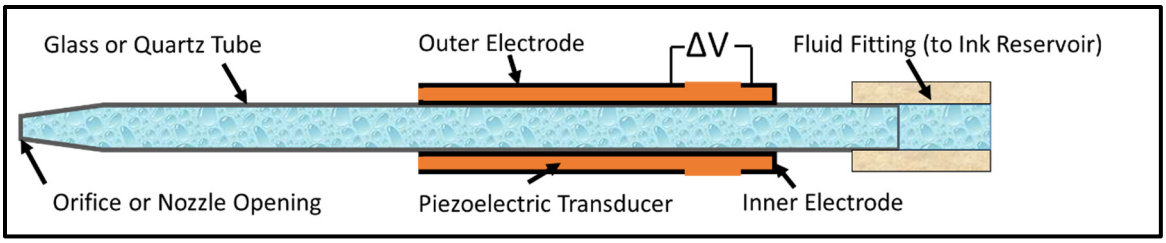

Figure 1.3 Schematic representation of a typical single nozzle inkjet printhead

Next in the line of complexity in the inkjet printhead technologies comes the inkjet cartridges, these cartridges consist of multiple nozzles attached to an ink reservoir located on the cartridge itself. Inkjet cartridges are the most commonly available inkjet printheads and can be found in most inkjet benchtop consumer printers. Typically, the nozzles are drilled into a silicon orifice plate. Orifice sizes typically available are between 9 μm and 21 μm, and nozzle numbers generally range between 16 and 1,048, depending on the cartridge manufacturer and cartridge options. The fact that the ink reservoir is located on the inkjet cartridge itself often makes the inkjet cartridge a single use consumable as once the ink reservoir is depleted it is often not trivial to refill. This can be advantageous for certain applications since it avoids the need for equipment cleaning and purging when using different ink materials for the same printing work. Instead of cleaning and refilling a separate ink reservoir, a new cartridge can simply be inserted in the printer and the printing work can be continued with minimal slowdown. However, since these cartridges are considered consumables and single use only, the specifications on the tolerances of the nozzle orifices are often not as good as the ones for industrial inkjet printheads. Therefore, some of the nozzles often come with small defects which can affect the jetting quality. For the typical user of these cartridges, the defects in the nozzles are not noticeable especially in graphical printing applications where the human eye may not discern the small printing errors. However, for PE, these defects can be a lot more serious. For example, an unstable ink-jet could inadvertently connect two separated electrodes creating an electrical short between them. Inkjet cartridges are well suited for short run prototyping jobs where the volume of ink required is limited. Inkjet cartridges are also benificial for R&D

purposes, for which multiple ink materials are often needed or where harsher ink materials can be used.

The third and most complex category of inkjet printhead technologies are the industrial inkjet printeheads. These are highly similar to the inkjet cartridges, typically with a much higher number of nozzles, and are connected to a separate ink reservoir. These printheads are developed to print in a continuous manner and the tolerances of the orifice diameters are often much smaller than for inkjet cartridges. Like the inkjet cartridges, the nozzles are typically drilled or etched into a silicon orifice plate. Orifice sizes are generally smaller than inkjet cartridges, typically between 7 μm and 9 μm. The number of nozzles found in industrial inkjet printheads can reach up to 70,400 nozzles. (Memjet, 2019) Multiple printheads can be placed in series or in parallel to increase the printing area or to print multiple ink layers. Due to the increased number of nozzles, the industrial inkjet printheads often require much more processing power to integrate in the printers than either the inkjet cartridges or the single nozzles. For all these reasons, the industrial inkjet printheads are well suited for large volume productions where ink jetting parameters are well known and where printing accuracy is of the upmost importance. The industrial printheads are also well suited for large area printing where the large number of nozzles is beneficial. The different inkjet printhead technologies are summarized in Figure 1.4 and includes the names of their main manufacturers.

Figure 1.4 Overview of the different types of inkjet printheads

Like the inkjet printhead technologies, inkjet printers can also be split into three categories covering different printing needs. The three categories are summarized in Figure 1.5 with examples of printers in each category. The most widely available inkjet printers are desktop consumer printers, these are the typical printers found in home offices or in small commercial shops. They are typically used for personal printing needs and for printing promotional materials such as posters and fliers. These printers make use of inkjet cartridges and are often limited in terms of the printing parameters which can be controlled. Generally, for these printers, only the printing resolution and the printing design can be controlled. Printing dot matrices, drop interpenetration, number of layers and geometry corrections are parameters which are adjusted automatically by the printing software depending on the printed design specified by the end user. These printers generally print in a sheet-to-sheet manner with a sheet

feeding mechanism. However, some printer designs allow for printing on continuous rolls of substrates and include a cutting mechanism to cut the roll into separate sheets.

Figure 1.5 Overview of the different types of inkjet printers

The next category of printers are R&D printers or prototyping printers. These printers are designed to allow for printing process development and often offer the greatest control over printing parameters and printhead compatibility. Some of these printers offer in situ pre- and/or post-printing processes such as photonic curing, ultraviolet (UV) light activation and/or surface

treatments. One such printer is the Ceradrop F-Series printer, which offer up to four (4) printhead slots and three (3) post-printing optical processing slots. The printhead slots can accommodate most of the inkjet printhead technologies; single nozzles, inkjet cartridges and industrial inkjet printheads. An extensive list of printing parameters can be controlled with these R&D geared printers via integrated printing software. Printing resolution, printing matrix arrangement, printing direction, printing height distance, number of printed layers, raster and layer overlap, and printing speeds are some examples of these controlled printing parameters. Moreover, these printers allow for control over jetting parameters such as the jetting waveform and jetting frequency. A jetting analyzer consisting of a camera and strobe light is typically found in these printers, allowing for jetting analysis and optimization. This total control over jetting and printing parameters makes this line of printers optimal for R&D purposes as it allows to optimize the full printing process. The ability to integrate different printhead technologies, from single nozzles to industrial printheads also allow the development of printing processes from ink jetting all the way to commercial and industrial viable processes. Figure 1.6 describes the Ceradrop F-Series printer used for this work with its key modules.

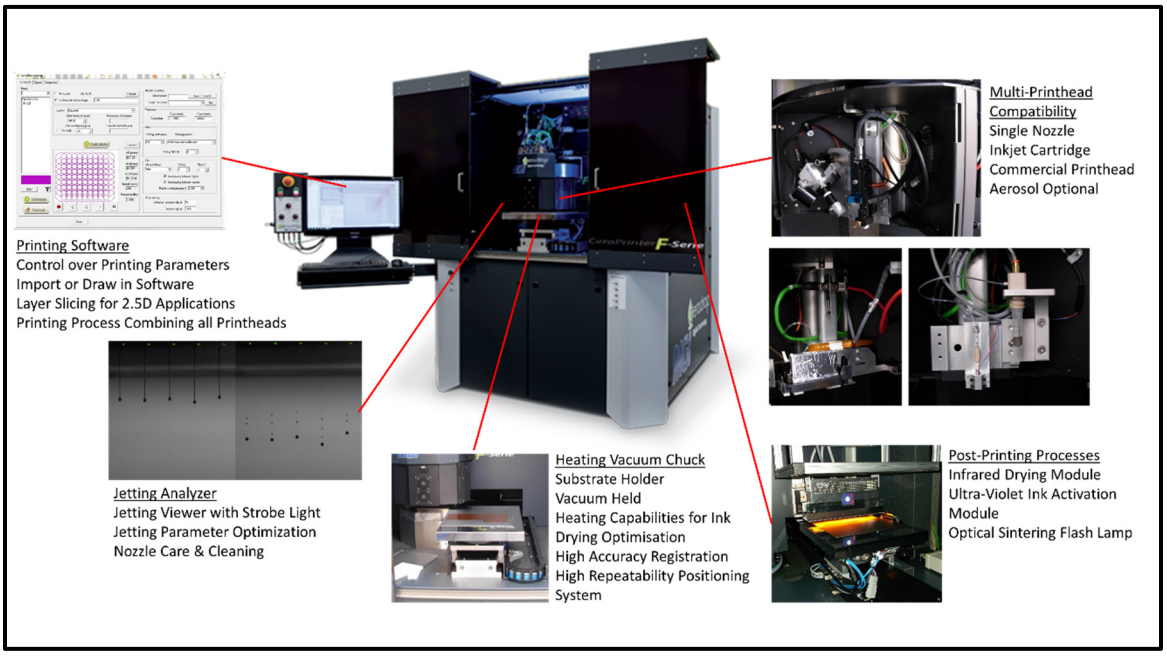

Figure 1.6 The Ceradrop F-series inkjet printer used in this work and its key components

The last category of printers are inkjet printing presses, these combine pre-printing processes, inkjet printing processes and post-printing processes to create a complete printing press where virgin substrates enter and final products exit. Printing presses can either be fed with rolls of substrates or work with a sheet feeding mechanism. Printing presses employ industrial printheads which can be placed in series (next to each other in a line) to cover wider areas and/or in parallel (one after another with respect to substrate movement) to print multiple layers of the same ink or to print different ink materials. These printing presses often offer the same control over printing parameters as the R&D printers although some parameters can be limited due to the other pre- and post-printing process limitations. The inkjet printing presses are optimal for medium to large volume productions, where printing processes have previously been optimized or are already well known. Typical printing presses contain the following process modules; a sheet feeder, a substrate priming module, inkjet printing module(s), ink drying or curing module(s), a substrate laminating module and substrate stacking and cutting module(s). An example of an inkjet printing press is depicted in Figure 1.7 with its key modules.

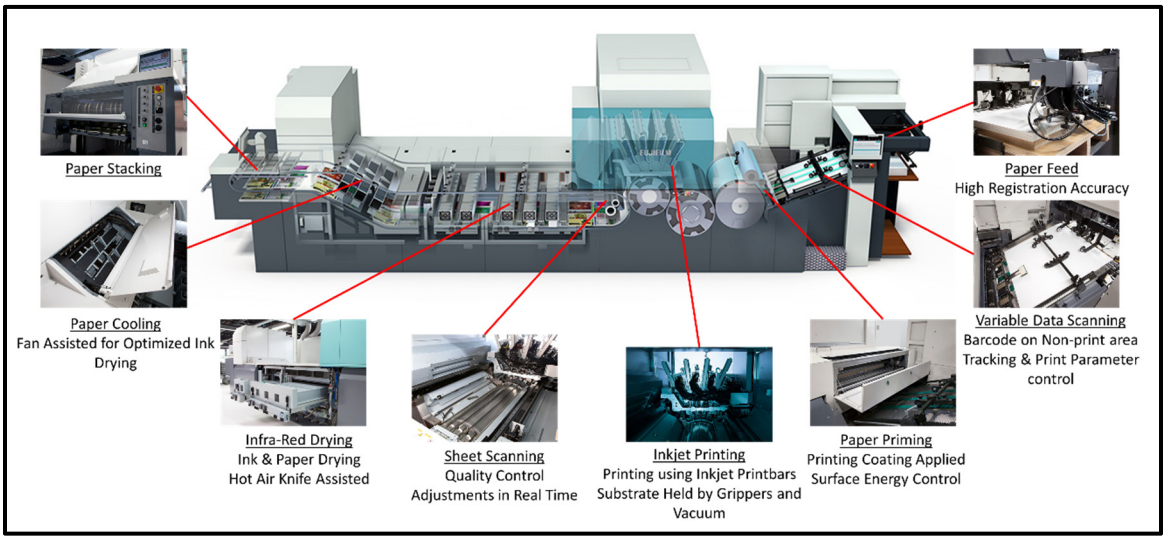

Figure 1.7 Overview of an inkjet printing press with its associated modules

With inkjet-printing, both the viscosity and the particle content of the ink are limited by the jetting process. Nozzle clogging happens readily with many types of inks due to thermal cycling, premature solvent evaporation and/or particle agglomeration at the nozzles. The typical viscosity range which can be adequately jetted with inkjet technologies is around 1 cP to 30 cP. This range can be expended somewhat and depends mostly on the nozzle diameter, this relationship is explored further in this work. (Alaman et al., 2016, p.910); (Derby, 2010, p.395-414) Particle sizes in inkjet ink should be kept below 10 % of the nozzle orifice diameter to avoid clogging at the orifice due to the agglomeration of particles. The main advantages of inkjet-printing, when compared to other printing processes, is;

1. Its flexibility in altering print designs.
2. The ability to print on almost any substrate.
3. The ability to have multiple print heads to print a multitude of different inks for device printing.
4. The low volume of ink material needed.
5. The reduced ink waste.

This makes inkjet printing optimal for prototyping purposes.

1.1.2 Other Printing Technologies

Digital Aerosol Printing

The digital aerosol printing process begins with atomization of an ink, either through sonication or a bubbler. This process typically producing micrometer sized to nanometer sized droplets. A mist is formed when the atomized droplets are carried in a gas stream to the print head. At this point, an additional flow of gas, called the “sheath gas”, is introduced to focus the mist into a tight beam, called the “aerosol jet”. Aerosol jets can be focused down to diameters as small as 10 μm with the right choice of gas flows and nozzle diameter (Mette, Richter, Horteis & Glunz, 2007, p.621-627); (Hedges & Marin, 2012, p.14-15). A mechanical shutter is used to block the aerosol jet flow to allow for controllable localized printing. The

aerosol printing process benefits from the wide range of inks that it can accommodate and adequately jet. Typical ink viscosities for aerosol printing range between 1 – 1000 cP (Navratil, Hamecek, Reboun & Soukup, 2015, p.36-39). However, for functional inks, the size and shape of particle content within the ink can be detrimental to the atomization and jetting processes. Aerosol jet printing is also advantageous for printing thin films (TFs) over large surface as it offers smaller ink droplets than with inkjet-printing and can be considered a continuous printing process. A schematic diagram of the aerosol jet printing process is shown in Figure 1.8.

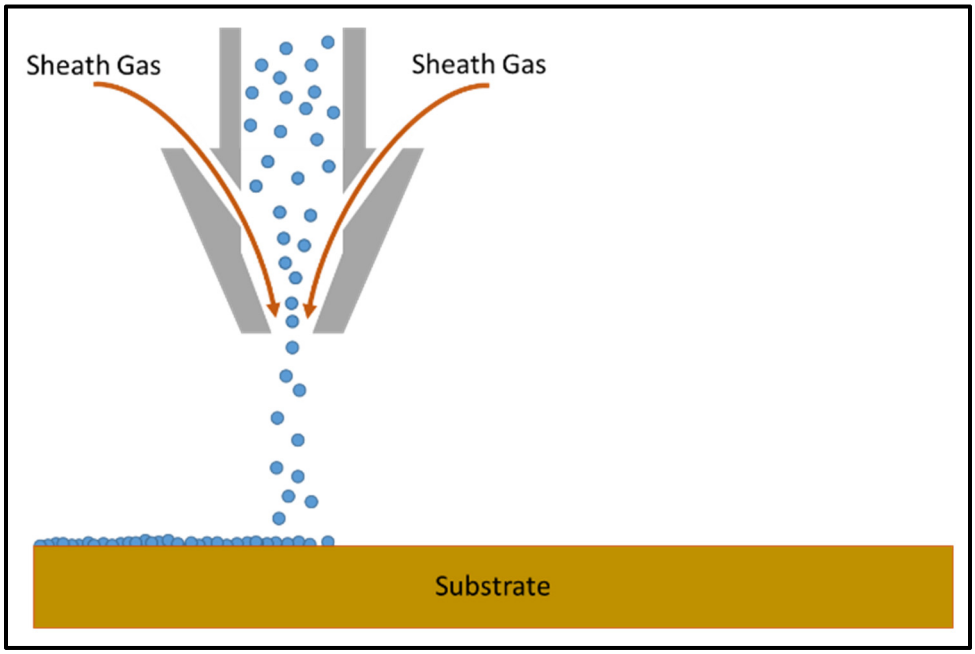

Figure 1.8 Schematic representation of the aerosol jet printing process

More recently, advances for printing on arbitrary 3D objects have been made using aerosol printing techniques. One of the novel state-of-the-art aerosol printer is the Optomec Aerosol Jet 5X printing system, and is presented in Figure 1.9. This 5X system consists of 2 rotational axes as well as 3 displacement axis to control displacement of the 3D object and the aerosol jet printhead. This allows for printing on all surfaces of an arbitrary 3D object. However, this

system can only accommodate small 3D objects and is not compatible for printing on large surfaces. Aerosol jet printing can be used in most of the same ways as inkjet printing, although larger starting ink volumes are required to form the aerosol, and thus is not as advantageous for R&D purposes where costly novel inks are often utilized. Additionally, aerosol jet printing is not as easily transferable to manufacturing-scale production systems, when compared to inkjet printing.

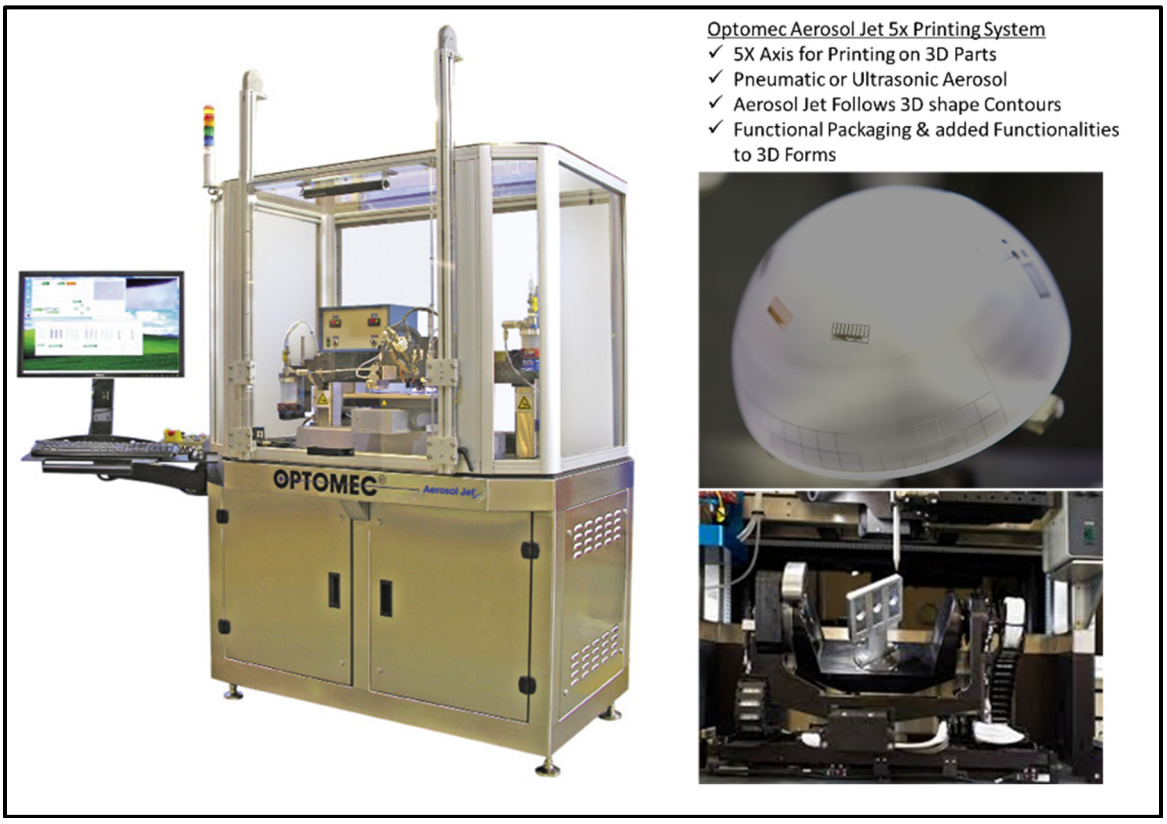

Figure 1.9 Overview of the Optomec aerosol jet 5X printing system

Roll-to-Roll Printing Processes

Roll-to-roll printing processes refer to any continuous printing processes on rolls of flexible substrates such as paper, plastics or metallic foil that are guided by rollers and re-reeled in an output roll. This output roll can then be cut or slit into sheets. The most common type of roll-

to-roll printing process is rotogravure printing. In this printing process, the ink is picked up through capillary action from an ink reservoir by engraved printing drums and deposited on the substrate by applying pressure with an impression roll. A doctor blade is often used to remove excess ink from the printing roll. Roll-to-roll processes benefit from very high printing speeds, in the range of 10s of meters per minute (Nguyen, Lee, Kim, Shin & Lee, 2013, p.095010), good reproducibility of the depositions and low production costs per unit. Roll-to-roll processes suffer from high start-up costs which come from the cost of the equipment, the large quantities of ink needed for running the equipment and the cost of fabricating the engraved printing drums. This results in a printing process that is ideal for very high-volume production but suffers greatly in terms of flexibility and adaptability of print design. A schematic diagram of a rotogravure roll-to-roll printing process is shown in Figure 1.10.

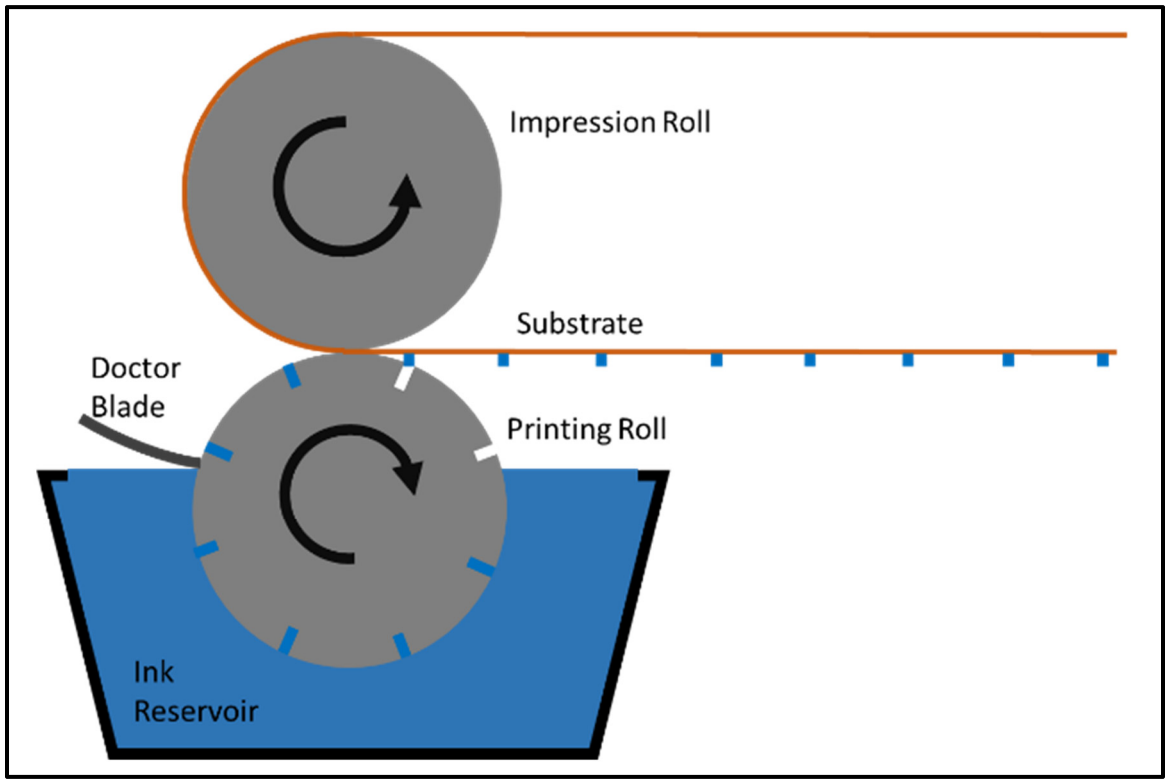

Figure 1.10 Schematic representation of the rotogravure roll-to-roll printing process

The most notable uses of roll-to-roll printing processes are for high volume printing presses for newspapers, fliers, catalogues and magazines. Although some advances have been made in the recent years for printing active materials to fabricate electronic and other active devices. While it generally uses non-digital printing approaches reserved for very high production volumes, digital inkjet printing can also be made compatible with roll-to-roll processes in state-of-the-art industrial inkjet printers, as shown in section 1.1.1. This can improve print flexibility by enabling printing design changes in real time.

1.2 Inks

Conductive inks form the basis for all printed electronic processes. There exist different types of conducting inks which are often tailored to specific applications. The most widely used conductive inks are spherical metallic nanoparticle (NP) inks. However, there also exists metallic nanowire inks which can also be considered metallic NP inks. Other conductive inks can take the form of graphene and carbon nanotube (CNT) based inks that can form conductive networks, conductive polymeric inks such Poly(3,4-ethylenedioxythiophene) polystyrene sulfonate (PEDOT:PSS) or conductive glass such as fluorine tin oxide (FTO) and indium tin oxide (ITO) solutions that can be adapted for PE.

Most NP inks are based on either Ag, Au or Cu metals, these metals are suited for PE due to their relatively low melting points (in NP form) for sintering purposes and their low reactivity with ambient atmospheric conditions. Ag NP inks are the most popular inks for general printing purposes due to their lower cost and comparative conductivities to Au NP inks (Kamyshny, Steinke & Magdassi, 2011, p19-36). Au NP inks are used when inert conductive printed lines or layers are needed, as is often the case for biocompatible applications (Li et al., 2010, p.689-700). Finally, Cu NP inks can be problematic due to their rapid oxidation in ambient atmosphere, as it creates a non-conductive oxide layer (Jeong et al., 2008, p.679-686). Nonetheless, commercially available Cu inks which are stable in ambient atmosphere are now available. These stem from adding an excess of reducing agent within the ink formulation (Grouchko, Kamyshny & Magdassi, 2009, p.3057-3062); (Wu & Chen, 2004, p.165-169).

These NP inks are generally very similar in their makeup, they are based on a suspension of metallic NPs in a dispersion of water based or alcohol-based solutions. Stabilizing agents or ligands are often used to cap the NPs to avoid aggregation and precipitations of the NPs (Kamyshny et al., 2011, p.19-36). The viscosity, surface tension and wettability of the inks should be tailored to the ink-jet printing process as well as to the printing substrate. This can be done by tailoring the concentration of polymeric additives, surfactants as well as the solvent composition of the inks (Magdassi, 2010, p.19-41).

There are some advantages to using other shapes of NPs such as nanowires. For example Ag nanowires are used instead of spherical NPs when transparent conductive layers are needed, the nanowires form a conductive network that offer a balance between optical transmission and conductivity based on the dimensions and concentration of the nanowires (Langley et al., 2013, p.452001); (Hu, Kim, Lee, Peumans & Cui, 2010, p.2955-2963). Metallic nanowire inks can be used to replace conventional transparent electrodes such as ITO and FTO as they can often offer better conductivity and transmission properties than these conventional materials. Additionally, nanowire inks can be tailored to achieve films with a range of haze factor between 1-30 %. A high haze factor can be useful for transparent electrodes in PV devices as it results in a larger effective absorption cross section due to the increased path length of the light from scattering (Langley et al., 2013, p.452001); (Preston, Xu, Han, Munday & Hu, 2013, p.461-468). Moreover, metallic nanowires inks in combination with an elastomer such as polydimethylsiloxane (PDMS) can be used to fabricate highly stretchable conducting films (Ho, Nie Tey, Lui, Kweng Cheng & Wei, 2013, p.044311); (Martinez et al., 2015, p.13467-13475). For ink-jetting purposes, nanowire-based inks can cause clogging problems at the nozzles due to their lengths which are often comparable to the commercially available inkjet nozzle diameters.

Spherical NPs size typically range from 40nm up to 130nm in diameter and primarily affects the sintering temperature of the ink which can range from 120 °C to 550 °C depending on the metal and the size of the particles (Qi & Wang, 2004, p.280-284); (Yeshchenko, Dmitruk, Alexeenko & Dmytruk, 2007, p.085434). The inks can vary in their metallic NP loading,

typical values range from 10 wt% to 60 wt% metallic NPs. Typical viscosities for ink-jet adapted metallic NP inks range from 1-20 cP.

Other conductive inks include carbon-based inks such as CNT and graphene. Like the metallic NP inks, these carbon-based inks consist of a suspension of the carbon material in an aqueous solution, typically water or alcohol based. Again, an addition of stabilizing agents, surfactants, polymeric additives and functional groups can be added to the ink formulation to tailor the rheological properties of the ink as well as to help with aggregation and precipitations of the carbon particles. CNTs, functionalized or not, offer the same advantages, in terms of transmission and stretchability, as metallic nanowire inks (Xie & Wei, 2016, p.159-191). Another advantage over other conducting inks is the option to functionalize the CNTs which can add new modalities and be used to create chemical sensors for example (Hester, Tentzeris & Fang, 2015, p.857-860).

Another material of interest is titanium dioxide (TiO_2), an amorphous material which can be crystallized into its three main crystal phases, namely rutile, anatase and brookite. As presented later in this work, TiO_2 can be used as an electron transport layer (ETL) for PV devices. TiO_2 materials come in many forms, from NPs powder suspensions (Reyes-Coronado et al., 2008, p.145605) to sol-gels (Ohya, Saiki, Tanaka & Takahashi, 1996, p.825-830); (Lee et al., 2010, p.1958-1965). These can be deposited via multiple methods such as screen printing (Lee et al., 2010, p.1958-1965), spin coating (Ohya et al., 1996, p.825-830); (Wang et al., 2015, p.9108-9115), spray coating (Fujihara, Kumar, Jose, Ramakrishna & Uchida, 2007, p.365709) and sputtering (Hong et al., 2005, p.946-949); (Lobl, Huppertz & Margel, 1994, p.72-79). The TiO_2 optimization in term of optoelectronic properties and transparency depends on the thickness, arrangement and composing ratio of the crystalline phases (Reyes-Coronado et al., 2008, p.145605); (Ohya et al., 1996, p.825-830); (Lee et al., 2010, p.1958-1965). Preliminary studies performed at École de Technologie Supérieure (ETS) have demonstrated the use of laser annealing in order to control this multi-phasic crystallization process. This is a step towards processing TiO_2 at low temperatures, as conventional crystallisation of TiO_2 is performed at relatively high temperatures, between 200 °C and 750 °C (Lee et al., 2010, p.1958-1965);

(Hong et al., 2005, p.946-949). There have been other development efforts to achieve low temperature processing of TiO_2. For example, with the inclusion of additive to the TiO_2 NP solution, annealing temperatures can now be reduced to 150°C (Wang et al., 2015, p.9108-9115).

1.3 Inkjet Printing in the Industry

1.3.1 Global Market

In broad terms, advances in the field of PE, no matter how small, play a role in the development of low-cost, flexible electronics and photonics. PE has emerged into a large worldwide market, a 2013 report on printed, organic and flexible electronics by IDTechEx showed an expected $38 billion market in 2018 and a projected market of ~$80 billion in 2023 (Dar & Harrop, 2013, p.110-166). The OLED display market is by far the most dominant market in the field of PE, with a $29 billion market, or a 76 % share of the whole PE market. This market encompasses mobile phone displays, television displays and other display applications. Printed electronic processes are often used in combination with other fabrication processes to achieve complete fabrication of the OLED displays. As such, there is ample room for further expansion of PE market for these applications. The next largest market are PVs and conductive inks. For PV applications, the ability to print on large surfaces and on flexible substrates is highly beneficial. This enables the fabrication of low weight PV modules which are more easily transported and installed. Once again, hybrid fabrication processes are often used but printed processes are starting to replace increasingly more conventional fabrication processes. The conductive ink market both drives and is dependent on the other markets. It is advances in the ink technologies which enable printing processes to be viable for device fabrication. When these processes are optimized, they become advantageous for device fabrication and in turn drive the need for larger ink volumes. Furthermore, application markets for sensors, batteries and OLED lighting have started to emerge in the recent years, these application markets are expected to boom exponentially in the next years. Advances in low temperature compatible processes as well as the increasing need for flexible and cheap devices are driving the market

for fabrication on flexible substrates. In 2013, devices on flexible substrates only accounted for 5 % of the device market, this is expected to increase to 15 % of the devices in 2023.

There are many market leaders in each of the application fields of printed, organic and flexible electronics. Some of these leaders are present in a few of the fields, bridging together ink production, printing technologies and device fabrication. A few notable market leaders are Kateeva, HP, Xerox and Fujifilm. These companies' work encompasses ink production, printing optimization, equipment fabrication and in some cases device fabrication. HP, Xerox and Fujifilm are well known companies which have started in the graphical arts domains, they are known as equipment fabricant and as ink manufacturers. More recently, these companies have started to enter the field of PE and have a wide range of products which are adapted for PE processes. Kateeva is a more recent company which manufactures inkjet printing equipment and develops processes for large scale OLED display printing, specifically for mobile phone and television displays. A wide range of large and small companies specializes in ink or solution production, such as Henkel, 3M, Advanced Nano Products (ANP), Ossila and Dupont. These companies range in offering a few specialized products to providing a wide variety of products for different applications. A full ecosystem of ink production, distribution, equipment fabrication, device fabrication and packaging and of commercial and industrial sales is currently being built to answer the rapidly expending printed, organic and flexible electronics market. A major part of the expending demand originates from the evolution of the IoT in which low-cost, flexible large area devices are wanted for communication, mass data collection and processing purposes.

1.4 Conclusion

The main printing technologies used in PE have been identified and explained. The state-of-the-art in inkjet printing equipment and processes have been explored, from single nozzle ink jetting to industrial scale printing presses. An overview of the ink materials currently used in PE and their properties has been presented. NP metallic inks are currently the most utilized inks in the PE field, although great advances in functional inks have already been made and

more are currently underway. Finally, the global market for PE is explored. An exponential growth in this market is projected for the future, with an estimated ~$80 billion market for 2023.

CHAPITRE 2

OVERALL RESEARCH OUTLINE

2.1 Research Objectives

Since 2012, MALH PS have shown tremendous potential for low-cost optoelectronic device integration (Snaith, 2013, p.3623-3630), including light-emitting diodes (Lin et al., 2018, p.245), solar cells (Saliba et al., 2016, p.1989-1997); (Lee et al., 2015, p.41-46) and photodetectors (Spina et al., 2016, p.4888-4893); (Fang et al., 2015, p.679-686); (Saidaminov et al., 2015, p.8724); (Ka, Gerlein, Nechache & Cloutier, 2017, p.45543); (Noh, Im, Heo, Mandal & Seok, 2013, p.1764-1769). For example, the power-conversion efficiencies from organometallic halide perovskite solar cells have increased to 22.1 % in less than ten (10) years (NREL, 2017); (Saliba et al., 2016, p.1989-1997); (Lee et al., 2015, p.41-46). This spectacular progress is largely attributed to improved processing and longer charge-carrier lifetimes directly related to increased material quality. Yet, fundamental challenges including low carrier mobilities still prevent the fabrication of large-area devices with performances competing with state-of-the-art technologies. For this reason, several groups including ours, began exploring hybrid perovskite films over the last five (5) years. Our team has made tremendous ground-breaking progress towards viable PS commercial devices produced from all-solution precursors by;

1. Enhancing PS structure and properties through solvent engineering (Gedamu et al., 2018, p.12885); (Hooper et al., 2015, p.482-487); (Hasan, Hamja & Islam, 2015, p.26-29); (Liang et al., 2014, p.3748-3754).
2. Increasing their conductivities by using MALH hybrids (Docampo et al., 2013, p.2761); (You et al., 2014, p.1674-1680) (Wang et al., 2015, p.9108-9115); (Tai et al., 2016, p.11105).
3. Improving stability and lifetime using doped MALH structures (Asuo et al., 2019, p.110029).

More importantly, we sought the ability to adapt precursor formulation and processing to realize stable high-quality PS based films and devices using commercial-grade digital inkjet printing capabilities.

As such, the primary objective of this thesis and research is to assess the potential of fabricating new flexible PS based optoelectronic devices based on established device architectures using commertial-grade digital inkjet printing processes. The work focuses on converting conventional fabrication processes to printing processes, efforts are also expended into modifying device architectures to achieve flexible device fabrication and improve printed device performances. This primary objective is expended into two sets of objectives, namely;

1. Objectives pertaining to digital inkjet printing optimization.
2. Objectives pertaining to MALH PS based optoelectronic device printing.

Furthermore, due to their compatibility with temperature sensitive flexible substrates and organic materials, optical post-printing processes are starting to replace conventional annealing processes, especially in the fabrication of flexible and organic devices. To gain a better understanding of optical post-printing processes and light – matter interactions, laser sintering simulations are performed, and transient heating behaviors are studied. The purpose of these simulations is to pave the way for future implementation of laser sintering processes for device fabrication using printing technologies. This provides the third set of objectives for this thesis;

3. Objectives pertaining to laser sintering simulations.

2.1.1 Specific Objectives Pertaining to Digital Inkjet Printing Optimization

The main objective of inkjet printing optimization is to become familiar with the inkjet printing process and to establish optimized printing procedures for a multitude of ink materials. Below is a breakdown of the key objectives for inkjet printing optimization;

1. Identify ink material candidates for device fabrication.
2. Establish ink manipulation procedures.
3. Perform jetting test plans to achieve stable jetting.
4. Establish substrate cleaning and manipulation procedures.
5. Establish and optimize pre-printing processes for optimized printing.
6. Perform printing test plans to achieve optimized printing parameters for given layer thicknesses.
7. Establish post-printing processes for ink layer activation.
8. Inkjet printing of passive device and generic device structures.

A list of necessary materials, or alternatives, in ink form needs to be acquired or formulated if not commercially available. For each of these materials, a process flow needs to be created which includes the pre-printing, post-printing and the actual printing processes with the required parameters to achieve final desired material and printed feature properties. These parameters include the jetting waveform and frequency, chuck and nozzle temperatures, printing matrix, drop volume, annealing times and temperatures, ink formulation, as well as the substrate treatment parameters. It is the combination of the printing process as well as the pre- and post-printing processes which will allow for the conversion of conventional device fabrication processes to device printing processes.

2.1.2 Specific Objectives Pertaining to Methylammonium Lead Halide Perovskite-Based Optoelectronic Device Printing

The main objective in MALH PS-based optoelectronic device printing is the fabrication of working optoelectronic device prototypes using optimized printing procedures established in this work. By doing this, the potential of fabricating PS-based devices using inkjet printing processes can be assessed. Starting from identified device architectures, device prototyping is first performed on rigid substrates, the process is then adapted for printing on flexible substrates and later for printing flexible device arrays. Below is a breakdown of the key objectives for MALH PS-based optoelectronic device printing;

1. Identify device architectures adapted for inkjet printing.
2. Use optimized printing parameters for printing devices on rigid substrates.
3. Adapt printing processes for printing devices on flexible substrates.
4. Adapt device architecture to enhance performances for devices printed on flexible substrates.
5. Use adapted device architecture for printing device arrays.
6. Perform optoelectronic device characterization.

At the start of this research, a literature review of PS-based PV devices will need to be performed to evaluate viable device architectures. It is envisioned that once device prototypes can be printed on rigid substrates, further optimization of the device architecture and of the printing process will be needed to achieve prototyping on flexible substrates. The original objective is to create PS solar cells, which are sensitive to the visible light spectrum. Finally, characterization of the printed materials and of the device prototypes will be performed to evaluate their properties and to allow for future optimization of the printing processes.

2.1.3 Specific Objectives Pertaining to Laser Sintering Simulations

The main objective for the laser sintering simulations is to acquire a better understanding of the effects of time-domain pulse shaping on laser sintering of Ag NP ink using COMSOL simulation software. The simulations are modelled after real-world experiments and are performed to understand and explain the experimental results as well as to facilitate optimization of time-domain pulse shaping for laser sintering. Furthermore, the simulations are performed to understand supporting substrate transient heating behavior induced by laser sintering of the supported ink trace. Below is a breakdown of the key objectives for the laser sintering simulations;

1. Model ink trace and substrate geometries with adequate material properties.
2. Model laser excitation pulse trains as heat source, based on experimental data.
3. Acquire transient heating behavior of the ink trace.

4. Relate transient heating behavior of the ink trace with experimental results.
5. Acquire transient heating behavior of the supporting substrate.

2.2 Outline of Thesis Chapters

This thesis is divided into eight (8) chapters. Chapter 1 pertains to the state-of-the-art of printing technologies and their use in the current industrial and commercial markets. Chapter 2 describes the research objectives of this work and the outline of this thesis. In Chapter 3 an extensive literature review of material properties, PS-based optoelectronic devices and device fabrication using digital inkjet printing processes, is performed. In Chapter 4 the optimization of the printing processes, from ink choice and ink jetting to optimization of printing parameters is presented. In Chapter 5, passive devices and generic multilayered device structures are printed using optimized printing parameters. Chapter 6 includes the digital inkjet printing process for PS-based optoelectronic prototyping on rigid and flexible substrates as well as the optoelectronic characterization of said devices. In Chapter 7, optical laser simulations using COMSOL 5.2 simulation software are presented and support real-world time-domain modulated laser sintering. Finally, envisioned future works are presented in Chapter 8. Figure 2.1 illustrates how each of the components of this thesis relate to one another to help form a clearer picture of this work.

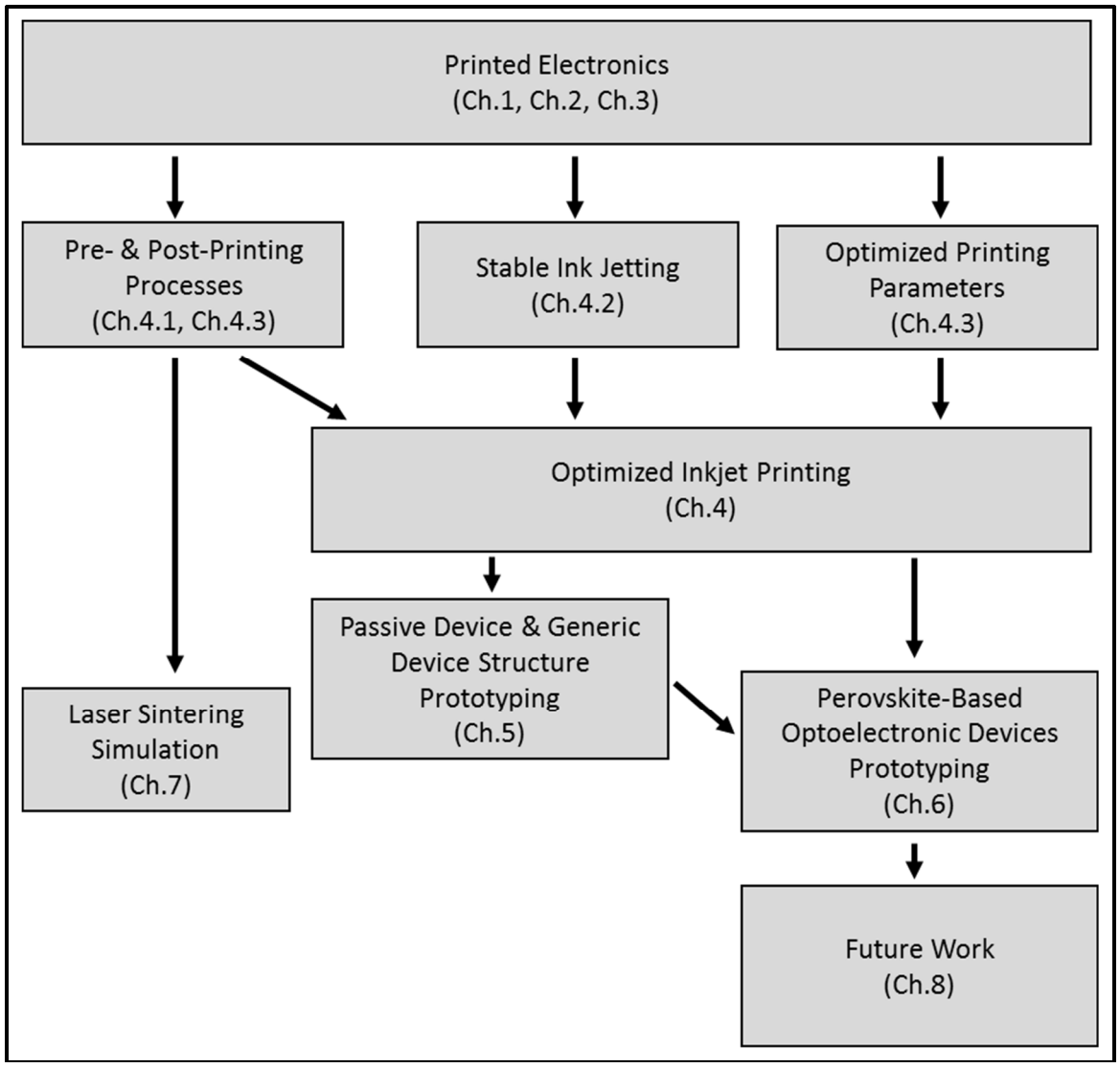

Figure 2.1 Thesis overview and structure

CHAPITRE 3

LITTERATURE REVIEW

In this chapter, an overview of the literature review performed for this thesis is presented. First, a short review of the working principles of the devices fabricated in this work are presented, namely photodetectors and thermistor devices. The importance of the PN junction and how it is used in photodetector devices for energy harvesting and current generation purposes, is presented. Performance metric characteristics for each device type are detailed and provide an understanding of the device characterization performed throughout this work.

Secondly, an overview of PS materials is presented and contains details of how their unique properties are used to replace conventional PN junctions for photodetector device operations. An extensive review of PS based photodetector devices is also presented, showing popular device architectures, fabrication methods and achievable device performances. Parallels are drawn between current fabrication techniques and the envisioned device fabrication using printing techniques.

Finally, a review of digital inkjet printing as a device fabrication method is presented. The complete printing process, including pre-printing and post-printing processes, is explored and detailed. This provides a basis for understanding the different processes used for device printing. The major hurdles to achieve stable jetting and optimised printing are also explored along with a literature review of current advances in terms of fully inkjet printed devices. In this review, the advancements made in the literature, in terms of device fabrication for the past 15 – 20 years, are detailed. From passive conductive trace printing to active multi-stack solar cell printing, these advancements are presented using a list of examples.

3.1 Devices and Working Principles

3.1.1 Photodetector

Photodetectors or photo sensors are devices which can sense light or other electromagnetic radiation. Typically, photodetectors have PN junctions that converts light or other electromagnetic radiation into an electrical current which can be measured. The absorbed photons make electron–hole pairs, also called excitons, in the depletion region. Photodiodes, photo transistors, photo-resistances and other PV devices such as solar cells are examples of photodetectors.

PN Junction

A PN junction generally consists of the junction between two types of extrinsic semiconductor materials, a p-type and an n-type material, somtimes inside a single crystal of semiconductor. Extrinsic semiconductors are semiconducting materials in which foreign dopants have been incorporated. The p-type material contains added electron acceptors which accept electrons from the lattice, creating vacancies (holes) in the valence band of the lattice while the n-type material contains added electron donors which release electrons to the conduction band of the lattice. Typically, these added electron acceptors and donors in PN junction are created by doping, such as ion implantation, by the diffusion of dopants, or by epitaxial growths of the two semiconductors. This allows an electrical current to pass through the junction but only in one direction. When two separate materials are used, grain boundaries can be introduced between the semiconductors and can reduce performances by scattering the electrons and holes and/or providing recombination centers (Seager, 1981, p.3960-3968); (Sherkar et al., 2017, p.1214-1222); Jensen et al., 2000, p.2639-2645). PN junctions are the elementary components of semiconductor electronic device operations such as photodetectors, PVs and transistors.

In a PN junction, with no external voltage applied, an equilibrium is reached in which a difference in potential, called the built-in potential, is formed across the junction. Near the

junction of the p- and n-type semiconducting materials, electrons from the n-type region diffuse to the p-type region. Similarly, holes diffuse from the p-type region to the n-type region. The diffused electrons and holes recombine with the opposite charge carriers and form negative charged ions in the p-type region and positive charged ions in the n-type region. The regions near the p–n interface lose their effective neutrality and most of their mobile carriers, forming a space charge region, also known as the depletion region. An electric field is created from the depletion region where charge carrier concentrations are non-constant, this electrical field opposes the diffusion of both holes and electrons. A schematic representation of a PN junction without an applied external bias is presented in Figure 3.1, along with representative charge carrier concentrations. A similar junction may be formed using an intrinsic semiconductor between the p-type and n-type extrinsic semiconductors, this is called a p-i-n junction. These junctions work in much of the same ways as PN junctions but tend to have larger depletion regions and weaker electric fields within this region due to the added material layer.

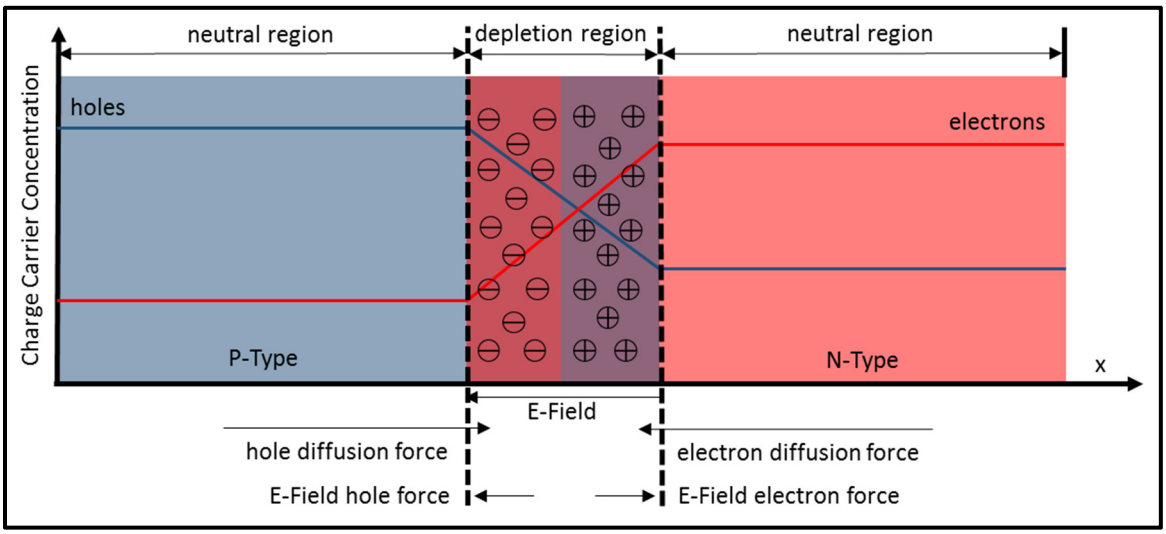

Figure 3.1 Schematic representation of a PN junction formation

An external forward or reverse bias can be applied to the PN junction. For a forward bias, the p-type material is connected to the positive terminal and the n-type material is connected to the negative terminal, countering the effective electric field and reducing the width of the

depletion region. For reverse bias, the p-type material is connected to the negative terminal and the n-type material is connected to the positive terminal, enhancing the effective E-field and increasing the width of the depletion region. In the case of forward bias, the majority charge carriers of the n-type material (electrons) are pushed across from the n-type region to the p-type region. If the depletion region is narrow enough, electrons can be injected into the p-type material. However, these electrons cannot flow indefinitely in the presence of a high concentration of holes and eventually recombine. The average length a minority charge carrier can travel through a semiconductor is called the diffusion length.

Energy Levels & Band Diagrams

Energy levels and band diagrams for devices or junctions can be obtained from charge carrier concentrations, applied electrical field and inherent material properties. The band diagrams are often utilized to explain the operation of semiconductor-based devices and to visualize band bending. Band diagrams depict four (4) main defining characteristics of the junction as a function of position;

1. The valence band.
2. The conduction band.
3. The Fermi level.
4. The band gap.

The valence band of a semiconductor refers to the outermost electron orbital of the atoms and is the highest energy a bound electron can occupy before it can be excited to the conduction band. The conduction band is the lowest energy level at which an electron can be considered as a free electron. Free electrons in the conduction band participate in electrical conduction. The Fermi level is the highest energy state occupied by electrons in a material at a temperature of absolute zero, the relation of the conduction and valence bands to the Fermi level are crucial in dictating electrical properties (Seto, 1975, p.5247-5254); (Tell, Shay & Kasper, 1971, p.2463); (Tang, Prasad, Sanjines, Schmid & Levy, 1994, p.2042-2047). The band gap of a

semiconductor is the difference in the energy levels of the conduction and valence bands, it is the minimum energy required to excite a bound electron in the valence band into a free electron in the conduction band. A schematic representation of a band diagram is presented in Figure 3.2.

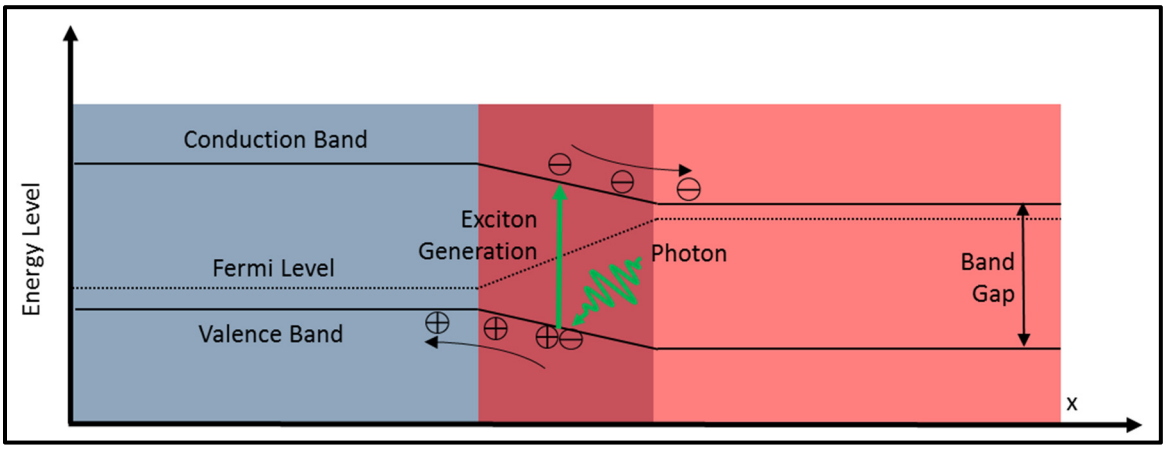

Figure 3.2 Schematic representation of energy band levels and exciton formation of a PN junction

Photo-Generated Current

The photo-generated current is the current which is generated from light incident on a solar cell. The photo-generation of current involves two key processes. The first process is the absorption of incident photons to create electron-hole pairs. The electron-hole pair is generated in the solar cell provided that an incident photon has an energy greater than that of the band gap. Thus, exciting the electron from the valence band to the conduction band. A hole is created where the electron was formerly bound, this hole also participates in conduction. Minority charge carriers are meta-stable and will recombine. On average, this recombination happens after a length of time equal to the carrier lifetime. If the carrier recombines, no current is generated. Therefore, the minority charge carriers need to be spatially separated and collected at their respective electrodes to avoid recombination. The second process in the photo-generation of current is this separation and collection of the minority charge carriers. The

electrical field inside of the PN junction is used to spatially separate the electron and the hole. As the minority charge carriers reach the PN junction, they are accelerated across the junction where they effectively become majority charge carriers and can then be collected by their respective electrodes. Electron-hole pairs must be generated close to the depletion region of the PN junction, as minority charge carriers are mainly affected by diffusive forces outside of the depletion region and must be able to reach it to be collected. If electron-hole pairs are generated further than one minority carrier diffusion length away from the depletion region of the PN junction, the collection probability of the charges is low. The amplitude of the photo-generated current is depended on the amount of generated charges which can be excited, separated and collected, which in turn is dependent on the number of photons that are incident on the device.

Effect of defects

Defects within PN junctions can take many forms, such as, point defects, impurities, grain boundaries and geometric defects such as uneven extrinsic semiconductor layer thicknesses, to name a few. These defects often result in the introduction of parasitic resistances and/or recombination centers for charge carriers, also known as trape states.

As noted above, recombination of charge carriers prior to collection is detrimental to solar cell operation as it reduces collection probability and thus the photo-generated current. To reduce the probability of introducing recombination centers, high purity semiconductors with large crystalline grain sizes are typically preferred. Moreover, recombination centers are often present at material boundaries and surfaces due to defects of the crystal lattices from boundary conditions. Materials with low surface roughness and homogeneous material layers are therefore beneficial as they reduce surface boundary areas.

Two types of parasitic resistances can be introduced in PN junctions and solar cells, namely, series and shunt resistances. The series resistance comes from contact resistances between the semiconductors and their respective electrodes, the resistances of these electrodes and the

current passing through the solar cell. This resistance causes dissipation of the power generated by the solar cell, thus reducing device performances. More specifically, a high series resistance reduces device fill factor and, in some cases, can also reduce the short ciruit current. Unlike series resistance, the shunt resistance is essentially the resistance of all alternate pathways for the photo-generated current to pass through, bypassing part of the theoretical device junction. A high shunt resistance is wanted to minimize power loss through these alternate pathways. A low shunt resistance reduces device fill factor and, and more importantly, has a greater negative impact on the open circuit voltage. Shunt resistances are often introduced from manufacturing defects such as incomplete or uneven extrinsic semiconductor deposition.

Device Characterization

Photodetectors can be characterized by the following performance metrics which describe the response of the devices;

1. Spectral response.
2. Quantum efficiency.
3. Responsivity.
4. Noise-equivalent power (NEP).
5. Gain.
6. Dark current.
7. Response time.

The spectral response is measured in A/W and is the current response of the device as a function of incident light of specified wavelengths. The quantum efficiency of the device is tied to number of generated charge carriers (electrons and holes) from each absorbed photon and is measured as a percentage following Equation 3.1. The external quantum efficiency (EQE) or the internal quantum efficiency (IQE) can be considered, where the latter takes into account only the photons that are absorbed by the device.

$$EQE = \frac{electrons/s}{photons/s} = \frac{(I/e)}{(P_{photon}/hv)} = IQE(1 - \mathbb{R}) \tag{3.1}$$

Where I is the current response, e is the elementary charge of an electron, P_{photon} is the total power of the incident photons, hv is the energy of one photon and $\mathbb{R}$ is the light reflection coefficient of the device.

The responsivity is the measured current response of a device divided by the power of incident light of specified wavelength or wavelength ranges and is also given in A/W. The NEP is given in $W/Hz^{0.5}$ and is tied to the amount of light power which is needed to generate a response similar to the electrical noise of the device. One method of calculating NEP values is with the specific detectivity and is presented in Equation 3.2.

$$NEP = \frac{\sqrt{A_{device} f}}{D^*}, \quad D^* = \frac{\sqrt{A_{device}}\,\mathfrak{R}}{S_n} \tag{3.2}$$

Where A_{device} is the device area, f is the frequency bandwidth and D^* is the specific detectivity, S_n is the noise root mean square (RMS) signal and $\mathfrak{R}$ is the responsivity.

The gain of a device is the ratio of the output current of the detector with the current directly produced by the incident photons. The dark current is a measure of the current at 0 bias when the device is not illuminated. Finally, the response time is the time required for the device to go from 10% to 90% output in the presence of a signal.

While PV devices can be further characterized with the following performance metrics, measured under standard light exposure;

1. Open circuit voltage (V_{oc}).
2. Short circuit current (I_{sc}).
3. Fill factor (FF).

4. Power conversion efficiency (PCE).

The V_{oc} is the voltage at which a zero (0) current is measured while the device is under standard illumination. The V_{oc} corresponds to the amount of forward bias on the PV device due to the bias of the PN junction with the light-generated current. The I_{sc} is the negative current measured while the device is operated at 0 V bias and under standard illumination. The I_{sc} is due to the collection of light-generated carriers. For an ideal solar cell, the I_{sc} and the light-generated current are identical. The FF is a measure of the total efficiency of the cell and represents the ratio in power from the maximum power point (MPP) and the theoretical power obtained from V_{oc} and I_{sc} values. The PCE is the total efficiency of the solar cell and is a ratio of the power obtained from the MPP and the power of a standard 1-sun illumination incident on the cell area. Figure 3.3 illustrates the main I-V characteristics of a solar cell under dark and illuminated conditions.

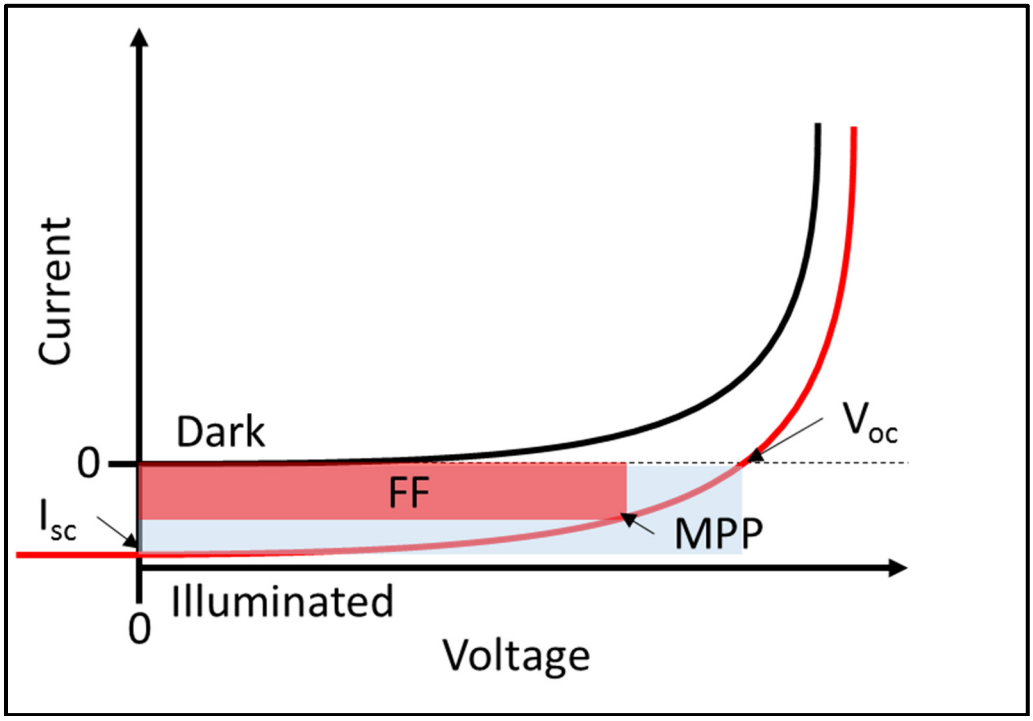

Figure 3.3 Schematic representation of typical solar cell I-V characteristics

3.1.2 Thermistors

Thermistors are types of resistors whose resistances are much more dependent on temperature than standard resistances. These devices can therefore measure temperatures changes by measuring the change in resistance. Thermistors are widely used as current limiters, temperature sensors, overcurrent protectors, and self-regulating heating elements (Dougal, 1996, p.304-310); (Muralidharan, Rohini, Sunny, Dayas & Seema, 2012, p.6481-6486) (Feteira, 2009, p.967-983); (Liang & Tsai, 2005, p.443-449); (Zhang, Pan & Zheng, 2000, p.424-429). There are two types of thermistors which work in fundamentally different ways.

Negative temperature coefficient (NTC) thermistors are thermistors in which the resistance decreases as temperature increases. NTC thermistors are typically used for direct temperature sensing and can be also be used as current limiters (Muralidharan et al., 2012, p.6481-6486). On the other hand, positive temperature coefficient (PTC) thermistors increase in resistance as the temperature increases. PTC thermistors are often used to serve as overcurrent protectors such as resettable fusses (Zhang et al., 2000, p.424-429).

NTC

Many NTC thermistors are made from a pressed disc, rod, plate, beads or cast chips of semiconducting material. As the temperature of the semiconductor increases, the chances of a charge carrier to be promoted to the conduction band is increased and results in an increased number of charge carriers participating in conduction. The more charge carriers can participate in conduction the less resistive the material becomes. Both p-type and n-type semiconductors can be used where holes and electrons are used as the charge carriers, respectively (Turner, 2013, p.6.29-6.41). The current in NTC thermistors can be calculated with Equation 3.3.

$$I = n \cdot A_{cross-section} \cdot v_{drift} \cdot e \tag{3.3}$$

Where I is the current in amperes, n is the density of charge carriers per unit volume and is dependent on temperature, $A_{cross\text{-}section}$ is the cross-sectional area of the material, v_{drift} is the drift velocity of the charge carrier and e is again the elementary charge of an electron in coulombs.

PTC

On the other hand, PTC thermistors are typically made from doped polycrystalline ceramic which have abrupt changes in resistances at certain critical temperatures. Some PTC thermistors make use of ferroelectric materials with dielectric constants which vary with temperatures. Below the Curie point temperature, a high dielectric constant is present and prevents potential barriers between crystal grains, promoting conduction and resulting in low resistances. Above this temperature the dielectric constant drops and potential barriers can form at the grain boundaries, resulting in a sharp increase in resistance.

Another type of PTC thermistor is the polymer PTC thermistor, which consists conducting carbon grains embedded in a polymer material. When the polymer is cooled, it shrinks and brings the carbon grains in contact with each other to form conductive pathways through the device. When the polymer heats up, it expands, breaking the carbon particle conductive pathways, resulting in an increase of resistance. These polymer PTC thermistors have highly nonlinear resistance/temperature response. They can be difficult to use for temperature measurement as they suffer from self-heating effects when current is passed at high resistances, which further increase the resistance of the devices (Zeng et al., 2014, p.6684); (Dostert, 1982, p.159-167). To use PTC thermistors for sensing, small currents must be used to minimize self-heating. Polymer PTC thermistor may also be used as resettable fuses or current limiters by taking advantage of the self-heating effect (Liang, C. K., & Tsai, C. C., 2005, p.443-449); (Macklen, E. D., 1991, p. 384-387).

Device Characterization

Thermistor devices are often characterized with the following performance metrics which describe the device response;

1. Operating temperature range.
2. Temperature coefficient of resistance (TCR).

The operating temperature range is the effective temperature range that the device will operate with a specified TCR. It is possible to define multiple temperature ranges with different TCR values. The TCR is the coefficient or coefficients that specify the resistance response of the device. There are three main types of resistance response from typical thermistor devices. For resistance responses which can be linearly approximated, the linear model presented in Equation 3.4 is used.

$$\frac{dR}{R} = \alpha dT \tag{3.4}$$

Where dR is the change in resistance in ohms resulting from the change of temperature dT in K or °C, R is the original resistance before the temperature change and α is the temperature coefficient in K^{-1} or $°C^{-1}$. The α parameter can be given in ppm/°C or as a percentage (%) and can be referred to as κ or directly as the TRC.

For thermistors with an exponential resistance response, as is often the case for NTC thermistors, the exponential model presented in Equation 3.5 is used.

$$R = r_{\infty} e^{\beta/T}, \qquad r_{\infty} = R_0 e^{-\beta/T_0} \tag{3.5}$$

Where R is the resistance in ohms of the device, R_0 is the resistance of the device at temperature T_0 (298 K) and the β parameter is the temperature coefficient in K and is calculated from device response measurements.

In the case that the resistance response is not linear and not strictly exponential, the Steinhart–Hart equation presented in Equation 3.6 can be used. The Steinhart-Hart equation is a third-order approximation which typically fit resistance responses very well with errors of less than 0.02 °C over temperature range of 200 °C (White, 2017, p.59); (Chen, 2009, p.1103-1111).

$$\frac{1}{T} = a + b\ln R + c(\ln R)^3 \tag{3.6}$$

Where T is the temperature in K, R is the resistance of the device and a,b and c are Steinhart-Hart coefficient which are calculated from device response measurement.

If non of these expressions represent the resistance response of a thermistor, then Equation 3.4 can be adapted to express the TCR as a temperature dependent function α(T).

$$\frac{dR(T)}{R(T)} = \alpha(T)dT \tag{3.7}$$

Where R(T) is the temperature dependent resistance of the thermistor.

3.2 Methylammonium Lead Trihalide Perovskite Based Optoelectronic Devices

Any material with the same crystal structure as calcium titanium oxide (CaTiO3) is referred to as a PS. The general PS structure takes the form of ABX_3 where “A” and “B” are two cations of very different sizes with an anion “X” which binds to both cations. PS materials have been well known for many years but have only recently shown tremendous potential for low-cost optoelectronic device integration (Snaith, 2013, p.3623-3630). The first occurance of PS intergration for PV devices came in 2009 and was reported by Tsutomu Miyasaka (Kojima,

Teshima, Shirai & Miyasaka, 2009, p.6050-6051). Since then, they have been the subject of much interest and improvements. Indeed, power-conversion efficiencies of organometallic halide PS solar cells have increased to 22.1 % in less than ten (10) years (NREL, 2017); (Saliba et al., 2016, p.1989-1997); (Lee et al., 2015, p.41-46). In this section, the operating principles of PS-based PV devices is presented as well as a review of recent devices found in the literature. The architectures and performances of said devices are also presented, with emphasis given to solution processable devices.

3.2.1 Principles

MALH is of great interest to PV applications. The ability to tailor the PS band gap between 1.5 eV and 2.3 eV by altering the halide composition allows for good quantum efficiency over most of the visible spectrum as well as energy level matching with hole transport layer (HTL) and ETL materials for more efficient devices (Liang et al., 2014, p.3748-3754); (Wang et al., 2015, p.9108-9115); (Zhou et al., 2014, p.542-546). The general structure of MALH is shown in Figure 3.4, with the methylammonium cation surrounded by 12 halide ions. There are two main crystalline phases that MALH can take, which are the tetragonal and cubic phases. In fact, there are no critical differences between the two phases, except a slight rotation of the PbI_6 octahedra along the c-axis (Kawamura, Mashiyama & Hasebe, 2002, p.1694-1697). Switching between the two phases can be achieved via temperature treatments (Stoumpos, Malliakas & Kanatzidis, 2013, p.9019-9038); (Oku, Zushi, Imanishi, Suzuki & Suzuki, 2014, p.121601).

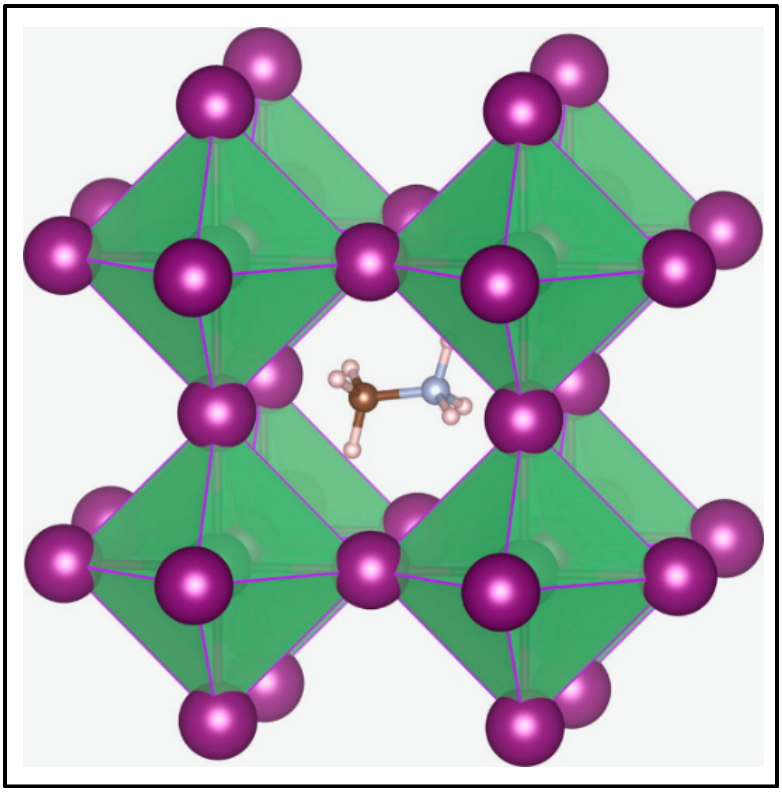

Figure 3.4 Schematic representation of the general structure of MALH PS showing the MA cation occupying the central site surrounded by 12 nearest neighbor halide
Taken from Eames et al. (2015, p.7497)

The X-ray diffraction (XRD) spectra for the two $MAPbI_3$ phases are presented in Figure 3.5. After transformation for the cubic to the tetragonal phase, the (100) and the (200) peaks splits and new (211) and (213) peaks appear. As such, the appearance of peak splitting can be used as an indicator of phase transformation. However, XRD analysis of $MAPbI_{3-x}Cl_x$ (a better suited PS composition for PV applications) often shows the cubic phase spectrum of $MAPbI_3$, with more prominent (100) and (200) peaks or (110) and (220) peaks for the tetragonal phase.

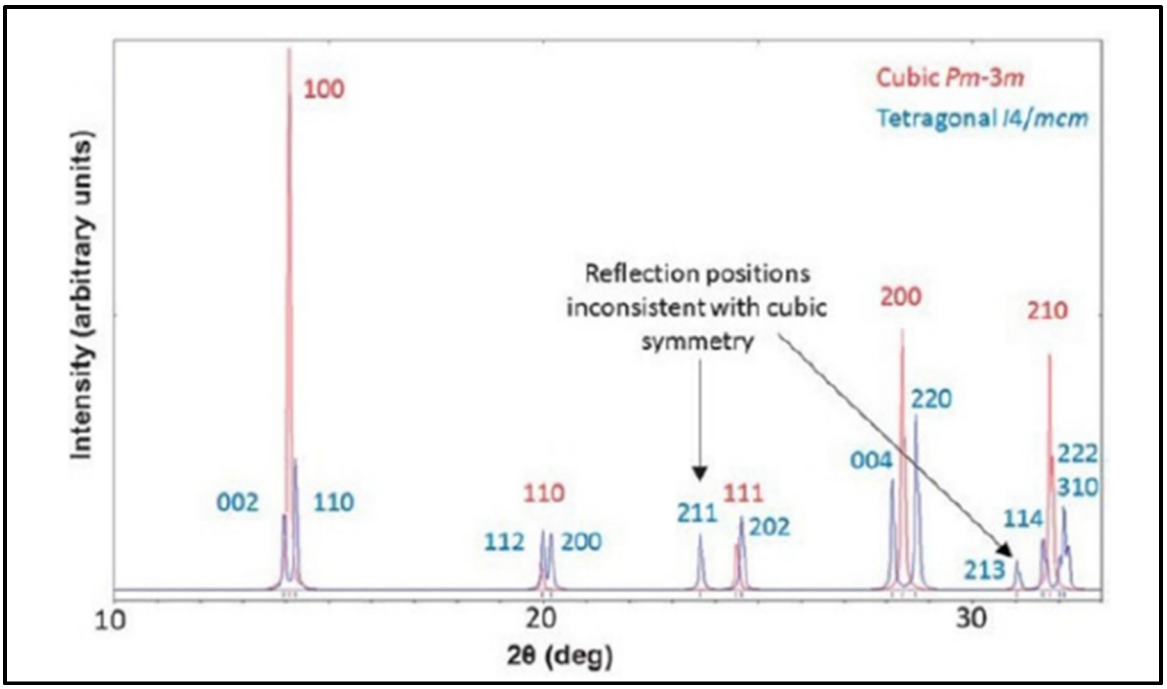

Figure 3.5 XRD spectra of the two $MAPbI_3$ phases and their respective peaks
Taken from Luo & Daoud (2016, p.123)

The enhanced crystallization of $MAPbI_{3-x}Cl_x$ along (110) and (220) plane of the tetragonal phase or (100) and (200) planes of the cubic phase may be due to the lowered phase transition temperature of $MAPbI_{3-x}Cl_x$ after the incorporation of Cl^- ions (Pistor, Borchert, Franzel, Csuk & Scheer, 2014, p.3308-3312). Studies of the changes in crystalline structure after thermal annealing have been performed to better understand the crystallization process and the structure of $MAPbI_{3-x}Cl_x$ (Luo & Daoud, 2016, p.123). This information is important to achieve adequate PS film structures when fabricating devices. The resulting XRD spectra of thermal annealing are shown in Figure 3.6 and present a clearer picture of the crystal formation of $MAPbI_{3-x}Cl_x$. The 15.7° and 31.5° peaks are associated with the (100) and (200) peaks of $MAPbCl_3$ (Pistor et al., 2014, p.3308-3312). Whereas, the corresponding peaks for $MAPbI_{3-x}Cl_x$ are shifted to 14.2 ° and 28.3 °. $MAPbI_3$ and $MAPbCl_3$ are observed to be formed first for the spin coated film prior to annealing, while MACl and PbI_2 traces are present. Total conversion of the $MAPbI_3$ to $MAPbCl_3$ after annealing at 100 °C for ten (10) minutes is observed, while traces of MACl can still be observed. Finally, the $MAPbCl_3$ and MACl traces are converted to $MAPbI_{3-x}Cl_x$ after 45 min of annealing (Yantara et al., 2015, p.2309-2314).

Further annealing results in the decomposition of $MAPbI_3$ to PbI_2 (Song et al., 2015, p.494-500). This oscillation of crystalline structure is quite interesting and further studies may provide insight into the inner workings of MALH PSs for applications in light harvesting, as many questions remain unanswered about these peculiar materials.

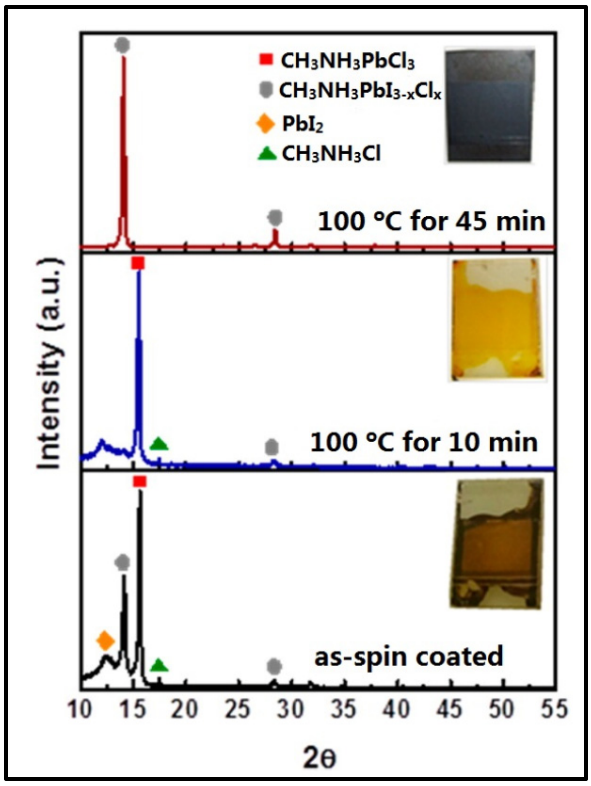

Figure 3.6 XRD spectra of the crystal formation of $MAPbI_{3-x}Cl_x$ from different annealing procedures
Taken from Luo & Daoud (2016, p.123)

Large efforts are currently underway to increase the scientific community`s understanding of the PS-light interactions for energy generation. Unlike extrinsic semiconductors which have been doped, PS are intrinsic semiconductors void of this doping. The main charge separation in PS solar cells is thought to occurs due to the built-in electric field in the intrinsic PS layer from the difference of potential between the electron and the hole transport layers, similar to

the workings of p-i-n junctions. However, as we will explore further in this section, this answer does not provide a complete picture of PS-light interactions.

Two main architectures of PS solar cells are typically employed; nanostructured (NS) PS solar cells which operate in a similar way to dye sensitized solar cells (DSSCs). Here, the PS is thought to be used for photo generation of charge, but charge transport is thought to be performed by other materials. Two (2) types of NS PS structures are shown in Figure 3.7; a PS sensitized and a PS meso-superstructure. In these structures, titanium dioxide (TiO_2) and aluminum trioxide are typically used for negative charge transport, respectively. In TF device architectures, the PS is thought to be used for both photo generation of charge and for charge transport. In this case electron and hole transport materials may be used as blocking layers (BLs) to inhibit recombination at electrode interfaces. Indeed, working TF devices void of ETL and/or HTL have been reported and show lower device performances (Lee, teuscher, Miyasaka, Murakami & Snaith, 2012, p.1228604); (Ball, Lee, Hey & Snaith, 2013, p.1739-1743); (Etgar et al., 2012, p.17396-17399); (Hooper, Smith, Baker, Greenwood & Waston, 2015, p.482-487). The TF PS structure is also shown in Figure 3.7, along with a pillared solar cell structure which employs similar charge generation and transport mechanisms.

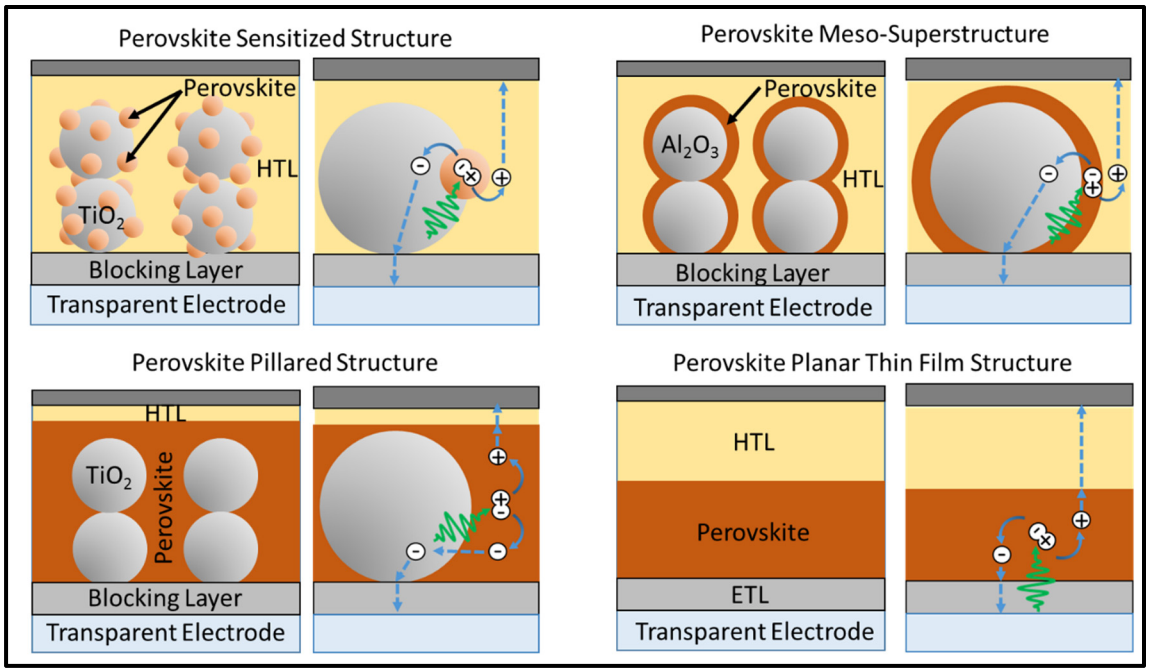

Figure 3.7 Schematic representation of MALH based optoelectronic device architectures

Furthermore, MALH PSs have been shown to essentially form PN junctions in PV applications, while not being inherently doped (Jiang et al., 2015, p.8397). Studies performed on the electrostatic potential profiles throughout cross sections of differently structured PS based devices show some insights to this phenomenom. The electrostatic potential profiles of three different device architectures are presented in Figure 3.8 a) (thin planar device), b) (thick planar device) and c) (mesoporous structured device). In this case the electrostatic potential profiles are acquired with Kelvin probe force microscopy (KPFM). Ideally, measurements taken with a 0 V applied bias (V_b = 0 V) should reflect the workfunction contrast of the materials, as shown from the workfunction equality in Equation 3.7.

$$W_{function} = -e_{\emptyset} - E_F \tag{3.8}$$

Where $W_{function}$ is the workfunction, e_{φ} is the electrostatic potential and E_F is the Fermi level.

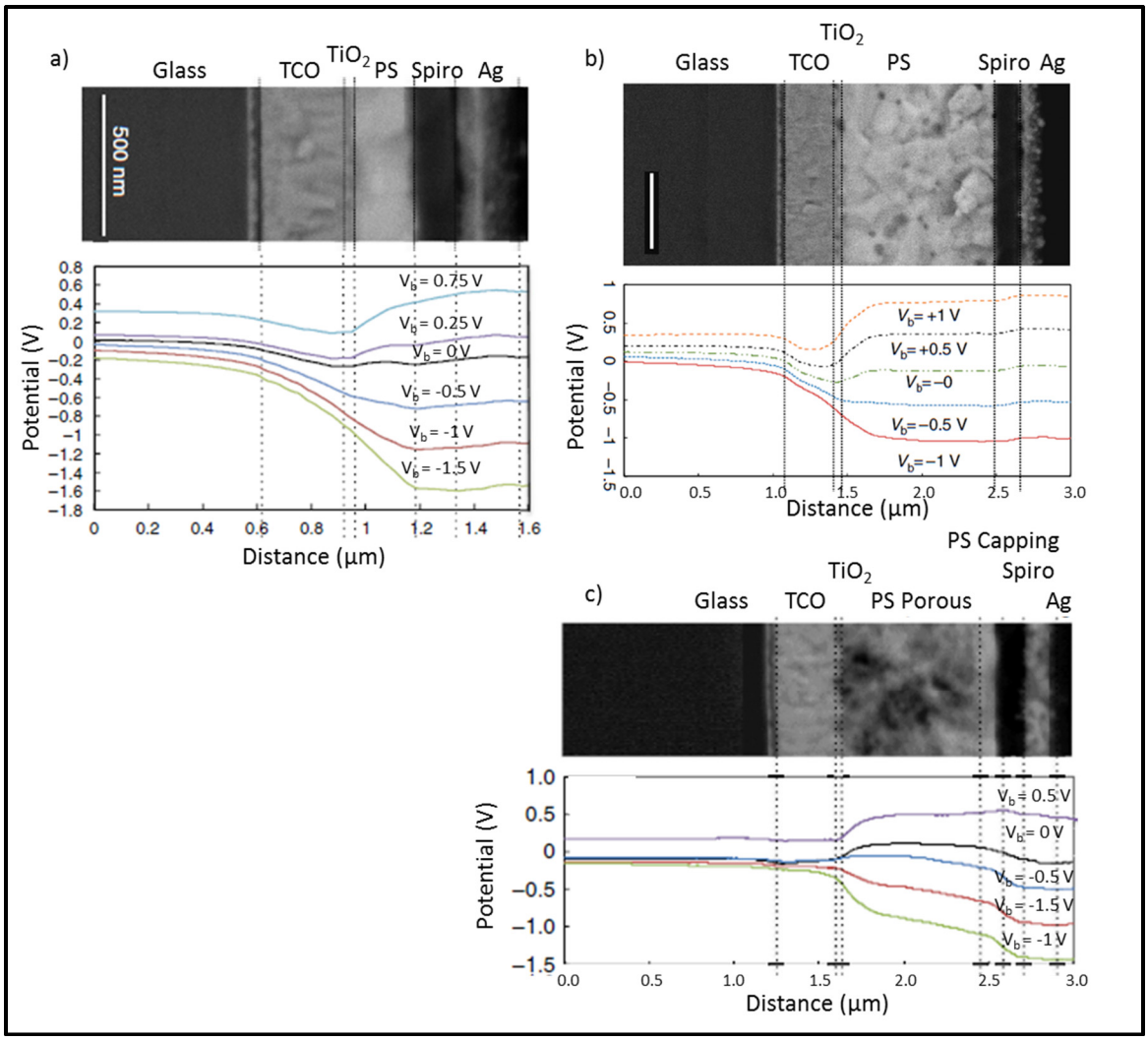

Figure 3.8 Electrostatic potential profiles of MALH PS based devices
in different architectures
Adapted from Jiang et al. (2015, p.8397)

For the electrostatic potential results of the thin planar device, it is observed that the potential drop occurs over the n-type layers of transparent conducting oxide (TCO) and TiO_2, as well as the PS absorber layer. The greatest change in potential is located at the TiO_2/ PS interface. Whereas towards the Spiro HTL interface, the potential is much more constant. This electrostatic potential behavior indicates that a PN junction is formed from the PS and the TiO_2/TCO layers. This is different from p–i–n junction of free carriers that could be expected from layers of n-type (TCO and TiO_2), inherently intrinsic PS and p-type (Spiro) materials. In

p-i-n junctions a constant change in potential across the absorber layer would be expected (Luque & Hegedus, 2011, p.12-16). The authors performed the same studies on devices void of an HTL and found that the potential profile inside the PS follows the same pattern as devices with the HTL, which further confirms the PN junction behavior at the TiO_2/PS interface.

Similar results are found for thick planar devices. The authors observed that the potential drop extends ~300 nm from the TiO_2/PS interface, whereas a constant potential is observed at deeper locations in the PS layer. This behavior further demonstrates the PN junction structure of the device at the TiO_2/PS interface. The width of the potential drop (300 nm) on the profile can be used to estimate the depletion width of the PN junction (Jiang et al., 2009, p.952-957); (Jiang et al., 2003, p.127-129). With the depletion width, the carrier concentration in the PS layer is roughly estimated to be ~7×10^{16} cm^{-3}, which is favorable for PV applications (Green, Emery, Hishikawa, Warta & Dunlop, 2015, p.805-812). It can be speculated that intrinsic defect doping could be responsible for the p-type carriers in PS. If the HTL layer played a role in introducing p-type carriers into the PS layer, it should introduce changes in potential behavior between device fabricated with and without an HTL layer (Guerrero, Juarez-Perez, Bisquert, Mora-Sero & Garcia-Belmonte, 2014, p.133902).

The results on the porous devices with a PS capping layer are similar to thick planar devices and are consistent with PN junction formation at the TiO_2/PS interfaces. Once more, the greatest potential drop is located at the TiO_2/porous PS interface and indicates the formation of a PN junction at this interface. The authors observed that the potential drop at the porous PS/PS capping interfaces is also significant. This distribution of potential across the device implies a $n–p^-$ junction at the TiO_2/porous PS interface, a weakly doped p^--porous PS layer and a p^-/p potential barrier at the porous PS/PS capping interface. The p^-/p potential barrier at the porous PS/PS capping interface can reflect minority carrier, and may be beneficial for carrier collection (Luque & Hegedus, 2011, p.7-8).

Overall, these results are quite interesting and suggest that the TiO_2/PS interface is the dominant factor in the formation of PN junction and that little benefit may be provided by a

thick PS layer (>300 nm). These results are consistant with transient photocharge collection results from another group, which suggest the formation of strong electrical fields at the TiO_2/PS (Maynard et al., 2016, p.173505). However, as will be presented further in this literature review, devices void of a TiO_2 ETL can still achieve relatively high energy conversion efficiencies. It could be speculated that without the TiO_2/PS interface the electrostatic potential profile within the PS layer may remain similar. As the TCO used for device fabrication is generally indium tin oxide (ITO) or FTO, which are considered n-type materials (Banyamin, Kelly, West & Boardman, 2014, p.732-746), a TiO_2 ETL may not be necessary to the formation of a PN junction with the PS.

Further studies on the general workings of MALH solar cells have been conducted to determine important solar cell performance parameters such as the conductivity (σ) and diffusion lengths (L_d) (Wang et al., 2015, p.9108-9115); (Gonzalez-Pedro et al., 2014, p.888-893). PS solar cells have been reported to achieve significant efficiencies void of either ETL or HTL. Further indicating that these solar cells work in a different configuration to DSSCs and that photo-generated electrons and holes can coexist in the PS, can be separated and collected on the respective contacts. Charge carrier diffusion lengths are of great importance when designing solar cells in TF architectures as they set upper bounds to the thickness of the TF. Again, in contrast with DSSCs, PS solar cell diffusion lengths were found to be practically constant at low applied voltages and found to decrease monotonically as the applied voltage is increased (Gonzalez-Pedro et al., 2014, p.888-893).

For TF configurations:

$$L_d \approx 1.4\ [\mu m],\ \ for\ \ V_b < 0.7\ [V] \tag{3.9}$$

And

$$L_d \approx 1.4 - 2.7(V - 0.7)[\mu m],\ \ for\ \ 0.7 \leq V_b \geq 1.0\ [V] \tag{3.10}$$

While in NS configuration:

$$L_d \approx 1.0\ [\mu m],\ \ for\ \ V_b < 0.6\ [V] \tag{3.11}$$

And

$$L_d < 0.5\ [\mu m],\ \ for\ \ V_b > 0.6\ [V] \tag{3.12}$$

This indicates that to achieve high TF device PCEs with elevated operational voltages, thinner PS layers are beneficial. If the PS layer thickness is greater than the diffusion length, then charge recombination within the PS material will be promoted and device efficiencies will suffer. This is further evidence that PS layer thickness if of great importance when fabricating devices.

The conductivity of the PS films used in TF device architectures are also variant with applied voltage, increasing exponentially with voltage. The resistivity of an MALH active layer in either NS or TF configuration was found to range from 5 x 10^{-7} $\Omega^{-1}cm^{-1}$ to 1 x 10^{-5} $\Omega^{-1}cm^{-1}$ for applied voltages $0 \leq V \geq 1.0$ [V] (Gonzalez-Pedro et al., 2014, p.888-893) An electrical model that matches the impedance spectroscopy (IS) characterization of the PS solar cells is shown in Figure 3.9 with a transmission line element for the TF structure (Gonzalez-Pedro et al., 2014, p.888-893).

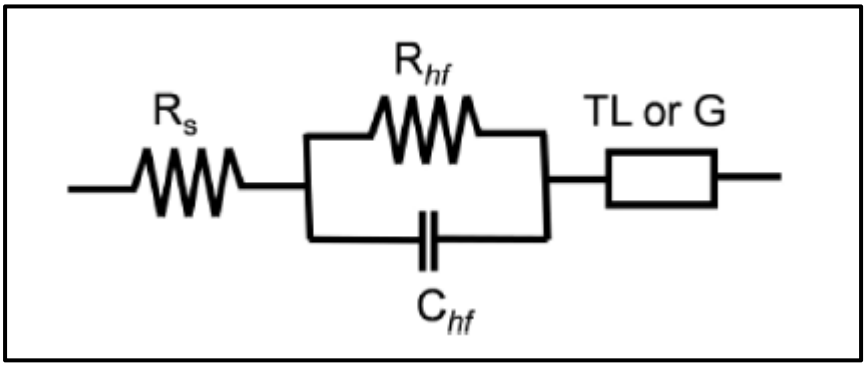

Figure 3.9 Electrical model of a PS based solar cell
Taken from Gonzalez-Pedro et al. (2014, p.888-893)

From the transmission line pattern observed in the IS spectra, transport processes coupled with recombination processes in PS solar cells can be deduced. Multiple sample configuration (NS and TF), show similar IS behavior, indicating a common and general working mechanism in PS solar cells. The transport rate is found to be nearly the same for the different cells structures indicating that the dominant transport pathway is the PS absorber.

Overall, these findings are quite interesting and point towards complex PS-light interactions which vary in some respects depending on solar cell architecture. For TF devices with a thin PS layer (< 300 nm), characteristics similar but not identical to p-i-n junctions can be observed. In this case, the electrical field is not constant across the junction and suggests stronger interactions at the PS/ETL interface with minimal interaction coming from the PS/HTL interface (Jiang et al., 2015, p.8397). For devices with thicker PS layers, this interaction is even more evident. A strong electric field is observed at the PS/ETL interface while no electric field is seen deeper inside the PS layer, suggesting the formation of PN junction at this interface. (Jiang et al., 2015, p.8397); (Maynard et al., 2016, p.173505). The difference between these findings and the typicall p-i-n junction formation expected from these solar cell architectures is not yet fully understood, however recent research points towards complex interactions from ferroelectric domains within the PS layer (Maynard et al., 2016, p.173505); (Chen et al., 2017, p.7519-7524); (Wang et al., 2019, p.7693-7697); (Röhm et al., 2019, p.1806661) and due to the heterogeneity of polycrystalline PS semiconductors (Tennyson, Doherty & Stranks, 2019, p.573-587); (Chen et al., 2017, p.7519-7524).

For PS-based device fabrication, a few key aspects are clear. PSs are deposited using precursors and need to be annealed to achieve crystallization. The temperature and time of this annealing process needs to be controlled precisely to achieve adequate crystallization composition for device function. PS layer thickness is also important to solar cell function, a layer thickness of < 300 nm should be targeted for optimal performances. The PS/ETL interface plays the main roll in junction formation. Devices void of this interface should see reduced device performances but may still be functional due to a PS/n-type TCO interface or

due to the weaker effects of the PS/HTL interface. As will be shown in the next section, these conclusions are supported by device performances seen in the literature.

3.2.2 Device Performances

Formulations of MALH have made tremendous headway due to their unique optoelectronic behavior and ability to essentially replace PN junctions. Recently PV device efficiencies as high as 22.1 % have been reported for small cells and up to 19.7 % for 1 cm^2 cells (NREL, 2017); (Saliba et al., 2016, p.1989-1997); (Lee et al., 2015, p.41-46). Moreover, PS-based photodetector responsivities between 10^2 and 10^6 $A.W^{-1}$ have been reported using various photodetector architectures (Spina et al., 2016, p.4888-4893); (Fang et al., 2015, p.679-686); (Saidaminov et al., 2015, p.8724); (Ka, Gerlein, Nechache & Cloutier, 2017, p.45543); (Noh, Im, Heo, Mandal & Seok, 2013, p.1764-1769). Typical spectral response of PS based optoelectronic devices spans most of the visible spectrum from ~400 nm to ~800 nm (Tai et al., 2016, p.11105); (Ka et al., 2017, p.45543); (Jeon et al., 2014, p.897).

Most PS solar cells are reported to be fabricated in TF configuration sandwiched between ETL and HTL materials on transparent electrode (ITO or FTO) covered glass. Additionally, fabrication on flexible substrates has been achieved with minimal losses to the PCE (Docampo, Ball, Darwich, Eperon & Snaith, 2013, p.2761); (You et al., 2014, p.1674-1680). Many groups have researched ways not only to improve device performances but also device stability, flexibility and ease of fabrication. These improvements can be achieved by interface or solvent engineering for optimized PS crystallization (Hooper et al., 2015, p.482-487); (Hasan, Hamja & Islam, 2015, p.26-29); (Liang et al., 2014, p.3748-3754) or from optimization of MALH composition for improved stability (Docampo et al., 2013, p.2761); (You et al., 2014, p.1674-1680) (Wang et al., 2015, p.9108-9115); (Tai et al., 2016, p.11105).

There are multiple ways to obtain MALH PS films, the most popular methods are solution processed spin coating methods using one-, two- or three-step processes to achieve thin crystalline PS films. In the one-step process, the MALH solution is spin coated and crystallized

with low-temperature annealing processes (80-120 °C) (Dubey et al., 2016, p.10231-10240). For the two-step process; first, a precursor solution of PbX_2 is spin coated and dried before a second precursor solution of MAX is spin coated. Low-temperature annealing is performed to achieve crystallization of the complete PS layer (Docampo et al., 2013, p.2761); (Hasan et al., 2015, p.26-29); (Liang et al., 2014, p.3748-3754); (Wang et al., 2015, p.9108-9115); (Tai et al., 2016, p.11105). The three-step process is invoked when either, the wanted PS has a combination of different halide ions, or solvent engineering is required. The three-step process is similar to the two-step process, with the addition of an extra spin coating step involving a different MALH solution (Guo et al., 2016, p.710-718) or solvent (Gedamu et al., 2018, p.12885) before the final low-temperature annealing step.

As mentioned earlier, there are many valid PS PV cell architectures which can achieve high efficiency. In this section, TF configurations for MALH solar cells are studied in more detail. The basic structure for PS solar cells is very similar to standard PN junction planar devices, consisting of a PN junction sandwiched between ETL and HTL materials. In this case, the PS TF itself forms the PN junction. Shown in Figure 3.10 are standard architectures for MALH solar cells and an example of the simplified band diagram for such structures is shown in Figure 3.11. A compact layer of TiO_2 NPs and Spiro-OMeTAD were found to be the most popular materials used for the ETL and HTL respectively. These materials are well suited as transport layer materials within PS solar cells as they offer well aligned band structures for the extraction of the respective charges.

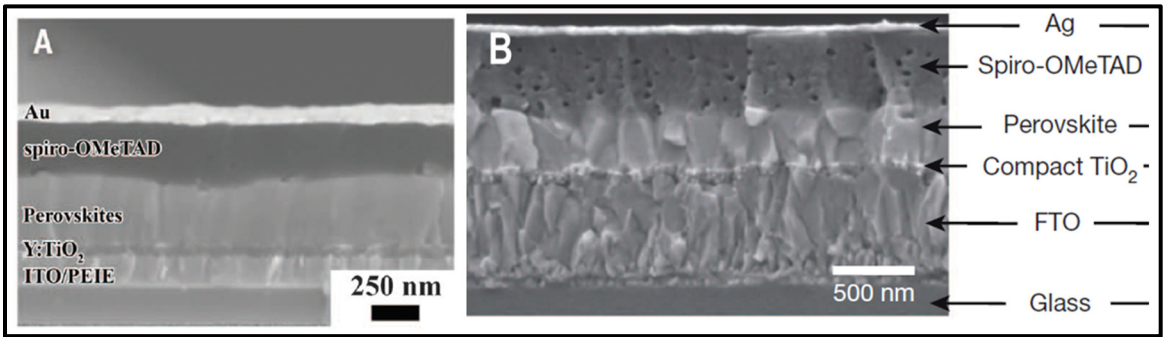

Figure 3.10 TF planar MALH solar cell structures with spiro-OMeTAD as HTL and compact TiO_2 as ETL, a) ITO and Au contacts, b) FTO and Ag contacts
Adapted from Zhou et al. (2014, p.542-546) and Liu, Johnston & Snaith (2013, p.395)

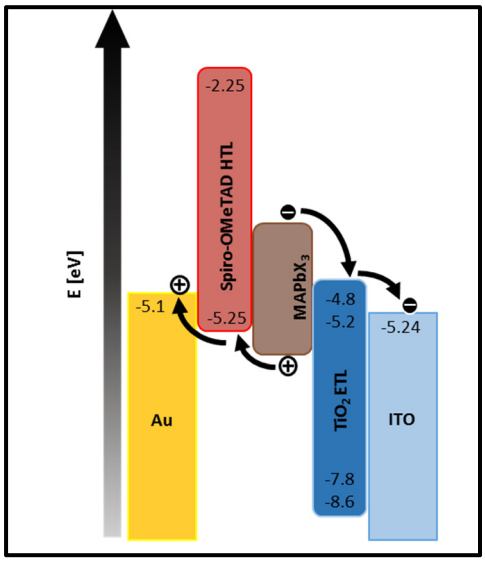

Figure 3.11 Schematic representation of the simplified bad diagram for the standard PS TF solar cell structure

The band gap of TiO_2 can range from 3.0 eV to 3.4 eV with a conduction band energy levels from -4.8 eV to -5.2 eV and valence bands from -7.8 eV to -8.6 eV, depending its crystalline phase (Scanlon et al., 2013, p.798); (Prasai, Cai, Underwood, Lewis & Drabold, 2012, p.7515-7521). For the Spiro-OMeTAD HTL, a band gap of 3 eV is estimated while lumo and homo energy levels are estimated to be -2.25 eV and -5.25 eV, respectively. Band energy levels of Spiro-OMeTAD may vary slightly with composition and additives (Krishna et al., 2014, p.2702-2709). The MALH band gap can range from 1.5 eV to 2.3 eV, similarly a wide range of conduction and valence band energy levels may be obtained and depend mainly on the halide composition (Liang et al., 2014, p.3748-3754); (Wang et al., 2015, p.9108-9115); (Zhou et al., 2014, p.542-546). Work functions for the ITO and Au electrodes are estimated as -5.24 eV (Schlaf, Murata & Kafafi, 2001, p.149-154) and -5.1 eV, respectively (Michaelson, 1977, p.4729-4733).

Other materials such as PEDOT:PSS and [6,6]-phenyl-C60-butyric acid methyl ester ($PC_{60}BM$) are also sometimes employed as ETL and HTL. This is often the case when special

fabrication needs are required, such as low-temperature processability for flexible devices fabrication. An example of this structure can be seen in Figure 3.12, along with a corresponding simplified band diagram. In this instance, the solar cell structure needs to be inverted for energy level matching with the ITO and metal electrodes. The n-type ITO or FTO transparent electrodes may inhibit cell performances due PN junction formation behavior presented earlier (Jiang et al., 2015, p.8397). Moreover, many groups have studied PS solar cells with only one transport material, be it as an ETL or HTL. A summary of champion solar cell device performances, obtained by various groups, with different materials for the ETL and HTL can be seen in Table 3.1.

.

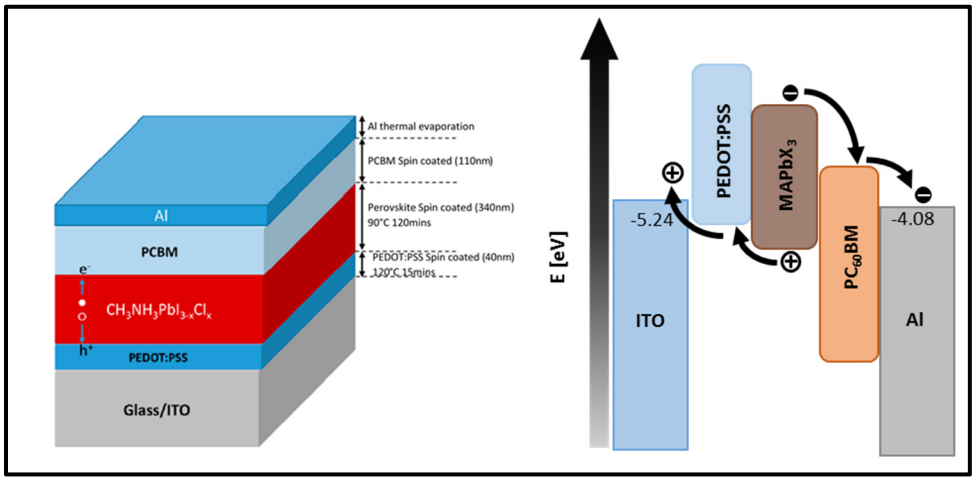

Figure 3.12 Schematic representation of an inverted MALH solar cell structure, with the associated simplified band diagram
Adapted from You et al. (2014, p.1674-1680)

One of the most common halide compositions for PS device fabrication was found to be $MAPbI_{3-x}Cl_x$, while $MAPbI_{3-x}(SCN)_x$ is used successfully for device fabrication in high humidity environment (Tai et al., 2016, p.11105). $MAPbI_3$ can still be used but has become disfavored due to degradation problems (Abdelmageed et al., 2018, p.566-571). The TiO2/PS/Spiro architectures are favored and tend to produce devices with more elevated Voc (0.9–1.1 V) values when compared to the PC60BM/PS/PEDOT:PSS architectures (0.87-0.95 V). However, Jsc and final PCE values are more dependent on fabrication methods than on the

choice of HTL and ETL between the two architectures. Fabrication of devices void of either HTL or ETL is observed to be detrimental to device performances. While Voc values suffer slightly from the exclusion of ETL or HTL, it is the Isc and the FF of the devices which suffer most. For devices architectures presented here with an ETL and an HTL, typical PCE values range between 8-20 %, while PCE values of devices void of ETL or HTL drop to 3-8 %.

Table 3.1 Overview of TF planar PS solar cell performances using different ETL and HTL materials

Reference	ETL	HTL	PS	V_{oc} [V]	J_{sc} [$mAcm^{-2}$]	FF [%]	PCE [%]
TiO_2 + Spiro-OMeTAD Devices							
(Liu, Johnston & Snaith, 2013, p.395)	TiO_2	Spiro	$MAPbI_{3-x}Cl_x$	1.07	21.5	67	**15.4**
(Wang et al., 2015, p.9108-9115)	TiO_2	Spiro	$MAPbI_3$	1.02	19.5	75	**15.0**
(Jiang et al., 2015, p.8397)	TiO_2	Spiro	$MAPbI_3$	1.07	21.6	69	**16.1**
(Tai et al., 2016, p.11105)	TiO_2	Spiro	$MAPbI_{3-x}(SCN)_x$	0.96	17.7	71	**12.2**
(Gonzalez-Pedro et al., 2014, p.888-893)	TiO_2	Spiro	$MAPbI_3$	0.95	17.5	51	**8.5**
(Guo et al., 2016, p.710-718)	TiO_2	Spiro	$MAPbI_{3-x}Cl_x$	1.03	20.45	74	**15.7**
(Zhou et al., 2014, p.542-546)	TiO_2	Spiro	$MAPbI_{3-x}Cl_x$	1.13	22.75	75	**19.3**
(Hooper et al., 2015, p.482-487)	TiO_2	Spiro	$MAPbI_{3-x}Cl_x$	0.90	19.36	55	**9.58**
(Gedamu et al., 2018, p.12885)	TiO_2	Spiro	$MAPbI_{3-x}Cl_x$	0.92	27.1	60	**15.1**
$PC_{60}BM$ + PEDOT:PSS Devices							
(Liang et al., 2014, p.3748-3754)	$PC_{60}BM$	PEDOT	$MAPbI_{3-x}Cl_x$	0.92	17.5	73	**11.8**
(You et al., 2014, p.1674-1680)	$PC_{60}BM$	PEDOT	$MAPbI_{3-x}Cl_x$	0.87	18.5	72	**11.5**
(Dubey et al., 2016, p.10231-10240)	$PC_{60}BM$	PEDOT	$MAPbI_3$	0.95	23.98	74	**16.8**
Mixed ETL and HTL Materials							
(Docampo et al., 2013, p.2761)	TiO_2+Al_2O_3	Spiro	$MAPbI_{3-x}Cl_x$	1.02	17.8	66	**11.8**
	TiO_2+$PC_{60}BM$	PEDOT	$MAPbI_{3-x}Cl_x$	0.94	15.8	66	**9.8**
(Wang et al., 2013, p.724-730)	TiO_2 + Gr	Spiro	$MAPbI_{3-x}Cl_x$	1.04	21.9	73	**15.6**
(You et al., 2014, p.1674-1680)	ZnO	PEDOT	$MAPbI_{3-x}Cl_x$	0.88	17.2	75	**11.5**
Only ETL or only HTL							
(Wang et al., 2013, p.724-730)	N/A	Spiro	$MAPbI_{3-x}Cl_x$	0.95	10.8	37	**3.7**
(Hasan et al., 2015, p.26-29)	TiO_2	N/A	$MAPbI_3$	0.89	17.392	50	**7.92**
(Hooper et al., 2015, p.482-487)	TiO_2	N/A	$MAPbI_{3-x}Cl_x$	0.80	19.72	50	**7.92**

Table 3.2 shows a detailed list of $MAPbI_{3-x}Cl_x$ devices which are of more interest to the work presented in this thesis. The devices presented utilize solution processes for material deposition, low temperature fabrication processes and/or fabrication on flexible substrates. These are used to evaluate the feasibility of the inkjet printing process for fabrication of these devices.

In the Mingzhen Liu et al. (2013) study, devices with a TiO_2/PS/Spiro architecture are fabricated using solution and vapor deposition processes for the PS layer (Liu et al., 2013, p.395). It is found that while V_{oc}, I_{sc} and FF performance values of the devices are decreased, relatively high PCE values (8.6 %) can be achieve with a solution processed PS layer. The decreases in performance metrics for the solution processed PS devices are attributed to decreases in film homogeneity and incomplete PS crystallization. Pinholes found in the solution processed PS layer lead to shunting pathways responsible for the lower FF and V_{oc} in the solution-cast planar heterojunction devices (Ball et al., 2013, p.1739-1743); (Snaith, Greenham & Friend, 2004, p.1640-1645).

Hsin-Hua Wang et al. 2015 and Pablo Docampo et al. 2013 performed studies on low temperature compatible processes for the fabrication of the TiO_2 ETL and for fabrication on flexible substrates (Wang et al., 2015, p.9108-9115); (Docampo et al., 2013, p.2761). In the case of Hsin-Hua Wang et al. 2015, the TiO_2 process temperature is brought down to 150 °C and could be used with some flexible substrates. Additives are used to increase TiO_2 performances but only result in marginal increases in cell performances. Interestingly, in this case, the whole TiO_2/PS/Spiro layers are fabricated using solution processes and result in high device PCE values (>15 %), further validating the use of solution processes for device fabrication. Pablo Docampo et al. 2013 have shown that device fabrication on flexible polyethylene terephthalate (PET) substrates is possible using similar solution processes for the TiO_2 ETL fabrication with process temperatures of 150 °C. Once again, the complete device stacks (not including electrodes) are solution processed, these results also validate the solution fabrication process for inverted cells using the $PC_{60}BM$/PS/PEDOT architecture. Device

performances show very little variation between identical devices fabricated on flexible PET or rigid glass substrates.

In the Qidong Tai et al. 2016 study, both the effects of halide composition of the PS and the PS thickness for solution process PS layers in high humidity environment are studied (Tai et al., 2016, p.11105). Layer thickness is found to be paramount to achieve high device performances as the thickness found to also affect the homogeneity and crystal sizes of the PS layer for spin-coating processes. Device performances are observed to drop quickly with a PS layer thickness below 140 nm due to incomplete layer coverage. On the other hand, device performances also drop with PS layer thicknesses above 240 nm, this drop is attributed to the formation of rough structures and inhomogeneous PS layer. From this study, it is evident that solution processes can yield very good devices but that complete homogeneous layers are extremely difficult to achieve due to the rheological properties of the solutions used. Furthermore, device fabrication is performed in air and high relative humidity (RH) environment (>70 % RH) and show that the halide composition of the PS plays a major role in its sensitivity to the environment. $MAPbI_{3-x}(SCN)_x$ is used with great result for fabrication in air and proves the feasibility of device fabrication in ambient conditions. Po-Wei Liang et al. 2014 have shown that additive can be added to PS precursors to affect the crystallization process and enhance device performances (Liang et al., 2014, p.3748-3754). The additives not only affected crystal quality but also reduced pinhole formation in the PS film. This shows that PS precursor solutions can be adapted with additive and effectively change their rheological properties, this illustrates the feasibility to adapt solutions for the inkjet processes.

Chun-Sheng Jiang et al. 2015 and Victoria Gonzalez-Pedro et al. 2014 have performed further studies on the effect of solution processed PS layer thicknesses and device structure (Jiang et al., 2015, p.8397); (Gonzalez-Pedro et al., 2014, p.888-893). The complete fabrication process of the TiO_2/PS/Spiro stack are solution based but require high temperatures (500 °C) and are not compatible for fabrication on most flexible substrates. Nonetheless, it is shown that a range of PS layer thicknesses can be achieved using solution processes. Moreover, the results of these

studies further demonstrate that TF devices perform better than NS devices and that thin PS films (<300 nm) are beneficial for device performances.

Commercially available PS precursors are difficult to find. At the time of writing, only Ossila sold PS precursor inks. They offer two types of PS inks, one for air processing and the other for nitrogen processing. The inks are adapted for spin-coating processes and can be used to achieve high device efficiencies in both the standard TiO_2/PS/Spiro (13.7 %) and the inverted $PC_{60}BM$/PS/PEDOT architectures (13.1 %). It must be noted that these device stacks are not fully solution processed, conventional fabrication techniques are used for the other material layers. Nonetheless, this demonstrates a step towards the commercialization of PS based device fabrication.

In conclusion, it is expected that inkjet printing processes may be used for PS based device fabrication in TF architectures. Solution processes compatible with low temperature substrates such as PET, have been successfully used to fabricate TF device stacks. Adapting these processes and solutions for inkjet printing should prove feasible. The device structure and PS layer thickness are of the upmost importance and should be kept below 1000 nm, while thinner layers (140 – 300 nm) are preferable if full layer coverage can be achieved. Fabrication on flexible PET substrates is expected to be feasible with minimal loss to device performances if similar TCOs are present on the substrates. Both standard and inverted device structures can be fabricated using solution processes and thus expected to be feasibly fabricated using inkjet fabrication processes.

Table 3.2 Detailed overview of TF PS solar cell performances fabricated using solution processes, low temperature processes or fabricated on flexible substrates

Device	ETL	HTL	PS	V_{oc} [V]	J_{sc} [mAcm^{-2}]	FF [%]	PCE [%]
(Liu, Johnston & Snaith, 2013, p.395)							
Vapor Deposited	Compact TiO_2	Spiro-OMeTAD	$MAPbI_{3-x}Cl_x$	**1.07**	**21.5**	**67**	**15.4**
Solution Processed	Compact TiO_2	Spiro-OMeTAD	$MAPbI_{3-x}Cl_x$	**0.84**	**17.6**	**58**	**8.6**
(Wang et al., 2015, p.9108-9115)							
no additive	TiO_2	Spiro-OMeTAD	$MAPbI_3$	**1.025**	**19.5**	**75.0**	**15.0**
0.05% YAc_3	TiO_2	Spiro-OMeTAD	$MAPbI_3$	**1.017**	**20.2**	**74.8**	**15.4**
0.1% $ZnAc_2$	TiO_2	Spiro-OMeTAD	$MAPbI_3$	**1.024**	**20.1**	**76.0**	**15.6**
0.1% $ZrAc_4$	TiO_2	Spiro-OMeTAD	$MAPbI_3$	**1.021**	**20.3**	**76.6**	**15.7**
0.1% MoO_2Ac_2	TiO_2	Spiro-OMeTAD	$MAPbI_3$	**1.009**	**20.0**	**76.6**	**15.4**
(Liang et al., 2014, p.3748-3754)							
Pristine (on ITO)	$PC_{60}BM$	PEDOT:PSS	$MAPbI_{3-x}Cl_x$	**0.90**	**15.0**	**58**	**7.9**
1% DIO (on ITO)	$PC_{60}BM$	PEDOT:PSS	$MAPbI_{3-x}Cl_x$	**0.92**	**15.6**	**71**	**10.3**
Pristine (on FTO)	$PC_{60}BM$	PEDOT:PSS	$MAPbI_{3-x}Cl_x$	**0.90**	**16.0**	**62**	**9.0**
1% DIO (on FTO)	$PC_{60}BM$	PEDOT:PSS	$MAPbI_{3-x}Cl_x$	**0.92**	**17.5**	**73**	**11.8**
(Jiang et al., 2015, p.8397)							
Planar (240nm)	TiO_2	Spiro-OMeTAD	$MAPbI_3$	**1.072**	**21.6**	**69.6**	**16.1**
Planar (1000nm)	TiO_2	Spiro-OMeTAD	$MAPbI_3$	**0.892**	**22.3**	**45.8**	**9.1**
Porous (280nm)	TiO_2	Spiro-OMeTAD	$MAPbI_3$	**0.964**	**22.5**	**67.3**	**14.6**
Porous (850nm)	TiO_2	Spiro-OMeTAD	$MAPbI_3$	**0.923**	**19.6**	**54.2**	**9.8**
(Tai et al., 2016, p.11105)							
1.5K r.p.m.	TiO_2	Spiro-OMeTAD	$MAPbI_{3-x}(SCN)_x$	**0.88**	**3.5**	**57**	**~2**
2K r.p.m.	TiO_2	Spiro-OMeTAD	$MAPbI_{3-x}(SCN)_x$	**0.91**	**4.0**	**60**	**~2**
3K r.p.m.	TiO_2	Spiro-OMeTAD	$MAPbI_{3-x}(SCN)_x$	**0.96**	**17.7**	**71.2**	**12.2**
4K r.p.m.	TiO_2	Spiro-OMeTAD	$MAPbI_{3-x}(SCN)_x$	**0.98**	**16.3**	**63.8**	**10.2**
5K r.p.m.	TiO_2	Spiro-OMeTAD	$MAPbI_{3-x}(SCN)_x$	**0.99**	**13.6**	**57.5**	**7.79**
$MAPbI_3$ (air)	TiO_2	Spiro-OMeTAD	$MAPbI_3$	**0.9**	**15**	**-**	**8.4**
$MAPbI_3$ (N_2)	TiO_2	Spiro-OMeTAD	$MAPbI_3$	**-**	**-**	**-**	**12**
(Docampo et al., 2013, p.2761)							
Regular (FTO)	TiO_2+Al_2O_3	Spiro-OMeTAD	$MAPbI_{3-x}Cl_x$	**1.02**	**17.8**	**66**	**11.8**
Inverted (FTO)	TiO_2+ $PC_{60}BM$	PEDOT:PSS	$MAPbI_{3-x}Cl_x$	**0.94**	**15.8**	**66**	**9.8**
Inverted (ITO)	TiO_2+ $PC_{60}BM$	PEDOT:PSS	$MAPbI_{3-x}Cl_x$	**0.92**	**14.4**	**47**	**6.3**
Inverted (ITO on PET)	TiO_2+ $PC_{60}BM$	PEDOT:PSS	$MAPbI_{3-x}Cl_x$	**0.88**	**14.4**	**51**	**6.4**
(Gonzalez-Pedro et al., 2014, p.888-893)							
Nano-structured	TiO_2+ZnO	Spiro-OMeTAD	$MAPbI_3$	**0.908**	**13.2**	**41**	**4.9**
Thin-Film	TiO_2	Spiro-OMeTAD	$MAPbI_3$	**0.950**	**17.5**	**51**	**8.5**
Ossila I101 PS Ink							
Standard	TiO_2	Spiro-OMeTAD	$MAPbI_{3-x}Cl_x$	**0.90**	**20.8**	**73**	**13.7**
Inverted	$PC_{60}BM$	PEDOT :PSS	$MAPbI_{3-x}Cl_x$	**0.950**	**18.8**	**72**	**13.1**

3.3 Inkjet Printing

3.3.1 Stable Jetting

Ink jetting is the first essential step in the inkjet printing process. The jetting waveform sent to the nozzle, the choice of cartridge nozzle and the ink properties, particularly the ink viscosities, are important in obtaining a stable adequate jet. An example of a stable jet is shown in Figure 3.13 c), while Figure 3.13 d) demonstrates the full stable jetting sequence. It is important that the stable jet is void of ink trails and satellite drops at the printing distance, examples of ink trails and satellite drops are shown in Figure 3.13 a) & b) respectively.

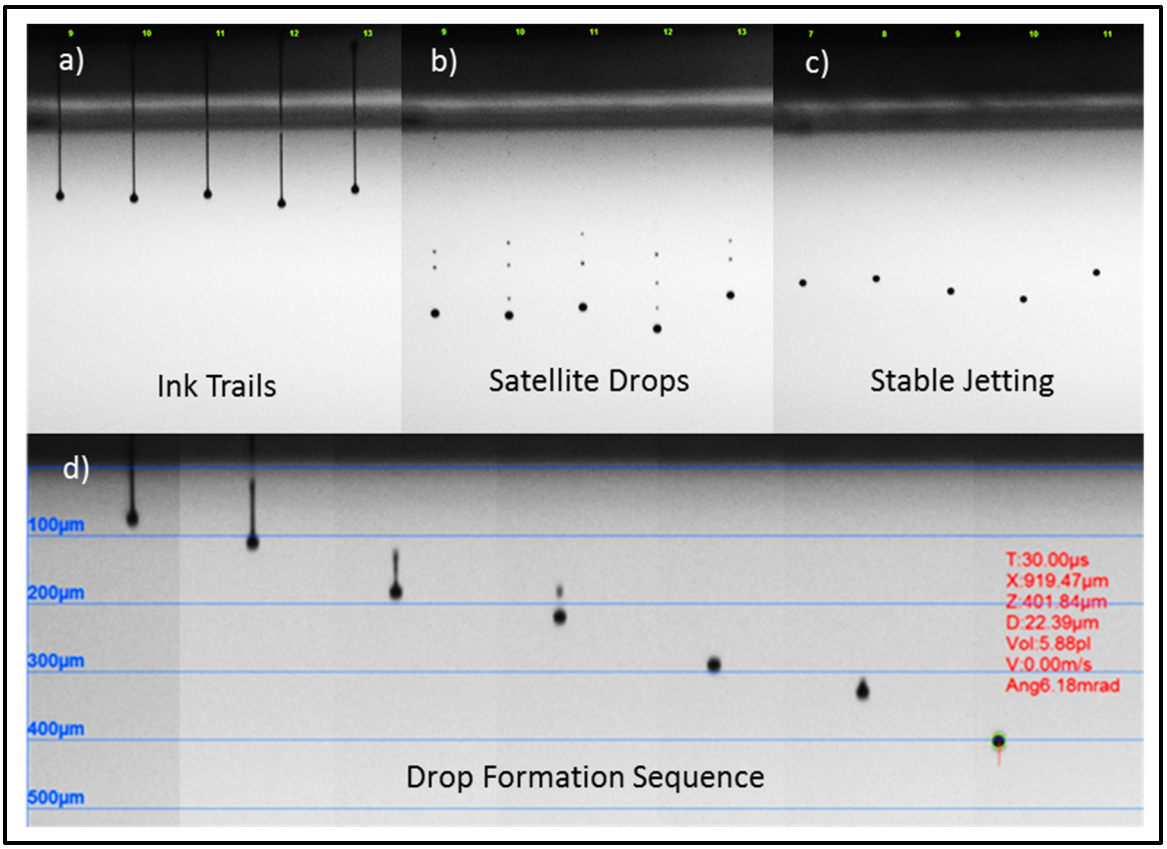

Figure 3.13 Drop formation and ink jetting images taken with stroboscopic camera on the Ceradrop F-Series printer, showing a) ink trails, b) satellite drops, c) stable jetting and d) complete drop formation sequence

Satellite drops can be generated from two (2) different pathways. The first, through unstable jetting which can happen from high jetting frequencies causing interference from previous and current transient pressure waves inside the ink liquid. Improper ink formulation, agglomeration of particles within the ink and/or partial blockage of the nozzles due to premature evaporation of low boiling point solvents can also generate unstable jetting with satellite drops.

The second route of generating satellite drops is through separation of the ink trail within stable jetting parameters. The separation of the ink trails into satellite drops is tied to the liquid ink properties, principally the ink viscosity. The ink viscosity is often dependent on the ink temperature and therefore can be adjusted while printing by controlling nozzle temperatures. In theory, the Ohnesorge number can be used to describe the drop formation and is a good indicator for the formation of satellite drops. The Ohnesorge number is the ratio of the viscous forces to the surface tension and inertial forces, it is presented in Equation 3.13.

$$Oh = \frac{\eta}{\sqrt{\rho L \sigma_L}} \tag{3.13}$$

Where η is the viscocity in Pa·s (1 Pa·s = 1000 cP), ρ is the density in kg/m^3, L is the nozzle diameter in m and σ_L is the surface tension in J/m^2.

If the Ohnesorge number is below 0.1 (pointing to a relatively low viscosity of the ink) then satellite drops are formed through a separation of the ink trail. For 0.1< Oh <1.0 the ink trail is reabsorbed into the main drop and/or back into the nozzle resulting in a single drop jet with no satellite drops (McKinley & Renardy, 2011, p.127101); (Alaman et al., 2016, p.910) Other good indicator for stable jetting are Reynold's number, Re , and the Webber number, We, which are presented in Equation 3.14.

$$Re = \frac{\rho v L}{\eta}, \qquad We = (Oh \cdot Re)^2 \tag{3.14}$$

Where, once again, η is the viscocity in Pa·s, ρ is the density in kg/m^3, L is the nozzle diameter in m and ν is jet velocity in m/s.

In order to achieve ejection of the ink from the nozzle, the *We* number should be equal to or more than four (4), ie. $We \geq 4$. When reaching the substrate, splashing of the ink drop can occur (Derby, 2010, p.395-414), this is an unwanted phenomenon which occurs for the relation described in Equation 3.15.

$$We^{1/2} \cdot Re^{1/4} \geq 50 \tag{3.15}$$

This information is summarized in Figure 3.14 which highlights the different zones of non-stable jetting as well as a printable zone in terms of the *Oh* and *Re* numbers.

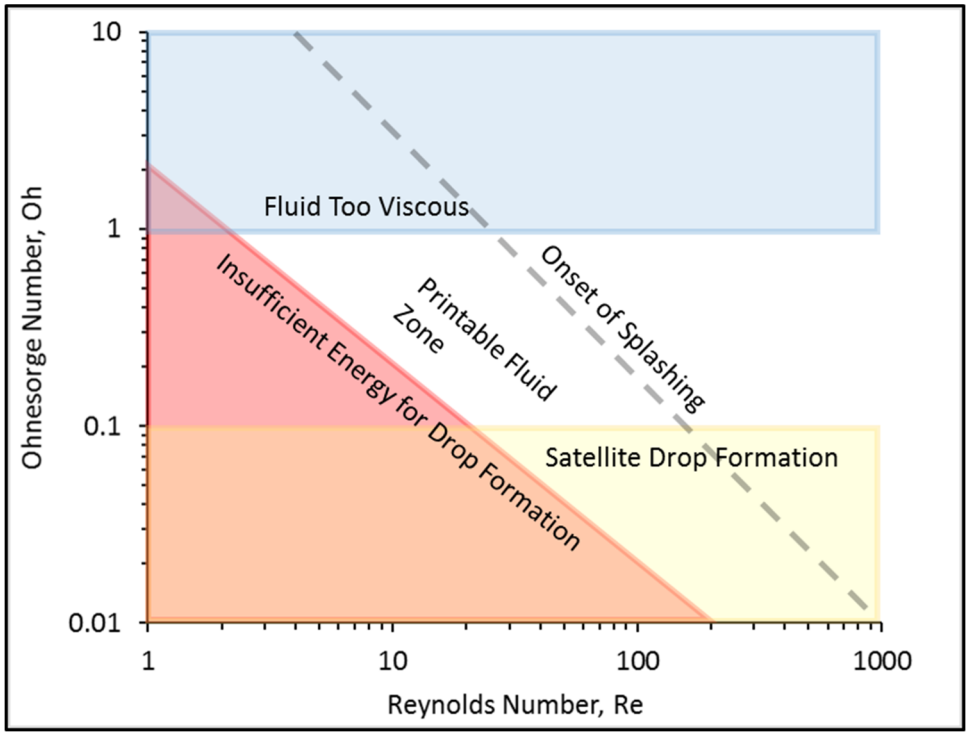

Figure 3.14 Schematic diagram showing stable operation regions for ink jetting using the *Oh* and *Re* numbers to represent the ink`s rheological properties

The ink properties relating to the *Oh*, *We* and *Re* numbers only dictate if a fluid is theoretically jettable with no satellite drops or splashing, however achieving stable jetting is not trivial and requires valid jetting waveforms adapted for each ink material.

3.3.2 Printing

Once stable jetting is achieved, we must understand the interactions of the printed liquid with the substrate to adapt printing parameters and achieve controlled printing. There are two main interactions that we need to understand; the effects of fluid dynamics of the ink and the interactions and effects of surface energies between the ink and the substrate. One such effect which encompasses both these aspects is the so-called coffee-ring or coffee-stain effect which occurs during drying of a drop of ink material. When a drop of liquid dries it will often leave an outer concentric circle of densely deposited material with an inner circle of sparsely deposited material. This effect is commonly seen with drying coffee spills, hence the name. It is due to the non-homogeneous evaporation of solvent from the edges of the liquid drop which introduces an outward convective flow which brings particulates to the edge of the drop. An example of the coffee-ring effect can be seen in the left section of Figure 3.15 showing the zone of densely deposited material (A), of sparsely deposited area (B) and a schematic diagram illustrating the solvent evaporation and outward convective flow. In the right section of Figure 3.15, we can see that this effect can be countered if we can introduce a Marangoni flows to counter the outward convective flow. The introduction of Marangoni flows results in a more homogeneous deposition of the particulate material (Still, Yunker & Yodh, 2012, p.4984-4988); (Kim et al., 2009, p.791-798) (C) with a smaller densely deposited edge (D). In this case, Marangoni flows are introduced via solvent engineering and controlling the drying atmosphere (Kim et al., 2009, p.791). The coffee-ring effect is tied to evaporation of the ink solvent and thus it can also be affected by the solvent boiling point, the temperature of the printed ink and the temperature of the printing substrate (Sette, 2014); (Soltman & Subramanian, 2008, p.2224-2231); (Kim et al., 2009, p.791). Ink drying and other post-printing processes are therefore seen as extremely important in controlling deposited material morphology.

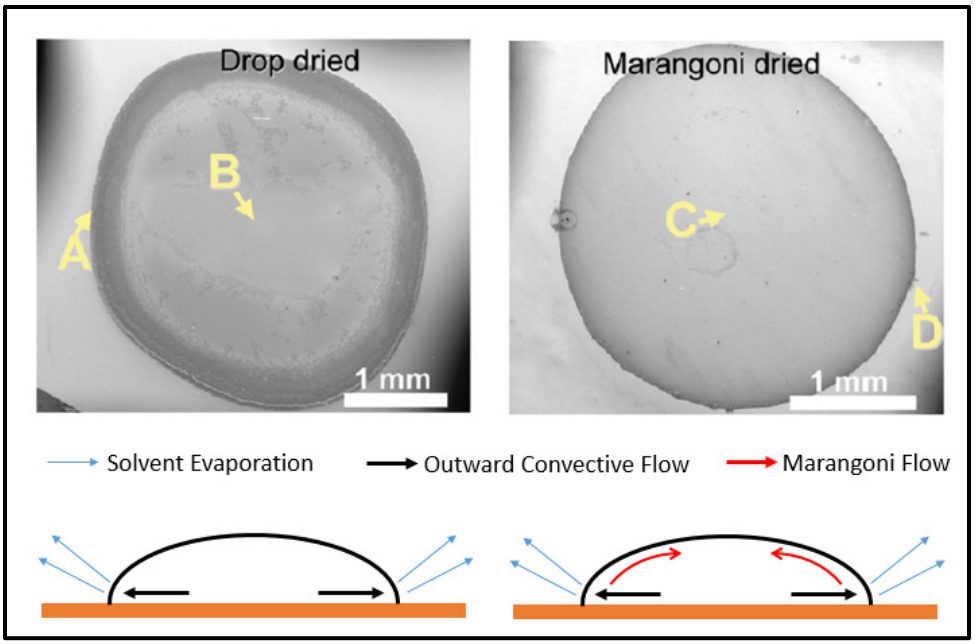

Figure 3.15 Photograph and schematic diagram of non-assisted (A,B) and Marangoni flow assisted (C,D) ink drop drying, showing the effects on the coffee-ring effect
Adapted from Kim et al. (2009, p.791)

Fluid dynamics also dictate how ink drops will comport themselves when printed next to one another. Figure 3.16 illustrates the behavior of the ink as drops are printed at different distances from one another. The liquid and substrate properties will dictate ink spreading and drop coalescence behavior for the formation of printed lines (Sette, 2014); (Alaman et al., 2016, p.910). While keeping the ink and substrate properties constant, varying the distance between each printed drop will result in different printed line formation behavior. With a large drop separation, the substrate surface energies and the ink surface tension prevent the drops from coalescing into a line and will result in a string of isolated drops (Figure 3.16 a)). When the drop spacing is reduced, the drops start to coalesce. At the start of this coalescing behavior most of the liquid is kept in its original position and creates a scalloped line (Figure 3.16 b)). When reduced further to an optimal drop spacing, a uniform line can be formed with straight edges (Figure 3.16 c)). Further decreasing the drop spacing will resulting in repeating bulges of material found along a mostly uniform line (Figure 3.16 d)).

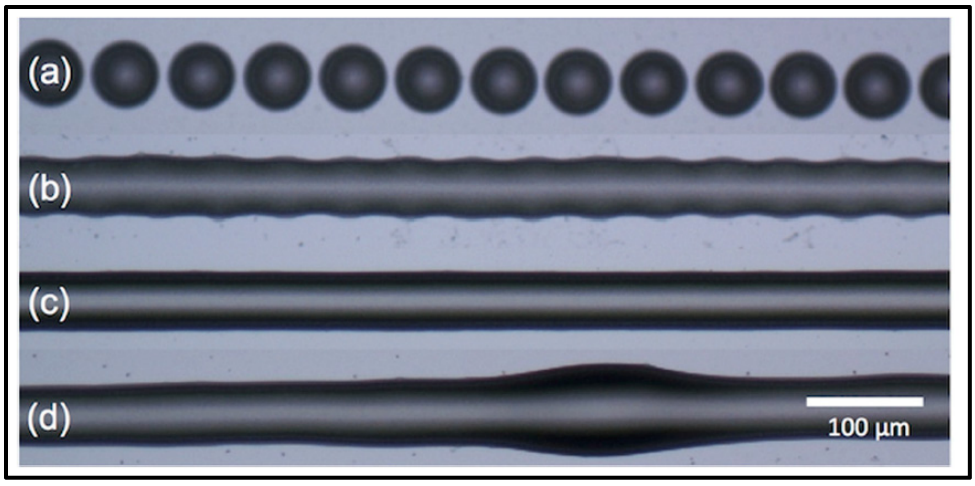

Figure 3.16 Photographs of ink drops deposited along a line with decreasing distances between adjacent drops (from a) to d)), showing a) isolated drops, b) scalloped line, c) uniform line and d) line bulging
Taken from Alaman et al. (2016, p.910)

3.3.3 Pre- and Post- Printing Processes

As mentioned earlier, printed materials often need pre-printing processes and/or post-printing processes to achieve final material properties. Annealing and/or evaporation processes are often employed to remove the solvent content of the ink material post-print. This is often done by heating the printed features in an oven or on a hotplate. Optical annealing processes can also be used. Infrared (IR) lamps (Tobjork et al., 2012, p.2949-2955), high power pulsed lights (Kim et al., 2009, p.791); (Chung et al., 2012, p.035202); (Eun, Chon, Yoo, Song & Choa, 2015, p.838-845) and laser exposure for local annealing (Kwon et al., 2014, p.1137-1145); (Yeo et al., 2014, p.562-568); (Yeo et al., 2012, p.e42315) are often used for optical annealing purposes.

Pre-Printing Processes – Surface Modification

Surface energies play an important role in the spread of the ink on the substrate, this is often referred to as the *wettability* of the substrate. An increase in surface energy of the substrate results in an increased wettability and a lower liquid contact angle. The surface energy can be

split into a polar and a dispersive component with the polar component having a greater effect on polar liquids (Hejda, Solar & Kousal. 2010, p.25-30). Figure 3.17 illustrates the effect on the liquid contact angle on low surface energy substrate (No Treatment) and a high surface energy substrate (Hydrophilic Surface Plasma Treatment), in this case, the increase in surface energy can be achieved using an oxygen plasma treatment. There are many processes which can be used to alter the surface energies of substrates, some examples include; plasma treatments (Jokinen, Suvanto & Franssila, 2012, p.016501); (Cho, Nguyen & Boo, 2011, p.5328-5333); (Walther et al., 2007, p.524); (Ashraf, Mattsson, Fondell, Lindblad & Thungstrom, 2015, p.086501), chemical treatments (Bodas & Khan-Malek, 2006, p.1277-1279), and UV exposure treatments (Efimenko, Wallace & Genzer, 2002, p.306-315). These treatments affect the surface energies by either;

1. Changing the surface chemistry by creating or passivating dangling bonds (Bodas & Khan-Malek, 2006, p.1277-1279).
2. Changing surface morphology by creating or removing high-curvature regions (Cho, Nguyen & Boo, 2011, p.5328-5333).

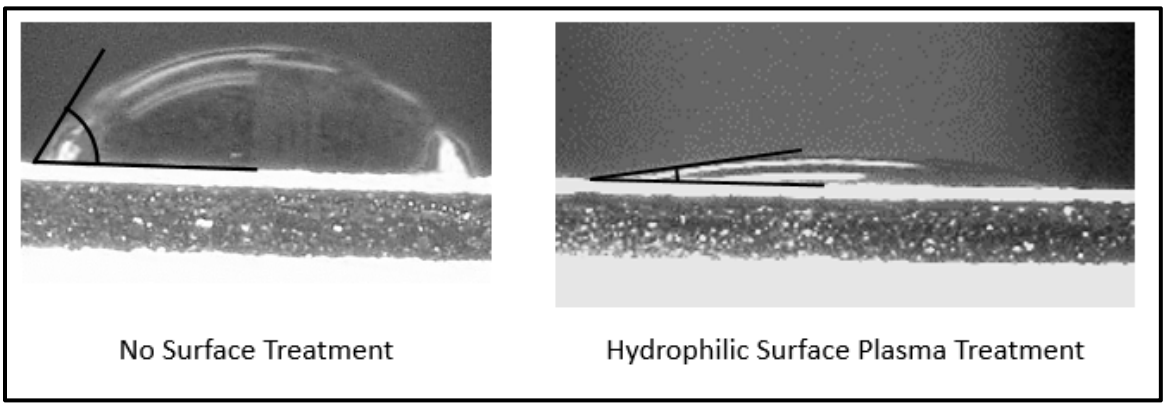

Figure 3.17 Effects of hydrophilic surface treatment on liquid-surface contact angle

The use of local modification to the substrate surface energy is also a successful approach to reducing the feature size of printed devices. In this case, high and low surface energy zones can be created on the substrate. These will either attract or repel the deposited ink and thus

limit the spread of the ink resulting in refined feature sizes (Suzuki et al., 2011, p.142-147); (Suzuki et al., 2009, p.1581-1584). This can be achieved using masked UV exposure or selective surface plasma treatments. These treatments work by either changing the surface chemistry by creating or passivating dangling bonds or by changing the morphology/surface roughness of the substrates (Cheng et al., 2017, p.350-356); (Juárez-Moreno, Ávila-Ortega, Oliva, Avilés & Cauich-Rodríguez, 2015, p.763-773). Shown in Figure 3.18 is an example of using the masked UV exposure approach. For this approach to work, polar ink formulations must be used. This process can also be used to create barriers to avoid bleeding or run-offs of ink from the printed features.

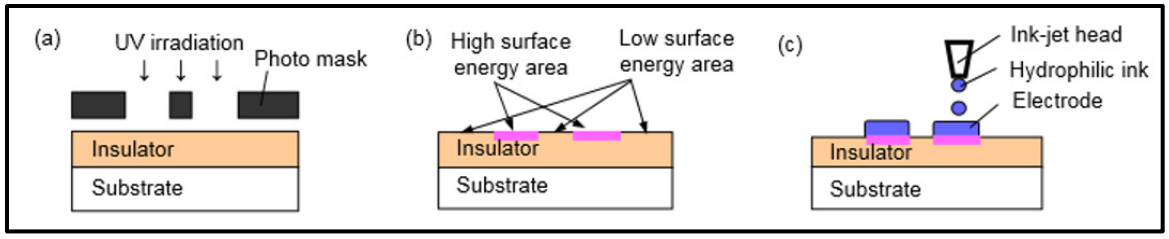

Figure 3.18 Schematic representation of the surface energy control for the inkjet printing process using a) local UV irradiation, b) formation of areas with adapted surface energy and c) fabrication of electrodes by inkjet printing
Adapted from Suzuki et al. (2011, p.142-147)

Surface energy modification treatments have already been mentioned for localized surface energy modifications. These treatments can also be used to modify the entirety of the substrate and/or printed layers to increase their wettability and allow for controlled printing on a multitude of surfaces. By increasing the wettability of substrates, the contact angle of ink drops is decreased, reducing the coffee-ring effect, increasing the adhesion of the ink material and allowing for thinner features to be printed. This also increases the minimal width of printed features as the drops' spread is increased.

Post-Printing Processes – Sintering, Annealing & Ablation

Some examples of post-printing treatments which are used in the field of PE are sintering, annealing and ablation treatments. Sintering and annealing treatments are essentially the same but often refer to fast optical processes and longer conventional heating processes, respectively. These heat treatments are used for solvent evaporation, metallic NP melting to form conductive networks and for crystallization purposes. On the other hand, ablation treatments often make use of laser processes. These are typically used to ablate printed material to achieve finer feature sizes.

Conventional oven annealing is still the most popular method of annealing. Annealing using IR exposure has recently gained popularity as processing speeds can be greatly increased and is compatible with roll-to-roll fabrication processes. Furthermore, optical sintering processes can be coupled to increase their effects. Figure 3.19 illustrates effects of the coupling of two optical processes for improved sintered Ag ink trace resistivities. These treatments take seconds instead of minutes or hours to effectively treat printed ink materials.

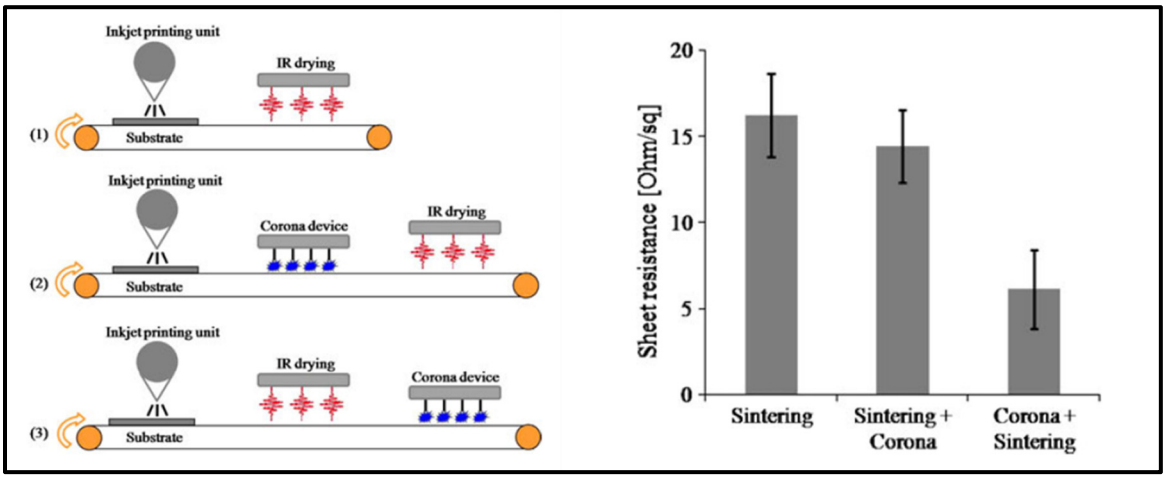

Figure 3.19 Schematic diagram of optical sintering processes and resulting conductive ink trace sheet resistances
Adapted from Denneulin, Blayo, Neuman & Bras (2011, p.3815-3823)

Another approach to optical sintering is the use of lasers for local sintering of NP inks. This treatment can be followed by a wash step to remove unsintered ink and can be used to reduce printed feature sizes (Ko, Pan, Lee, Grigoropoulos & Park, 2010, p.0EC03); (Yeo et al., 2012, p.e42315). This process is represented in Figure 3.20 and results in feature sizes of the order of the laser beam spot size (1-50 μm). Overall, using optical sintering processes is also advantageous as it is considered a low temperature process and will not damage temperature sensitive substrates which are often used for flexible device fabrication.

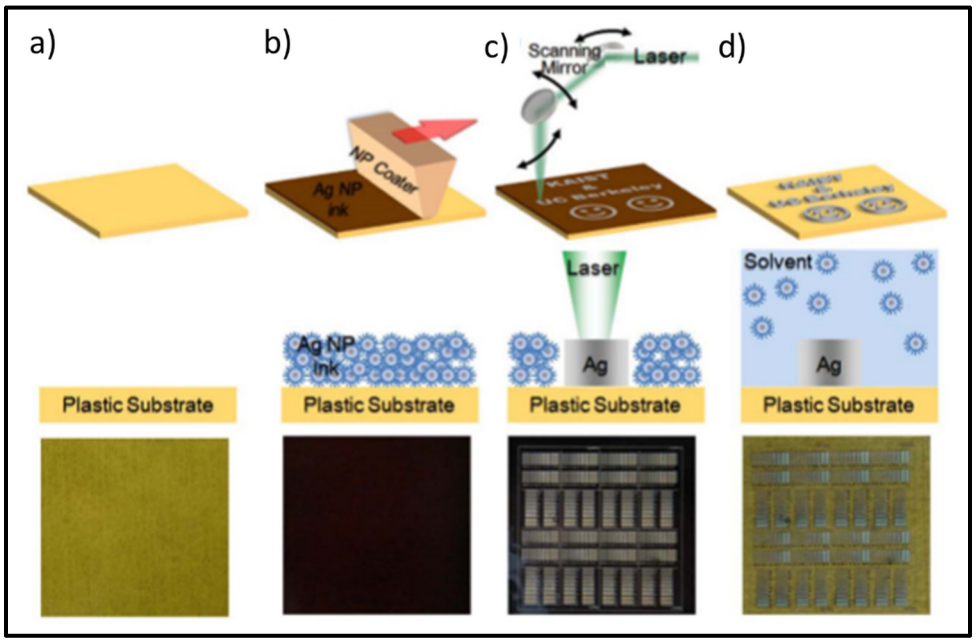

Figure 3.20 Schematic representation of the digital direct metal patterning (DDMP) process, a) polymer substrate preparation, b) Ag NP ink coating on a polymer substrate, c) laser scanning and local melting of the printed Ag NP ink film, d) washing out non-laser-processed Ag NPs to leave laser-processed Ag patterning on a polymer substrate. Middle row shows the cross section and bottom row shows the top view
Adapted from Yeo et al. (2012, p.e42315)

For ablation purposes of already printed and sintered ink traces, lasers can also be used. Laser parameters can be controlled to result in ablation of the unwanted material while not damaging the underlying substrate. Using this technique, feature sizes of the order of the laser beam spot

size can be achieved. A schematic representation of this approach is shown in Figure 3.21. As an example, OTFTs based on ink-jet printed electrodes in which a reduced channel length is accomplished by laser ablation have been demonstrated (Kim, Jeong, Moon, Han & Chung, 2007, p.071114). Indeed, channel lengths of 5 μm have been achieved using this process.

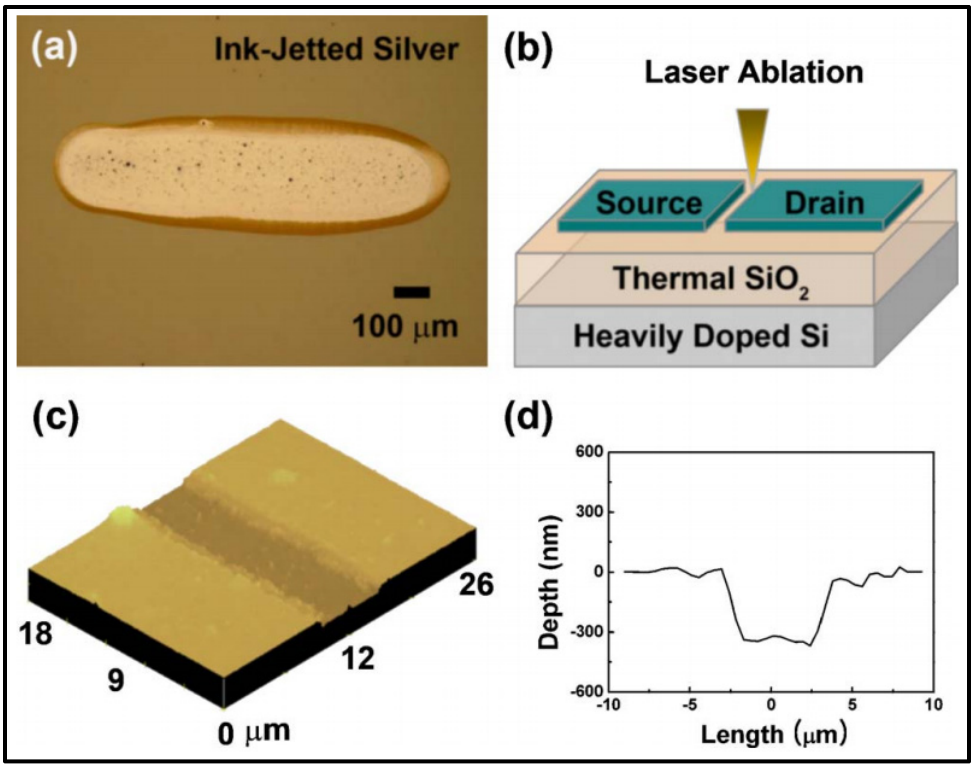

Figure 3.21 a) Optical microscope image of inkjet printed Ag NP ink electrode, b) schematic representation of the separation of the source and drain by laser ablation for the fabrication of OTFTs, c) confocal laser scaning microscopic three-dimensional image showing the channel region produced by laser ablation, d) corresponding two-dimensional profiles of the channel region Taken from Kim et al. (2007, p.071114)

3.3.4 Device Printing

Few electronic and optoelectronic devices are currently completely fabricated using purely inkjet-based printing processes. Most printed devices make use of hybrid fabrication processes

taking advantage of the benefits of printing processes while keeping conventional processes for some fabrication steps where it is still advantageous to do so. This section will look at the state-of-the-art of what is currently done and what can be achieved in terms of device fabrication using printing processes. Devices which are fully fabricated using inkjet printing processes and devices which are fabricated using a hybrid of printing and conventional fabrication processes are reffered to as inkjet printed devices and hybrid printed devices, respectively.

Passive and active device fabrication using only inkjet printing processes have been explored by many research groups over the past 10-15 years. From simple devices such as capacitors, resistors and inductances to more complex active devices such as PV and OTFTs have been fabricated. Many successes have been achieved and printed device architecture are now increasing in complexity. However, it must be noted that the performance of inkjet printed devices are often inferior to the performances of corresponding devices fabricated using conventional processes. What follows is an exploration of the state-of-the-art of current inkjet printed devices by way of examples, from simple passive devices to more complex devices. Figure 3.22 illustrates the evolution of the complexity of inkjet printed devices over the past 10-15 years.

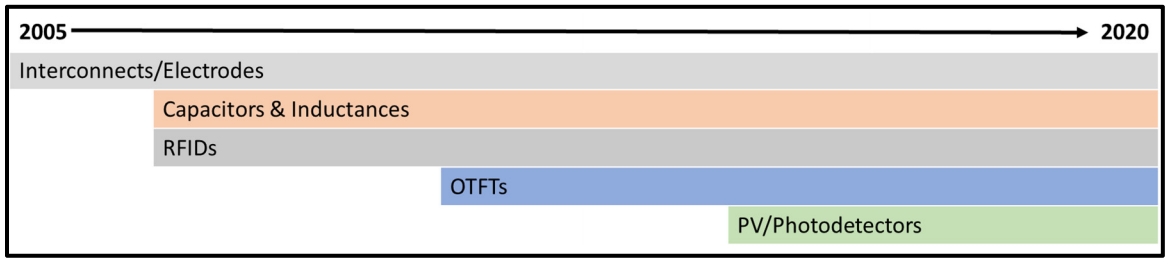

Figure 3.22 Overview of the evolution of inkjet printed device complexity from 2005 to 2020

Initially in the early 2000's, inkjet printing was starting to be used for printed electronic purposes. Interconnects and electrodes consisting of printed conductive ink traces where the first "devices" to be fully inkjet printed. For these devices, uniform printing of conductive

traces was the main problematic to overcome. For example, in 2003 Steven Molesa et al. presented improvements to the uniformity of inkjet-printed layers using Au NP ink. The authors were able to demonstrate high-quality inkjet-printed interconnects (Molesa, Redinger, Huang & Subramanian, 2003, p.769). Figure 3.23 illustrates the advancement to printed conductive trace uniformity achieved by Molesa et. al.. Pathways to minimize negative effects including the formation of coffee rings, have since been developed. Furthermore, it was found that ink formulation and post-printing process parameters are paramount for improved printing uniformity and repeatability. Similar problematics and uniformity enhancement pathways have been explored by multiple research groups for other conducting inks (Gamerith et al., 2007, p.3111-3118); (Jeong et al., 2008, p.679-686); (Lee, Chou & Huang, 2005, p.2436). From these works, we achieved a better understanding of the fluid dynamics of the printing process when applied to conductive inks.

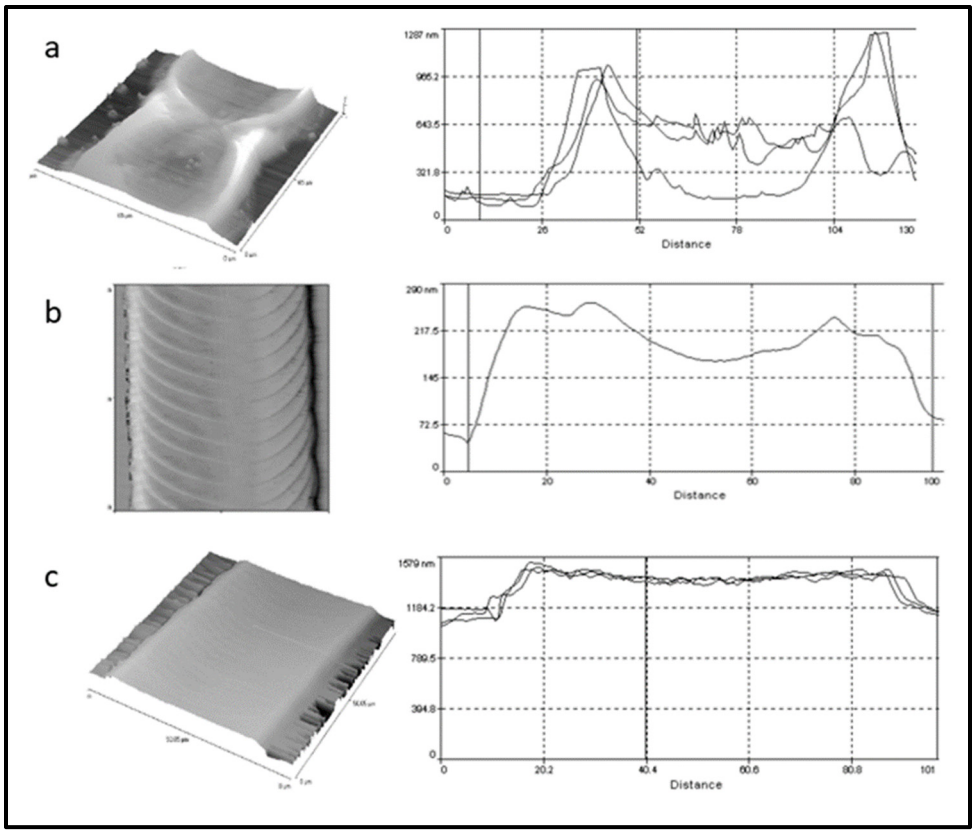

Figure 3.23 a) Atomic force micrograph showing the characteristics of the coffee-ring effect structure resulting from drop splashing, b) overlaying of successive drops to reduce the coffee-ring effect, c) smooth conductive traces obtained by optimization of printing temperature and ink solvent
Taken from Molesa et al. (2003, p.769)

Building on the research published on inkjet printed conductive traces for interconnects and electrodes, simple inkjet printed devices such as capacitors and inductors followed. An example of inkjet printed capacitors by Seung Hwan Ko et al. in 2007 (Ko, Chung, Pan, Grigoropoulos & Poulikakos, 2007, p.161-168) is illustrated in Figure 3.24. These capacitor structures are achieved by printing homogeneous layer of Au NP conductive inks sandwiching a layer of printed dielectric ink material. Similarly, other capacitive structures have been fully inkjet printed by many research groups using a range of different conductive and dielectric materials (Pech et al., 2010, p.1266-1269); (Bidoki, Nouri & Heidari, 2010, p.055023); (Liu, Cui & Varahramyan, 2003, p.1543-1548).

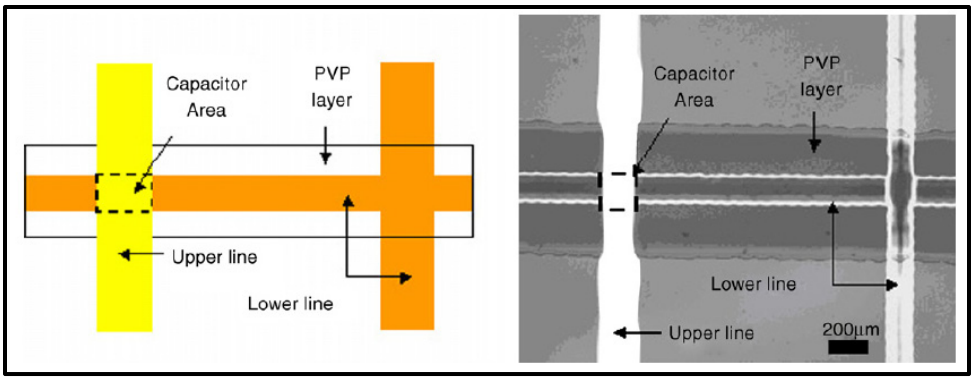

Figure 3.24 Schematic representation and microscope image of a crossover capacitor on polyimide film, the PVP layer is sandwiched between the lower and upper lines
Taken from Ko et al. (2007, p.161-168)

Likewise, inductive devices can also be inkjet printed (Bidoki et al., 2010, p.055023); (Wassmer, Diel & Krueger, 2010, p.205-213); (Cook et al., 2014, p.1-4). For example, vertically integrated high-performance inductors can be actively printed on flexible liquid crystal polymer (LCP) substrates (Cook et al., 2014, p.1-4). Similarly to capacitive devices, inductive devices are printed using conductive and dielectric inks, Figure 3.25 illustrates a simple device architecture with the conductive/dielectric/conductive ink material stacking required to achieve working inductive devices.

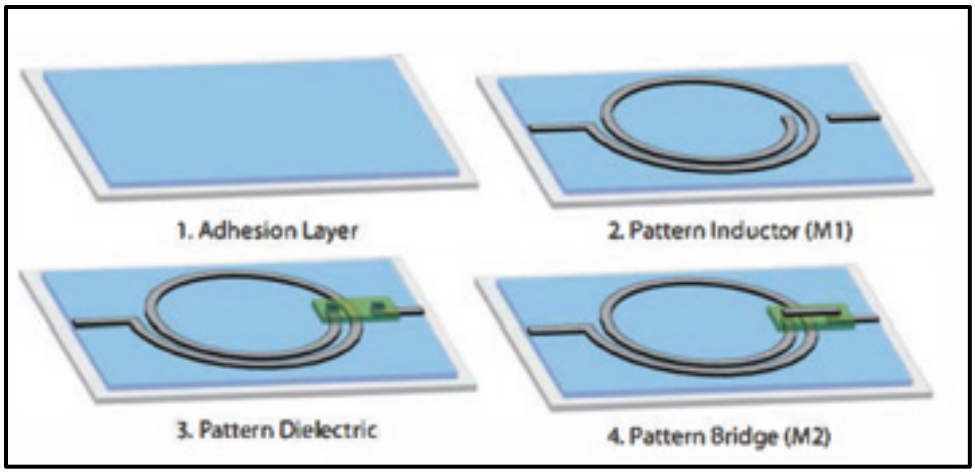

Figure 3.25 Schematic representation of the fabrication process for vertically integrated spiral inductors
Adapted from Cook et al. (2014, p.1-4)

By slightly adapting these capacitive and inductive devices structures, transistors, inverters, radio-frequency identification (RFIDs) devices and transformers can be printed. For example, the capacitive structures shown in Figure 3.26 can be modified by creating a channel using laser ablation to separate the top electrode to create a source and drain electrodes. By subsequently printing a semiconductor to fill the newly formed channel, an organic field effect transistor (OFET) can be fabricated.

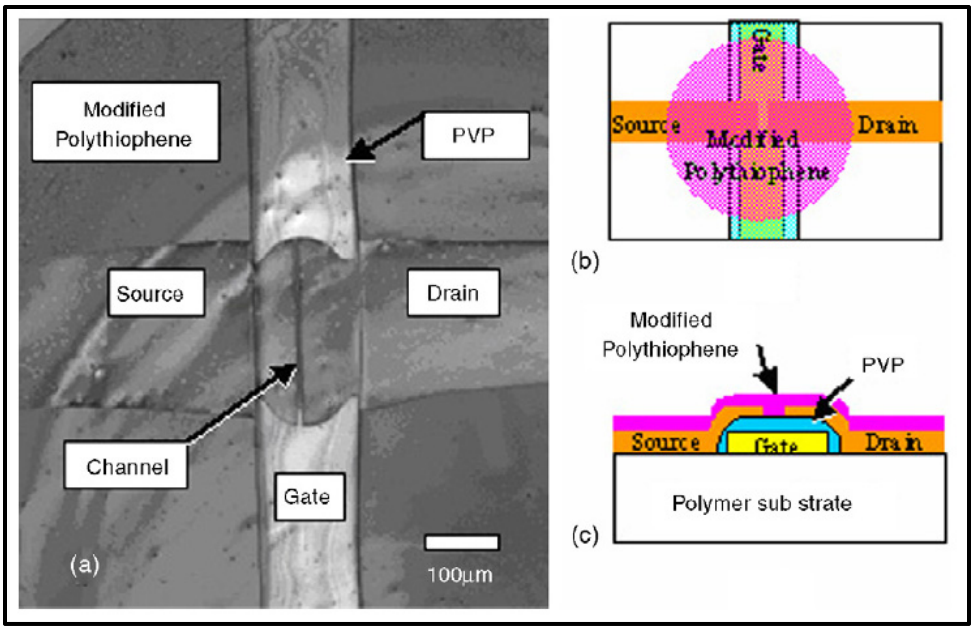

Figure 3.26 a) Micrograph image of an inkjet printed top gate OFET layer on top of a polymer substrate, b) and c) schematic representation of the OFET structure
Taken from Ko et al. (2007, p.161-168)

Similarly, other groups such as Chung et al. have been able to show working inkjet-printed OTFTs and inverters (Chung, Kim, Kwon, Lee & Hong, 2011, p.1134-1136), as illustrated in Figure 3.27. Interestingly, these inkjet printed devices show comparable electrical properties to similar devices fabricated using more conventional processes, as seen in Table 3.3.

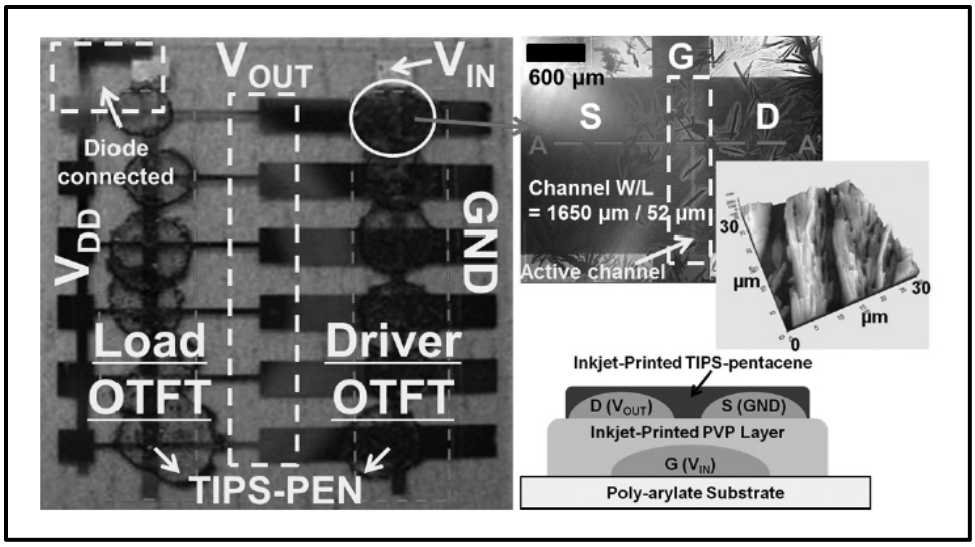

Figure 3.27 Overview of a fully inkjet printed OTFT structure
and inverter ensemble
Taken from Chung et al. (2011, p.1134-1136)

Table 3.3 Electrical properties of devices using different methods of deposition for the TIPS-pentacene active layer
Adapted from Chung et al. (2011, p.1134-1136)

Property	**Inkjet**	**Spin-coated**	**Drop-Casted**	**Evaporated**
Saturation Mobility [$cm^2V^{-1}s^{-1}$]	0.06	0.03	0.09	0.04
On/Off Ratio	10^4	$3x10^3$	10^4	10^4
Threshold Voltage [V]	-1.4	-5.1	-2.8	0.48

Likewise, the inductive devices shown in Figure 3.25 can be adapted to create transformers. This can be done by coupling inductive coils in more complex patterns. The increased printing complexity, in this case, comes from printing multiple stacks of conductive/dielectric ink material layers on top of each other, Figure 3.28 illustrates the fabrication process of such transformers.

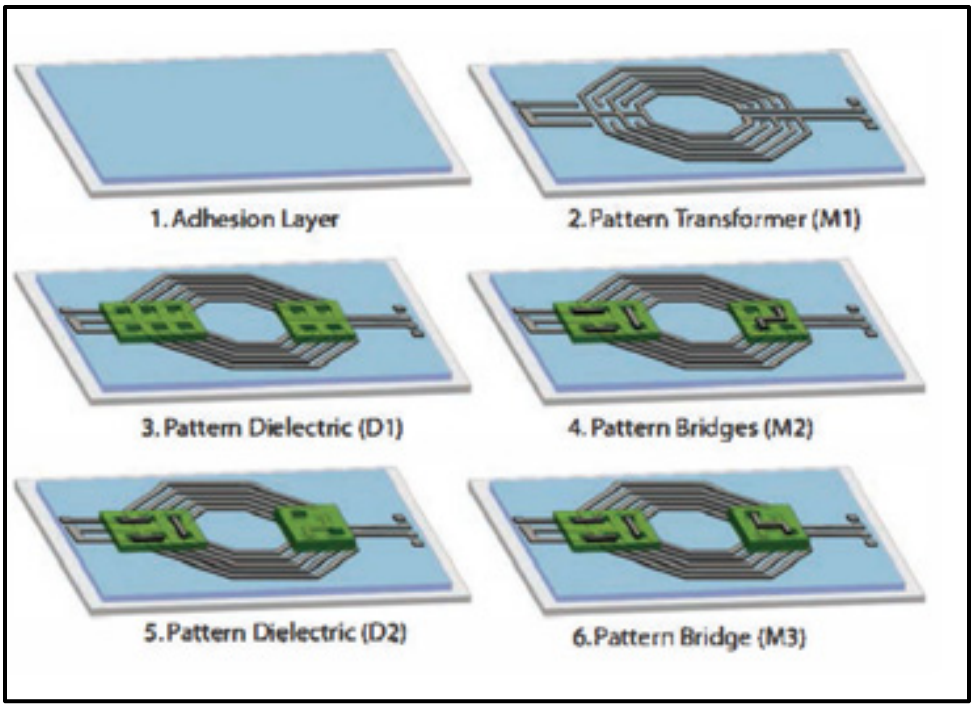

Figure 3.28 Schematic representation of the fabrication process for vertically integrated transformers
Adapted from Cook et al. (2014, p.1-4)

From 2014/2015 onwards, publications on inkjet-printed active optoelectronic and PV devices start appearing in the literature. Ranging from simple single junction PV devices (Eggenhuisen et al., 2015, p.7255-7262); (Jung et al., 2014, p.1400432) to tandem 9-layer inkjet-printed PV devices (Gevaerts et al., 2016, p.1630-1631). A good example of simple single junction PV devices which highlights the freedom of design associated with digital inket printing process are OPV devices printed by Eggenhuisen et. al. in 2015 which are illustrated in Figure 3.29 (Eggenhuisen et al., 2015, p.7255-7262). It should be noted that this device design is not fully optimized for performance, and therefore losses arise due to the limited conductivity of the narrow busbars and/or nonoptimal length of the fingers and busbars, for example.

When printing processes and PV design architectures are well understood, complex PV device stacks can be fabricated using inkjet printing. This is evident from the inkjet-printed tandem

9-layer PV devices fabricated by Gevaerts et. al. in 2016 which are illustrated in Figure 3.30 (Gevaerts et al., 2016, p.1630-1631).

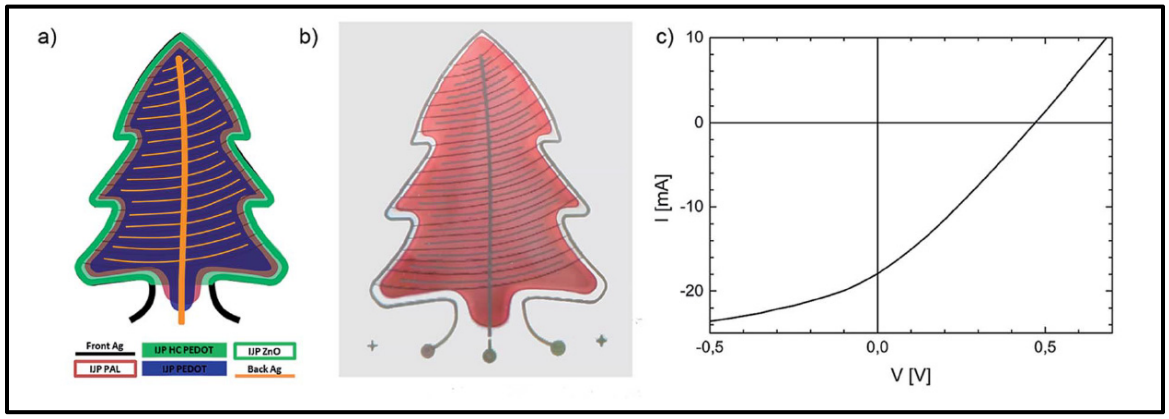

Figure 3.29 Organic solar cell in the shape of a Christmas tree, a) schematic representation of printed layers lay-out, b) photograph of finished fully inkjet printed OPV Christmas tree, and c) I–V curve recorded for a single device with Christmas tree shape
Taken from Eggenhuisen et al. (2015, p.7255-7262)

To achieve this complexity in device printing, each material must be adapted for inkjet printing on top of the previous layer. Secondly, each post-printing process, such as annealing, drying or activation, needs to be optimized for performances and to preserve the layers underneath. Even when these two aspects are considered, PV device performances are often lacking and barely reach 5 % energy conversion efficiencies. (Eom et al., 2010, p.1516-1522); (Gevaerts et al., 2016, p.1630-1631); (Eggenhuisen et al., 2015, p.7255-7262); (Jung et al., 2014, p.1400432); (Peng et al., 2017, p.1703704); (Mitra, Alalawe, Voigt, Boeffel & Baumann, 2018, p.642).

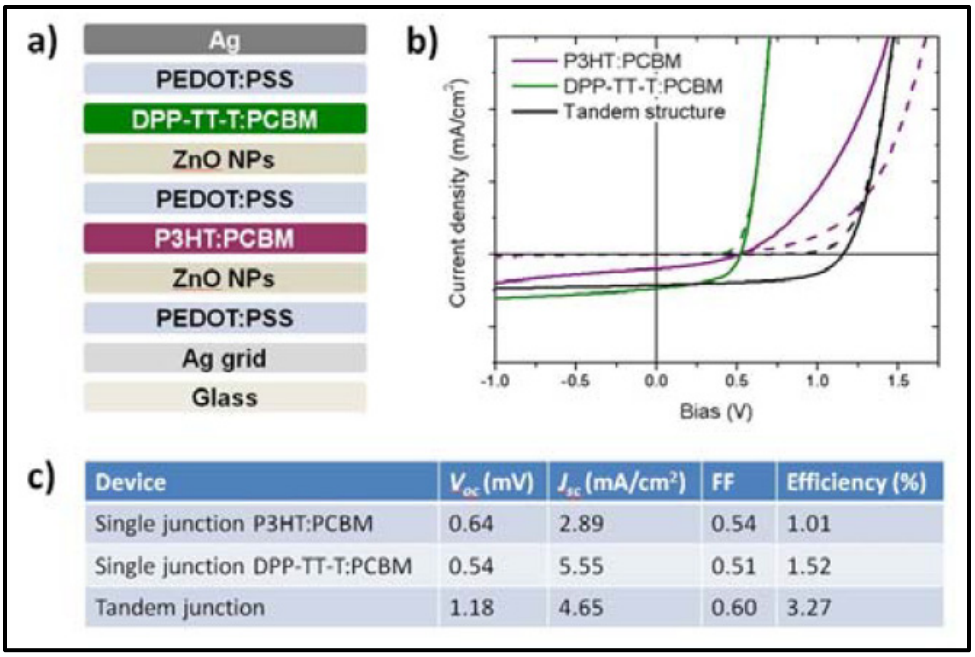

c)

Device	V_{oc} (mV)	J_{sc} (mA/cm²)	FF	Efficiency (%)
Single junction P3HT:PCBM	0.64	2.89	0.54	1.01
Single junction DPP-TT-T:PCBM	0.54	5.55	0.51	1.52
Tandem junction	1.18	4.65	0.60	3.27

Figure 3.30 a) Schematic representation of a tandem solar cell device comprising of 9 sequentially inkjet printed layers, b) I-V characteristics of single junction and tandem devices, c) champion device solar cell characteristics
Adapted from Gevaerts et al. (2016, p.1630-1631)

3.4 Conclusion

In this chapter an extensive literature review is presented on photosensing and thermistor device principles and operation. While PS optoelectronic device inner workings, principles and performances are reviewed in more detail. Additionally, a review of the complete inkjet printing process is presented.

From the literature review on photosensing devices and PS optoelectronic device inner workings, we find that PS materials can form PN junctions although being intrinsically un-doped. Charges can effectively separate, can be transported and collected in a PS layer. PS devices in TF architectures sandwiched between an HTL and an ETL are favored for their increased performances, although architectures void of either still show working behavior. The thickness and morphology of the PS film is paramount for device operation and should be kept

below 300 nm for optimum device performances. Solution processed PS based device are viable and adapting processes for inkjet printing should prove feasible.

From the literature review on the inkjet printing process, we find that attaining stable jetting is an achievable but non-trivial process. The rheological properties of the ink, most notably its viscosity, are important in achieving stable jetting void of ink trails and satellite drops. The effects of printing parameters and ink-substrate interactions are found to be important to achieve homogeneous printing. Pre- and post-printing treatments play a major role in resulting printed material surface morphology and properties. Fluid dynamics are shown to play a major role in the final morphology of dried inks which can result in unwanted coffee-ring effects when not accounted for.

Finally, an overview of the advances in inkjet-printed devices over the last 10-15 years is presented, with examples ranging from simple interconnects to complex 9-stack active devices. Adapting inkjet printing processes for passive device fabrication have been demonstrated and can result in minimal performance losses. However, for inkjet-printed active devices, performances are still often lacking. Indeed, fully printed PV device energy conversion efficiencies have barely reached 5 % (Eom et al., 2010, p.1516-1522); (Gevaerts et al., 2016, p.1630-1631); (Eggenhuisen et al., 2015, p.7255-7262); (Jung et al., 2014, p.1400432); (Peng et al., 2017, p.1703704); (Mitra et al., 2018, p.642).

CHAPITRE 4

OPTIMIZATION OF THE INKJET PRINTING PROCESS

In this chapter, we describe the optimization of inkjet printing processes for chosen inks and substrates. First, substrates are chosen, and substrate cleaning and manipulation procedures are described. Surface pre-printing processes using oxygen plasma treatments are performed on the chosen substrates and resulting surface energies are measured using drop contact angle measurements. These treatments are optimized and a standard treatment for all substrates is defined. Second, ink materials are chosen and acquired. Lab-made solutions are formulated when no commercial options are available. Ink storage and manipulation procedures are described. The optimization of the jetting parameters is performed, and final jetting process is described for each ink. The interaction of the jetted inks with pre-treated substrates are recorded, establishing the splat size at different temperatures. Finally, printed test plans are performed for the chosen inks, various printing parameters are examined while resulting layer thickness and homogeneity are recorded. Optimized printing parameters are found for each ink and for different resulting layer thickness. Additionally, the optimization of post-printing treatments (annealing, sintering and/or UV activation processes) is also performed. For each ink, a complete printing procedure is established, from ink manipulation to post-printing treatments.

4.1 Substrates

Choosing adequate substrates for inkjet printing and device prototyping can be a daunting tasks as multiple factors can come into play. The first questions to ask oneself when choosing an apropriate substrate should be: what is the role of the substrate? Is it needed simply as a mechanical structure to receive the deposition of material for device fabrication or will it play a role in device inner workings? Once the role of the substrate is understood, its choice can be further limited by the device fabrication process and the desired device characteristics. For example, if the fabrication process of a device requires high processing temperatures, the choice of substrate is limited to substrates which can withstand such temperatures. Substrate

transparence, processing temperature range, flexibility, elasticity, surface energies, surface coatings and/or composition are some examples of substrate characteristics which can play a role in device inner workings and in the device fabrication process.

Substrate transparency can be beneficial or detrimental to device operation depending on the type of device and material used. For example, some light sensitive materials which deteriorate rapidly upon UV exposure benefit from substrates which block this light. In contrast, LEDs or optoelectronic devices which makes use of the light for energy harvesting will obsviously need a substrate which is transparent in the region of interest. Substrate flexibility can be sought for allowing roll-to-roll process compatibility, increased transport efficiency and/or for shape conforming devices. Substrate elasticity can be important if stretchable devices are wanted, for either shape conforming purposes, microelectromechanical systems (MEMS) or other mechanical applications. Substrate surface energies can be very important parameters, a hydrophilic substrate will allow polar liquids to form thinner layers, while a hydrophobic substrate allows for smaller lateral printed feature dimensions. Surface coatings are also sometimes deposited onto the substrates in order to control the surface energy or to add new functionalities. These can take the form active materials such as ITO to form a TCO layer or the glossy coatings found on photo paper to improve printing quality.

For this work, several substrates have been identified for the prototyping of the proposed devices. The three main substrate characteristics which are sought for the prototyping of the proposed devices are;

1. Substrate transparence.
2. Surface energy.
3. TCO layer surface coating.

Our goal is to fabricate PV, photodetector and other optoelectronic devices which are sensitive, in part, to visible light. Therefore, transparent substrates in this region of interest are required for optimum device efficiencies. Since most device prototypes proposed for this work use TF-

based architectures, hydrophilic substrates which facilitate the fabrication of thin layers are preferred. Finally, to facilitate the fabrication process of the proposed PV and photodetector devices, substrates with a TCO coatings are also preferred as it will remove the need to print the transparent electrode layer.

For the printing test plans, Kapton flexible substrates (FT Kapton-FPC 300, Dupont) are chosen for their flexibility and high temperature processing range, which should not limit the use of post-printing processes for most ink materials. ITO coated glass (TEC 15, MTI Corporation) and PET (OCF2520, Thorlabs) substrates are acquired to test prototyping of the MALH PS devices on both rigid and flexible substrates. A PET substrate with a hydrophobic coating (Novalene IJ-220, Novacentrix) is chosen for all printing purposes where feature size is of greater importance than layer thickness such as for the terahertz (THz) vortex phase plate (VPP) devices shown in Chapter 5. Glass and PET (Melinex ST-505 Polyester, Tekra) void of additional coatings are also used in this work to test the effect of plasma treatments on surface energies.

The substrates used in this work amd described above are summarized in Table 4.1, showing the substrate composition, thickness, temperature processing range and the substrate coatings.

Table 4.1 List and property overview of chosen substrates

Name	**Material**	**Supplier**	**Thickness [mm]**	**Coating**	**Processing Range [°C]**
FT Kapton-FPC 300	Polyimide	Dupont	0.125	None	<400
Novele IJ-220	PET	Novacentrix	0.14	Proprietary	<120 (<180*)
OCF2520 ITO-Coated PET Film	PET	Thorlabs	0.2	ITO	<120
Melinex ST-505 Polyester	PET	Tekra	0.125	None	<120
Glass	Glass	Varied	Varied	None	<800
ITO Coated Glass Substrates (TEC 15)	Glass	MTI Corporation	0.7	ITO	<800

*minimal structural damage observed up to a processing temperature of 180 °C

4.1.1 Substrate Cleaning

While the device prototyping printing process presented in this work takes place entirely inside class 100,000 clean-rooms, it was found that some contamination of the substrates is still possible and happens quite readily especially on Polyimide substrates where static charge build up occurs and attracts particles to its surface.

Prior to substrate pre-printing treatments and prior to inkjet printing, the substrates need to be inspected and cleaned. The substrates need to be void of particles or defects as this can translate to defects of printed features. An optical inspection of the substrates is carried out prior to any manipulation, substrate showing visible defects seen with the naked eye are rejected in favor of pristine substrates. Once the substrates have been inspected for defects, they are cleaned to remove any particles and contaminants.

For glass-based substrates, the cleaning procedure is as follows:

1. 10 minutes in Acetone sonicating bath.
2. 10 minutes in isopropyl alcohol (IPA) sonicating bath.
3. Dry with Nitrogen.
4. Wipe with lint-free non-abrasive clean room wipe.

Step one (1) is omitted for PET and other plastic based substrates, since it would damage the integrity of the substrates. For the Novele PET substrate, only the last step is performed as IPA is found to damage the integrity of the proprietary coating.

4.1.2 Substrates Pre-Printing Treatments

As stated previously, the surface energies of the substrates play an important role in its wettability. An increase in surface energy of the substrate results in an increased wettability and a lower liquid contact angle, which is beneficial for the formation of thinner material

layers. The surface energy is split into its polar and dispersive components, with the polar component having a greater effect on polar liquids (Hejda, Solar & Kousal, 2010, p.25-30).

In this Chapter section, the effects of oxygen plasma pre-printing treatments on the surface energies and liquid contact angles are explored. The treatments are performed on the substrates chosen for this work and on a printed dielectric layer (SU-8, MicroChem). A PlasmaTherm Unaxis 790 Plasma Etch system is used for the plasma treatment pre-printing processes. Four (4) test liquids are used in conjecture with the Owens/Wendt method to calculate the substrate energies before and after the plasma treatments. The four (4) test liquids are acquired from Sigma-Aldrich and are listed in Table 4.2, along with their surface tension in mJ/m^2 separated into their dispersive and polar components.

Table 4.2 Characteristics of test liquids used for Owens/Wendt calculations of surface energies

	Surface Tension [mJ/m^2]			
Test Liquid	*Total (σ_L)*	*Dispersive Component (σ_{LD})*	*Polar Component (σ_{LP})*	*Character*
DI Water	72.8	21.8	51.0	Bipolar
Diiodomethane (99%, EC:200-841-5)	50.8	50.8	0.0	Apolar
Formamide (≥99.5%, EC: 200-842-0)	58.0	39.0	19.0	Bipolar
Glycerol (≥99%, EC: 200-289-5)	64.0	34.0	30.0	Bipolar

To measure the contact angles of the test liquids, 10 µL drops are deposited on the test substrate using a micropipette. Images of the drops in contact with the substrate are then taken with an optical microscope aligned parallel to the substrate as illustrated in Figure 4.1. The images are processed through ImageJ software, where the contact angle between the test liquid drops and the substrate can be measured. An example image of a glycerol test liquid drop on a FT Kapton-FPC 300 substrate before and after a typical oxygen plasma surface treatment process is

performed, is shown in Figure 4.2, highlighting the increase of wettability achieved via this process. This experiment uses much higher drop volumes (10 µL) than what is typically used when inkjet printing (1-10 pL). It is not representative of the contact angles of printed drops, rather it is meant to optimize the plasma treatment parameters for maximum substrate wettability.

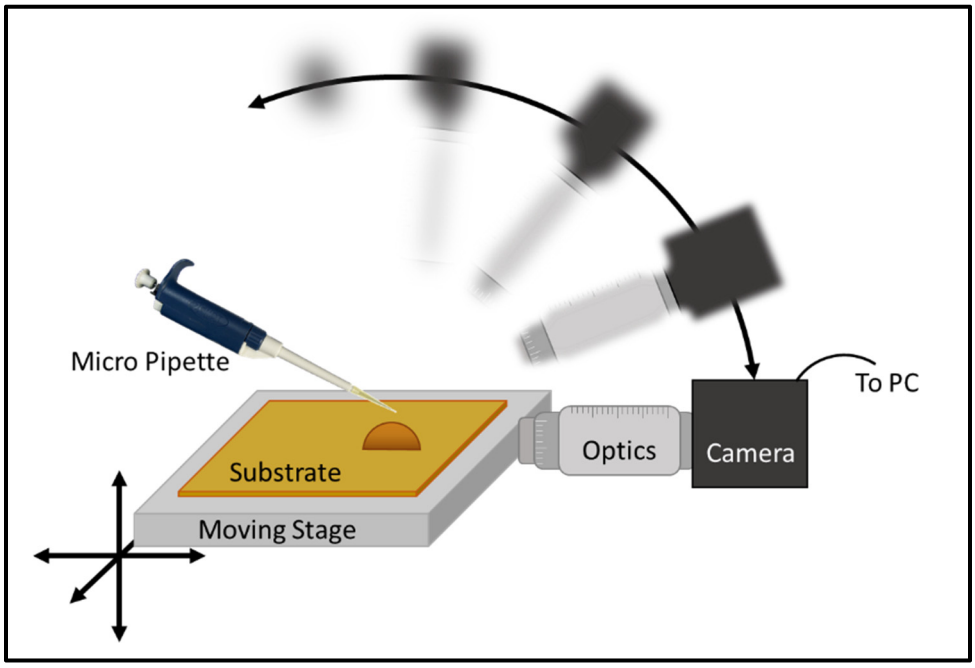

Figure 4.1 Schematic representation of the liquid-surface contact angle measurement set-up

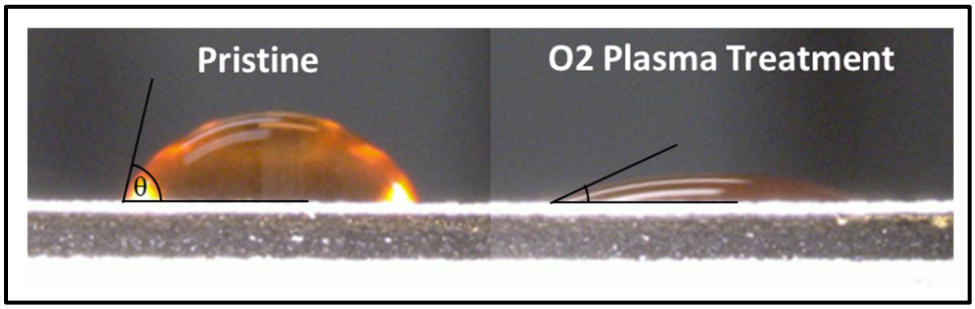

Figure 4.2 Effects of the hydrophilic oxygen plasma surface treatment on the liquid-surface contact angle

The Owens/Wendt theory and method of calculating the dispersive and polar components of the substrate surface energy is derived from the combination of Young's relation and Good's equation. The former relates the contact angle to the surface energies of the solid and the liquid, while the latter relates the interface tension to the surface energies. The resulting principle can be expressed in terms of a linear expression and is expressed in Equation 4.1.

$$\frac{\sigma_L(\cos\theta + 1)}{2\sqrt{\sigma_{LD}}} = \frac{\sqrt{\sigma_{SP}}\sqrt{\sigma_{LP}}}{\sqrt{\sigma_{LD}}} + \sqrt{\sigma_{SD}} \tag{4.1}$$

Where σ_L is the liquid surface tension in mJ/m^2. σ_{LD} and σ_{LP} are the dispersive and polar components of the liquid surface tension, respectively. σ_{SD} and σ_{SP} are the dispersive and polar component of the solid surface energy in mJ/m^2, respectively. θ is the contact angle between the solid and the liquid.

This equation can be expressed in the form of y=mx+b:

$$y = \frac{\sigma_L(\cos\theta + 1)}{2\sqrt{\sigma_{LD}}} = mx + b\,, \tag{4.2}$$

Where

$$m = \sqrt{\sigma_{SP}}\,, \qquad x = \frac{\sqrt{\sigma_{LP}}}{\sqrt{\sigma_{LD}}}\,, \qquad b = \sqrt{\sigma_{SD}} \tag{4.3}$$

By plotting x against y for each test liquids, the σ_{SP} can be calculated from the gradient of the line and σ_{SD} from its intercept at the y axis.

This process is carried out first on FT Kapton-FPC 300 substrates to gauge the primary parameters and their range for achieving adequate treatment results. Both the treatment time and the plasma power are varied, the results of this primary test plan are shown in Figure 4.3. Figure 4.3 a) shows the effects of increasing the treatment time while keeping the plasma power constant at 30 W, whereas Figure 4.3 b) shows the effects of increasing the plasma power while

keeping a treatment time of 120 s. It is found that increasing the plasma power above 10 W has very little effect in further changing the substrate surface energy. Similarly, the plasma treatment is found to fully activate the substrate after only 10 s of treatment. Nonetheless, from the literature we find that increasing the plasma treatment time extends the lifetime of treatment's effects, up to months (Jokinen et al., 2012, p.016501); (Walther et al., 2007, p.524). Since printing in this work is done within the same day of the plasma treatments, a short treatment time of 2-5 minutes with a plasma power of 50 W is deemed more than adequate.

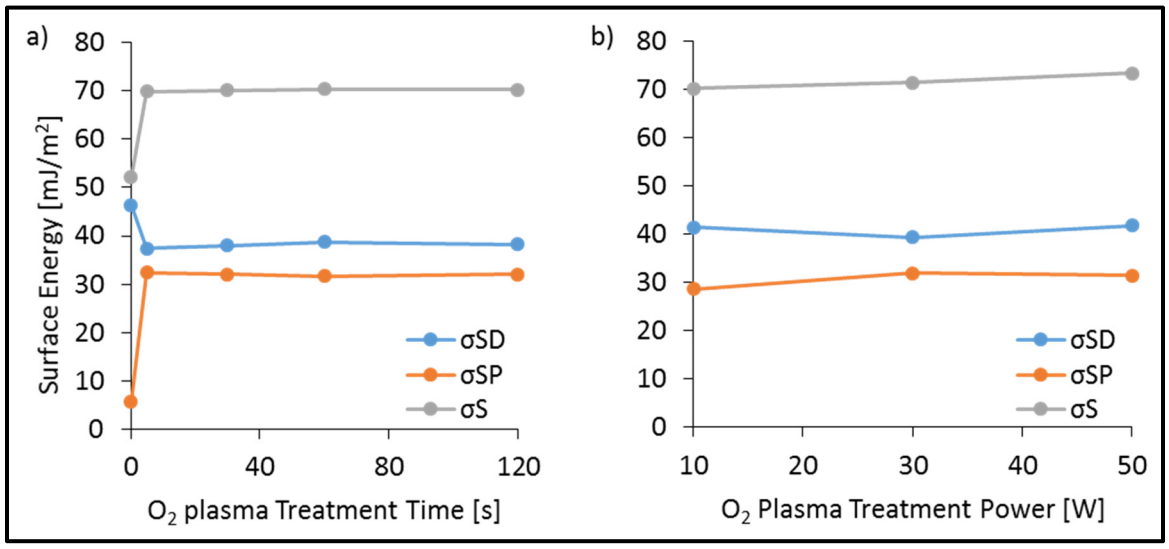

Figure 4.3 Kapton surface energy results of a hydrophilic oxygen plasma surface treatment with a) increasing treatment time and constant 30 W power and b) increasing treatment operation power and constant 120 s treatment time

Using a plasma power of 50 W and a treatment time of 120 s, the Owens/Wendt method was used to calculate the surface energies of all the substrates specified in section 4.1 of this work in addition to SiO_2 and a printed SU-8 dielectric layer. The surface energies are calculated before and after the oxygen plasma treatments. The results are plotted in Figure 4.4 showing the Owens/Wendt graphs and the linear fitting used to calculate the dispersive and polar components of the surface energies of the substrates before and after treatment. These results are also summarized in Table 4.3.

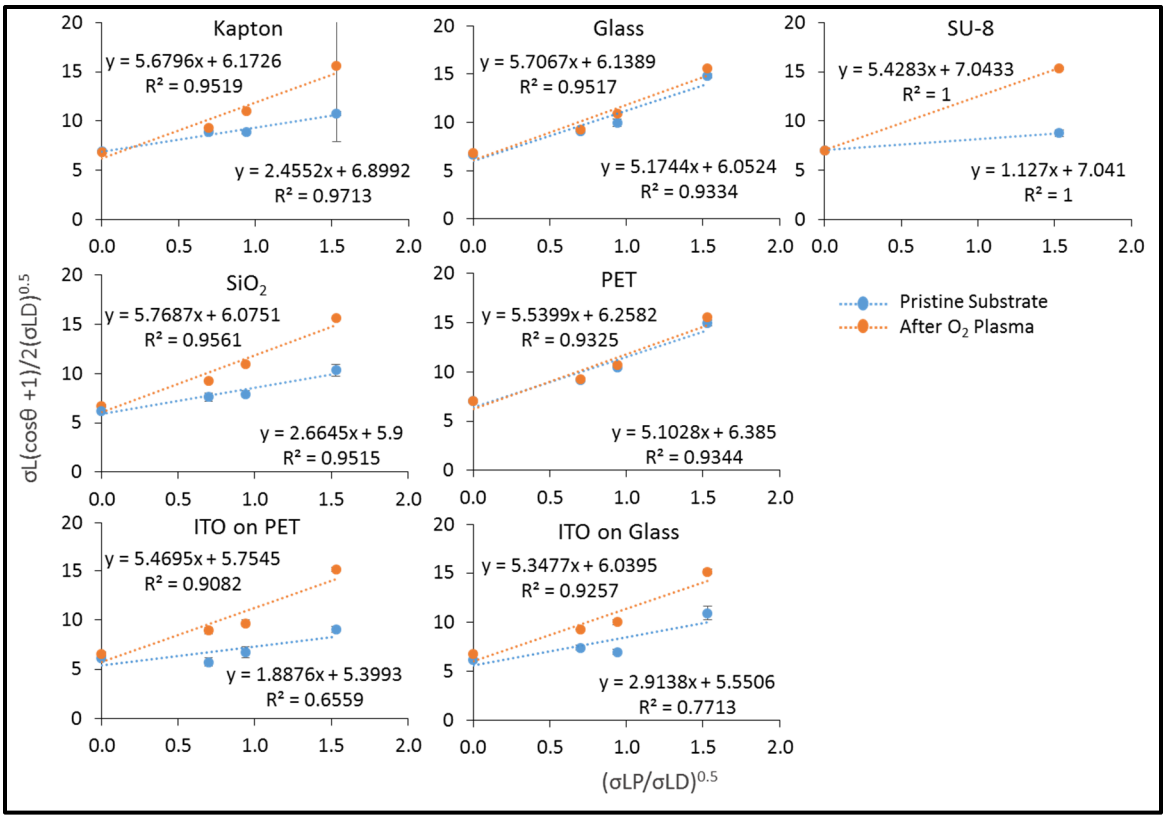

Figure 4.4 Owens/Wendt surface energies graphs using the four (4) test liquids on the chosen substrates, before and after hydrophilic oxygen plasma surface treatments

Table 4.3 Overview of the surface energy results of the hydrophilic oxygen plasma treatments on the chosen substrates

	Pristine Substrate				After O_2 Plasma Treatment			
Substrate	***σSD***	***σSP***	***σS***	θ_{Water}	***σSD***	***σSP***	***σS***	θ_{Water}
Kapton	47.6	6.0	53.6	**67.7**	38.1	32.3	70.4	**3.9**
SiO_2	34.9	7.1	42.0	**71.0**	36.9	33.3	70.2	**0.0**
PET	40.8	26.0	66.8	**22.9**	39.2	30.7	69.9	**0.0**
ITO on PET	29.2	3.6	32.7	**81.0**	33.1	29.9	63.0	**19.1**
ITO on Glass	30.8	8.5	39.3	**66.4**	36.5	28.6	65.1	**20.0**
Glass	36.6	26.8	63.4	**26.2**	37.7	32.6	70.3	**0.0**
Su-8	49.6	1.3	50.9	**82.9**	49.6	29.5	79.1	**14.4**

The plasma treatment has the desired effect of increasing the wettability of the substrates, while being more effective on some substrates than others. Interestingly, we find that it is the polar component of the substrate surface energies which are the most affected, where an average increase of 19.6 ± 10.1 mJ/m^2 is found over all substrates. The polar component of the surface energies of the PET and glass substrates with no coatings were affected the least, with an increase of 4.7 and 5.8 mJ/m^2, respectively. The effect of the oxygen plasma treatment on the dispersive component of the surface energies is varied across the different substrates. Some substrates show an increase in the dispersive component of the surface energies while others show a decrease or even no discernable change at all, as is the case for the printed SU-8 layer. An average change of 0.2 ± 4.9 mJ/m^2 is calculated for the dispersive component of the surface energies across all the tested substrates.

The greater effect which is of more importance for this work, is the stabilization of the surface energies over all tested substrates after the oxygen plasma treatment. By looking at the values of the water contact angle (ϑ_{water}) for the tested substrates before and after the oxygen plasma treatment, this trend becomes evident. The average values of ϑ_{water} before and after the oxygen plasma treatment are 59.7 ± 24.9 ° and 8.2 ± 9.3 °, respectively. For three (3) of the substrates

the ϑ_{water} is relatively close to 0 ° after the treatment and could not be measured accurately. The ϑ_{water} for the two ITO coated substrates are relatively close after the treatment (19.2 ° and 20.0 °). Therefore, one common printing procedure can be used for printing on the substrates showing ϑ_{water} = 0 ° and another common printing procedure can be used for both ITO covered substrates after the oxygen plasma treatment is performed. Furthermore, the lower variation in water contact angle with respect to the other substrates is beneficial since the ink printing recipes can be more readily adapted from printing on the remaining substrates.

4.2 Inks & Optimizing Ink Jetting

4.2.1 Ink Choice

Similarly to choosing the adequate substrates for device prototyping, choosing the adequate ink materials to print and fabricate devices is essential. To fabricate most optoelectronic devices, three (3) materials types are needed; electrical conductors, dielectrics and semiconductors. From the literature review performed in Chapter 3, we find that for PS based photodetectors and/or PVs, ETL and HTL materials are not necessary but can help boost device performances. The right PS material must be chosen for the purposes of inkjet printing in ambient atmosphere conditions. The solvents used in the inks are also of importance when choosing ink materials for device fabrication. In theory, orthogonal solvents are desired for each ink material that will come into contact, so that the solvent content does not interact with the underlying printed material. In practice, we find that activating the underlying material either by annealing, UV activation or solvent drying can sometimes allow non-orthogonal solvents-based inks to be printed on top of each other. The same was often found for consecutive printed layers of the same ink material. The chosen ink materials for this work, their compositions and liquid properties are presented in Table 4.4. The viscosities of the ink materials are measured using a RheoSense microVISC portable viscocimeter while the liquid surface tensions are calculated from contact angle measurements on multiple substrates.

Table 4.4 Overview and characteristics of chosen ink materials

Ink	**Components**	**Composition**	**Density [kg/m^3]**	**Viscosity [cP]**	**Surface Tension [mJ/m^2]**
ANP DGP 40TE-20C	TGME	~96 vol%	3920	15.7	36
	Ag NPs (≤50nm)	30.9 wt%			
Ossila I101 PS	MAI	378.6 mg/ml	1548	3.9	16
	PbCl	221.4 mg/ml			
	DMF	~95 vol%			
Spiro-OMeTAD	Chlorobenzene	~85 vol%	1165	1.7	10
	Acetonitrile	~4 vol%			
	TBP	~3 vol%			
	Spiro-OMeTAD Powder	67.3 mg/ml			
	LiTFSI	0.847 mg/ml			
	FK209	8.09 mg/ml			
SU-8 (MicroChem)	Cyclopentanone	~45 vol%	1037	8.9	30
	1-Methoxy-2-propanol acetate	~30 vol%			
	Proprietary Epoxy Resin	~15 vol%			
	Gamma-Butyrolactone	~10 vol%			
PEDOT:PSS Poly Ink HC	Water	~92 vol%	985	3-8	40
	Diethylene Glycol	~5 vol%			
	Ethanol	~2 vol%			
	PEDOT-PSS + MwCNT	1.0-1.2 wt%			

Conductive Material

Currently, conductive inkjet compatible inks are readily available from many suppliers. For this work ANP's conductive Ag NP ink DGP 40TE-20C is chosen due to its solvent content, relatively low annealing temperature of 180-200 °C and low advertised resistivity of ~7 μΩ-cm. It should be noted that since the start of this work, the conductive ink market has exploded and many conductive ink products now advertise annealing temperatures as low as 60°C (Mou, Zhang, Cheng, Peng & Chen, 2018, p.249-256); (Dupont, 2018). These novel inks should be better suited for printing on low-cost flexible substrates.

Dielectric Material

Dielectric materials can be used to isolate conductive materials, as encapsulation and/or as mechanical structures. For this work, MicroChem's SU-8 inkjet ink, a photo-resin based inkjet compatible ink, is used as a dielectric which meets the requirements for all the aforementioned uses in some capacity. This material was chosen in part due to its versatility and its usefulness for further PE works. The photo-induced cross-linking (photo-reticulation) of the resin is a beneficial process which is well suited with the printing equipment used in this work. The in-situ Phoseon Technology UV exposure system is capable of emission in both the i-line (365 nm) and g-line (405 nm) and is compatible with MicroChem's SU-8 ink curing specifications. Moreover this ink material has been shown to be adequate for printing 3D mechanical features in the 10s -100s μm dimensions (Persano et al., 2018, p.105290V); (Humood et al., 2018, p.1703852); (Lorenz et al., 1997, p.121) and can even act as a rudimentary encapsulation (Hammond & Cumming, 2004, p.893-897); (Kwon et al., 2009, p.2795-2800).

Transparent Electrode Material

A water based PEDOT:PSS inkjet compatible ink: Poly Ink HC is chosen as a transparent conducting polymer material for then eventual replacement of the ITO coating on flexible substrates. This ink is doped with multi-walled carbon nanotubes (MWCNTs) to increase its

conductivity. PEDOT:PSS is also shown to be compatible as a HTL for TF PS optoelectronic devices (Liang et al., 2014, p.3748-3754); (You et al., 2014, p.1674-1680); (Dubey et al., 2016, p.10231-10240), and could be used as a replacement for Spiro-OMeTAD for inverted device architectures. The versatility of the material to act either as a semiconductor or as an ITO transparent electrode replacement is of interest since its usefulness can also be extended for future works.

Active Perovskite Materials

The choice in commercially available PS solutions is currently very limited, with no inkjet adapted formulations on the market yet. We find that Ossila's I101 PS ink is the best suited for this work, this ink is specified for air processing in low humidity environment of 20 % to 35 % and is based on MAI and PbCl precursors in dimethylformamide (DMF) solvent. This ink material is adapted for spin coating processes and has a rather low viscosity of less than 1cP at 20 °C. Ossila advertises PV device power conversion efficiencies of over 13 % for FTO/TiO_2 Compact + Mesoporous/I101/Spiro-OMeTAD/Au TF architecture devices fabricated via spin coating on rigid substrates (Ossila, 2016). However, both aspects of the ink; the low viscosity and the low humidity processing environment are not suited to the inkjet printing equipment and environment used in this work. The RH varies between 20 % and 60 % within the class 100,000 clean-room and between 25 % and 45 % within the printer enclosure.

Hole Transport Layer Material

Spiro-OMeTAD is identified as the HTL of choice for PS optoelectronic devices, however no ink formulation is currently available commercially. As such, the ink must be formulated from its components. The Spiro-OMeTAD ink is formulated following an already established procedure (Gonzalez-Pedro et al., 2014, p.888-893), the process is depicted in Figure 4.5. First, a solution (A) is prepared by vortex mixing 144.6 mg of Spiro-OMeTAD M292 powder (Ossila) with 2 ml of Chlorobenzene (CB) (Sigma-Aldrich) for 10 minutes. A second solution (B) is prepared from 520 mg of lithium bis(brifluoromethanesulfonyl)imide (LiTFSI) powder

(Sigma-Aldrich) and 1 ml of Acetonitrile (Sigma-Aldrich). A third solution (C) is prepared from 300 mg of FK209 powder (Sigma-Aldrich) and 1 ml of Acetonitrile. 35 µl of solution B, 58 µl of solution C and 56.6 µl of 4-tert-butylpyridine (TBP) solution (Sigma-Aldrich) are added to solution A, the whole is vortex mixed until fully dissovled. Many Spiro-OMeTAD formulations can be found in the literature with varying concentrations of Spiro-OMeTAD powder, LiTFSI powder, TBP and FK209 powder, however the ink formulation presented here is very well suited for the inkjet printing process.

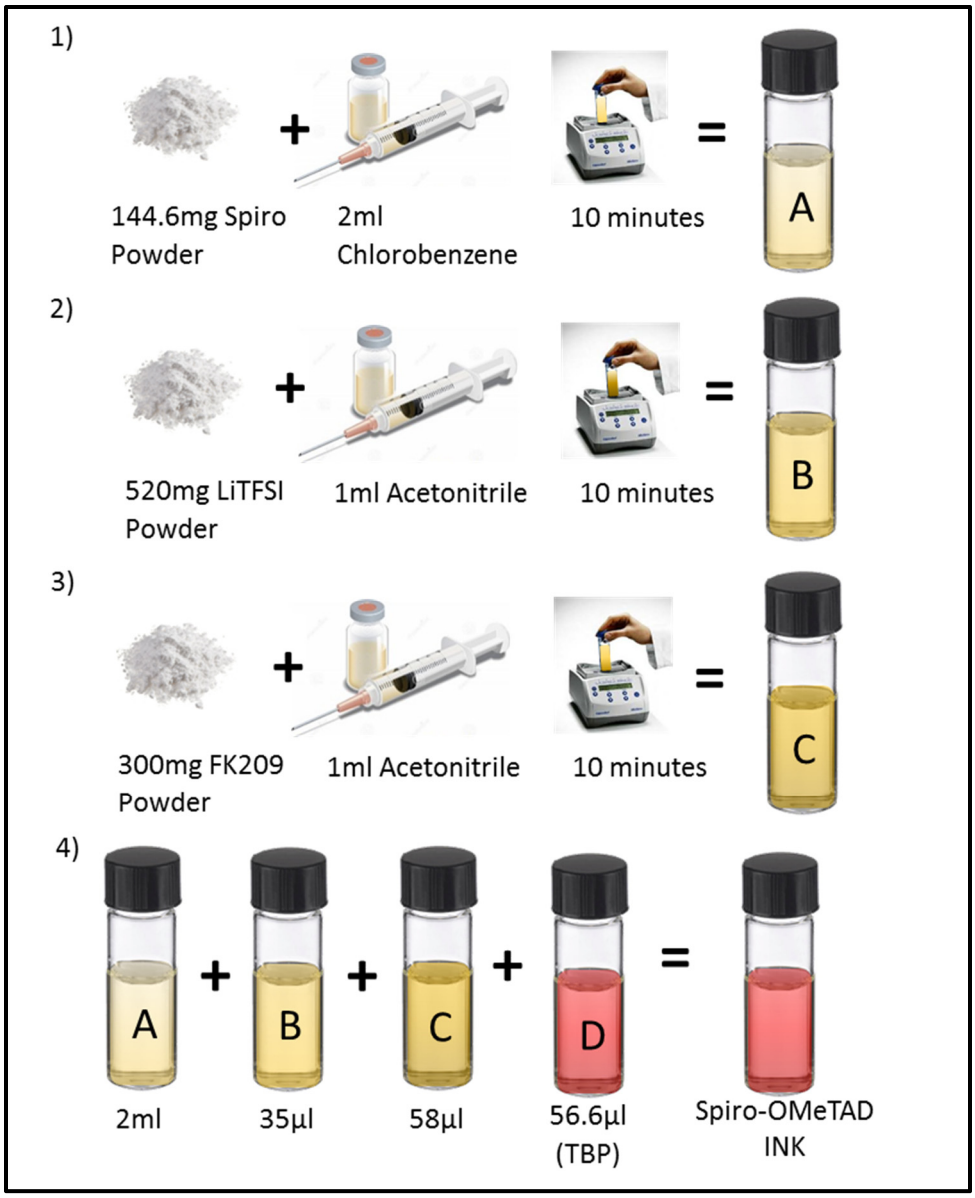

Figure 4.5 Schematic representation of the synthesis of the spiro-OMeTAD solution for inkjet printing

Electron Transport Layer

Two main electron hole transport materials have been identified in Section 1.5 as being compatible for PS TF optoelectronic devices architectures, namely, TiO_2 and $PC_{60}BM$. In either case, no commercially available inkjet compatible inks currently exist on the market. It

can be argued that $PC_{60}BM$ is more suited for inkjet printing since it is soluble in solvents which are better suited to inkjet printing such as toluene and CB. This is mainly due to their higher boiling points and viscosities when compared to typical solvents used for TiO_2 dispersion such as ethanol (EtOH). Additionally, TiO_2 requires high annealing temperatures above that of the processing temperatures of PET and even Kapton. However, it can be found in the literature that amorphous TiO_2, which requires no annealing - only solvent evaporation, can work as an ETL layer. (Wang et al., 2015, p.9108-9115); (Docampo et al., 2013, p.2761) Furthermore, device architectures void of ETL have also been shown to work, albeit with lower device performances. (Wang et al., 2013, p.724-730) In this work, only TiO_2 is explored as an ETL layer and is the only active layer which is not deposited via inkjet printed methods.

4.2.2 Ink Storage & Manipulation

Ink Storage

Ink storage and manipulation are important aspects of PE, each ink needs to be stored adequately for their mechanical, electronic and photonic properties to remain stable over time. Some avenues of ink degradation are;

1. Light exposure.
2. Solid content agglomeration and precipitation.
3. Solvent evaporation.
4. Temperature cycling.
5. Gelation.

Every ink formulation used in this work is kept in sealed glass vials to prevent solvent evaporation and limit reaction with the ink content as glass is known to be inert with chosen ink constituents. Any inks with particle content are agitated at least once a week, when not in day to day use. Additionally, they are vortex mixed for the (10) minutes prior to filling printing cartridges before printing. Some inks are light sensitive such as Ossila's I101 PS ink, the Spiro-

OMeTAD formulation and MicroChem's SU-8 ink, these inks are stored in a dark environment in tinted glass vials. MicroChem's SU-8 ink, PEDOT:PSS Poly Ink HC and ANP's DGP 40TE-20C are stored in a refrigerator at 4 °C while the other ink formulations are kept in a dry, well ventilated cupboard at room temperature. Due to the humidity sensitivity of Ossila's I101 PS ink, this ink is only manipulated and printed when the laboratory and printer enclosure environments are below 35 % RH.

Ink Manipulation: Filling Dimatix Cartridges

To print the ink materials, Ceradrop printer compatible printing cartridges must be filled with the functional inks. All ink material in this work are printed using Dimatix printing cartridges of either 1 pL or 10 pL drop size, mounted on a Ceradrop F-series inkjet printer. The nozzle diameter for the 1 pL and 10 pL drop size Dimatix printing cartridges are 9 μm and 21 μm respectively. 1 pL Dimatix printing cartridges are used to jet ANP's DGP 40TE-20C Ag ink while 10 pL cartridges are used for the remaining ink formulations. As stated above, any ink with solid particle content needs to be agitated before filling the cartridges to render the formulation homogeneous. Additional steps must also be taken for Ossila's I101 PS ink, which needs to be heated to 70 °C for two (2) hours to allow the dissolution of any solids and allowed to cool to room temperature before filling the cartridges, as specified by Ossila.

Care must be taken when filling the Dimatix printing cartridges as to not to introduce impurities and to filter out any solid content agglomeration. First, micro-filters are chosen for the specific inks. In this work, 4.5 um polytetrafluoroethylene (PTFE) micro-filters are used and found adequate for every ink formulation. Prior to transferring the ink from their storage vials to the printing cartridge, the filters are cleaned by passing the solvent of said ink through the filter. This removes particles left inside the filters from their fabrication process, while not contaminating them with unwanted solvents. The ink is then transferred to a clean syringe via a sterilized needle, the needle is removed from the syringe and the filter is attached to the syringe. A new clean needle attachment, provided with the Dimatix cartridges, is then attached to the filter and the ink is pushed through the filter into the printing cartridge. The Dimatix

nozzles are then clipped to the reservoir section of the cartridge. Additionally, when filled with light sensitive inks, the printing cartridges are covered with aluminum tape so that light is inhibited from entering the otherwise semi-transparent printing cartridge. The Dimatix cartridges are specified as single use consumables, however it was found that for MicroChem's SU-8 and ANP's DGP 40TE-20C inks, the cartridges can be used over a multiple day period and can be changed when empty or once nozzles start clogging. For all other formulation except the Spiro-OMeTAD formulation, it is found best not to reuse the cartridges over more than a single day period as irreversible nozzle clogging can happen overnight from solvent evaporation. In the case of Spiro-OMeTAD, it is found best to change the cartridge after more than two (2) hours of non-utilization, again to avoid nozzle clogging.

4.2.3 Optimizing Ink Jetting Parameters

Jetting Waveform

The jetting waveform is essential to achieve stable jetting conditions while inkjet printing. Typical jetting waveforms take the form of symmetrical pulses with a certain intensity and frequency or time segments. This is not always the case, where for some inks, a non-symmetrical jetting waveform is found to generate a more stable jet. A concrete example of this phenomenom, is the MicroChem's SU-8 ink jetting waveform used in the present work.

The waveform intensity refers to the strength of the electric pulse sent to the printing nozzle's piezo transducer. A large peak to peak intensity increases the force of the expulsion of the liquid drop from the nozzle. This generates larger drop volumes which are typically jetted at higher velocities. The time segment of the waveform refers to the length of time taken to switch from a positive to a negative bias and the length of time that the positive or negative bias is kept constant. Shorter time segments tend to form smaller drop volumes by cutting the ink trail prematurely and may generate unwanted satellite drops. To visualize the effects of the jetting waveform on drop diameter, the drop diameters for the commercial inkjet inks (ANP DGP 40TE-20C, Poly Ink HC PEDOT:PSS and MicroChem SU-8) are measured for different

waveform intensities using both the 1 pL and 10 pL Dimatix cartridges. The results are shown in Figure 4.6.

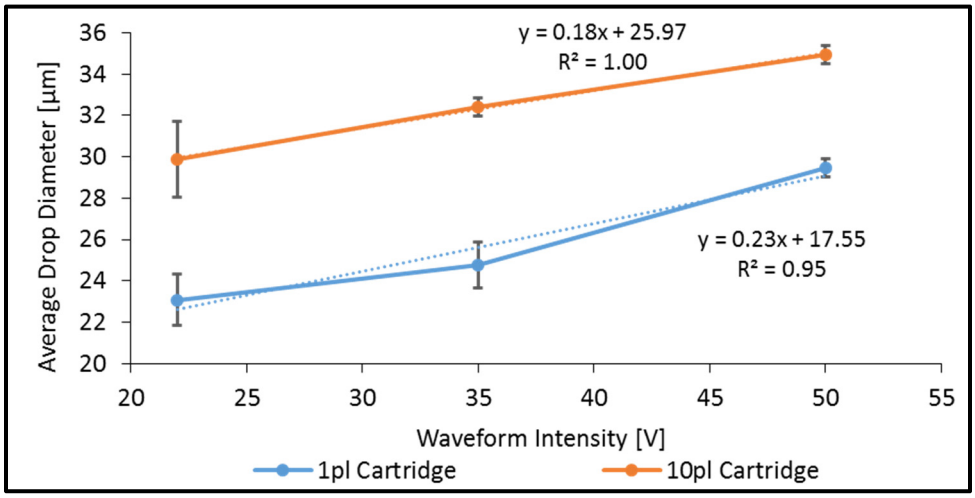

Figure 4.6 Average drop diameter results using 1 pL and 10 pL Dimatix cartridges with varying jetting waveform intensities

As is expected, an increase in the waveform intensity results in an increase in the average drop diameter. Interestingly the increase is extremely linear for the range of waveform intensities examined, for the 1 pL and the 10 pL cartridges the average drop diameters follow the Equations 4.3 and 4.4 with R^2 values of 0.95 and 1.00, respectively.

$$\overline{D_D} = 0.23 \times W_I + 17.55 \tag{4.4}$$

$$\overline{D_D} = 0.18 \times W_I + 25.97 \tag{4.5}$$

Where $\overline{D_D}$ is the average drop diameter in µm and W_I is the waveform intensity in V.

For each of the inks specified in section 4.2.1, jetting waveforms resulting in stable jetting sequences were identified and are shown in Figure 4.7. All the waveforms identified followed a symmetrical pulse shape except for MicroChem's SU-8 ink. To facilitate the identification

and optimization of the jetting waveform as well as to analyze the stability of the jetted drops, ejection reports are generated by the Ceradrop printer and software.

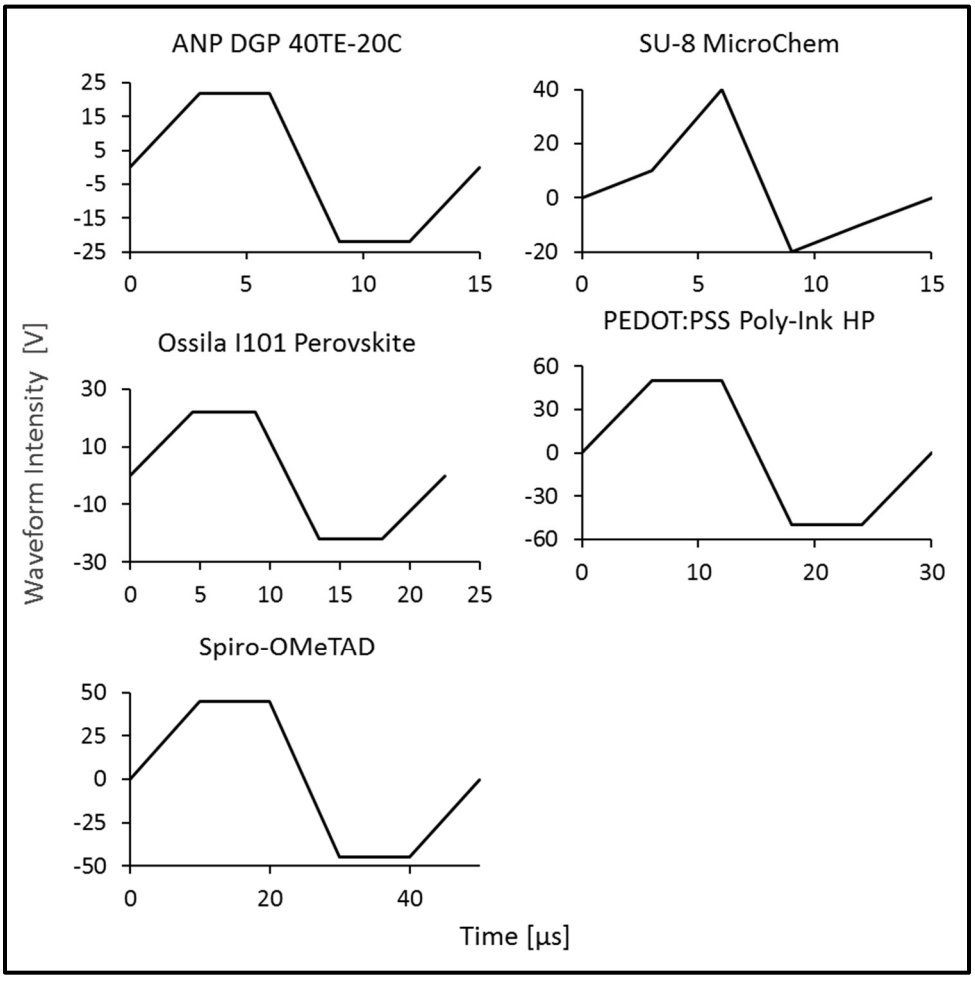

Figure 4.7 Optimized jetting waveform used for printing the various ink materials

Ceradrop Ejection Report

The Ceradrop ejection report is generated using an in-situ strobe light and camera which images jetted drops at high frequencies. The images are processed via the Ceradrop software

to measure the stability of the ink jetting for a given waveform. An example of an ejection report is illustrated in Appendix I, this report can be split in four (4) sections;

1. Ink Information.
2. Pulse Information.
3. Jetting Statistical Analysis.
4. Static and Dynamic Analysis.

In the first section, the Ink information entered in the jetting software is duplicated and the jetting report is timestamped. This information is presented to identify the jetting report and is shown in Figure-A I-1. In the Pulse Information section presented in Figure-A I-2, the waveform used for the ejection report is graphed and each point of the pulse is listed for each nozzle separately as the software allows for different waveforms for each nozzle. The temperature of the nozzles is also recorded in this section of the ejection report. In the next section; Jetting Statistical Analysis, presented in Figure-A I-3 and Figure-A I-4, the active nozzles are depicted, showing if there are clogged nozzles within the print cartridge and if the piezo transducers are active. A mosaic of the complete nozzles while jetting, taken at two specified time stamps, are shown to give a visual representation of the jetting process. A statistical analysis of the stability of the ejected drops is also included in this section. This statistical analysis measures the minimum, maximum, average and standard deviation in the x and z positions as well as the volume of the drops and the angle of ejection from the nozzles. The Static and Dynamic Analysis section of the ejection report, presented in Figure-A I-5, provides the same information as the Jetting Statistical Analysis section, with the addition of the drop velocity. However, in this section, the information is presented for each individual nozzle.

Jetting Stability

Using the waveforms specified in this section, for each of the inks used in this work, ejection reports are generated, and the stability of the jetted drops are presented. Images taken from

the ejection reports showing the stability of the jetted drops as well as some of the analysis and measurements taken are shown in Figure 4.8. The x and z positions of the jetted drops are seen to be very stable across the nozzles for most of the inks. Small deviations in the z position from nozzle to nozzle are seen for Ossila I101 PS ink and Poly Ink HC PEDOT:PSS. Variation in the x and z drop positions from nozzle to nozzle can be readily identified upon inspection using the Drop Analysis software of the Ceradrop printer. To reduce the overall variation, nozzles can be discriminated and switched off manually for more uniform printing.

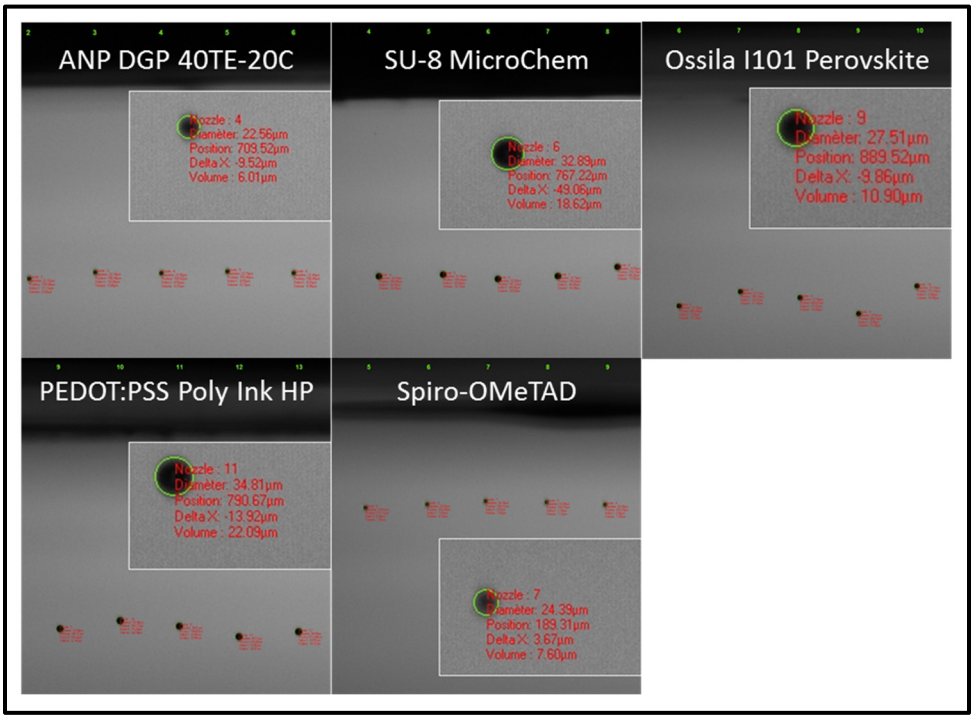

Figure 4.8 Images of stable ink jetted drops of the various chosen ink materials with drop size measurements taken from ejection reports

The variation in drop size from one nozzle to the next is harder to discern at a glance but gives an overall notion of the jetting stability as variables influencing the x and z positions also play a role in the drop size.

From the ejection reports, the distribution of the drop diameter for each ink are calculated and presented in Figure 4.9. Most of the inks show drop sizes distribution which follow the general

shape of normal distributions, and thus, achieve stable jetting across the totality of the nozzles as long as clogging does not happen. However for the Spiro-OMeTAD and Poly Ink HC PEDOT:PSS inks a binomial or trinomial distribution is seen. For these inks, only semi-stable jetting can be achieved, and nozzle discrimination is always required while printing to keep the printing process as homogeneous as possible.

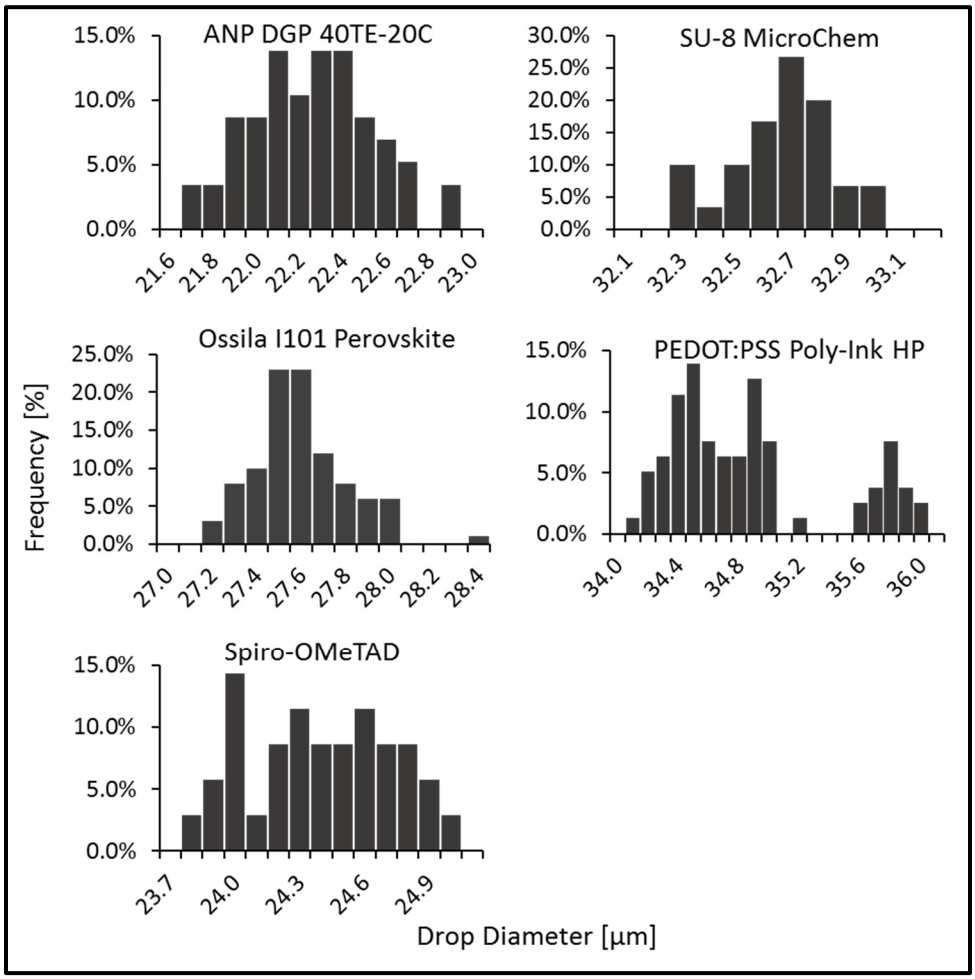

Figure 4.9 Distribution of drop diameters obtained from stable jetted drops using the optimized jetting parameters of the various ink materials

Nozzle Clogging

Nozzle clogging happens readily when using some inks and rarely with others. Full blockage of nozzles is not necessary to render the nozzle unusable, partial clogging results in non-stable or semi-stable jetting and is detrimental for homogeneous printing. The primary way in which nozzles can become either fully or partially blocked is through solvent evaporation which can leave solid residue in the nozzle openings, altering subsequent jetting. Inks with a high solid content or with low boiling point solvents are more prone to nozzle clogging from this effect. In general, inkjet adapted commercial inks are formulated to avoid clogging by using combinations of high boiling point solvents and other additives. In this work, ANP DGP 40TE-20C and MicroChem's SU-8 ink could be use with minimal clogging over long periods of time without replacing the Dimatix cartridge. Ossila's I101 PS ink and Poly Ink HC PEDOT:PSS are found to be prone to partial clogging when in use. However, purging the nozzles at 500 mbar for 1 second can typically remove any clogging. These inks cause irreversible complete clogging in the Dimatix cartridges when not in use for extended periods of time, thus cartridges must be replaced daily. The Spiro-OMeTAD formulation clogs more readily when in use and should be purged before any printing is performed. Moreover, the cartridge is prone to irreversible clogging when left out of use for more than two (2) hours and should be replaced when this is the case.

Careful control of the nozzle temperature is needed to limit these clogging effects. Keeping a low nozzle temperature is beneficial to limit the solvent evaporation and clogging effects. A purge can be performed to remove any partial clogging which occurred due to nozzles heating.

Optimised Jetting Parameters

The optimized jetting parameters for each ink used in this work are summarized in Table 4.5, the resulting average drop diameters and their standard deviation are also presented as metric for jetting stability.

Table 4.5 Overview of the optimized jetting parameters and resulting drop diameter of the various chosen ink materials

Ink	**Inkjet Nozzle**	**Waveform Voltage [V]**	**Waveform Time Segment [µs]**	**Jetting Velocity [m/s]**	**Nozzle Temp. [°C]**	**Drop Diameter [µm]**
ANP DGP 40TE-20C	Dimatix 1 pL	22	3	8	28	22.3 ±0.28
SU-8 Michrochem	Dimatix 10 pL	10-40	3	7	30	32.7 ±0.19
Ossila I101	Dimatix 10 pL	22	4.5	3.3	30	27.6 ±0.21
Spiro-OMeTAD	Dimatix 10pL	45	10	5.3	28	24.4 ±0.34
PEDOT:PSS Poly Ink HC	Dimatix 10 pL	50	6	9.3	25	34.9 ±0.54

From the ink's properties found in Table 4.4 and the jetting parameters in Table 4.5, the *Oh* and *Re* numbers associated to each ink are calculated using equations 3.13 and 3.14, respectively. These are represented in Figure 4.10 where the inks are shown to fit within the printable fluid zone, these inks are therefore expected to print relatively well and are not expected to need adjustment to their formulations.

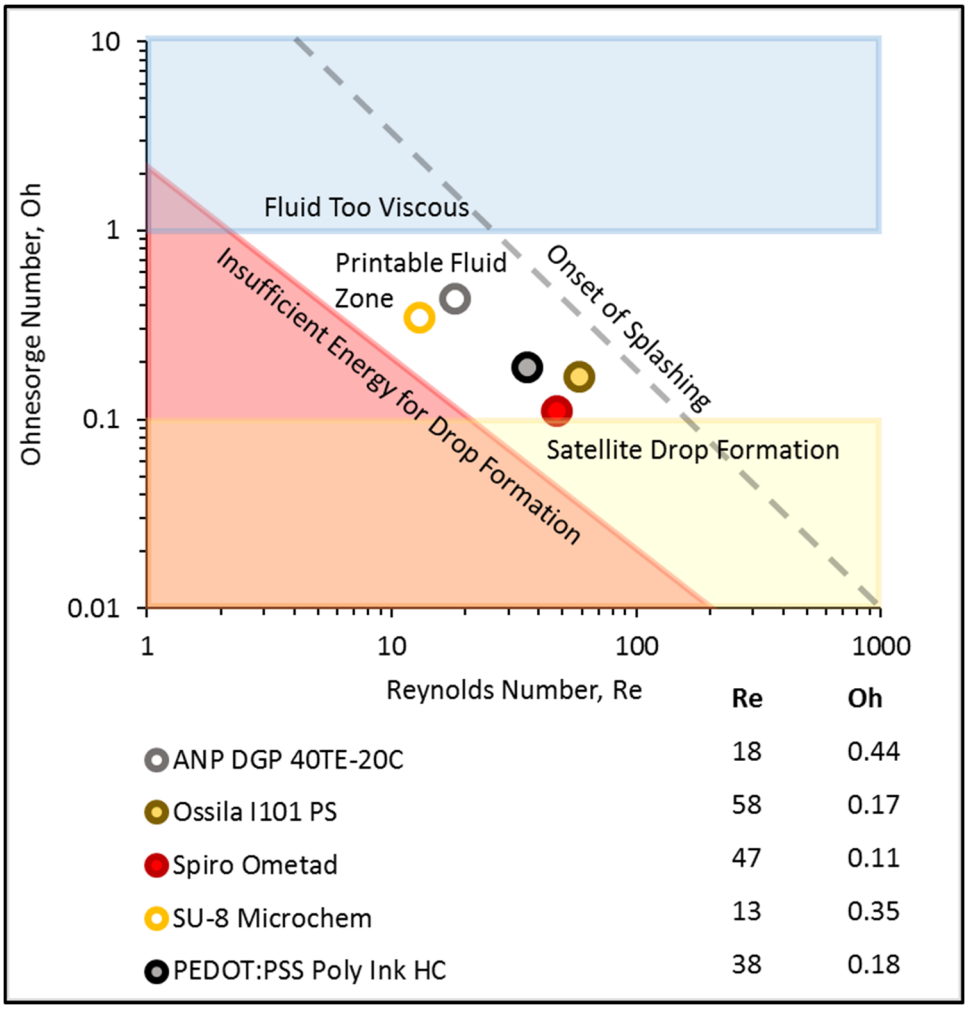

Figure 4.10 Jetted inks' *Re* and *Oh* numbers represented in printable fluid zone

4.2.4 Interactions Inks/Substrates

The surface energies of the substrates are important to understanding the interactions between the substrate and the inks, however, they do not show the whole picture. The rheological properties of the inks are also important proprieties which come into play in the interactions of the liquid inks and the solid substrates. The temperature of the inks play an important role in changing their rheological properties and affects how they interact with the substrates. In this section, as a primary step to performing printing test plans, the effects of chuck temperature on the spread of the ink upon contact with the substrate are examined. The printing chuck on

the F-Series Ceradrop printer is limited in temperature range, from room temperature to 60 °C, with no active cooling capabilities. The spread of the ink is measured as the diameter of the drop splat on a plasma treated FT Kapton-FPC 300 substrate when jetted using the specified waveform in section 4.2.3. For most inks, 3 splat diameters using chuck temperatures of 25 °C, 40 °C and 60 °C, are measured. For Ossila I101 PS ink, splat diameters are taken at 4 temperatures to provide a more accurate trend in the effects of chuck temperature on the wettability or spread of the ink on the substrate. The splat diameters are measured using the in-situ camera and image processing software on the F-Series Ceradrop printer and are shown in Figure 4.11.

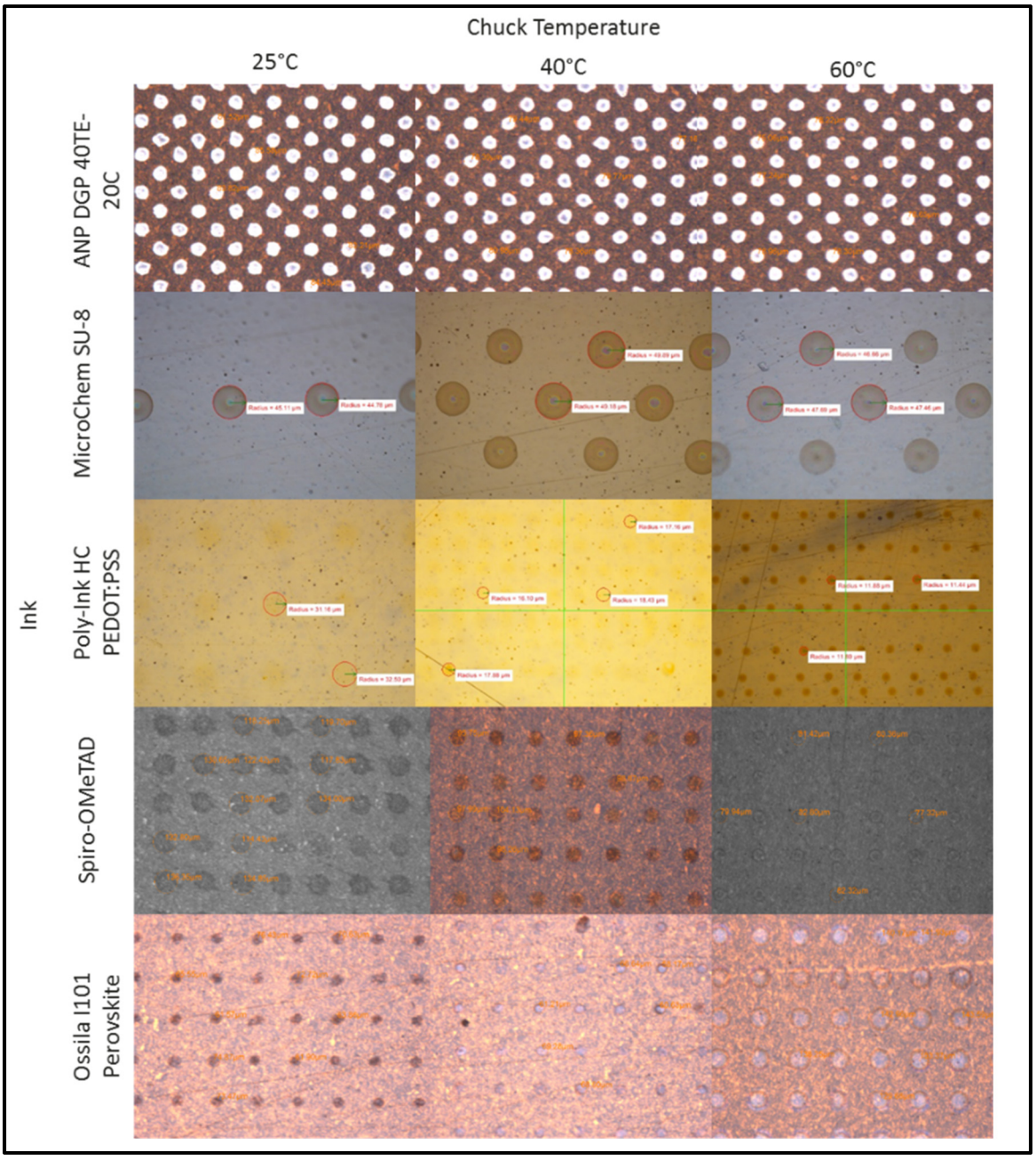

Figure 4.11 Photographs showing the drop splat diameter of the various ink materials on a Kapton substrate at varying substrate temperatures

The results are also plotted in Figure 4.12, showing the overall trends in the spread of the inks on the FT Kapton-FPC 300 substrates as the chuck temperature is changed. For the commercial inkjet adapted inks; DGP 40TE-20C and MicroChem SU-8, the change in splat diameter is

minimal as their rheological properties remain more or less constant over these temperature ranges. For Poly Ink HC PEDOT:PSS and the Spiro-OMeTAD formulations, a noticeable decrease in splat diameter is seen as the chuck temperature is increased. This means that the contact angle between the liquid and the substrate is increased and points to an increase in the surface tension of the liquid. Liquids generally decrease in surface tension as the temperature is increased, which would increase the splat diameter. The inverse relationship seen with these inks is believed to result from an increase in evaporation of the solvents contents; water and CB, respectively. The boiling points of water and CB are 100 °C and 131 °C respectively and an increased evaporation rates of these solvents at or above 40 °C is expected. For higher boiling point solvents this relationship is limited or even reverse. This is the case for triethylene glycol monomethyl ether (TGME) in the DGP 40TE-20C ink and DMF in Ossila's I101 PS ink with boiling points of 216 °C and 153 °C, respectively. Indeed, for Ossila's I101 PS ink, the splat diameter is somewhat constant between 30 °C and 40 °C but increases rapidly after 40 °C. Expectedly, the variation in splat diameter for the non-inkjet adapted formulations, namely Ossila's I101 PS ink and the Spiro-OMeTAD formulation, are much larger than those found for the inkjet adapted commercial inks. As a result, less homogeneous printed layers are expected for these formulations when compared to inkjet adapted commercial inks, which often contain additive to control the rheological properties of the liquid (Derby, 2010, p.395-414).

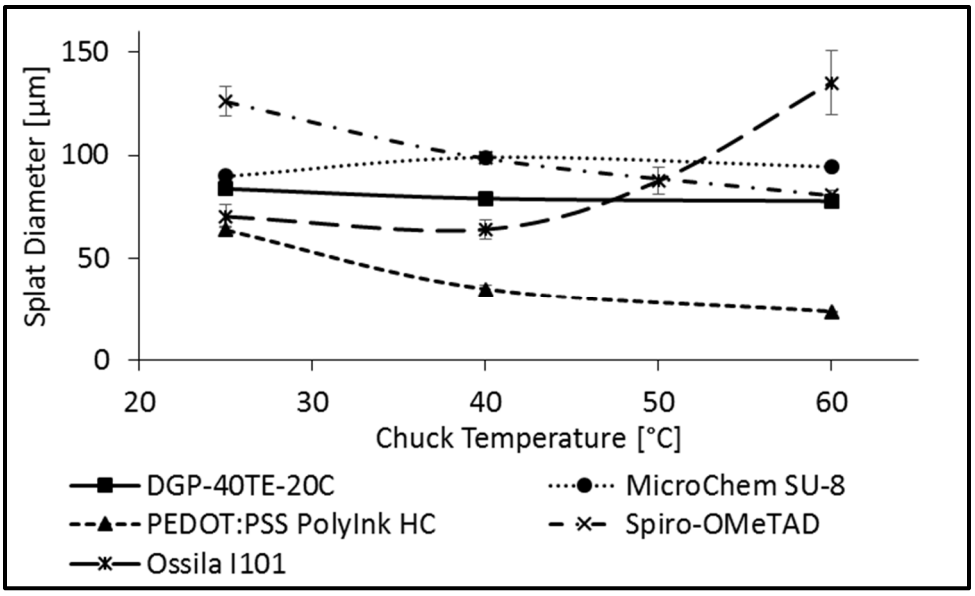

Figure 4.12 Overview of the tendencies of the drop diameter of the various chosen ink materials with increasing chuck temperatures

4.3 Optimizing Printing Parameters

Once the inks can be jetted adequately and the liquid interactions with the substrate are known, printing test plans can be carried out using the Ceradrop F-Series printer and Ceraslice printing software. First, we run broad printing test plans to acquire the range of viable printing parameters, followed by optimization of the printing parameters to achieve optimal printing on chosen substrates. In these test plans, the printing parameters explored include, the drop spacing or interpenetration, the printing lattice as well as the chuck temperature and the number of printed layers. For this work, the drop interpenetration is expressed as a percentage of the drop diameter, as shown in Figure 4.13. For higher drop interpenetrations, the distance between the printed drops is smaller and more material is deposited within a single printed layer. Layer thicknesses are expected to increase as a function of the square of the interpenetration as it factors both the x and y axes. Negative drop interpenetrations are also used for printing some inks. Negative drop interpenetrations refer to drops which are separated by a greater distance than their diameters, leaving voids in the deposition of the ink layer. To fill the voids, multiple layers of the ink are printed.

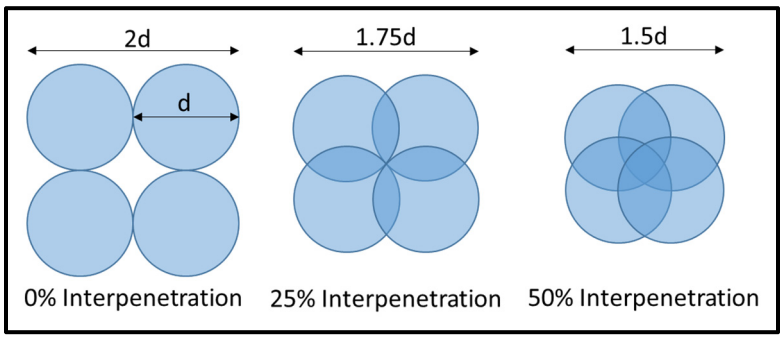

Figure 4.13 Schematic representation of the drop interpenetration parameter

The choice in printing lattice is another important parameter for inkjet printing as it affects the position of the printed drops in relation to each other. Some printing lattices offer denser packing arrangements resulting in a more uniform coverage. There are five (5) printing lattices to choose from in the Ceraslice printing software; Square lattice, Centered Square lattice, Rectangular lattice, Hexagonal Centered lattice (Hex Fab) and Hexagonal Shifted lattice (Hex Shift). The Rectangular lattice was omitted from the test plans as it only differs from the Square lattice by allowing for different interpenetration in the x and y axes. This aspect was deemed not useful for the purposes of this work but could be worth exploring in cases of long chain polymer deposition where polymerization alignment may be affected by different x and y axes drop interpenetration, for example. The printing lattices used in the preliminary test plans are illustrated in Figure 4.14. Individual printing lattices can also offer benefits in terms of printed feature edge cleanliness. For example, printing using a Hex Fab lattice will result in straighter more well-defined horizontal edges (x-axis), while the Hex Shift lattice will have similar results but for vertical edges (y-axis). This is due to the drop alignment along each respective axis. In section 4.2.4, the interactions of the chuck temperatures for the different inks are shown to affect each ink differently. This is expected to affect the deposition of the ink layers differently, depending on how the splat diameter is affected. An increase in the number of printed layers is expected to increase the thickness of the overall printed feature while also improving surface coverage.

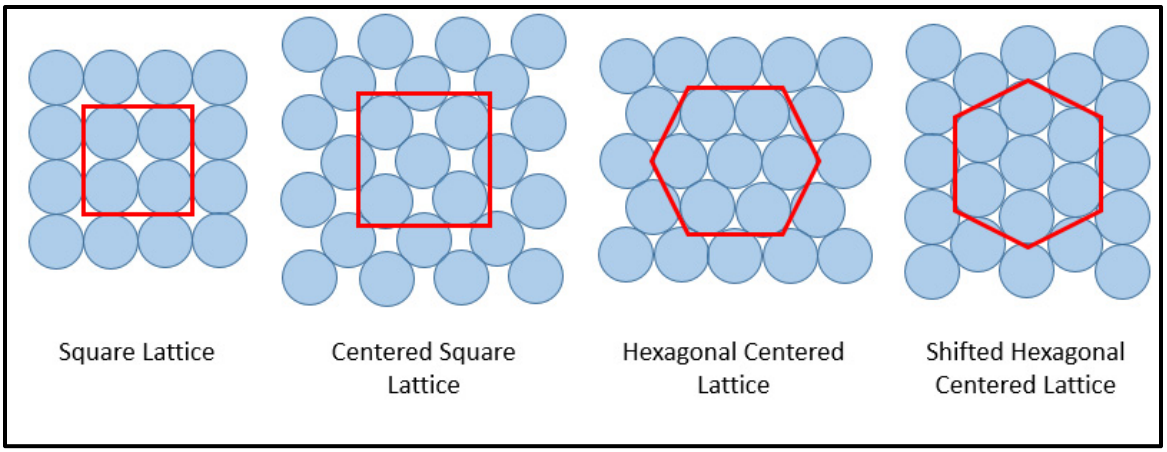

Figure 4.14 Schematic representation of the different printing lattices used in the printing test plans

After the preliminary test plans are conducted, further optimization of the printing parameters is carried out and the optimized printing parameters are adapted for the specific substrate that the ink will be used on. Printing parameters such as raster overlap, layer interweaving and printing distance are often utilized to increase the homogeneity of the printed surface. Raster overlap and layer interweaving, depicted in Figure 4.15, can be especially useful when printing multiple layers and when gaps between the printed raster occur due solvent evaporation between raster and/or other rheological phenomena (Sette, 2014). Since the atomospheric conditions inside the printer can affect these aspects, raster overlap is often adusted at the time of printing to provide optimized printing.

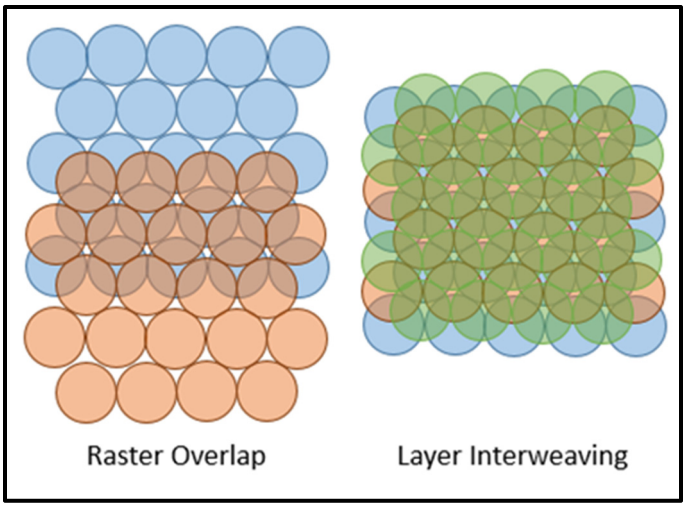

Figure 4.15 Schematic representation of the raster overlap and layer interweaving possibilities

The test plans are carried out by printing constant features while varying printing parameters. The tests are characterized in terms of thickness and variation between the average and maximum thickness of the printed materials as a method to quantify the homogeneity of the printed surface. The printed layer thicknesses are measured using a Bruker 3D NPFLEX interferometry microscope system, this method of measuring layer thickness was found to be the simplest and most accurate method when measuring TFs on flexible substrates. In the case of Ossila I101 PS ink, the layer thicknesses are measured using a Hitachi S-3400N scanning electron microscope system to give accurate measures of the crystal heights. In this case, it is observed that all other methods tested for measuring the thickness gave inaccurate results. Surface coverage of the PS layers are calculated using light thresholding methods with an Eclipse L200N optical microscope (Nikkon) system.

Since layer thickness plays a major role in TF device performances, we often want to be able to target certain thickness for different materials in the device architecture. We have derived Equation 4.6 to provide an estimate layer thickness from printing parameters and ink properties. This equation provides a good lower bound layer thickness estimate for most inks used in this work.

$$THK = \frac{C_{PL} N_L V_R V_d C_{PT}}{\left(S_d(T)\left(1 - \frac{I_{\%}}{100}\right)\right)^2} \quad (4.6)$$

Where THK is the thickness in m. C_{PL} is a constant associated with the drop packing of the printing lattice (Square = 1, Centered Square = 1, Centered Hexagonal = $2/\sqrt{3}$, Shifted Centered Hexagonal = $2/\sqrt{3}$). N_L is the number of printed layers. V_R is the ink's volume ratio of active material content to solvent content. V_d is the liquid volume of one jetted drop in m^3. C_{PT} is a constant associated with post treatment effects such SU-8 shrinkage from UV curing. $S_d(T)$ is the temperature dependent splat diameter of a jetted drop in m and $I_{\%}$ is the printed drop interpenetration in %. This equation assumes complete uniform coverage, no raster overlap and complete solvent evaporation. The V_r and C_{FF} constants for each ink used in this work are presented in Table 4.6.

Table 4.6 Theoretical film thickness constants

Ink	**V_r**	**C_{FF}**	**Film Formation Effect**	**Reference**
ANP-DGP 40TE 20C	0.04	2.17	54% film porosity	(Cauchois et al., 2012, p.7110-7116)
SU-8 MicroChem	0.15	0.5	50% film shrinkage	(Natu, Islam, Gilmore & Martinez-Duarte, 2018, p.17-27)
Poly-Ink HC PEDOT:PSS	0.007	1	N/A	N/A
Spiro-OMeTAD	0.11	1	N/A	N/A
Ossila I101 Perovskite	0.05	1	N/A	N/A

Some of the inks require post-printing processes to either activate, crystalize or anneal the material to achieve the desired electronic, photonic and/or mechanical properties. In this work and in general for the field of PE, photonic processes are preferred over other processes. There are three main reasons for this preference;

1. They typically do not require specific atmospheric conditions.
2. They are compatible with temperature sensitive substrates.
3. They are faster than other processes.

The Phoseon Technology UV lamp and the CER-42-250 Adphos® NIR lamp found on the F-Series Ceradrop printer are used where and when possible to achieve more streamline processing methods. This allows for printing and ink activation to be done without removing the printed substrate from the printer and thus avoids introducing possible miss-alignment problems if subsequent printed layers are needed.

To estimate the heating effects of the Adphos® NIR lamp, thermocouples are attached to the surface of the printer chuck using Kapton tape. The temperature of the chuck surface is then measured for different photonic annealing parameters. The NIR and UV lamps are situated in the back of the printer and stay fixed, the printer chuck moves with a constant speed under the lamps while the photonic treatments are performed. The lamp power is varied from 25% to 100 % of its maximum power while the chuck speed is varied from 2.5 mm/s to 25 mm/s. The results of the Adphos® NIR lamp heating effects are shown in Figure 4.16. Above 300 °C the adhesive of the Kapton tape used to hold the thermocouples in place deteriorates and contact between the thermocouples and the chuck is lost. As such, no readings above this temperature could be taken. Nonetheless, temperature estimates can be evaluated using the fitted power curves which follow the experimental results closely for the range of annealing speeds tested.

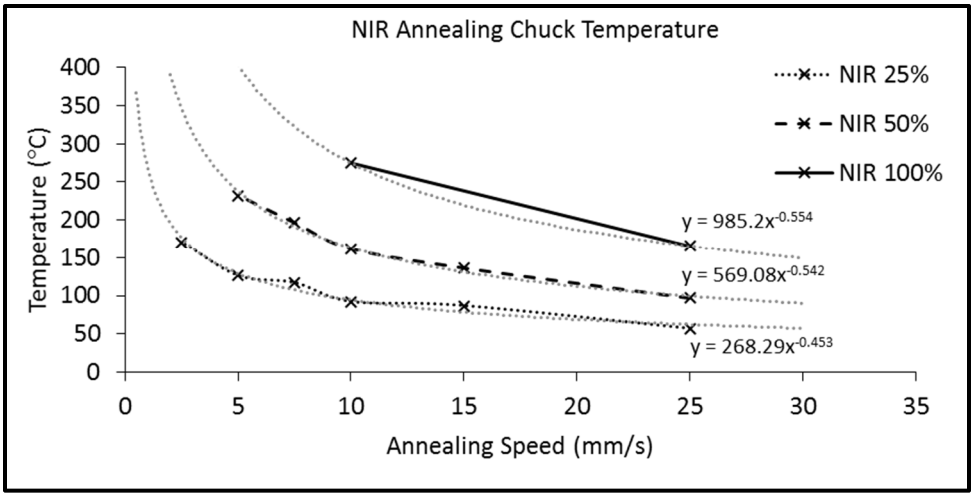

Figure 4.16 Experimental results and fitting of the resulting chuck temperatures from the optical NIR sintering process with varying process parameters

4.3.1 ANP-DGP 40TE-20C

Printing Test Plan

The detailed printing test plan performed for the ANP DGP 40TE-20C ink is presented in Appendix II, while the results are summarized in this section.

The largest trends in terms of printed feature thickness arise from chuck temperature and drop interpenetration dependences, while the results showed minimal dependence on the printing lattice. The chuck temperature and drop interpenetration dependence of the single and two layer printed feature thickness are graphed in Figure 4.17 (a,b) while theoretical values are shown in Figure 4.17 (c,d). To measure surface homogeneity, the average thickness is expressed as a percentage of the maximum thickness of the printed feature. As such, higher values point to a more uniform surface with less variation, while lower values suggest large thickness fluctuations. The results are again observed to be most dependent on chuck temperature and drop interpenetration, while little dependence is seen for the printing lattice choice. The results for single and two layer printed features are graphed in Figure 4.17 (e,f).

As expected, the trends are similar for single layer and two layered printed features. The layer thickness is seen to follow theoretical trends from increased drop interpenetration but not from increased chuck temperatures. A decrease in thickness at higher temperatures when compared to theoretical values is observed. This effect is more pronounced at higher drop interpenetrations and is explained by the coffee-ring effect drawing much of the material to a very limited area, leaving the remaining areas with little material deposition. This is also reflected in lower surface homogeneity for the same conditions. Ink bleeding effects are observed at low temperatures when using higher drop interpenetration, this effect is more pronounced for the two layered printed features. This results in lower measured thicknesses and layer homogeneity. For thicker printed features, annealing of the ink must be performed to allow the subsequent printed layers to be deposited on solid surfaces and reduce ink bleeding.

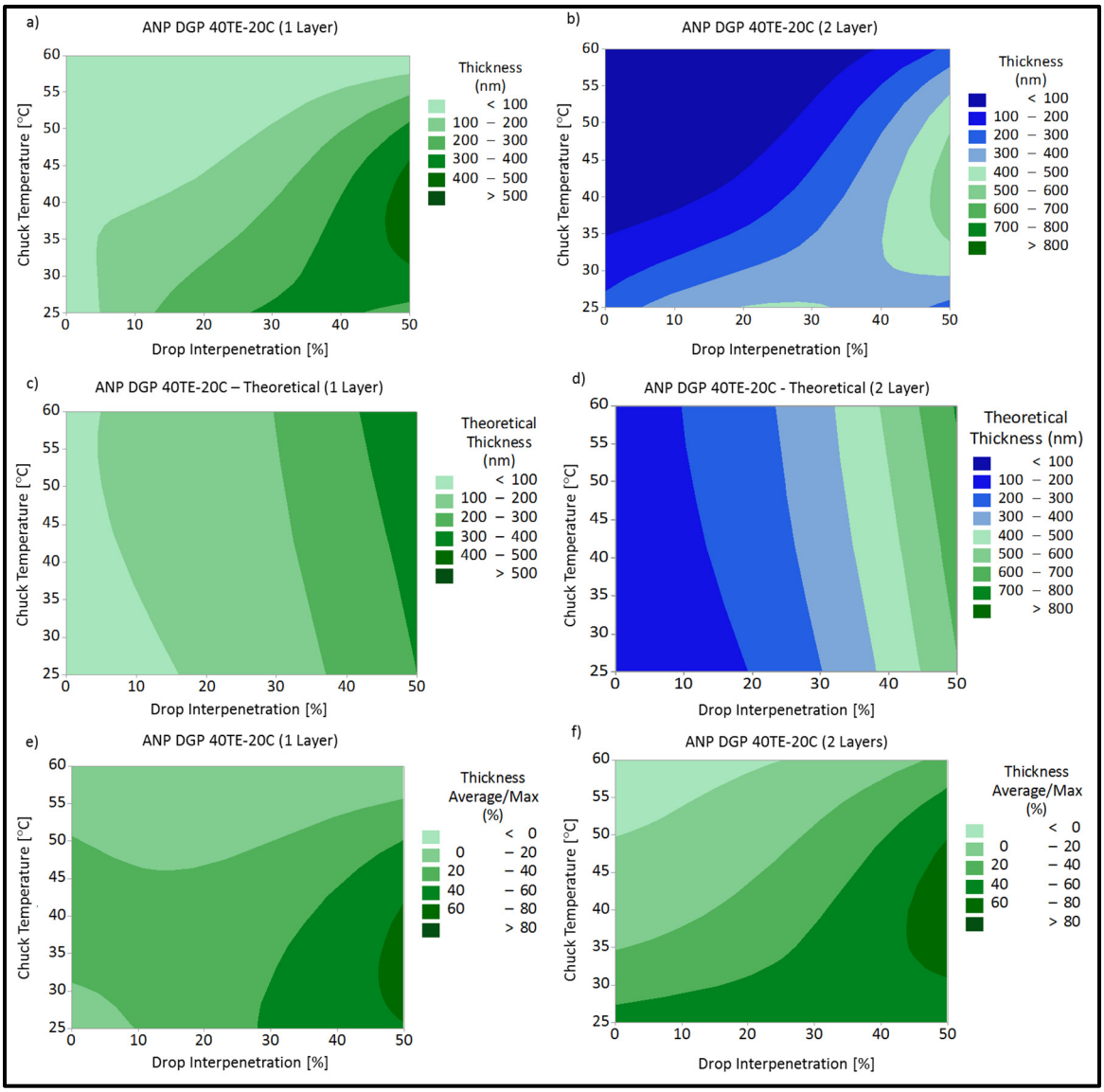

Figure 4.17 Printing test plan results for ANP-DGP 40TE 20C Ag ink on a Kapton substrate. a) Experimental thickness results for one-layered features. b) Experimental thickness results for two-layered features. c) Theoretical thickness results for one-layered features. d) Theoretical thickness results for two-layered features. e) Experimental surface homogeneity results for one-layered features. f) Experimental surface homogeneity results for two-layered features

Multiple sets of parameters can be deemed adequate for layer printing, while three (3) sets of parameters are deemed optimal. The optimal parameter sets are presented in Table 4.7 along with the resulting average/maximum thickness values.

Table 4.7 Optimal printing parameter sets for ANP DGP 40TE-20C ink

Parameter Set	No. of Printed Layers	Chuck Temp. [°C]	Interpenetration [%]	Printing Lattice	Average/Max. Thickness [%]
1	1	25	50	Hex Shift	42.9
2	1	40	25	Centered Square	80.4
3	2	40	25	Centered Square	80.0

Parameter Set 1 is evaluated to give the overall best printing result. This printing result is presented in Figure 4.18, along with the corresponding 3D interferometry image and height profile. The following considerations are taken to evaluate the best printing parameters;

1. Visually clean deposition of material (no ink bleeding and complete coverage) are necessary.
2. Preference is given to chuck temperatures that match the nozzle temperature of the inks, to allow for continuous printing over longer periods while minimizing temperature changes of the nozzles over time.
3. Average/Maximum thickness values are given less importance as multiple layers of conductive inks are expected to be printed on top of each other after annealing to provide better overall conductivity of features by increasing the thickness. This is expected to even out non-homogeneous surfaces as more layers are printed.

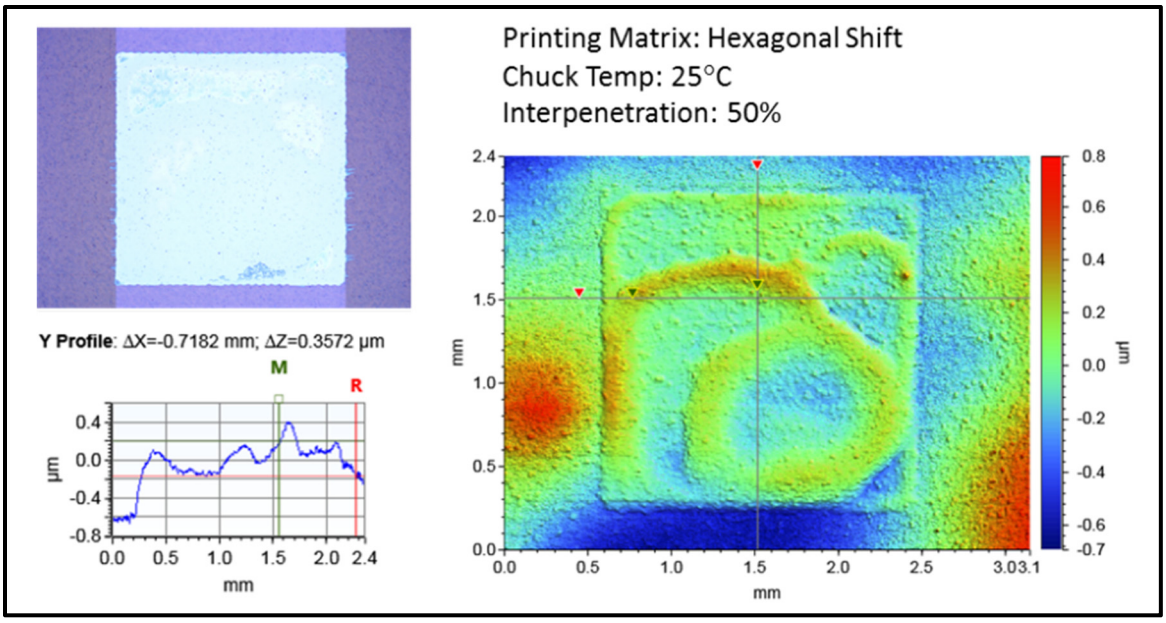

Figure 4.18 Optimal printing results for ANP-DGP 40TE 20C Ag ink on a Kapton substrate and corresponding height profile and surface morphology

Post-Printing Process

Post-printing processes are required for ANP DGP 40TE-20C Ag ink to achieve adequate conductivities of the printed features. For annealing, enough energy should be provided to evaporate the solvent content of the ink and to start melting the Ag NPs together to form a connected structure allowing for increased electrical conduction. Annealing tests are performed using both the in-situ NIR lamp and a conventional oven to compare both annealing methods. In-situ optical annealing using the NIR lamp offers three (3) main advantages over oven annealing methods;

1. Compatibility with temperature sensitive substrates.
2. Faster annealing times (seconds/minutes instead of minutes/hours).
3. No manipulation of substrates or printed features required.

The results of the optical annealing tests are illustrated in Figure 4.19, while the results for oven annealing are presented in Figure 4.20. For the optical annealing tests, both the NIR lamp power and the chuck speed (annealing speed) is varied. For the oven annealing tests, only the annealing temperature is varied while keeping a constant annealing time of one (1) hour. The ink manufacturer (ANP) recommends oven annealing at 180-200 °C for 1 hour to achieve specified resistivity values of 7 μΩ-cm, which equate to sheet resistance values of 0.175 - 0.233 Ω/□ for printed feature layer thickness of 300 – 400 nm.

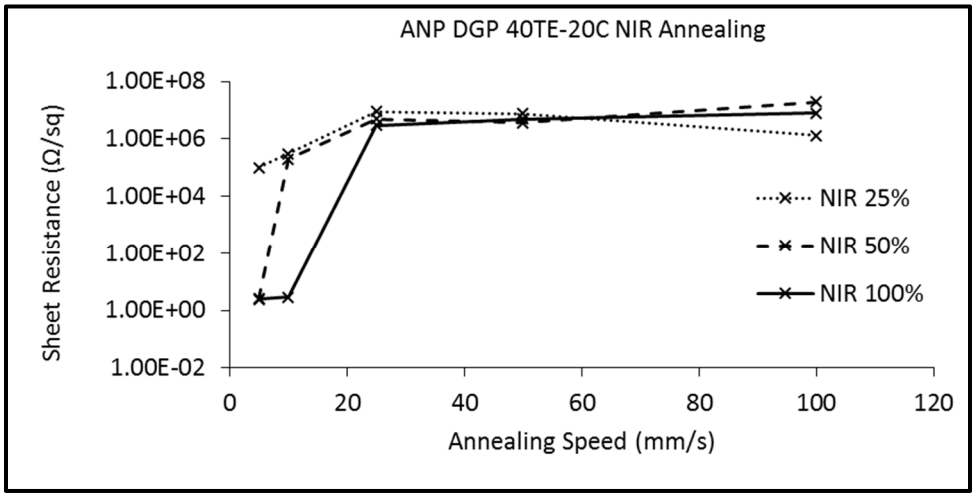

Figure 4.19 ANP DGP 40TE-20C optical NIR sintering sheet resistance results

Optical annealing using the in-situ NIR lamp did not provide enough energy to achieve the manufacturer specified resistance values. Indeed, when using the maximum power intensity of the lamp and an annealing speed of 5 mm/s, resistivity values as low as 2.4 Ω/□ were obtained. Additionally, minimal reduction in sheet resistance is seen when reducing annealing speed from 10 mm/s to 5 mm/s at the maximum lamp power intensity. Although values of sheet resistance of 2.4 Ω/□ are ~10 times higher than the manufacturer specified value, they are adequate for many applications, where some electrical losses are not detrimental to operations. Nonetheless, this optical process is adequate as a pre-annealing process to dry the printed feature and allow for subsequent printed layers before final oven annealing is performed.

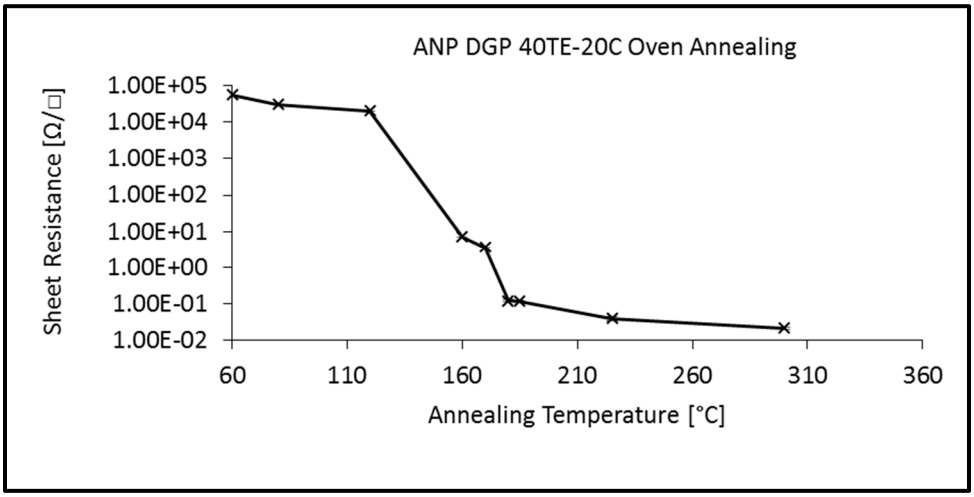

Figure 4.20 ANP DGP 40TE-20C oven annealing sheet resistance results

Oven annealing tests match the manufacturer recommendations and specifications, sheet resistance values of 0.12 Ω/□ are reached for annealing temperatures of 180 °C. Increasing temperatures further decreased the sheet resistance values to 0.04 Ω/□ and 0.02 Ω/□ for temperatures of 225 °C and 300 °C respectively. However, these higher temperatures may be detrimental if printing on heat sensitive substrates.

4.3.2 SU-8 MicroChem

Printing Test Plan

The detailed printing test plan performed for the MicroChem SU-8 photoresit ink is presented in Appendix III, while the results are summarized in this section.

Again, the printed feature thickness results show the largest dependence from the chuck temperature and the drop interpenetration, with minimal dependence from the printing lattice. The chuck temperature and drop interpenetration dependence of the single and two layer printed feature thickness are graphed in Figure 4.21 (a,b) while theoretical values are shown in Figure 4.21 (c,d). The same method of estimating the surface homogeneity as performed for

the ANP DGP 40TE-20C ink is also performed for MicroChem SU-8 ink. The results are again observed to be most dependent on chuck temperature and drop interpenetration, while little dependence is seen for the printing lattice choice. These results are graphed in Figure 4.21 (e,f). Very similar trends are seen for the one- and two-layered printed features and the experimental results are seen to follow closely theoretical calculated values. Moreover, the results show an almost exact doubling of the thickness when two layers of material are printed, pointing to no ink bleeding behavior. This aspect is beneficial as it means that multiple layers of printed MicroChem SU-8 ink can be printed with no post-printing processes required between subsequent layers. The range in layer thickness achievable from adequate printing parameters is quite large, from ~1 μm to at least 6 μm.

Surface homogeneity is observed to improve as more ink material is printed, both when printing with increased drop interpenetration and when printing two-layered features. Increased ridged surfaces can be observed when printing is performed with higher chuck temperatures and lower drop interpenetration, this results in the lower surface homogeneity seen with these conditions.

Multiple sets of printing parameters are deemed to be adequate for layer printing, while the optimal set of parameters is presented in Table 4.8 along with the resulting average/maximum thickness value. It is expected that the thickness will increase linearly with increased number of printed layers and that surface homogeneity will also improve, up to a certain point where the ink will start to bleed out. The optimal printing result is presented in Figure 4.22, along with the corresponding 3D interferometry image and height profile.

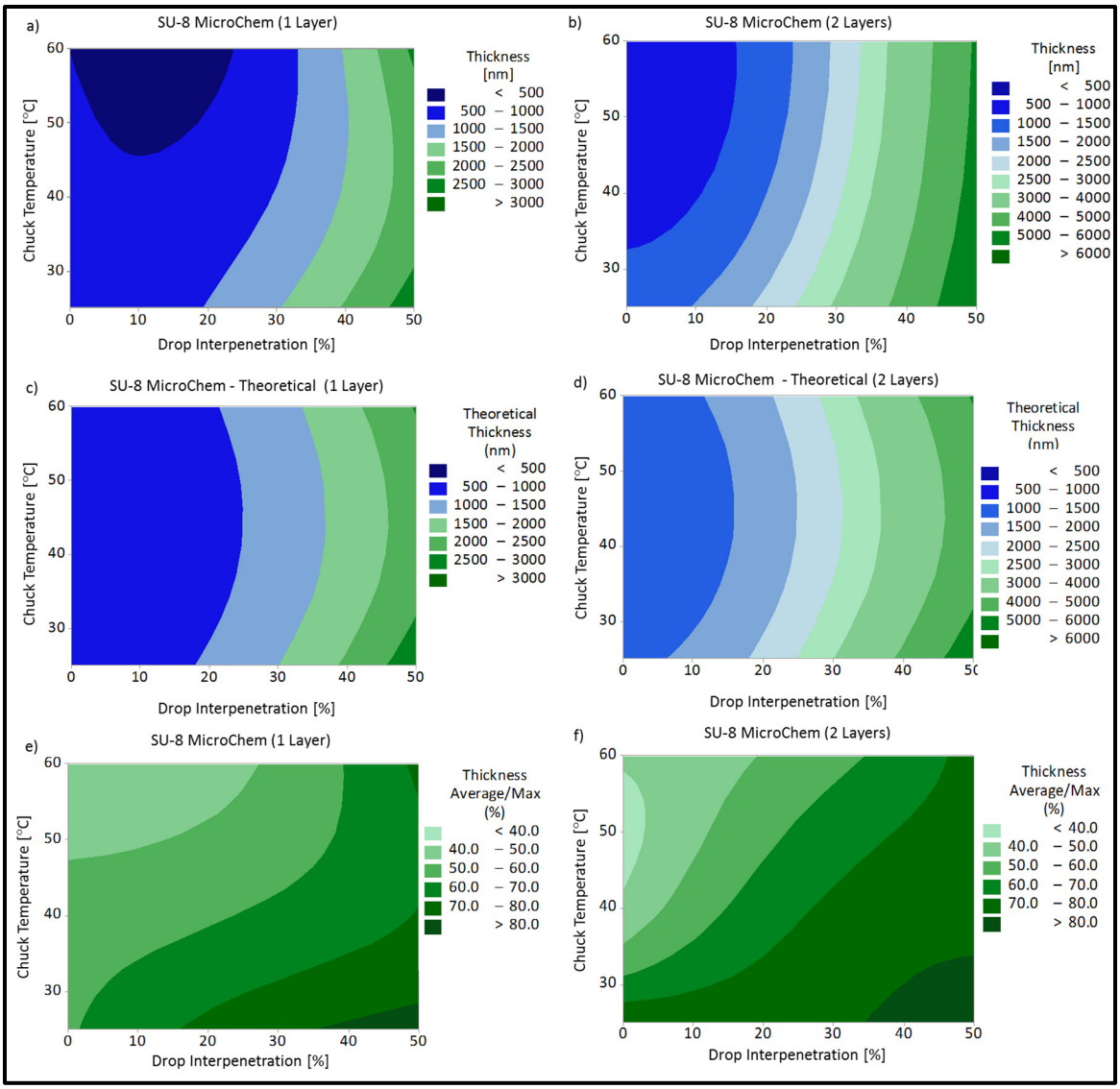

Figure 4.21 Printing test plan results for MicroChem SU-8 ink on a Kapton substrate. a) Experimental thickness results for one-layered features. b) Experimental thickness results for two-layered features. c) Theoretical thickness results for one-layered features. d) Theoretical thickness results for two-layered features. e) Experimental surface homogeneity results for one-layered features. f) Experimental surface homogeneity results for two-layered features

Table 4.8 Optimal printing parameter set for MicroChem photoresit ink

Parameter Set	No. of Printed Layers	Chuck Temp. [°C]	Interpenetration [%]	Printing Lattice	Average/Max. Thickness [%]
1	1	40	50	Centered Square	87.1

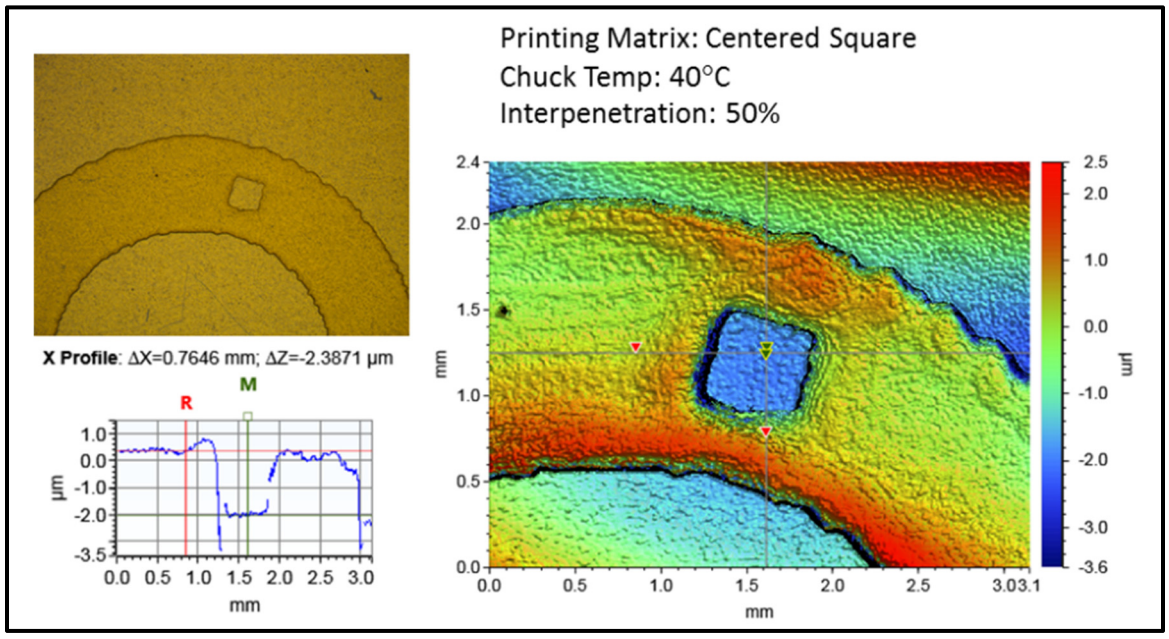

Figure 4.22 Optimal printing results for MicroChem SU-8 ink on a Kapton substrate and corresponding height profile and surface morphology

Post-Printing Process

Post-printing processes are required for MicroChem SU-8 photoresist ink to achieve adequate mechanical properties. The manufacturer (MicroChem) recommends complicated post-deposition treatments to achieve optimal properties, starting from an edge-bead removal process, followed by a soft-bake process, UV exposure, post-exposure bake, a developing step, a rinse and dry step and finished with an optional hard bake step. This complicated procedure is necessary when using MicroChem SU-8 as a photoresist for lithography purposes since edge

cleanness and physiochemical properties are important. For this work, MicroChem SU-8 ink is used for structural and/or electrical insulating purposes. As such, only mechanical and insulating properties are important. Simplified post-processing of MicroChem SU-8 ink is expected to achieve sufficient properties for this work. In-situ optical processes are again preferred over conventional processes for the same reasons as stated in section 4.3.1. We expect that the in-situ NIR lamp can replace the soft-baking and post-exposure baking processes recommended to be performed at 95 °C. While UV exposure can be directly performed with the in-situ UV lamp. The developing, rinse and dry steps can be omitted as digital inkjet printing allows local deposition of material, therefore, no removal of material is required. The final hard-baking process which is recommended to be performed at temperatures between 150 – 250 °C may be difficult to substitute with optical processes. However, as stated by the manufacturer, this step only provides small benefits in terms of final mechanical properties. Post-printing processes using the in-situ NIR and UV lamps are tested as standalone and combined processes. The printed features are inspected manually to determine the effects of the processes. The results are separated into three (3) categories;

1. Non-baked (still fluid, leaves residue to the touch).
2. Soft-baked (solid, no residue, easily pliable and deformed but springs back to original shape).
3. Hard-baked (solid, no residue, not easily pliable or deformed, once deformed does not spring back to original shape).

The results of the post-printing processes using the in-situ NIR and UV lamps are shown in Table 4.9, with the non-baked, soft-baked and hard-baked categories depicted in red, yellow and green, respectively.

Table 4.9 MicroChem SU-8 optical processing results

		Annealing Speed		
Lamp Power		**5 [mm/s]**	**10 [mm/s]**	**25 [mm/s]**
Adphos NIR	25 %			
	50 %			
	100 %			
Phoseon UV	25 %			
	50 %			
	100 %			
Adphos NIR + Phoseon UV	25 %			
	50 %			
	100 %			

Overall, most of the optical post-processes tested result in soft-bake conditions. Exposure with only the NIR lamp while using high annealing speeds results in non-baked conditions. Hard-bake conditions are reached when using a combination of NIR and UV exposure at high power intensities and low annealing speeds. However, since no quantitative mechanical properties are measured or given by the manufacturer for the post-treated material, these results cannot be compared directly to the recommended post-treatment processes. Following these tests, a post-printing process consisting of NIR exposure at 50 % power and 25 mm/s followed by a UV exposure using the same parameters is used to achieve soft-bake conditions. While a post-printing process consisting of NIR exposure at 50 % power and 10 mm/s followed by UV exposure at 75 % power and 5 mm/s is used to achieve hard-bake conditions.

4.3.3 Poly Ink HC PEDOT:PSS

Printing Test Plan

The detailed printing test plan performed for the Poly Ink HC PEDOT:PSS ink is presented in Appendix IV, while the results are summarized in this section.

Once more, the printed feature thickness results show the largest dependence from the chuck temperature and the drop interpenetration, with minimal dependence from the printing lattice. The chuck temperature and drop interpenetration dependence of the seven layered and ten layered printed feature thickness are shown in Figure 4.23 (a,b) while theoretical values are shown in Figure 4.23 (c,d). The resulting average/maximum thickness values for the seven and ten layered printed features are plotted in Figure 4.23 (e,f). The thickness results are much lower than theoretically expected while also showing different trends than the theoretical values. Drop interpenetration is observed to affect the layer thickness to a much lesser extent than expected, while chuck temperatures are seen to have a much greater effect. Full coverage for most of the printing parameters tested was not achieved when using seven printed layers but is improved for ten printed layers. However, this would not explain the discrepencies between theoretically expected and experimental thickness results. We suspect that the active material in the PEDOT:PSS ink may undergo densification once solvents are evaporated. However, no support for this hypothesis could be found in the literature.

From the experimental results, two (2) trends are identified;

1. Printing performed at higher chuck temperatures and higher drop interpenetration results in more homogeneous surfaces.
2. For seven printed layers, printing performed at -25 % drop interpenetration results in less homogeneous printed surfaces, while the opposite is true for ten printed layers.

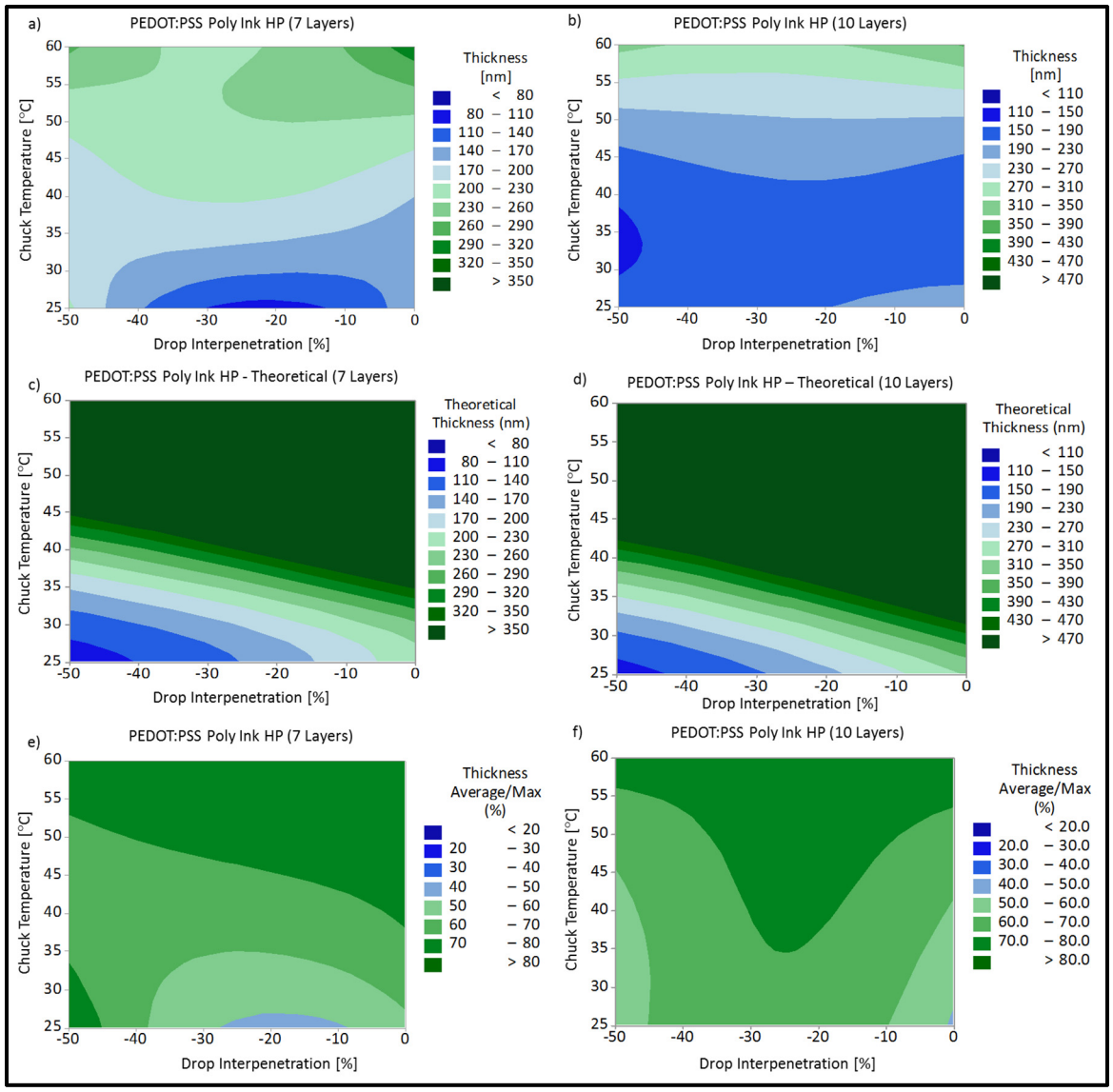

Figure 4.23 Printing test plan results for PEDOT:PSS Poly Ink HP on a Kapton substrate. a) Experimental thickness results for 7-layered features. b) Experimental thickness results for 10-layered features. c) Theoretical thickness results for 7-layered features. d) Theoretical thickness results for 10-layered features. e) Experimental surface homogeneity results for 7-layered features. f) Experimental surface homogeneity results for 10-layered features

Two sets of printing parameters are deemed to be best suited for PEDOT:PSS printing, these are presented in Table 4.10 along with resulting average/maximum thickness values.

Table 4.10 Optimal printing parameter sets for Poly Ink HC PEDOT:PSS ink

Parameter Set	No. of Printed Layers	Chuck Temp. [°C]	Interpenetration [%]	Printing Lattice	Average/Max. Thickness [%]
1	7	25	-50	Centered Square	82.2
2	10	40	-25	Centered Square	72.3

Parameter set 1 is deemed optimal for printing the Poly Ink HC PEDOT:PSS ink. The resulting printed feature is presented in Figure 4.24, along with the corresponding 3D interferometry image and height profile. For further layer printing optimization, a raster overlap of 10-50 µm, depending on jetting behavior, is found to close the voids between rasters.

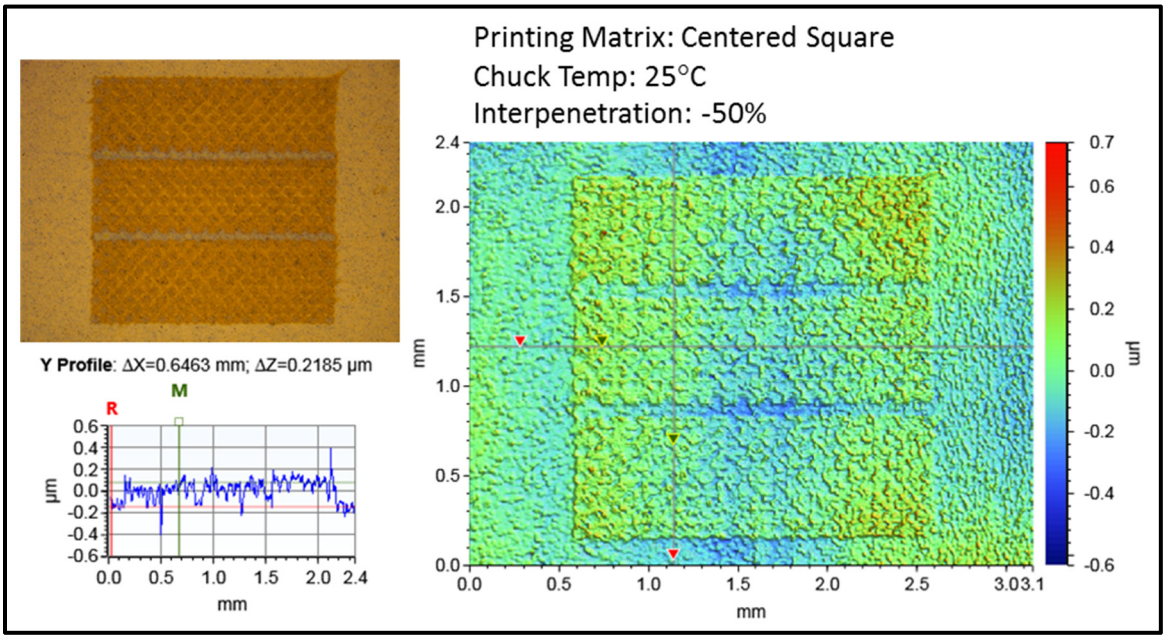

Figure 4.24 Optimal printing results for Poly Ink HC PEDOT:PSS ink on a Kapton substrate and corresponding height profile and surface morphology

Post-Printing Process

No post process is required to activate this ink, although solvent evaporation needs to be performed if other materials are to be subsequently printed. The manufacturer of this ink (Poly-Ink) have specified this material as an ITO replacement, the sheet resistance of the printed layers is therefore measured after solvent evaporation for comparison. Multiple optical treatments are tested to achieve solvent evaporation but are deemed unnecessary and even detrimental in most cases. The ink dries quickly and only slight differences in sheet resistivity are seen between optically post-processed samples. UV exposure is seen to slightly decrease sheet resistivity when compared to NIR exposure and only shows little dependence from the lamp power and annealing speed. Overall, UV exposed PEDOT:PSS printed layers achieved sheet resistivity of 2360 ± 300 Ω/□, while NIR exposed samples achieved sheet resistivity of 2780 ± 1000 Ω/□. Interestingly, untreated samples achieved the best sheet resistivity values of 1890 ± 300 Ω/□. This value of sheet resistivity is somewhat elevated when compared to ITO coatings, which typically range from 9 Ω/□ to 500 Ω/□ on rigid and flexible substrates, respectively (MTI Corporation, 2019); (Thorlabs, 2019). For coating on flexible substrates this material is still interesting for applications where a loss in conductivity of the transparent electrode, when compared to ITO, is not essential to operations.

4.3.4 Spiro-OMeTAD

Printing Test Plan

The detailed printing test plan performed for the Spiro-OMeTAD ink is presented in Appendix V, while the results are summarized in this section.

Like the previously printed inks, the printed feature thickness results show the largest dependence from the chuck temperature and the drop interpenetration, with minimal dependence from the printing lattice. The chuck temperature and drop interpenetration dependence of the single layered printed feature thickness is shown in Figure 4.25 a), while

theoretical results are shown in Figure 4.25 b). This time, the resulting average/maximum thickness values are observed to be most dependent on the printing lattice, with some dependence from the drop interpenetration and chuck temperatures. The results of average/maximum thickness values are plotted as a function of chuck temperature and drop interpenetration in Figure 4.25 c), as a function of printing lattice and drop interpenetration in Figure 4.25 d), and as a function of printing lattice and chuck temperature in Figure 4.25 e).

Experimental printed feature thicknesses are observed to match closely with theoretical values, with some differences when printing at high chuck temperatures and low drop interpenetration. This can be explained by non-complete surface coverage of the ink at these conditions. Three (3) trends are identified regarding the surface homogeneity of the printed features;

1. Printing using a Hex Shift lattice results in the least homogeneous surfaces.
2. Printing performed using Square and Centered square lattices results in the most homogeneous surfaces.
3. Printing performed at a chuck temperature of 40 °C results in less homogeneous surfaces than higher or lower chuck temperatures.

Multiple sets of printing parameters are deemed to be adequate for spiro-OMeTAD printing. One set of parameters was deemed optimal as it provided the best average/maximum thickness value and a thickness close to the targeted 300 - 400 nm for device fabrication. These parameters are presented in Table 4.11 along with the resulting average/maximum thickness value. The resulting printed feature is presented in Figure 4.26, along with the corresponding 3D interferometry image and height profile. Using a raster overlap of 5-10 μm, depending on jetting behavior, is observed to reduce the appearance of the raster ridges.

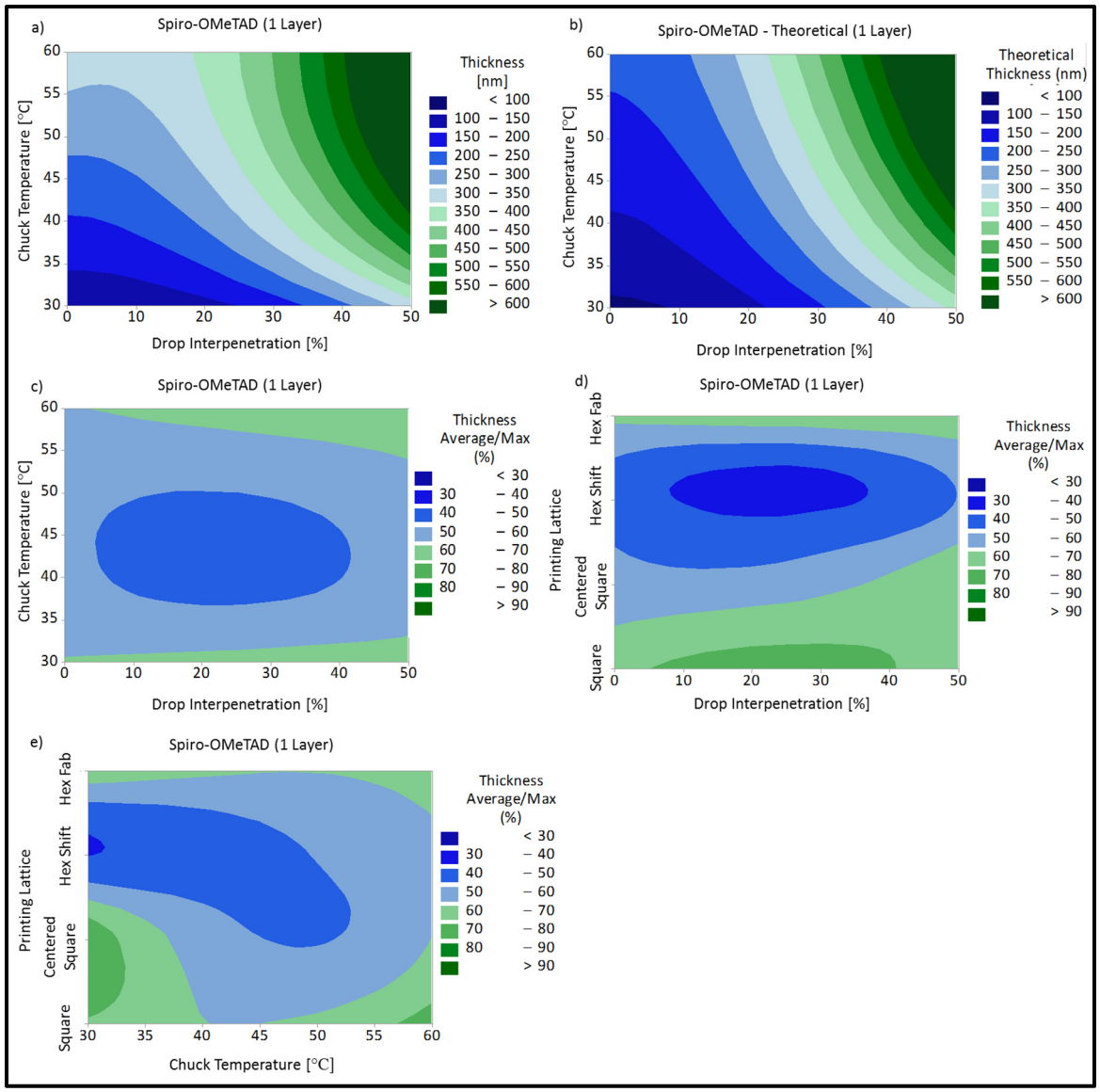

Figure 4.25 Printing test plan results for the Spiro-OMeTAD ink on a Kapton substrate. a) Experimental thickness results for one-layered features. b) Theoretical thickness results for one-layered features. c), d) and e) Experimental surface homogeneity results showing dependence on chuck temperature and drop interpenetration, printing lattice and drop interpenetration and printing lattice and chuck temperature, respectively

Table 4.11 Optimal printing parameter sets for the spiro-OMeTAD ink

Parameter Set	No. of Printed Layers	Chuck Temp. [°C]	Interpenetration [%]	Printing Lattice	Average/Max. Thickness [%]
1	1	60	25	Square	93.4

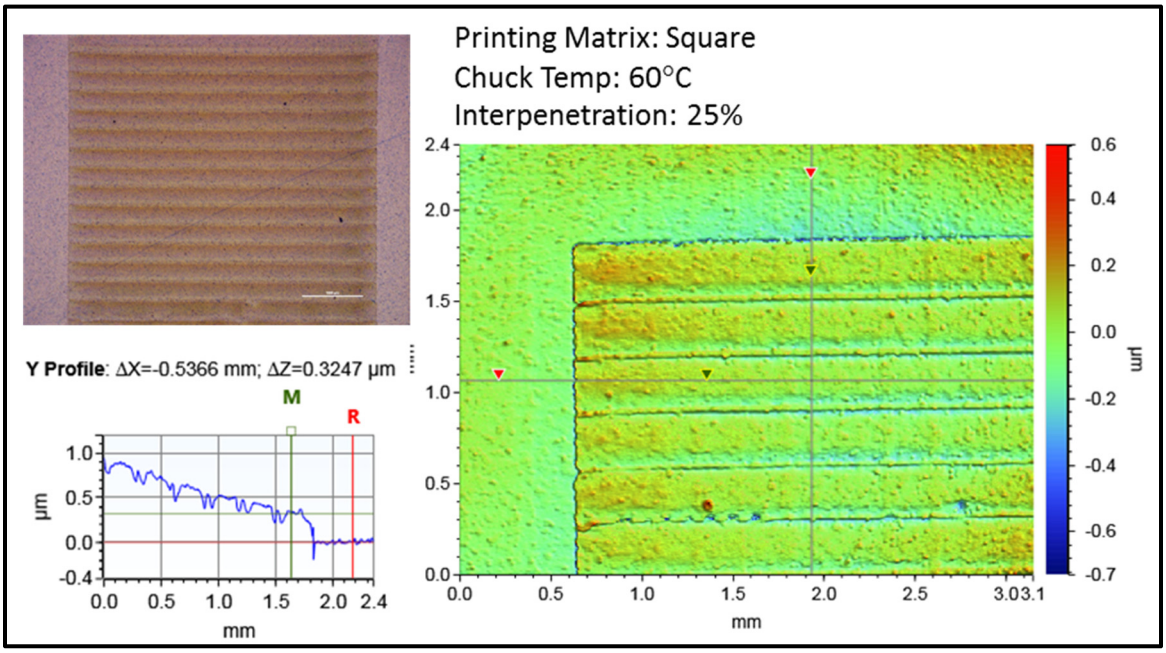

Figure 4.26 Optimal printing result for the spiro-OMeTAD ink on a Kapton substrate and corresponding height profile and surface morphology

Post-Printing Process

Spiro-OMeTAD formulations are known to be sensitive to light exposure for short durations after the material is deposited and while solvent evaporation begins (Sanchez & Mas-Marza, 2016, p.189-194); (Wang, Yuan & Meng, 2015, p.24791-24798). From the literature, it is advised to bake the spiro-OMeTAD for a short duration after deposition to evaporate solvents (Fang, Wang, Wang, Huang & Wu, 2014, p.2809-28160) and to keep the deposited spiro-OMeTAD material in a dark environment for up to 24 hours to increase charge carrier mobility (Gonzalez-Pedro, 2014, p.888-893). Leaving the printed feature on the 60 °C chuck for 10

minutes was deemed adequate for solvent evaporation as no visual change of the printed layer is seen after this time. In this work, it was noted that resting the spiro-OMeTAD layer for at least 12 hours in dark conditions was necessary for device operations, this is explored in more detail in Chapter 6 which relates to device fabrication and operation.

4.3.5 Ossila I101 Perovskite

Preliminary Printing Test-Plan

The detailed preliminary printing test plan performed for the Ossila I101 PS ink on plasma treated FT Kaption-FPC 300 substrates is presented in Appendix VI. Its results are summarized in this section and are used as a basis for further optimization for printing on ITO covered substrates.

During the preliminary printing test plan, we observe that Ossila I101 PS ink is prone to ink bleeding effects when printing on the plasma treated FT Kapton-FPC 300 substrate. Printing SU-8 retaining walls is established as a method of containaing the PS ink to the printed area and avoid ink bleeding effects, these structures are reffered to “SU-8 pools” in the remainder of this work. Furthermore, solvent assisted annealing is initially performed of the printed PS ink using a 25 % EtOH: 75 % CB solvent mix deposited via inkjet printing. This is shown to improve surface coverage on Kapton substrates. This technique is later abandoned for annealing on ITO covered substrates as no such benefit was found.

Layer thicknesses of printed perovskite layers using the SU-8 pools and solvent annealing are measured using SEM imaging and are plotted in Figure 4.27 and Figure 4.28, showing results for single layer printing with varying drop interpenetration and multiple layer printing using 2 different layer interpenetration, respectively. These results are also summarized in Figure 4.29 (a) along with theoretical values in Figure 4.29 (b). We observe that the theoretical PS thickness values calculated from Equation 4.6 provide a good lower bound estimate to actual printed layer thicknesses. Experimental values closely match theoretical values for single

layered printed features but diverge slightly for multiple-layered features, this may be explained by the incomplete coverage in the PS feature observed with most printing parameters used.

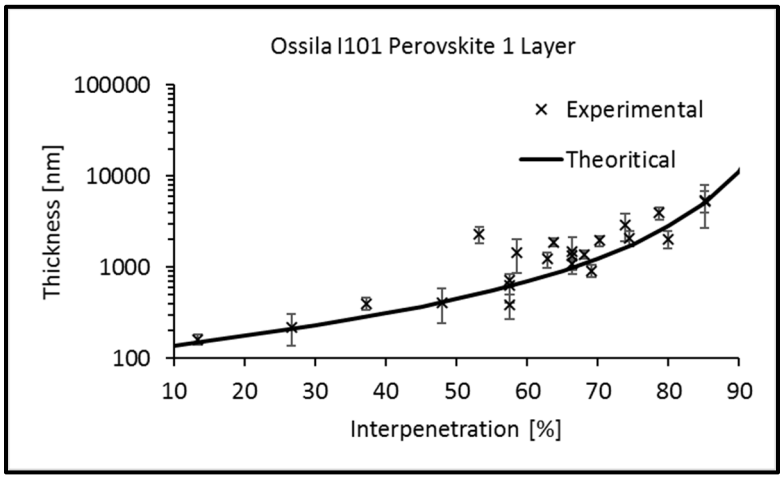

Figure 4.27 Overview of the 1-layer thickness measurements of the printed Ossila I101 PS ink features, presented as a function of drop interpenetration

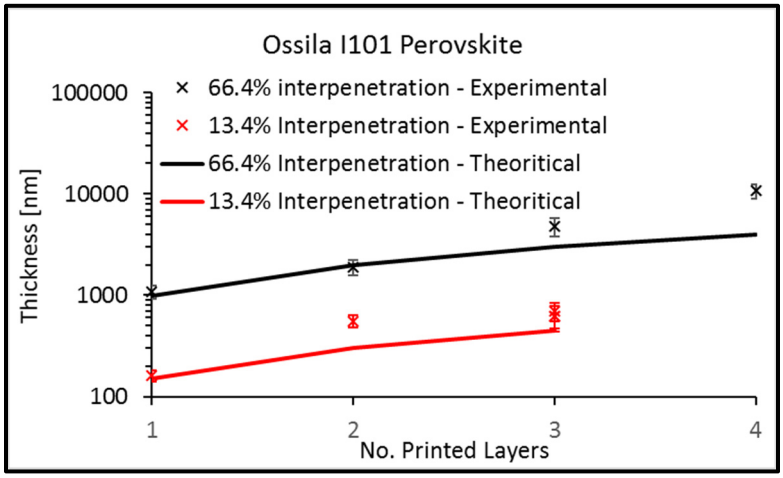

Figure 4.28 Overview of the total layer thickness measurements of the printed Ossila I101 PS ink features using 2 distinct drop interpenetration parameters, presented as a function of the number of printed layers

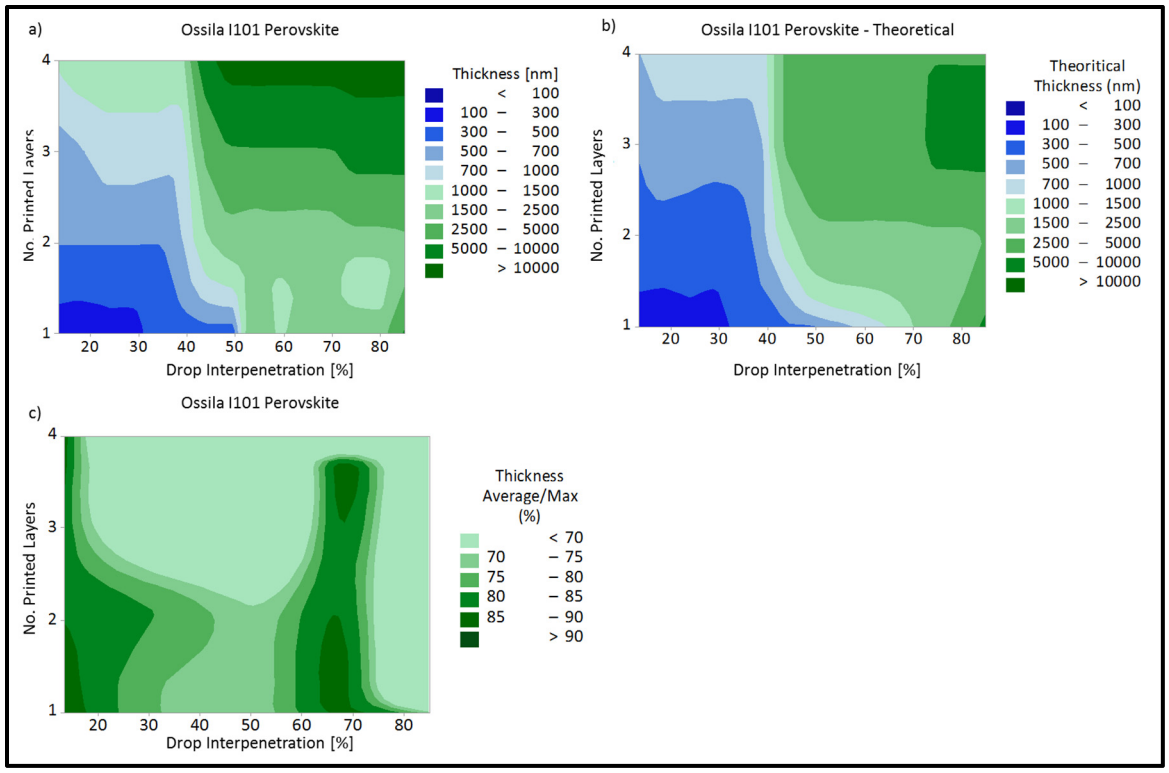

Figure 4.29 Printing test plan results for Ossila I101 PS ink on a Kapton substrate.
a) Experimental thickness results. b) Theoretical thickness results.
c) Experimental surface homogeneity results

Other important characteristics of PS layers for their use in optoelectronic applications are; the layer coverage, the uniformity of the layer and the crystal sizes. The layer coverage is important since incomplete coverage will result in pinholes and lead to shunting pathways which may be detrimental to device performances (Ball et al., 2013, p.1739-1743); (Snaith, Greenham & Friend, 2004, p.1640-1645). Layer uniformity is important as TF device performances are inherently tied to PS layer thickness, inhomogeneous layer thicknesses may lead to lower performances (Liu D., Gangishetty, M. K., & Kelly, T. L., 2014, p. 19873-19881). Lastly, PS crystal size is an important layer characteristic since it may also affect device performances. Larger PS crystals are preffered as they reduce the number of grain boundaries which impede charge mobility (Barnett, J. L., Cherrette, V. L., Hutcherson, C. J., & So, M. C., 2016, p.1-12). These layer characteristics are measured and their tendencies with respect to various printing parameters are presented in Figure 4.30.

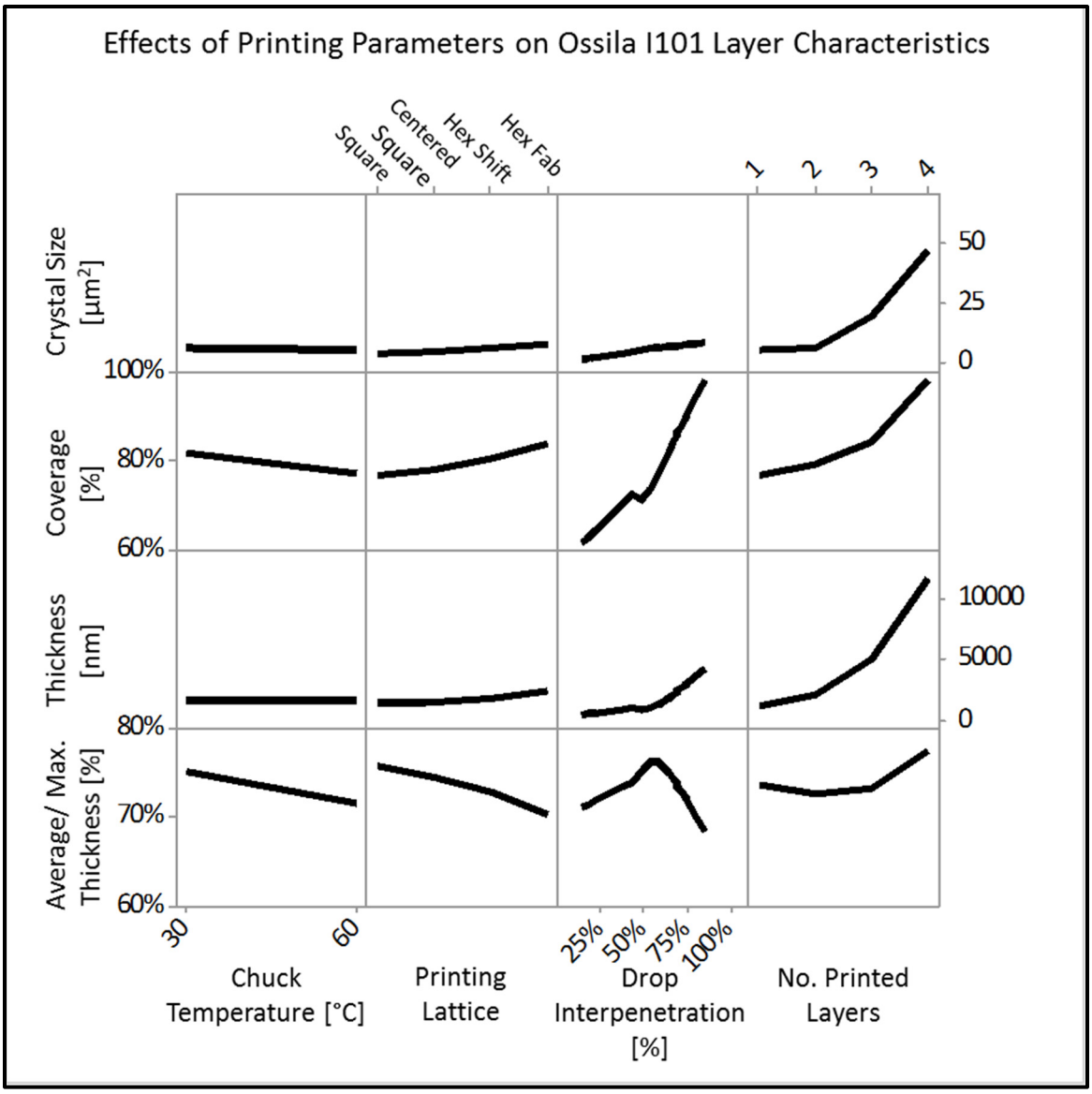

Figure 4.30 Effects of printing parameters on Ossila I101 printed layer characteristics

Slight negative correlations between the chuck temperature and all the measured layer characteristics are observed. A lower chuck temperature provides improved coverage and layer homogeneity while less effet is seen on the layer thickness and crystal sizes. We speculate that this is due to elevated chuck temperatures inadvertently heating the nozzles past the ink's stable jetting temperatures while printing.

Increased drop packing from printing lattice and increased drop interpenetration show positive correlations with the PS crystal size, the layer coverage and the layer thickness. The increase in layer coverage and layer thickness are expected from the increase in total printed material, while we suspect that increase in crystal size is also tied to increased material deposition. While, increased drop packing from the printing lattice provides reduced layer homogeneity.

We find that increasing the number of printed layers increases the layer coverage and thickness as expected from increased material deposition. Interestingly, the PS crystal size is most affected by the number of printed layers, giving credence to our belief that increased crystal size is tied to increased material deposition. We find that layer homogeneity remains somewhat constant for one to three printed layers and improves drastically for the fourth printed layer.

The codependence tendencies in layer characteristics are also studied and are shown in Figure 4.31. The PS crystal size–layer thickness and layer coverage-layer thickness codependences stand out from all other layer characteristics codependences. As expected from our belief that PS crystal size is tied to the amount of deposited material, we observe that the PS crystal size is highly correlated with the layer thickness. Similarly, we also find that crystal size is positively correlated with the layer coverage. As expected, we observe that the layer coverage increases with increased layer thickness until complete coverage is achieved.

From the State-of-the-Art and Literature Review sections, a layer thickness of < 300 nm is targeted for the implementation of the MALH PS active layer for TF device applications in photo-sensing and energy harvesting. From the experimental results, two methods of obtaining this targeted thickness are found. The first method involves printing a single layer of PS ink with a drop penetration of 50 - 60 %. The second method involves printing multiple layers using lower drop interpenetrations. The first method is preffered as it results in more homogeneous layers with increased layer coverage, while PS crystal sizes remain similar for both methods.

Figure 4.31 Codependence of Ossila I101 printed layer characteristics

From the literature we know that PS annealing conditions can have an important effect on the resulting layer coverage. (Eperon, G. E., Burlakov, V. M., Docampo, P., Goriely, A., & Snaith, H. J., 2014, p.151-157). From the test plan results, we find that complete crystal coverage does not happen readily for layer thicknesses below ~1.5 µm. Solvent annealing is shown to increase surface coverage overall, however, it is found to be detrimental for thin PS layers (< 1 µm). This is a result of the semi-stable solvent jetting conditions which can introduce material splashing. This may leave room for further optimizing in future works, throught the formulation of solvent annealing inks adequate for inkjet printing.

Optimized Printing on ITO covered Substrates

The printing test plans on plasma treated FT Kapton-FPC 300 substrates give a good basis for further printing optimization on the targeted ITO covered PET and glass substrates. The decrease in surface energy of the plasma treated ITO covered substrates with respect to plasma

treated Kapton substrates is expected to increase the contact angle of the PS ink with the substrate thus decreasing splat diameter and decreasing ink bleeding effects. Indeed, this is what is observed. The splat diameter is decreased to 65 μm while the chuck temperature is kept at 30 °C and ink bleeding effects are not seen for printed features with the targeted thickness. Therefore, for printing PS on ITO covered substrates, the SU-8 pools used in the preliminary test plan are not necessary to avoid ink bleeding effects. The printing parameters are adapted for printing on ITO covered substrates, only small changes to the printing parameters are needed to achieve optimized coverage for the targeted layer thickness. The adapted printing parameters for ITO covered substrates are shown in Table 4.12 along with the resulting crystal thickness range, while jetting parameters are kept identical from those stated in section 4.2.3.

Table 4.12 Optimized printing parameters for Ossila I101 PS ink adapted for printing on ITO covered susbtrates

Chuck Temp [°C]	**Splat Diameter [μm]**	**Splat Overlap [%]**	**Raster Overlap [μm]**	**Printing Lattice**	**Layer Thickness [nm]**
30	65	61.5	7	Square	330-830

Using these printing parameters, further annealing optimization is performed. Conventional oven annealing performed at 90 °C for 2 hours is compared to optically assisted annealing using the in-situ NIR lamp and solvent assisted annealing using 25 % EtOH:75 % CB solvent printing, the resulting printed features are shown in Figure 4.32, Figure 4.33 and Figure 4.34, respectively. Crystal thicknesses are once again measured using SEM imaging while surface coverage is calculated via light thresholding, using an optical microscope system.

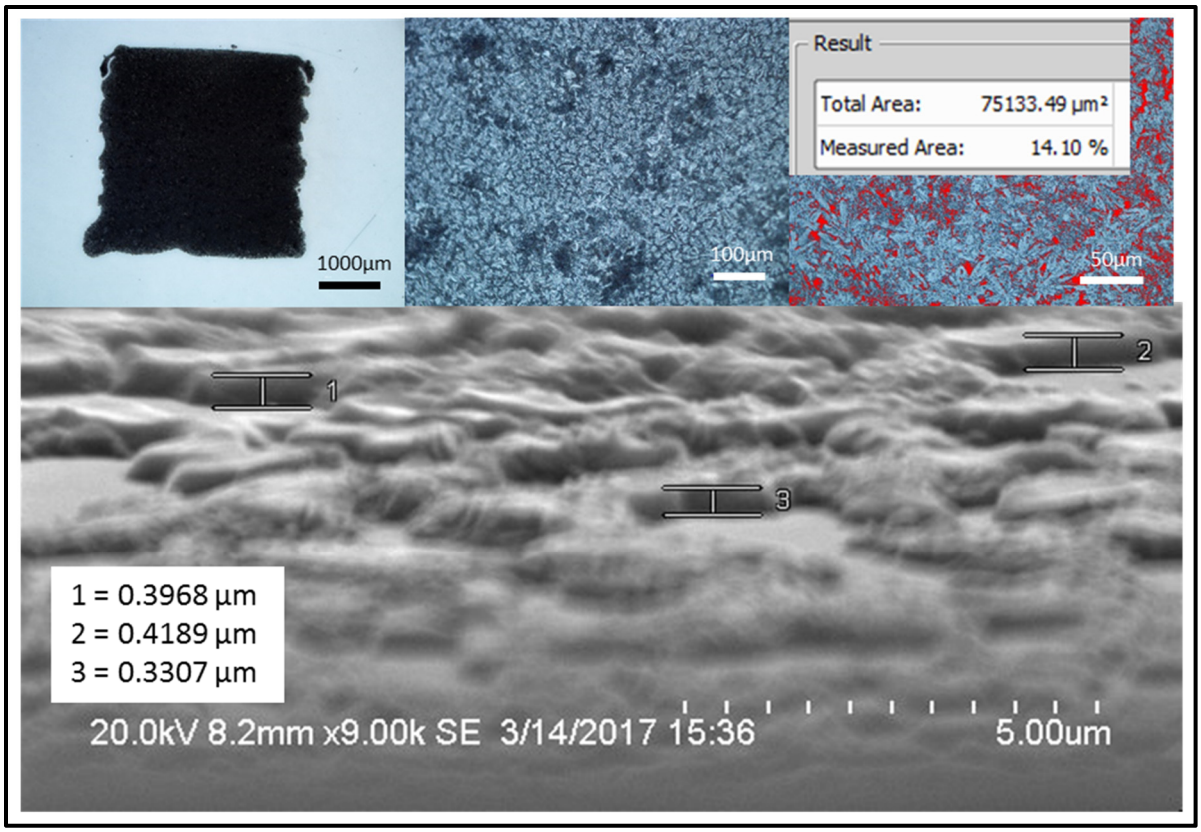

Figure 4.32 Optimized printing of Ossila I101 PS ink layer characterization using oven annealing processes only

Conventional oven annealing of optimized printed PS layers, following the ink manufacturer annealing specifications, is observed to result in surface coverage of ~86 % with crystal thicknesses varying between 330 nm and 420 nm and an average crystal thickness of ~380 nm. The surface coverage is homogeneous on a macro scale within most of the printed feature area. Coverage close to the edges of the deposition show some variation and results in irregular edges. Device fabrication can be adapted to only utilize the homogenous section (no edges) of the PS layer by limiting the area of the deposited electrodes for charge extraction. Interestingly, the resulting PS crystal shapes are not as regular as those found in the literature or when printing thicker layers with increased crystal packing and surface coverage. For these printed films, the PS forms elongated or "star" shaped crystals which contrasts with more cubic shaped crystals obtained when better crystal packing is present. The effects that PS crystal shape has on film properties or device operations are not fully understood. Incomplete surface coverage

of the PS crystals, on the other hand, is expected to be detrimental to device operations. Firstly, incomplete surface coverage of the PS crystals effectively reduces the active area of the device, thus reducing overall device efficiencies. Secondly, devices which utilize this printed film as an active layer can no longer be considered as TF architectures and resemble more NS device architectures which operate in a different manner. As seen in section 3.2, TF devices rely on the PS for charge transport which is only effective when the TF is thinner than the charge diffusion length, whereas NS devices rely on another material for charge transport as PS thickness is much greater than charge diffusion length in these device architectures (Gonzalez-Pedro et al., 2014, p.888-893). These printed films can be considered a hybrid TF-NS film as crystal thickness remain below charge diffusion length while creating a NS pattern which can be infiltrated with charge transport material.

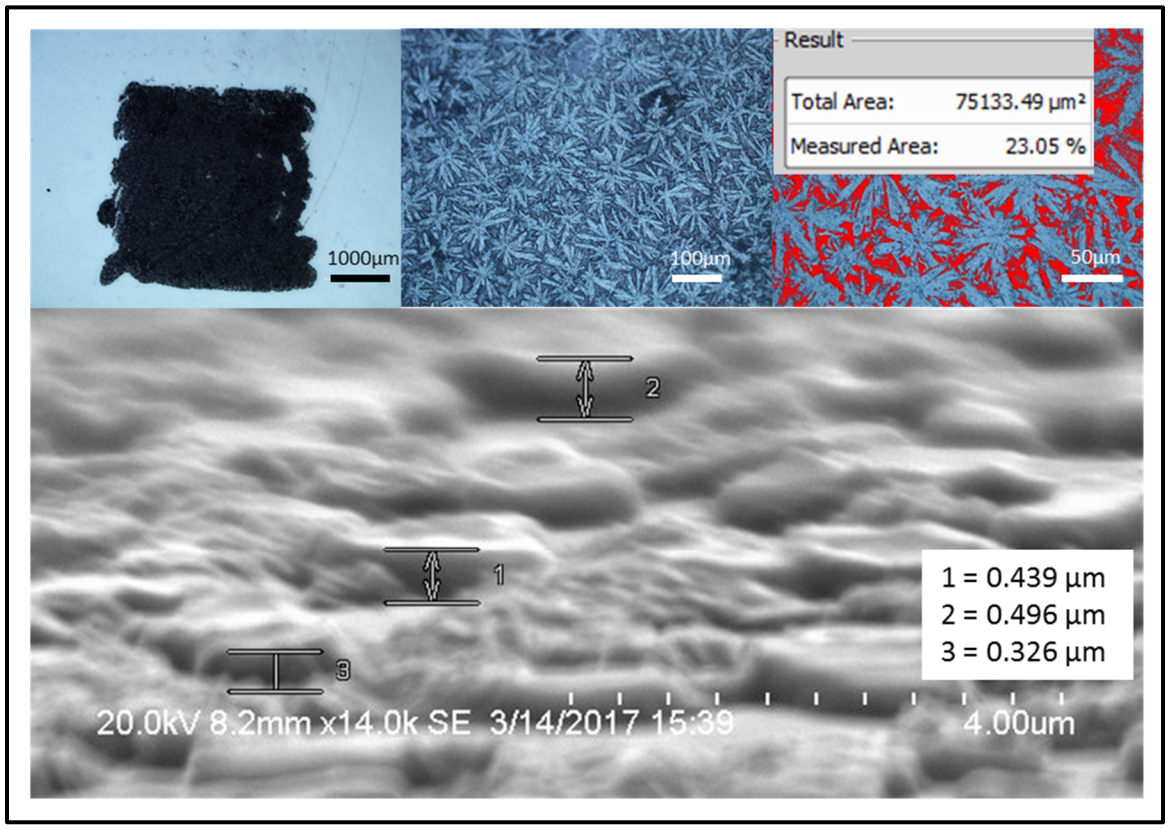

Figure 4.33 Optimized printing of Ossila I101 PS ink layer characterization using a preliminary NIR optical treatment prior to the oven annealing process

The effects of the preliminary NIR optical treatment prior to solvent annealing are tested. A NIR optical treatment is performed at 5 % lamp power using a chuck displacement speed of 20 mm/s which is followed by oven annealing performed at 90 °C for 2 hours. Surface coverage is reduced when compared to oven annealing only, a surface coverage of ~77 % is found for these annealing conditions. The surface coverage is again homogeneous over most of the printed area, however, the resulting edges are more irregular than from oven annealing alone. Since the PS crystal cover a smaller proportion of the printed area, using the same material volume, thicker PS crystals are expected. Indeed, not only do the PS crystals have a larger variation in thicknesses, which range from 320 nm to 500nm, but the average crystal thickness is also increased to ~420 nm. The preliminary NIR optical treatment also affect the shape of the PS crystals, an accentuation of the "star" shaped crystals with longer "arms" is observed. Moreover, the crystal sizes are significantly increased when compared to oven annealing alone. It is speculated that the preliminary NIR optical treatment starts crystal formation at a faster rate with a higher temperature, resulting in increased crystal sizes, similarly to hot casting methods of PS crystal growth (Nie et al., 2015, p.522-525). From the literature, increased crystal sizes are expected to be beneficial to device operation, however, reduced surface coverage could counterbalance any benefit from increased crystal sizes. The beneficial aspects on device operation of the preliminary NIR optical annealing treatment are explored in Chapter 6 of this work which relates to device fabrication and operation. Nonetheless, from a purely architectural perspective, both films are viable for device fabrication.

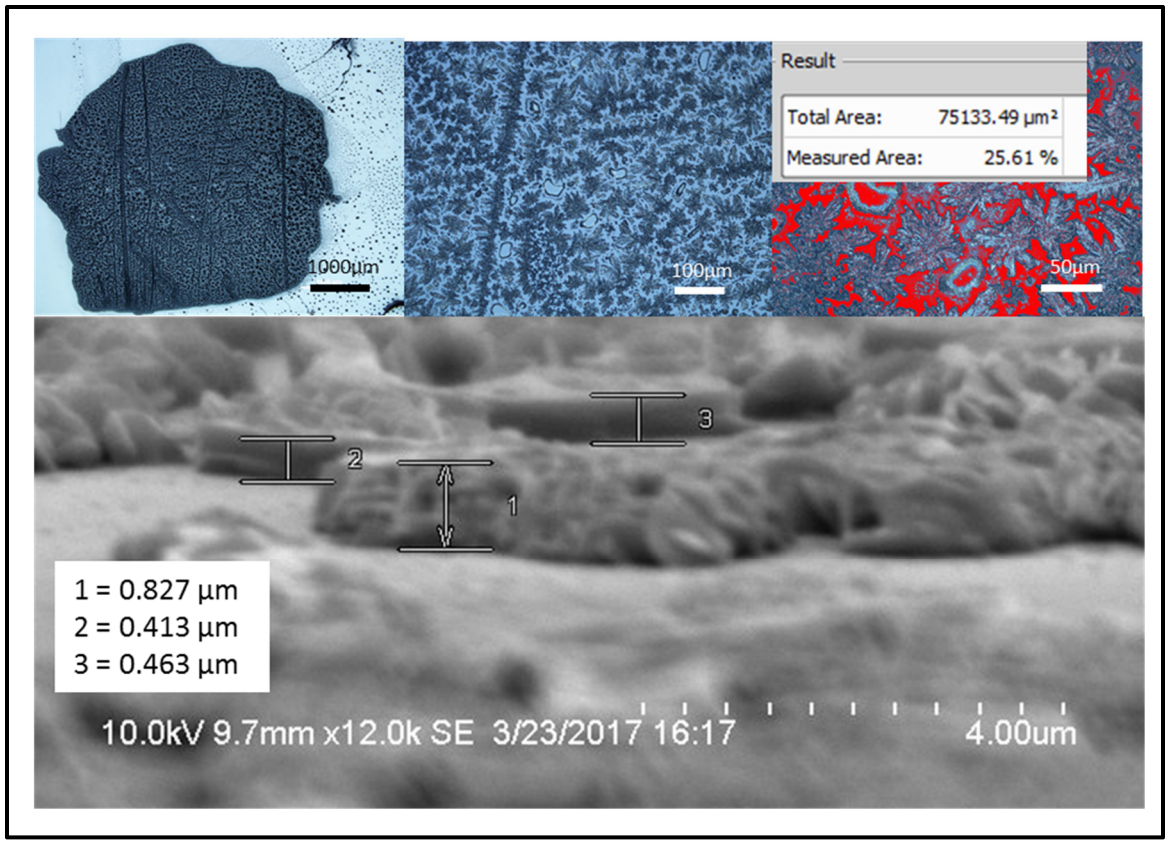

Figure 4.34 Optimized printing of Ossila I101 PS ink layer characterization using solvent assisted annealing with a preliminary NIR optical treatment prior to the oven annealing process

The effects of solvent annealing on the printed PS architecture is also explored on ITO coated substrates. The effects on device operations are explored latter, in Chapter 6 of this work, which relates to device fabrication and operation. This annealing treatment consists of the preliminary NIR optically annealing treatment performed at 5 % lamp power using a chuck displacement speed of 20 mm/s, followed by 25 % EtOH: 75 % CB solvent printing and finished with oven annealing at 90 °C for two (2) hours. The results are similar in this case when compared to annealing performed without the solvent printing step, although a few differences are apparent. "Star" shaped PS crystals of dimensions similar to those found for NIR assisted oven annealing are formed throughout the sample. Other crystals are observed to result in ring formations, possibly due to PS displacement from solvent splashing while printing. The resulting crystal thicknesses range from 410 – 850 nm with an average thickness of ~570 nm, while average

surface coverage is reduced to ~74 %. The surface coverage is not as homogeneous on a macro level as when following either NIR assisted oven annealing or oven annealing alone, with some areas showing increased surface coverage while others show areas of decreased coverage (dark lines and light spots in center of the deposition in Figure 4.34 top left, respectively). The improvement in crystal packing and uniformity that printed solvent assisted annealing provided for thicker PS layers is not observed in this case. Additionally, leftover residue is found around the printed area after the final annealing step. This may be detrimental to device fabrication processes and/or device operations as these impurities could act as charge recombination centers for example.

Optimized printing of non-inkjet adapted PS inks is non-trivial as it introduces new challenges in terms of optimizing crystal growth and coverage. Nonetheless, printed PS layers with targeted thicknesses are achieved and show potential as active layers for optoelectronic devices. A tradeoff between layer thickness and surface coverage is observed for layers of < 1500 nm as full coverage could not be achieved for these thicknesses. Adapting the ink content is necessary for further printing optimization of Ossila I101 ink.

4.4 Conclusion

Throughout this chapter, a greater understanding of the inkjet printing process from substrate and ink preparation to the optimization of printing and jetting parameters, is acquired. The use of pre-printing plasma hydrophilic treatments is deemed essential for some substrates and for preparing some printed ink materials for subsequent material printing. Studies on the effects of hydrophilic oxygen plasma treatments are performed on a multitude of flexible and rigid substrates identified for inkjet printing prototyping. The Owens/Wendt method is utilized along with four (4) test liquid to measure polar and dispersive components of the substrate surface energies, before and after treatment with oxygen plasma. Standard procedures for substrate cleaning are described and use henceforth whenever substrate manipulation is performed.

A multitude of commercial ink materials are identified for device prototyping and for compatibility with inkjet printing processes. Where commercial options for ink material are not available, custom ink solutions are prepared. Manipulation procedures for the individual inks are established and describe storage, manipulation and cartridge filling procedures. Optimized ink jetting parameters with Dimatix inkjet cartridges are experimentally found for each ink material. Jetting stability and resulting jetted drops are characterized using Ceradrop ink jetting reports. Printing test plans of the ink materials are performed on flexible Kapton substrates at different temperatures to acquire a better understanding of the printing process and to evaluate optimized printing parameters for the different inks. Finally, conventional and optical post-printing treatment procedures for annealing, solvent evaporation and ink activation purposes are established for each ink material where needed.

In conclusion, complete inkjet printing process, including pre- and post-printing processes for single ink materials are established for ANP DGP 40TE-20C Ag NP ink, MicroChem SU-8 photoresist ink, Poly Ink HC PEDOT:PSS ink, Spiro-OMeTAD solution and Ossila I101 PS ink.

CHAPITRE 5

FABRICATION OF PASSIVE DEVICE STRUCTURES

In this chapter, the optimized jetting and printing parameters found in the previous chapter are used and further adapted for printing multiple layers of different ink materials for passive device structure fabrication. Thin film transistor (TFT) structures, isolated electrodes, interdigitated electrodes and THz VPPs are printed on flexible PET and Kapton substrates to evaluate the feasibility and challenges of inkjet printing for device fabrication. These devices are chosen to test different aspects of the printing process while also providing some of the building blocks for works presented in the next chapters. The TFT structures are used to evaluate the feasibility of printing multiple material layers on top of each other, this information is then used later for the fabrication of the PS PV devices. The silver isolated electrodes are used in part to evaluate the effects of printing subsequent ink layers of the same material. These isolated electrodes are then used in Chapter 6 as electrical connections for ease of characterization and operation of printed PS PV device arrays. The interdigitated electrodes are used for the foundation of the PS bolometer devices presented in Chapter 6, and to evaluate the minimal feature sizes achievable with the Ceradrop printer. The THz VPPs are also used, in part, to evaluate minimal printable feature sizes, while adding extra constraints. All these devices are also printed to gain familiarity with the printing equipment and printing process before printing the more complex PS PV devices.

Most multilayered device fabrication follow similar layer-by-layer flow process. Fabrication typically starts with substrate surface treatments. As seen in section 4.1, these treatments can take the form of hydrophilic/phobic surface treatments or surface cleaning processes. Subsequently, the first device layer can be printed using previously optimized printing parameters to form a homogeneous layer of desired characteristics. Once the layer is printed, post processes, such as annealing or layer activation, are performed to transform the ink to its final state (Kim & Moon, 2005, p.J30-J33); (West, Carter, Smith & Sears, 2012, p.174-185). This flow process is then repeated for each subsequent layer until the device is fully printed.

5.1 TFT Device Structure

To evaluate the feasibility of printing multiple material layers on top of each other, generic multilayered TFT device structures are printed on FT Kapton-FPC 300 substrates. These structures consist of an ANP-DGP 40TE-20C Ag gate layer, a MicroChem SU-8 dielectric layer and a Poly Ink HC PEDOT:PSS active layer.

5.1.1 Fabrication and Characterization

First, the Kapton substrate is cleaned and treated using oxygen plasma following the procedures laid out in sections 4.1.1 and 4.1.2, respectively. The PEDOT:PSS active layer is printed by following the optimized printing parameters found in section 4.3.3 (seven (7) layers, -50 % drop interpenetration, Centered Squared lattice and 25 °C chuck). To achieve a greater active layer thickness, thee (3) stacks of seven (7) layers of PEDOT:PSS are printed on top of each other for a total of 21 layers resulting in thickness of ~460 nm. The second and third printed stack of PEDOT:PSS are observed to homogenize the deposition as material fills the voids found in the first printed stack, as such the total layer thickness is only increased by a factor of 2.3. MicroChem's SU-8 is then printed directly on the PEDOT:PSS active layer with no treatments or processes performed on the printed PEDOT:PSS active layer. It is found that as the solvents in the PEDOT:PSS (water) and SU-8 (Cyclopentanone, 1-Methoxy-2-propanol acetate and Gamma-Butyrolactone) inks are not miscible with one another, one material can be printed on top of the other without affecting the underlying printed layer. It is also found that the PEDOT:PSS layer provided an adequate printing surface for the SU-8 ink, as printing parameters did not have to be adapted from their optimized values found in section 4.3.2. Two (2) stacks of SU-8 ink are printed using the optimized printing parameters found in section 4.3.2 (two (2) layers, 50 % drop interpenetration, Centered Square lattice and 40 °C chuck). This results in a total SU-8 thickness of ~ 5 μm, effectively doubling the 2.4 μm thickness achieved when printing a single stack. The SU-8 layer is then hard baked using the UV and NIR optical post-printing process specified in section 4.3.2. Subsequently, the SU-8 layer is treated using hydrophilic oxygen plasma to achieve an adequate printing surface for the Ag

gate electrode. The final Ag gate electrode is printed using a single layer of ANP DGP 40TE-20C Ag ink using the printing parameters specified in section 4.3.1 (Single layer, 50 % drop interpenetration, Hex Shift lattice and 25 °C chuck), resulting in a ~700 nm thick layer. This layer is slightly thicker than while printing directly on Kapton substrate as the surface energies of hard baked SU-8 are higher than those of plasma treated Kapton, thus increasing the contact angle of the ink with the surface. NIR annealing is performed at 100 % lamp power and a chuck displacement speed of 10 mm/s, followed by oven annealing at 200 °C for one (1) hour to provide improved inter-layer adhesion. The structure passed a mechanical integrity testing (tape-test) using 3M MIL-A-AA-113-B tape after oven annealing. An SEM micrograph is presented in Figure 5.1 illustrating the final TFT device structure stack on a Kapton substrate.

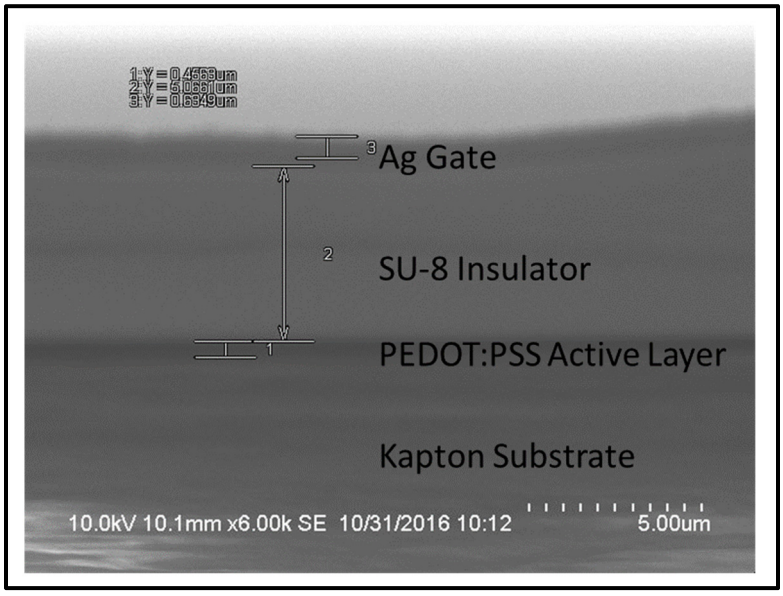

Figure 5.1 SEM micrograph of the generic TFT structure, showing the layer thicknesses

5.2 Silver Electrodes

Electrical routing and electrodes are essential aspects of printed circuit boards (PCBs), integrated circuits (ICs) and device fabrication and integration for read out purposes. In this section non-isolated interdigitated electrodes and isolated routing electrodes are printed on

PET and Kapton substrates, respectively. The interdigitated electrodes can serve as a basis for capacitive and resistive sensor device fabrication. Applications for interdigitated electrode sensor structure vary wildly, from chemical sensing to temperature and pH sensing, depending on the sensing material deposited between the electrodes (Van Gerwen et al., 1998, p.73-80); (Rajapaksha, Hashim, Gopinath & Fernando, 2018, p.1965-1974); (Yassine et al, 2016, p.15879-15883). In contrast, isolated routing electrodes are not used for sensing but for read out purposes to facilitate the connection of devices to either characterization equipment or for read out and/or data processing. It is generally beneficial to electrically isolate the electrodes (with open contacts) to avoid electrical contamination from other sources and for mechanical protection.

5.2.1 Isolated Routing Electrodes

Design

The isolated routing electrodes are printed on FT Kapton-FPC 300 substrates using ANP DGP 40TE-20C Ag ink for the conductive traces and MicroChem's SU-8 ink to electrically isolate the conductive traces. The routing electrodes are designed to contact a 10-device array in TF vertical architectures, or to provide the positive and negative contacts for five (5) devices in horizontal architectures. The device contacts consist of 2 mm x 2 mm un-covered pads, while the connections at the edge of the substrate consists of 4 mm x 4 mm un-covered pads for easy connections with alligator clips. Devices can later be printed directly on the electrodes in a bottom-up approach, or the electrodes can be connected to already fabricated devices in a top-bottom approach.

Fabrication and Characterization

The complete isolated routing electrodes printed on Kapton substrates are depicted in Figure 5.2, along with the height profile of the Ag traces. Kapton substrates are cleaned and oxygen plasma treated following the procedures laid out in sections 4.1.1 and 4.1.2, respectively. The

Ag electrode traces are printed using 8 stacks of ANP DGP 40TE-20C Ag ink using the printing parameters in section 4.3.1 (Single layer, 50 % drop interpenetration, Hex Shift lattice and 25 °C chuck) resulting in a total Ag trace thickness of ~ 4 μm as seen from the height profile depicted in Figure 5.2 c) & e). A NIR annealing at 100% lamp power using a chuck displacement speed of 10 mm/s is performed after printing each of the Ag layers to provide an adequate surface for printing the subsequent Ag layers. After the last layer is printed, a final oven annealing is performed at 200 °C for 1 hour to improve the conductivity and mechanical stability of the structures. Two stacks of SU-8 ink are printed on the Ag traces to electrically isolate them, as shown in Figure 5.2 d), using the optimized printing parameters found in section 4.3.2 (two (2) layers, 50 % drop interpenetration, Centered Square lattice and 40 °C chuck). No SU-8 is printed on the contact pads as shown in Figure 5.2 b). The SU-8 layer is then hard-baked using the UV and NIR optical post-printing process specified in section 4.3.2. The pad-to-pad resistance of the electrical routing is an important aspect of to take into consideration and should be minimized as much as possible to minimize electrical losses. Furthermore, the SU-8 electrical insulation needs to be tested to evaluate its validity. As such, the pad-to-pad resistivity of the routing electrodes are measured using 2-point resistivity measurements. Two resistance measurements are taken, separating the “top” and “bottom” electrodes as they both have ink traces of different lengths, with the “top” electrodes consisting of the longer ink traces, as seen in Figure 5.2 a). A pad-to-pad resistance of 55.7 ± 0.8 Ω is measured for the “top” electrodes, whereas a pad-to-pad resistance of 35.2 ± 0.7 Ω is found for the “bottom” electrodes.

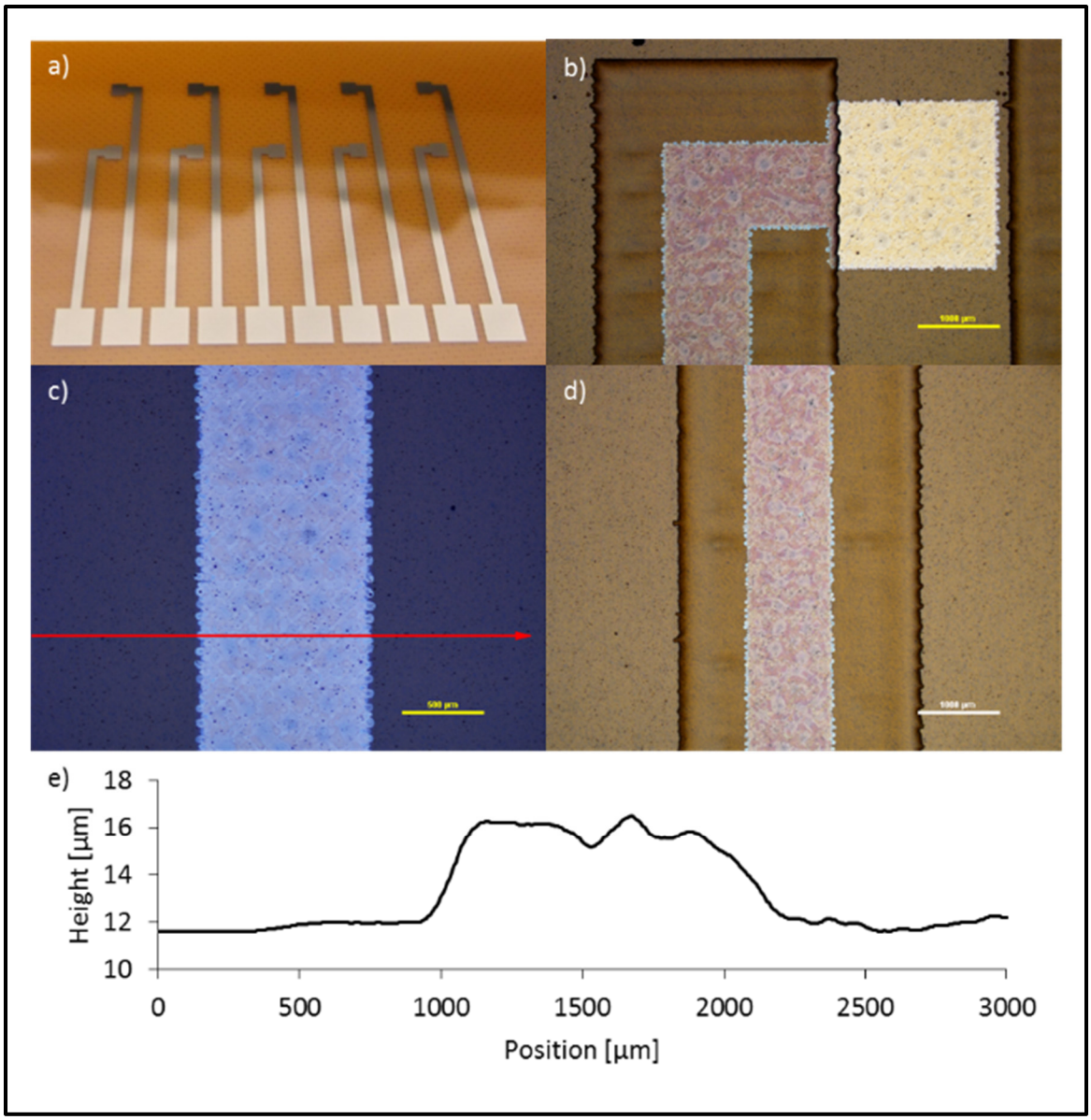

Figure 5.2 a) Photograph of the printed Ag electrodes, b) microscope image of the isolated printed electrode showing the uncovered contact pad, c) microscope image of the printed Ag electrode trace with the identified cross section for the height profile, d) microscope image of the printed Ag electrode covered with printed SU-8 and e) height profile of the printed Ag trace

5.2.2 Interdigitated Electrodes

Design

Interdigitated electrodes can serve as a basic building block for sensor architectures where the addition of sensing materials between the electrodes can determine the sensing capabilities of the devices. A few aspects of the design of the interdigitated electrodes are important and play a major role in device operations and sensing capabilities. These aspects include the geometrical properties of the interdigitated electrodes, such as the distance between the electrodes, the length of the electrodes, the number of electrode digits and the total area of the interdigitated electrodes. As for any electrodes, electrical properties of the interdigitated electrodes are also important for device operations. Since the geometrical properties of the interdigitated electrodes plays such a major role in device operations and sensing capabilities, advanced control over printing feature sizes is deemed beneficial. As such, Novele^{TM} IJ-220 PET from Novencentrix was chosen as printing substrate due to its proprietary coating adapted for inkjet printing. The proprietary coating on the PET substrate surface is created specifically to improve homogeneity of printing and provides a somewhat hydrophobic surface. This increases the contact angle between the inks and the substrate thus reducing possible feature sizes, while also providing adequate ink adhesion (Novacentrix, 2011).

The interdigital electrodes are designed with respect to the lowest feature size achievable, both in terms of printed feature width and distance between printed features. Vector mode printing is used for printing the interdigitated electrodes. In vector mode printing, only a single nozzle is used for jetting and printing. This results in more homogeneous printing as jetting variations between nozzles do not come into play. To estimate the minimum feature sizes feasible on Novele^{TM} IJ-220 PET substrates with ANP DGP 40TE-20C Ag ink, the splat diameter of the ink is measured and shown in Figure 5.3. A splat diameter of 36.2 ± 1.9 μm is measured at a chuck temperature of 60 °C, this value is estimated as the minimal feature size achievable for this combination of substrate and ink.

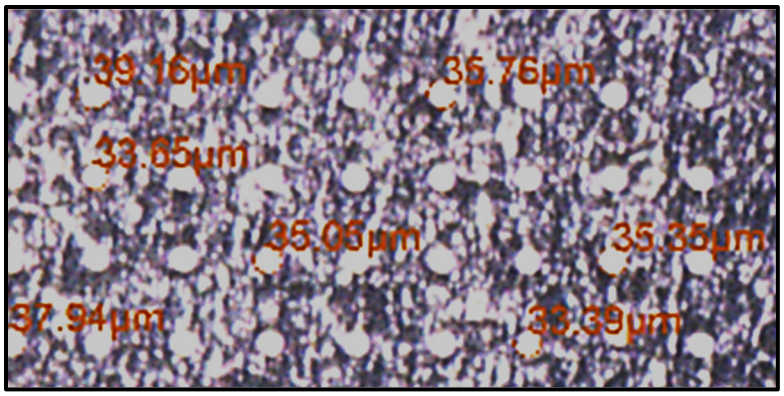

Figure 5.3 ANP DGP 40TE-20C Ag ink drop splat diameter on Novele^{TM} IJ-220 PET substrate with a chuck temperature of 60 °C

The interdigitated electrodes are designed over an area of 8 mm x 10 mm with an overlap area of 8 mm x 7 mm, 1 mm collection bars finishing in 2 mm x 3mm pads complete the design. The complete design is illustrated in Figure 5.4. As the minimal feature sizes are estimated but have not been measured at the time of first design, the interdigitated electrodes are designed with three (3) different interdigit distances: 50 µm, 45 µm and 40 µm, resulting in a total of 160, 177 and 200 electrode digits, respectively. The gap between electrodes is estimated to be 13.8 µm, 8.8 µm and 3.8 µm, respectively.

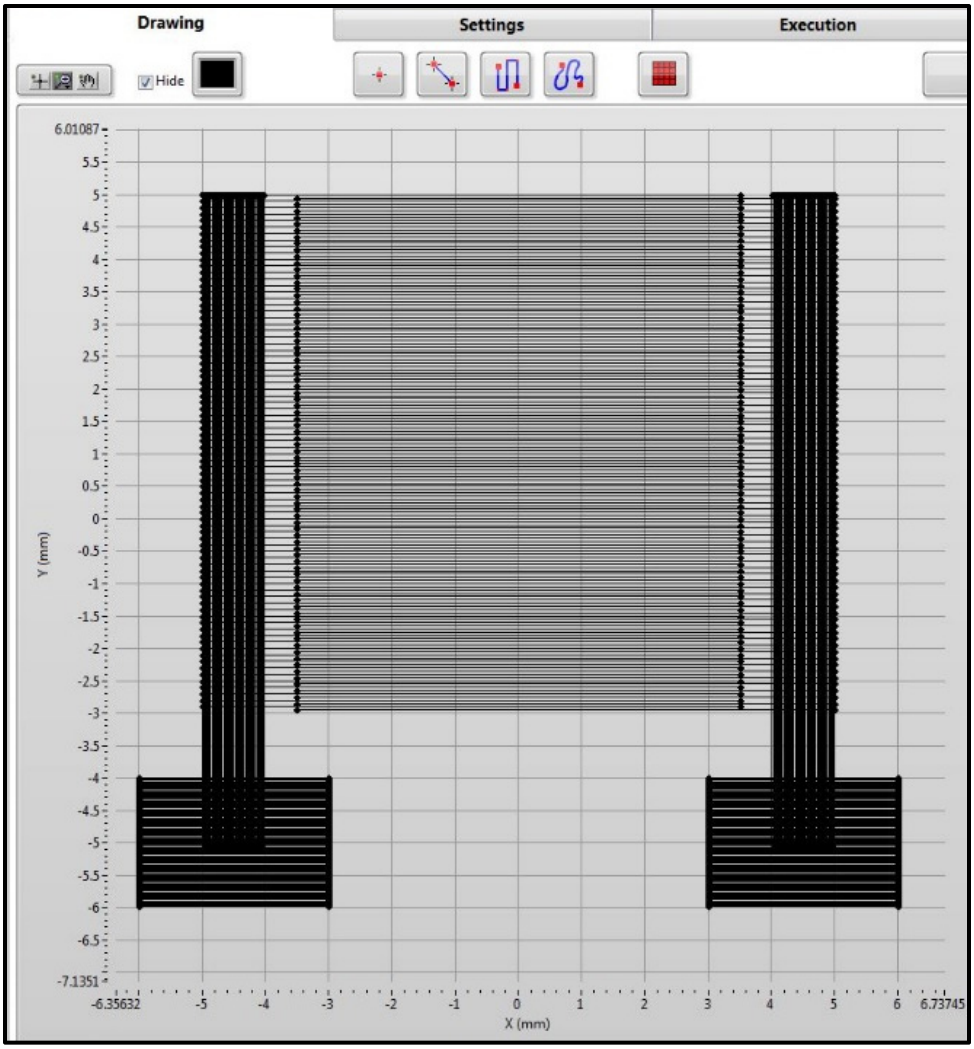

Figure 5.4 Design of the interdigitated electrodes in Ceraslice software

Fabrication and Characterization

The printing parameters found in section 4.3.1 of this work are used as a basis for printing the interdigitated electrodes and are adapted to provide improved control over feature sizes. The chuck temperature is increased to 60 °C, and drop interpenetration is slightly increased from 50 % to 55 % to compensate for printing in 1 dimension (single nozzle). Since printing is performed in vector mode, there is no printing lattice, however, when printing 2 dimensional objects such as the collection bars and the pads, the interpenetration between the print lines is

kept the same as the drop interpenetration effectively creating a square printing lattice. A single layer of ink is used for printing the electrode digits, whereas 2 layers are used for printing the collection bars and the pads to improve conductivity.

After printing, NIR optical annealing is performed at 60 % lamp power and 5 mm/s chuck displacement speed, followed by oven annealing at 180 °C for one (1) hour. PET based substrates are generally rated only for low temperature uses, up to 120 °C. However, it is found that if the substrate is anchored to a dummy glass slide, temperatures up to 180 °C can be used with minimal damage to the substrate. After oven annealing at 180 °C using this method, a small loss in substrate flexibility is noticed upon substrate manipulation and slight discoloration is observed.

The printed interdigitated electrodes are characterized both in terms of geometry and electronic properties. The electrode digits are characterized in terms of their width (W_{IE}), the gap between electrodes (G) and as a function of the designed distance between the electrode digit positions (D), depicted in Figure 5.5.

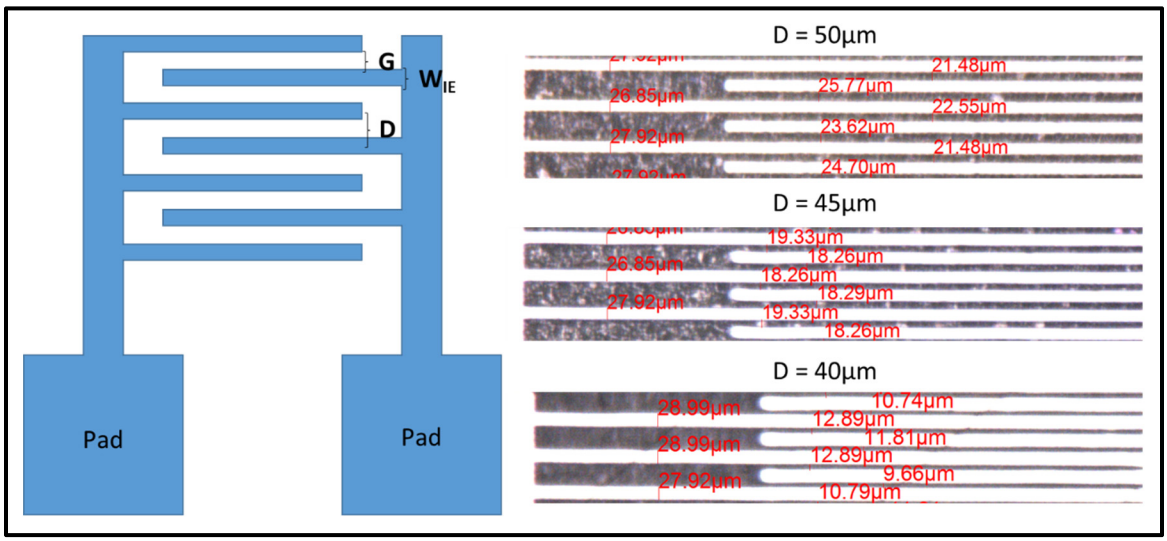

Figure 5.5 Schematic representation and photographs with measurements of the interdigitated electrode characteristic parameters

The widths of the electrode digits are measured to be 28 ± 1 µm, 27 ± 1 µm and 29 ± 1 µm for D = 50 µm, 45 µm and 40 µm, respectively. The widths of the electrode digits are smaller than the estimated minimal feature size (splat diameter). This is due to a known phenomenon in inkjet printing where the deposited ink in the printed line is essentially being pulled by subsequent printed drops, reducing its width when compared to a lone drop (Sette, 2014). The resulting gaps between the electrodes are measured to be 24 ± 2 µm, 19 ± 1 µm and 12 ± 1 µm for D = 50 µm, 45 µm and 40 µm, respectively. The thicknesses of the electrode digits are also characterized and are measured to be 420 ± 120 nm, showing more variation from digits within the same electrode than from electrodes with different D values. Z profile data, for the electrode digit thickness, acquired using 3D reconstruction at constant focal with an Eclipse L200N optical microscope (Nikon) are shown in Figure 5.6.

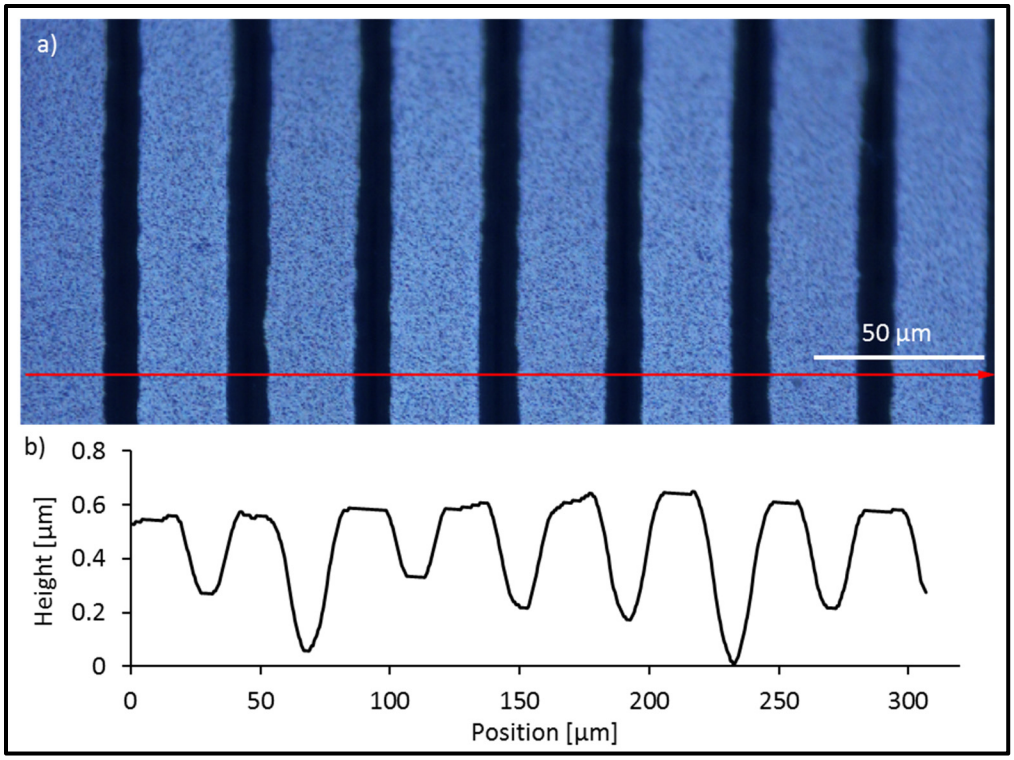

Figure 5.6 a) Microscope image of the interdigitated electrode digits with a red line representing the cross section used for presented height profile in b)

Upon visual inspection, very few electrical shorts can be detected between the electrode digits over the entire electrode area for D = 50 µm and D = 45 µm samples, for D = 40 µm samples shorting between the electrode digits are more numerous. Clear examples of electrical shortings between the electrode digits are circled in red in Figure 5.7. These shorts lead to large variations in the pad-to-pad resistance values which are measured to be $1.5 \pm 0.3 \times 10^9$ Ω, $4.4 \pm 0.7 \times 10^6$ Ω and 9.7 ± 5.4 Ω for D = 50, 45 and 40 µm respectively. The D = 40 µm electrodes are deemed not suitable for use as a basis for fabrication of sensors due to the high amount of electrical shorting between the interdigital electrodes and the resulting low pad-to-pad resistance. The overall geometric characteristics and pad-to-pad resistance of the printed interdigitated electrodes are summarized in Table 5.1.

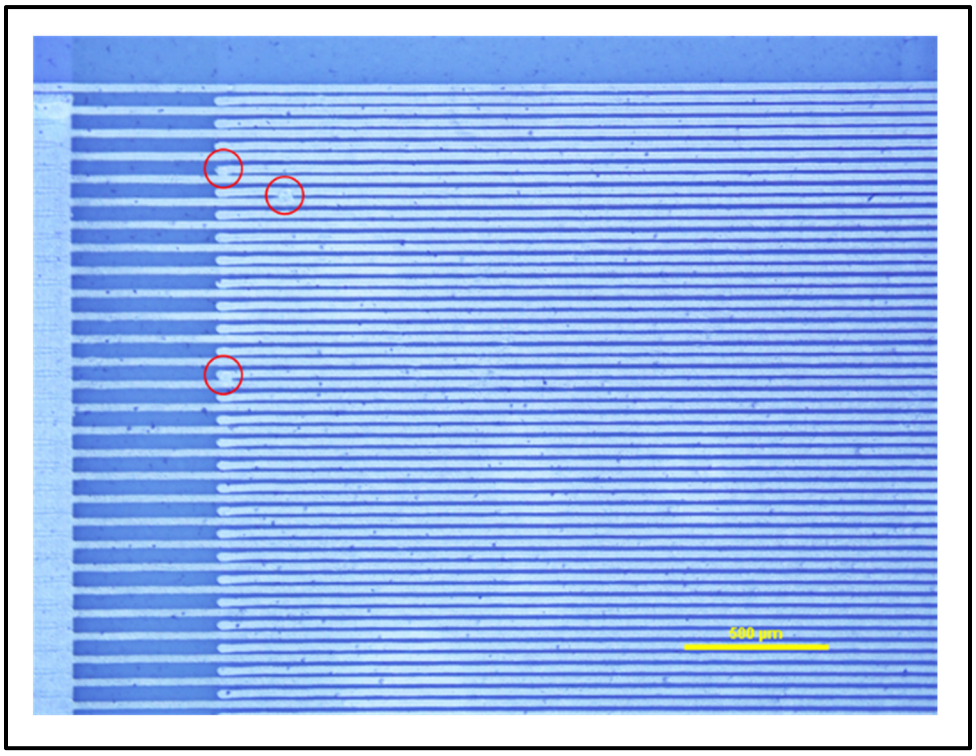

Figure 5.7 Microscope image of the interdigitated electrodes showing zones of electrical shorting between the electrode digits

Table 5.1 Overview of the characteristic parameters of the printed interdigitated electrodes

Interdigit Distance (D) [µm]	Electrode Width (W_{IE}) [µm]	Electrode Gap (G) [µm]	Resistance Between Pads [Ω]
50	28 ± 1	24 ± 2	$1.5 \pm 0.3 \times 10^9$
45	27 ± 1	19 ± 1	$4.4 \pm 0.7 \times 10^6$
40	29 ± 1	12 ± 1	9.7 ± 5.4

5.3 THz VPPs

VPPs can be considered optical lenses which create vortex beam shapes from incident light flux. Vortices have attractive properties, such as a helical wavefronts, topological beam shapes, and the ability to carry orbital angular momentum (He et al., 2013, p.20230-20239). Owing to these unique properties, vortex beams have been applied in many industrial and research fields for many applications, such as optical micro-manipulation (He, Friese, Heckenberg & Rubinsztein-Dunlop, 1995, p.826); (Simpson, Dholakia, Allen & Padgett, 1997, p.52-54), bio-medical applications (Steubing, Chen, Wright, Numajiri & Berns, 1991, p.505-510); (Finer, Simmons & Spudich, 1994, p.113); (Seeger et al., 1991, p.497-504), optical information transmission (Gibson et al., 2004, p.5448-5456); (Vaziri, Weihs & Zeilinger, 2002, p.240401); (Molina-Terriza, Torres & Torner, 2001, p.013601) and high resolution microscopy (Yu et al., 2011, p.1210713). In this section, ultrathin VPPs in the THz frequency range are fabricated based on complementary V-shaped antenna structures using inkjet printing of ANP DGP 40TE-20C Ag ink. Electronic and mechanical characterization of the VPP devices is also presented in this section, whereas THz characterization of the devices are performed by another group and are presented elsewhere (Zhuldybina et al., 2018, p.1); (Zhuldybina et al., 2019, p.444). As mentioned previously, the fabrication of the THz VPPs is used, in part, to evaluate minimal printable feature sizes while adding extra constraints when compared to the interdigitated electrodes.

Design

The THz VPPs are designed based on V-shaped antenna structures explored by the work of Jignwen He et al (He et al., 2013, p.20230-20239). Unit cell dimension and V-shaped antenna length have been adjusted with respect to the minimal feature size achievable with the inkjet printing equipment available. As shown in the previous section (5.2.2), feature width of ~ 30 μm can be achieved readily when printing ANP DGP 40TE-20C Ag ink on Novele^{TM} IJ-220 PET substrates. As such, the unit cell dimensions and the length of the V-shaped antennas have been increased three-fold when compared to those found in (He et al., 2013, p.20230-20239), resulting in 500 μm x 500 μm unit cells. The design of the THz VPP is shown in Figure 5.8 a) along with a printed device in Figure 5.8 b), illustrating how the 32 x 32 V-shaped antennas are arranged around the device in a spiral fashion. Each of the V-shaped antennas, including the positions of the three (3) vector points within the unit cells, are presented in Figure 5.8 c).

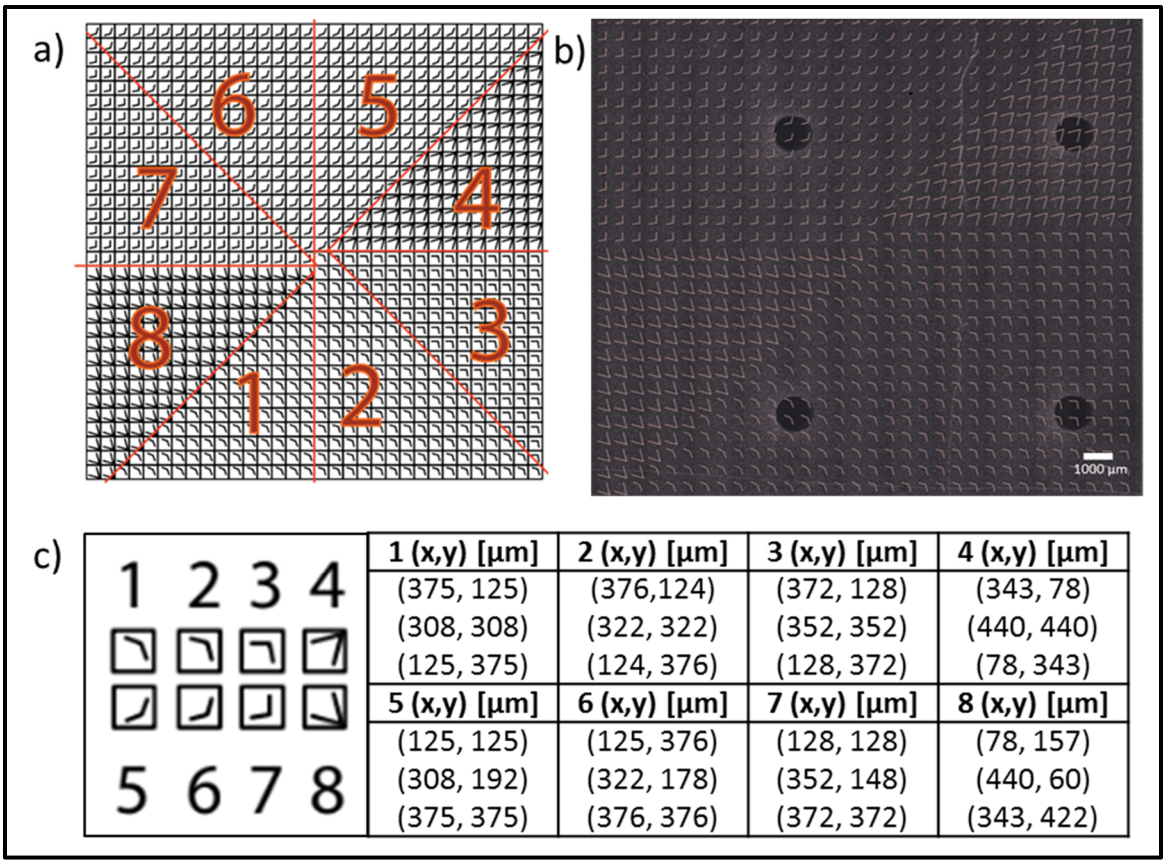

1 (x,y) [µm]	2 (x,y) [µm]	3 (x,y) [µm]	4 (x,y) [µm]
(375, 125)	(376,124)	(372, 128)	(343, 78)
(308, 308)	(322, 322)	(352, 352)	(440, 440)
(125, 375)	(124, 376)	(128, 372)	(78, 343)
5 (x,y) [µm]	**6 (x,y) [µm]**	**7 (x,y) [µm]**	**8 (x,y) [µm]**
(125, 125)	(125, 376)	(128, 128)	(78, 157)
(308, 192)	(322, 178)	(352, 148)	(440, 60)
(375, 375)	(376, 376)	(372, 372)	(343, 422)

Figure 5.8 a) 32 x 32 V-shape antenna THz VPP design, b) image of inkjet printed THz VPP and c) V-shape antenna design and coordinates within the 500 µm x 500 µm unit cells

Fabrication and Characterization

The VPP devices are printed on Novele™ IJ-220 PET substrates using the ANP DGP 40TE-20C Ag ink in vector mode printing. Like the interdigitated electrodes, minimizing the feature sizes and improved printing position control is desired. As such, the adapted printing parameters found in section 5.2.2 are used for printing the VPP devices. Namely, a drop interpenetration of 55 % (20 µm interpenetration, 36.2 µm splat diameter) and a chuck temperature of 60 °C are used while printing. The printing speed is found to play a major role in the quality of the printed V-shaped antennas. If the printing speed is too high, voids can

form in the corner of the V-shaped antennas as shown in Figure 5.9. These voids are detrimental to device operations and should be minimized by lowering the printing speed.

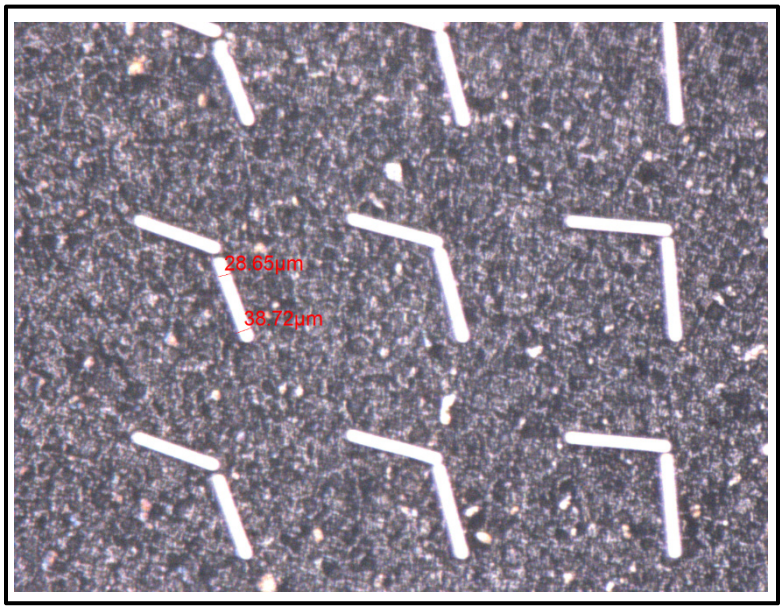

Figure 5.9 Inkjet printed V-shaped antennas showing gaps between the printed vertices

The V-shaped antennas are characterized in terms of line width and thickness. A slight increased line width is found for the V-shaped antennas when compared to the interdigitated electrodes. This effect can be attributed to the same phenomenon explained in the previous section (5.2.2) as the printed lines are not as elongated in this case. Line widths of 30 - 40 µm are measured, bulging is noticed around the ends of the V-shaped antennas and accounts for the upper line width limit, as seen in Figure 5.10 b). V-shaped antenna thicknesses of 300 ± 40 µm are measured, Z profile data, acquired using 3D reconstruction at constant focal with an Eclipse L200N optical microscope (Nikon) is shown in Figure 5.10 c) for the cross section shown in Figure 5.10 a).

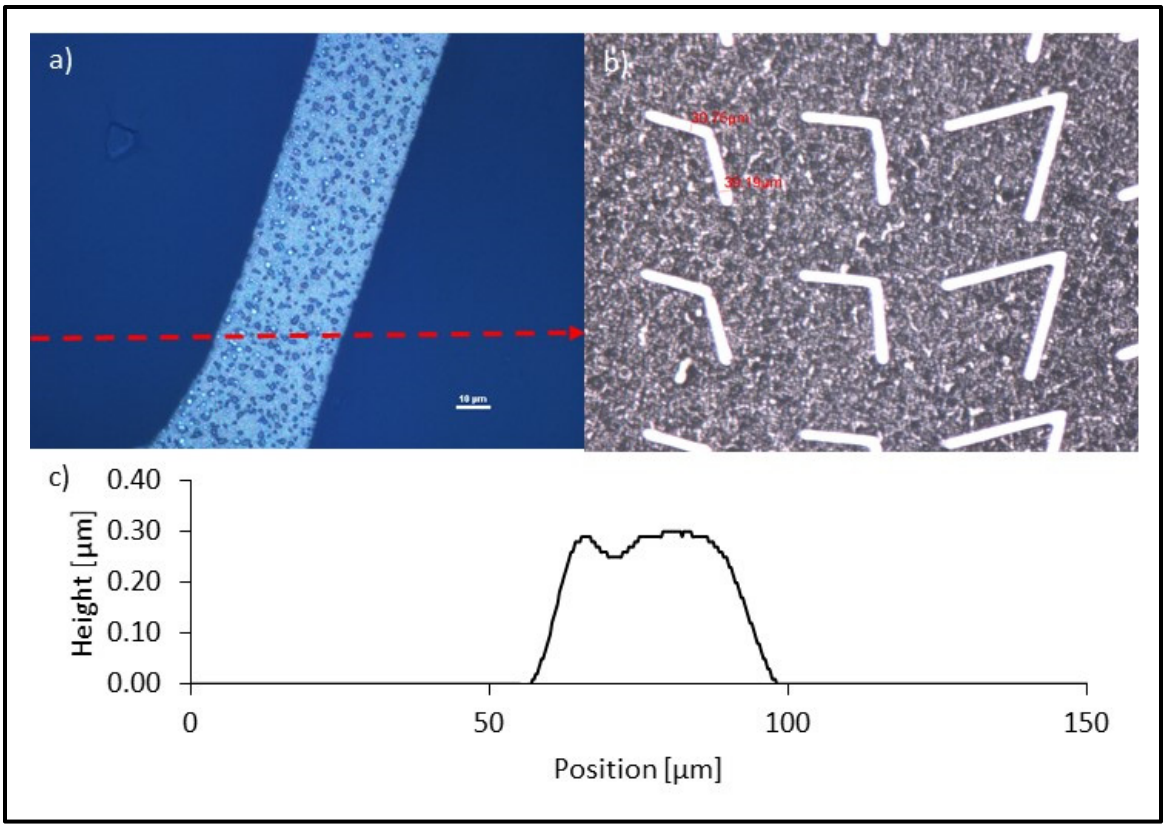

Figure 5.10 a) Microscope image of printed V-shaped antenna trace, the red line represents the cross section used for the height profile, b) image of the V-shaped antennas showing the width of the printed vertices, c) height profile

In this case, samples with different conductivity were required for THz characterization and operation purposes. The devices are optically annealed with varying NIR annealing parameters, while no oven annealing is performed. Devices are annealed at 100 % NIR lamp power with a chuck displacement speed varying from 30 mm/s to 5 mm/s, resulting four (4) point-probe conductivity measurements are presented in Table 5.2.

Table 5.2 Conductivity results of THz VPPs V-shaped antenna optical NIR sintering

NIR Sintering Chuck Displacement Speed	**Resulting THz VPPs V-shaped Antenna Conductivity**
Not annealed	$1.1 \pm 0.1 \times 10^6$ S/m
30 mm/s	$1.3 \pm 0.1 \times 10^6$ S/m
20 mm/s	$1.4 \pm 0.2 \times 10^6$ S/m
15 mm/s	$2.6 \pm 0.3 \times 10^6$ S/m
5 mm/s	$2.8 \pm 0.3 \times 10^6$ S/m

5.4 Conclusion

In this chapter passive devices and generic multilayered devices are fabricated based on the optimized printing processes established in Chapter 4. A multilayered TFT structure is fabricated using PEDOT:PSS, SU-8 and Ag ink materials to gain a better understanding of the challenges tied to printing multiple ink materials in layered stacks. It was found that ink materials with orthogonal solvents tend to not affect the underlying ink layer as they cannot dissolve the material, especially when the underlying ink layer has been post-treated. An underlying ink layer can introduce challenges for subsequent ink printing if it does not offer a flat surface for printing or if it possesses surface energies, which differ greatly from the original substrate. We find that printing subsequent ink layers of the same material on an underlying layer with gaps in the coverage will tend to fill these gaps. For underlying ink layers, which possess surface energies greatly different than the original substrate, plasma treatments may be used after post-printing treatments to adjust surface energies.

Three (3) passive structures are also fabricated using inkjet printing processes; interdigitated Ag electrodes, isolated routing Ag electrodes and Ag THz VPPs. These structures are printed to form the basis for active device fabrication, to ease connections for device prototyping and/or to help establish minimal feature sizes achievable with the ANP DGP 40TE-20C Ag ink.

The interdigitated Ag electrodes are fabricated using ANP DGP 40TE-20C on Novele^{TM} IJ-220 PET substrate with a proprietary coating adapted for inkjet printing. These electrodes form the basis for the fabrication of bolometers detailed in Chapter 6. Vector mode printing is used to achieve constant minimal interdigital finger widths of ~27 μm with interdigital gaps as low as 18 μm and minimal electrical shorting. While smaller interdigital gaps can be achieved, electrical shorting between interdigital fingers in increased exponentially.

Isolated routing electrodes are fabricated on FT Kapton-FPC 300 substrates using ANP DGP 40TE-20C Ag ink for the conductive traces and MicroChem's SU-8 ink for electrically isolation. These electrodes are used later in Chapter 6 as electrical connections for ease of characterization and operation of printed device arrays. The isolated routing electrodes are designed to accommodate ten (10) TF vertical architecture devices or 5 devices with horizontal architectures.

Finally, THz VPPs are fabricated using ANP DGP 40TE-20C on Novele^{TM} IJ-220 PET substrate. These VPPs consists of hundreds of v-shaped antennas with different v-angles. Feature size, printing accuracy and homogeneity are of the upmost importance while printing these VPPs as they affect their inner workings. Vector mode printing is used to achieve minimal v-shaped antenna feature sizes of 30 μm, while line budging is observed at the ends of the v-shaped antennas. The printing speed is found to be a key parameter for printing continuous v-shaped antennas.

CHAPITRE 6

METHYLAMMONIUM TRIHALIDE OPTOELECTRONIC DEVICE PRINTING

In this chapter, the optimized jetting and printing parameters found in Chapter 4 are utilized and further adapted for printing multiple layers of different ink materials for the fabrication of TF optoelectronic devices architectures based on MALH PS active layers. The knowledge presented in previous chapters is used in this section. The same layer-by-layer process flow for printing multilayered structures is used for printing the TF optoelectronic devices. Multiple device architectures are tested for their fabrication feasibility using inkjet printing as a primary fabrication method. First, devices are printed on rigid substrates, and later the fabrication process is transferred to flexible substrates. The proposed architectures are based on those found in the literature and explored in Chapter 3. Two (2) device architectures are printed and tested. First, devices consisting of a TiO_2 ETL, a PS active layer and a Spiro-OMeTAD HTL are printed. Second, devices with a PS active layer and a Spiro-OMeTAD HTL but void of an ETL are printed. The device architectures with the best performances are then used to print device arrays, which are attached to printed electrodes for ease of readout and characterization.

Inkjet printing using the Ceradrop F-Series printer is used as a primary pathway for device fabrication. However, a few conventional fabrication methods are still employed for the fabrication of the devices where inkjet printing could not be used for various reasons. The TiO_2 ETLs could not be inkjet printed as no solutions could be found commercially or otherwise that could be stably jetted. Therefore, spin- or dip-coating methods are used for TiO_2 deposition for the device structures which utilize an ETL. Moreover, device electrodes are not printed, the top transparent electrodes made from ITO are purchased already deposited on the rigid glass or flexible PET substrates. The bottom Au electrodes are deposited, as the final device fabrication step, using conventional evaporation methods. This method is chosen since typical gold inks require high annealing temperatures, which could be detrimental to the device operations and performances through PS degradation (Divitini et al., 2016, p.15012); (Conings et al., 2015, p.1500477).

The device architecture design, including simplified band diagrams are presented along with the complete fabrication methodology for each device architecture. Device performance characterization and PS active layer characterization are also presented in this chapter, along with statistical analysis of device performances for the printed device arrays. PS active layer crystallization characterization is performed using a PW3040 X-ray diffractometer (PANalytical), with measured X-ray diffraction spectrum from 10 ° to 50 °. A 91160-1000 solar simulator (Oriel Instruments) with a 1000 W Xenon lamp is used as 1 sun illumination source along with a Keithley 2400 power supply for current-voltage (I-V) characterization in the dark and under 1 sun illumination. Visible spectrum light responsivity measurements of the PS based devices are taken using a setup comprising of a 63368 200W Quartz Tungsten Halogen lamp (Newport) linked to a M300 monochromator (Bentam) with a T312R0U5 grating to select incident wavelength. A PDA-750 photodiode amplifier (Terahertz Technologies Inc.) is used for photocurrent measurements and a PDA36A switchable gain, amplified silicon detector (Thorlabs Inc.) is used for light output calibration. Transient current behavior of the devices is measured with varying laser light excitation power to show working photodetector behavior. To measure this behavior and device responsivity for different incident light intensities, the devices are connected to a load in series. A DSO-X 3034A oscilloscope (Agilent) is used to measure the voltage across the load and a Torus 532 nm laser (Laser Quantum) is used along with a fan chopper as the illumination source. NEP values are calculated using transient current behavior, where the frequency bandwidth is estimated from device rise times. Responsivity values are given as the average responsivity of the devices over the range of 400 nm - 780 nm.

6.1 Printing Rigid Device on Glass

6.1.1 Design

The design of the architecture of the MALH PS based device is taken from known working device architectures explored in section 3.2. The TF architecture consists of an ITO transparent top electrode, crystalline rutile TiO_2 hole BL and ETLs, a $MAPbI_{3-x}Cl_x$ PS active layer, a Spiro-

OMeTAD HTL and an Au bottom electrode. The band gaps, the conduction band and valence band energy levels for the different material components are estimated from the literature. The band gap of crystalline rutile TiO_2 is estimated to be 3.03 eV with a conduction band energy level of -4.8 eV and a valence band of -7.83 eV (Scalon et al., 2013, p.798). For the Spiro-OMeTAD HTL, a band gap of 3 eV is estimated while lumo and homo energy levels are estimated to be -2.25 eV and -5.25 eV, respectively (Krishna et al., 2014, p.2702-2709). The $MAPbI_{3-x}Cl_x$ band gap is estimated to be 1.5 eV, while conduction and valence band energy levels are estimated to be -3.9 eV and -5.4 eV, respectively (Butler, Frost & Walsh, 2015, p.228-231). Work functions for the ITO and Au electrodes are estimated as -5.24 eV (Schlaf et al., 2001, p.149-154) and -5.1 eV, respectively (Michaelson, 1977, p.4729-4733). A simplified band diagram of the architecture is presented in Figure 6.1, along with a schematic of the device architecture with the expected layer thicknesses. The band alignments of the Spiro-OMeTAD and of the crystalline TiO_2 are such that they inhibit electron and hole migration from the PS active layer to the Au and ITO electrodes, respectively, while promoting migration of opposing charge carriers. Some of the results from these devices have been previously published (Trudeau, Bolduc, Beaupré, Benavides-Guerrero, Tremblay, Cloutier, 2018, p.1837-1842)

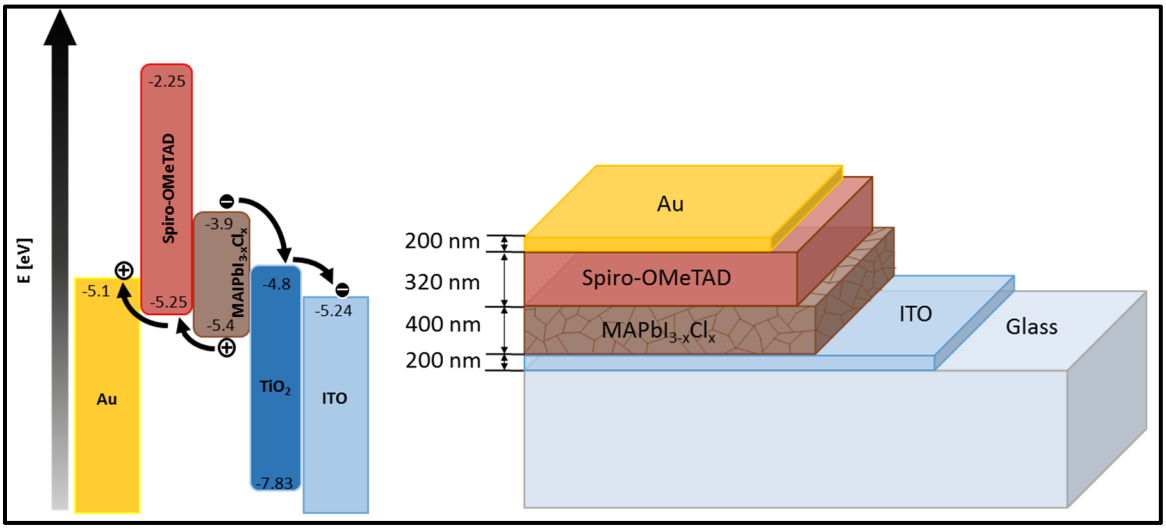

Figure 6.1 Schematic representation of the simplified band diagram and of the designed rigid TF $MAPbI_{3-x}Cl_x$ optoelectronic device architecture

6.1.2 Fabrication

The MALH PS-based optoelectronic devices are fabricated onto ITO-covered glass with a TiO_2 porous ETL and a compact TiO_2 BL of 1.8 μm and 200 nm thickness, respectively. The fabrication and deposition of the TiO_2 layers are performed by another group and are presented elsewhere (Xu, Benavides, Ma & Cloutier, 2012, p.1-6). A schematic representation of the printing process, including pre- and post-printing treatments is depicted in Figure 6.2.

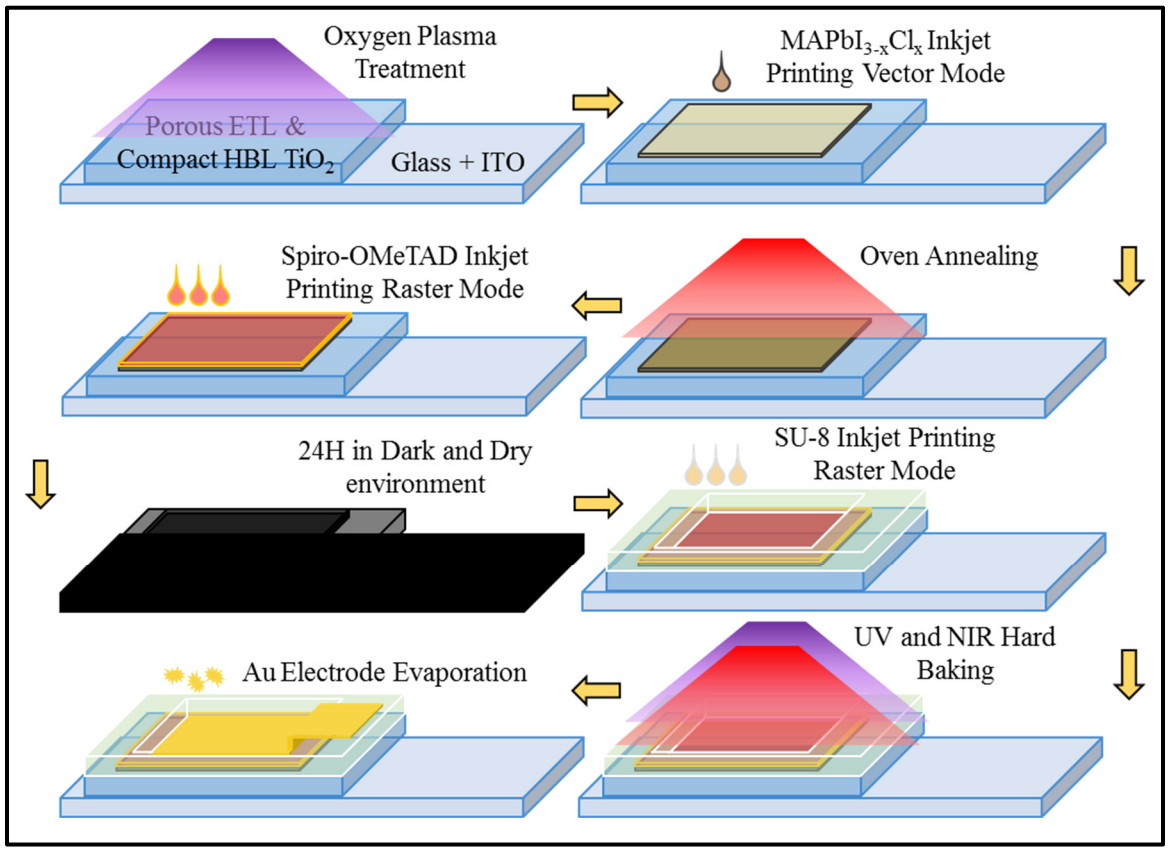

Figure 6.2 Schematic representation of the fabrication process for the proposed $MAPbI_{3-x}Cl_x$ optoelectronic devices on rigid glass substrates

First, the substrates with the ETL and BL are treated with a hydrophilic oxygen plasma using a PlasmaTherm Unaxis 790 Plasma Etch system operated at 30 W for 5 minutes. Prior to

printing, the Ossila I101 PS solution is heated to 70 °C for 120 minutes and allowed to cool down to room temperature for complete redissolution of the solutes. The PS solution is then printed in a square 5 mm x 5 mm pattern onto the substrate, using vector-mode printing (single nozzle) with adapted printing parameters for printing on TiO_2 ETL and BL. The PS jetting parameters are kept the same as those presented in section 4.3.5. Whereas, the printing parameters are slightly adjusted, decreasing the drop interpenetration to 46.2% and increasing the chuck temperature to 50 °C, this provides a more uniform printed PS layer although layer uniformity comparable to printing on ITO could not be achieved while printing on the compact TiO_2 surface. The PS layer is then oven annealed at 90 °C for 120 minutes to allow for complete crystallization. The Spiro-OMeTAD solution is prepared following the established recipe found in section 4.2.1. This solution is then printed in a square 5 mm x 5 mm pattern on top of the PS layer using raster-mode printing with the optimized printing parameters presented in section 4.3.4, resulting in a layer thickness of 300 - 400 nm. The Spiro-OMeTAD layer is left to oxidize overnight in a dark dry-box to increase charge carrier mobility as specified in section 4.3.4 (Gouda et al., 2015, p.4640-4645). Two layers of SU-8 encapsulation are then printed in a rectangular 7 mm x 10 mm with a square 4 mm x 4 mm gap centered on the PS/Spiro-OMeTAD layers using raster-mode printing and followed by vector-mode printing to fill any non-covered areas around the PS/Spiro-OMeTAD layers. SU-8 encapsulation is necessary to avoid electrical shorting from the Au electrode. The optimized printing parameters used for printing the SU-8 ink are found in section 4.3.2. The SU-8 layer is hard baked following the specifications found in section 4.3.2. A 200 nm-thick Au electrode is evaporated on top of the exposed Spiro-OMeTAD layer and Ag epoxy is used to bond two electrical leads, one to the Au electrode and the other to the exposed ITO electrode. While the Ag epoxy sets, a glass slide is pressed on top to complete the rudimentary encapsulation. A fabricated device is shown in Figure 6.3.

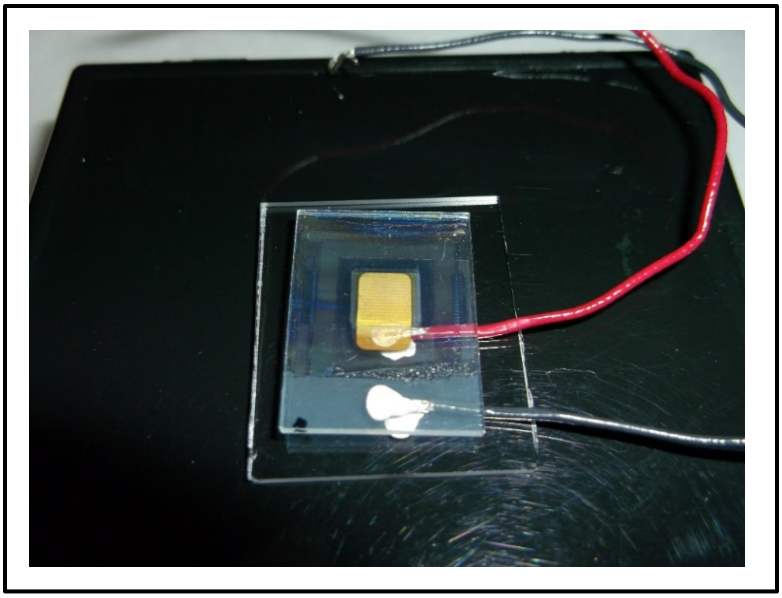

Figure 6.3 Photograph of a rigid inkjet printed $MAPbI_{3-x}Cl_x$ PS based optoelectronic device

6.1.1 Device Characterization

Cross sectional SEM micrographs are taken to characterize the device stack, an example of which is depicted in Figure 6.4. From the cross-sectional SEM image, the compact and porous TiO_2 layers can be clearly identified along with the ITO coating on the glass substrate, these layers are measured to be ~183 nm, ~1.95 μm and ~183 nm respectively. The PS deposition is observed to be not as homogeneous as when deposition is performed on ITO surfaces (section 4.3.5). In this case, the PS crystals show increased heights variation and the Spiro-OMeTAD solution is seen to have infiltrated the gaps in the PS layer to form a combine layer of ~890 nm. This creates the hybrid TF-NS architecture discussed in section 4.3.5 and provides a flat surface for the Au electrode deposition. A photograph of the PS layer surface showing the decreased surface coverage of the PS crystals when compared to printing directly on ITO surfaces is shown in Figure 6.5.

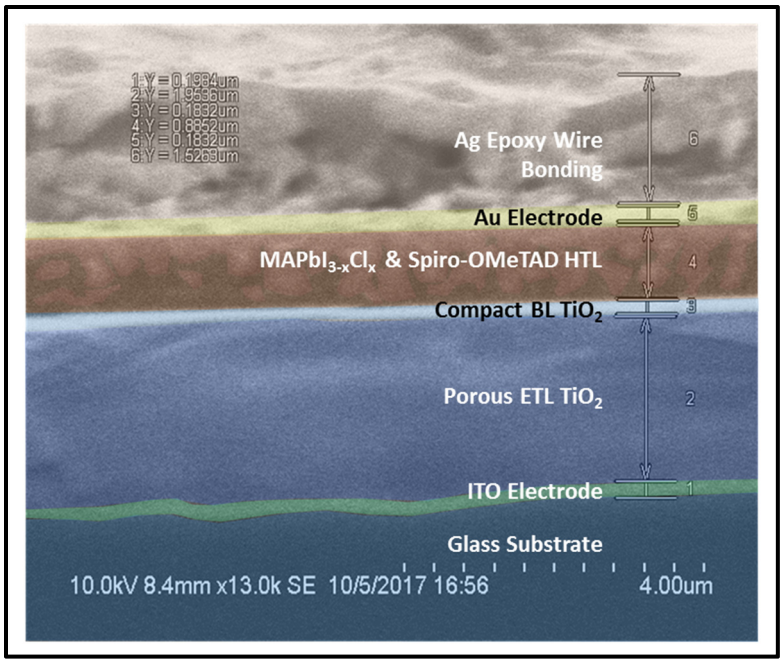

Figure 6.4 Color enhanced SEM micrograph of inkjet printed $MAPbI_{3-x}Cl_x$ PS based optoelectronic device cross section

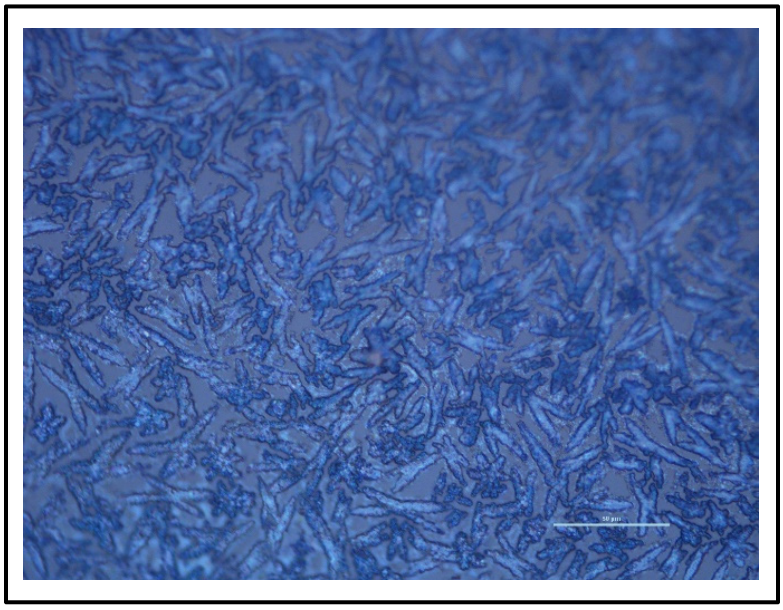

Figure 6.5 Microscope image of the surface of the inkjet printed $MAPbI_{3-x}Cl_x$ layer on TiO_2 compact layer

A 2-thetha XRD spectrum is taken of the printed PS layer after annealing but before the Spiro-OMeTAD is printed. The 2-thetha XRD spectrum shown in Figure 6.6, demonstrates near complete crystallization of the $MAPbI_{3-x}Cl_x$ PS to the tetragonal crystal phase with only traces of PbI_2 present after annealing (Luo & Daoud, 2016, p.123). ITO XRD peaks are present in the 2-thetha XRD spectrum and are identified as such in red. Although presence of PbI_2 is known to be detrimental for device operations, complete crystallization with no trace of PbI_2 is rarely achieved in the literature but still provides adequate device performances for energy harvesting and photo-detection purposes (Luo & Daoud, 2016, p.123); (Liang et al., 2014, p.3748-3754); (Zhang et al., 2015, p.6142).

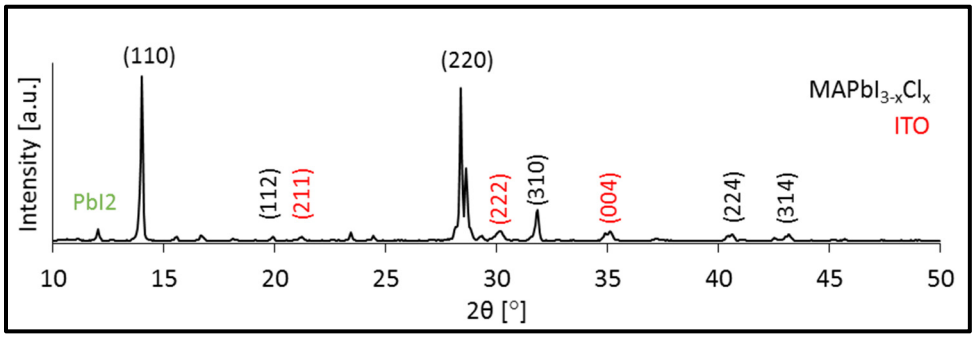

Figure 6.6 2-thetha XRD spectrum of printed MAPbI3-xClx PS layer after oven annealing

The I-V characteristics of the printed devices under 1 sun AM 1.5 illumination and under dark conditions are shown in Figure 6.7. These curves show working PV behavior with open circuit voltages of 0.50 V and 0.35 V, short circuit currents of 1.5 $\mu A/cm^2$ and 1.6 $\mu A/cm^2$, for forward and reverse scanning modes, respectively. FFs of 30 % and 61 % for forward and reverse scanning modes are calculated from the maximum power points, respectively. From these results, an average PCE of 0.0017 % is calculated. As such, it is evident that the devices are inadequate for energy harvesting, nonetheless the device performances show that these devices can be used for photo-sensing applications.

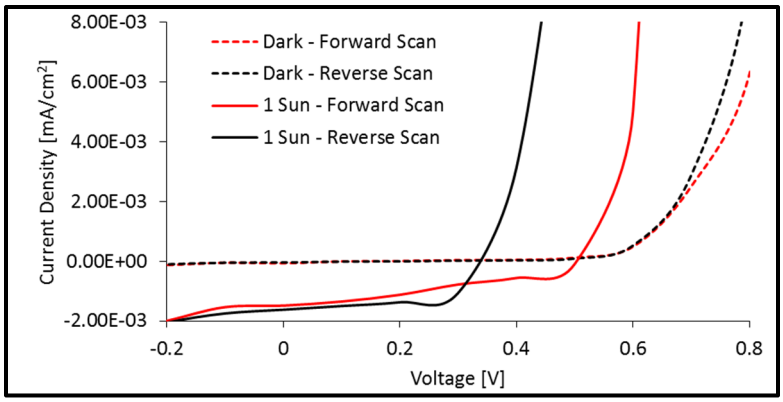

Figure 6.7 I-V characteristics of the rigid inkjet printed $MAPbI_{3-x}Cl_x$ PS based optoelectronic device under standard 1 sun AM 1.5 illumination and under dark conditions

To characterize device dark current, photocurrent and response time, the 1 sun AM 1.5 illumination is chopped at 0.1 Hz using a fan chopper and transient current behavior is recorded. The transient current behavior of the device is shown in Figure 6.8. Device dark current and photocurrent at 1 sun AM 1.5 illumination of -43.8 ± 1.8 nA/cm^2 and -1.3 ± 0.1 μA/cm^2 are measured, showing a gain of 2 order of magnitude. Symmetrical on/off and off/on behavior is observed from the devices and a response time of 253 ± 147 ms is measured. Stable behavior showing no drift in device response after multiple on/off switching is observed.

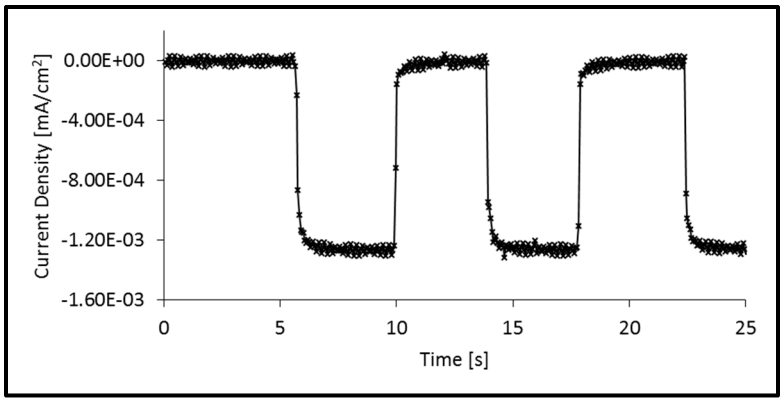

Figure 6.8 Transient current behavior of the rigid inkjet printed $MAPbI_{3-x}Cl_x$ PS based optoelectronic device under standard 1 sun AM 1.5 illumination chopped at 0.1 Hz

The spectral responsivity of the device is characterized and is presented in Figure 6.9. The device responsivity is dominated by a peak of 43.8 mA/W at ~330 nm wavelength which is associated to the charge generation effects at the TiO2/Spiro-OMeTAD junction where gaps in PS coverage are located (Bai, Shen & Tian, 2017, p.10543-10548). From 400 nm to 780 nm, the responsivity stabilizes to an average value of 0.519 mA/W, followed by a sharp drop in responsivity after 780 nm. The signal obtained from 400 nm to 800 nm indicates that the PS layer is working consistently with stable responsivity over most of the visible spectrum.

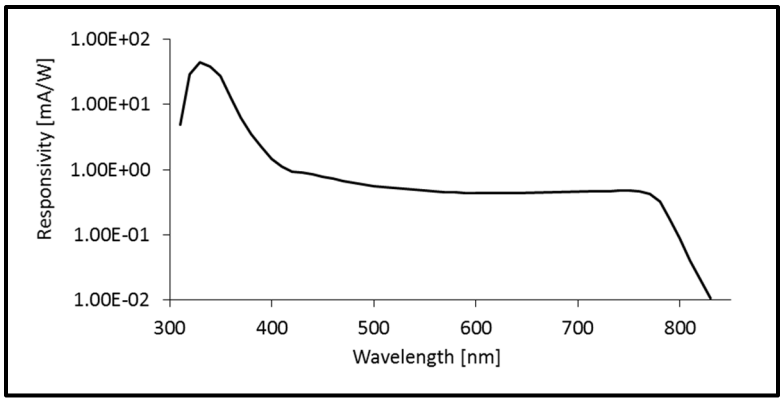

Figure 6.9 Spectral responsivity of rigid inkjet printed $MAPbI_{3-x}Cl_x$ PS based optoelectronic device

The I-V device characteristics for both forward and reverse scan directions under 1 sun AM 1.5 illumination and under dark conditions are summarized in Table 6.1 along with photodetector device performances including calculated NEP values.

Table 6.1 Overview of rigid inkjet printed $MAPbI_{3-x}Cl_x$ PS based optoelectronic device performances

Device: TiO2/$MAPbI_{3-x}Cl_x$/Spiro-OMeTAD on ITO/Glass				
Scan Direction	**V_{OC} [V]**	**I_{SC} [mA/cm_2]**	**FF [%]**	**η [%]**
Forward	0.5	-1.5×10^{-3}	30	0.0014
Reverse	0.34	-1.6×10^{-3}	61	0.0021
Photocurrent [mA/cm^2]	**Dark Current [nA/cm^2]**	**Response Time [ms]**	**Average Responsivity [mA/W] (400-800nm)**	**NEP [$W/Hz^{0.5}$]**
$-1.3 \pm 0.1 \times 10^{-3}$	-43.8 ± 1.8	253 ± 147	0.519	3.3×10^{-5}

6.2 Printing Flexible Device on PET

Transferring the fabrication process of the MALH PS based optoelectronic devices from rigid glass substrates to flexible PET substrates imposes new challenges. PET substrates cannot be processed at temperatures much greater than 120 °C without structural damage to the substrate (Demirel, Yaras & Elcicek, 2016, p.26-35), although minimal damage is observed for heat stabilized PET substrates processed with temperatures up to 180 °C as seen in sections 4.3.1 and 5.2.2. The lower processing temperature range compatible with PET substrates, when compared to glass substrates, limits the use of some materials which require high temperature annealing or other post-printing process. One such material, used in the design and fabrication of the PS based optoelectronic devices presented in section 6.1 is TiO_2. This material requires high annealing temperatures, well above 180 °C, to achieve anatase or rutile crystalline phases which are beneficial to device operations (Mathews, Morales, Cortes-Jacome & Antonio, 2009, p.1499-1508); (Radecka, Zakrzewska, Czternastek, Stapinski & Debrus, 1993, p.227-234). Moreover, flexible substrates also pose additional challenges in terms of keeping structural stability when the devices are bent or rolled for storage or during manipulation. Using TF architectures helps to overcome this challenge as TFs are generally much more flexible than bulk structures. Delamination may still occur especially when employing increasing numbers of TF layers. (Yu & Hutchinson, 2002, p.39-55); (Dauskardt, Lane, Ma & Krishna, 1998, p.141-62); (Ha et al., 2006, p.6405-6408).

Two different device architectures are tested, and preliminary characterization is performed to evaluate best working architectures. First, a device following the same architecture as the devices fabricated on rigid glass substrates while replacing crystalline TiO_2 ETL and BL with a single amorphous TiO_2 ETL, is tested, this architecture is referred to as a “full architecture”. Secondly, a simplified device architecture void of ETL is tested. This simplified device architecture is used to move towards complete inkjet printing processes for the fabrication of MALH PS based devices. Once the best architecture for device fabrication and operation is found, further characterization is performed, and this architecture is implemented for the fabrication of pixel arrays.

6.2.1 Full Architecture

Design

The design for the full architecture flexible devices follows the previous design of the full architecture fabricated on rigid glass substrates and includes a TiO_2 ETL. However, crystalline TiO_2 cannot be achieved through conventional annealing means on flexible PET substrates due to the substrate low temperature process compatibility. Thin amorphous TiO_2 layers (50 nm – 100 nm) have been shown to be adequate for replacing crystalline TiO_2 to form an ETL with minimal loss to device performances (Wang et al., 2013, p.724-730); (Qiu et al., 2017, p.511-520); (Wang et al., 2015, p.9108-9115). The change from crystalline to amorphous TiO_2 is expected to affect the workings of the devices as energy levels of amorphous TiO_2 are shifted when compared to crystalline TiO_2. The band gap of amorphous TiO_2 is estimated to be 3.4 eV with a conduction band energy level of -5.2 eV and a valence band of -8.6 eV (Prasai et al., 2012, p.7515-7521). A simplified band diagram of the designed full architecture device using amorphous TiO_2 as the ETL is shown in Figure 6.10 along with a schematic representation of the device stack with the estimated expected layer thicknesses.

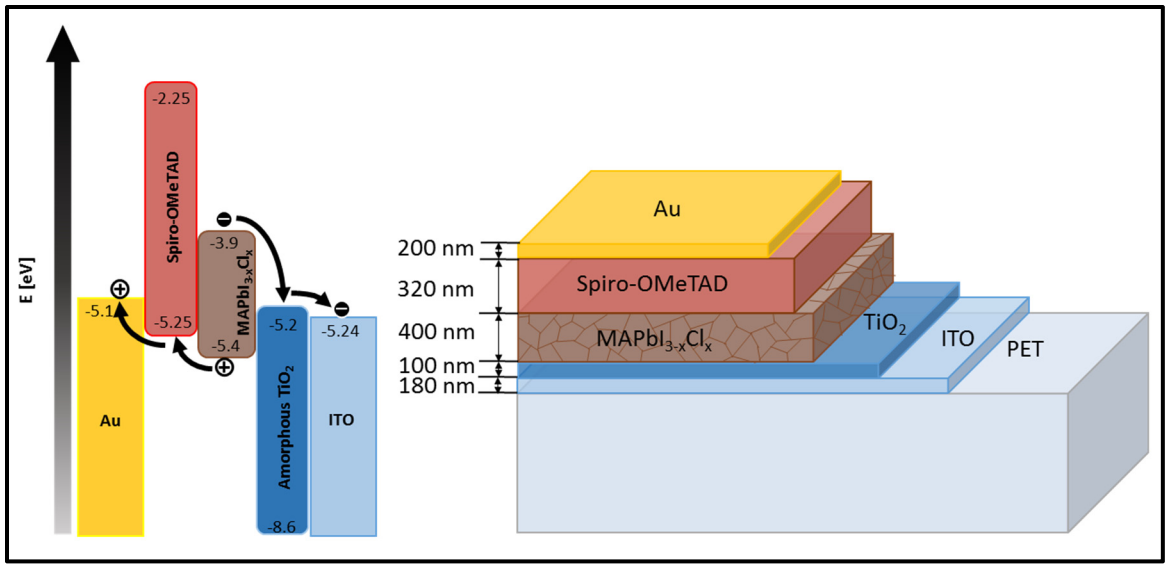

Figure 6.10 Schematic representation of the simplified band diagram and of the flexible designed TF $MAPbI_{3-x}Cl_x$ optoelectronic device using the full architecture

The energy levels of the amorphous TiO_2 still align well with the energy levels of the $MAPbI_{3-x}Cl_x$ PS active layer and the ITO electrode. As such, it is expected to act as both an ETL and hole BL. From the value of its conduction band energy between that of the PS and the ITO, and from its valence band which is much lower than that of the PS. The proximity of the amorphous TiO_2 conduction band to the work function of the plasma treated ITO is expected to decrease charge extraction efficiency and be slightly detrimental to device operations under null bias. For the remaining layers, the design of the device is not changed.

Fabrication

The flexible MALH PS-based optoelectronic devices are fabricated on ITO-covered PET. The amorphous TiO_2 compact ETL is deposited through spin coating after substrate cleaning and hydrophilic oxygen plasma is performed. To fabricate the amorphous TiO_2 ETL, a sol-gel TiO_2 solution prepared by another group and presented elsewhere (Xu et al., 2012, p.1-6) is first diluted 1:1 vol. in EtOH. 150 µl of the diluted solution is deposited and spread on the substrates using a micropipette, the solution is then spin coated for 120 seconds using a spin velocity of

6000 rpm with an acceleration of 500 rpm/s, resulting in an amorphous TiO_2 layer thickness of 100 nm. TiO_2 layer thickness are measured using cross sectional SEM imaging are shown in Figure 6.11 b), along with the resulting thicknesses of the spin coated amorphous TiO_2 layers using various spin coating parameters in Figure 6.11 a).

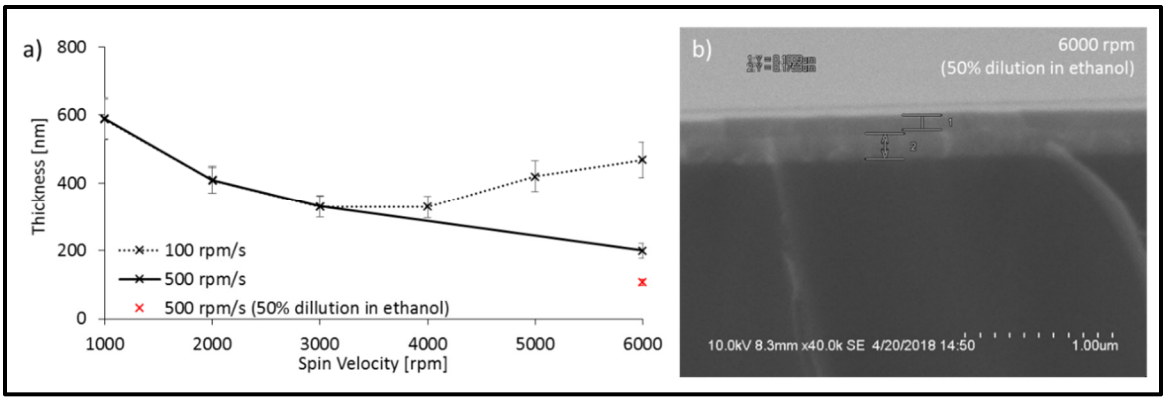

Figure 6.11 a) Thickness measurements of spin-coated amorphous TiO_2 ETL and b) SEM micrograph of the spin-coated amorphous TiO_2 cross section

The amorphous TiO_2 layer is annealed on a hot plate at 90 °C for one (1) hour to allow for solvents to completely evaporate. The second oxygen plasma treatment is performed on the amorphous TiO_2 surface, again in order to improve the wettability of the substrate and to enable the formation of thin and homogeneous printed PS layer. The PS layer is printed using the same printing process described in Section 6.1.2 for printing on TiO_2. The PS layer is then subjected to an NIR preliminary annealing step using the in-situ NIR lamp operated at 5 % lamp power and a chuck displacement speed of 20 mm/s followed by oven annealing at 90 °C for 120 minutes. The Spiro-OMeTAD solution is printed and post-treated following the same processes described in Section 6.1.2. Finally, the 200 nm-thick Au electrode is evaporated on top of the exposed Spiro-OMeTAD layer and on an exposed ITO area. Bonding electrical leads using Ag epoxy is found to not be compatible with flexible substrates as delamination of the leads and epoxy occurs readily when the flexible device is manipulated. As such, pogo pins are used when connecting the devices for characterization and/or operations. A schematic

representation of the complete fabrication process of these devices, including pre- and post-printing treatments is depicted in Figure 6.12.

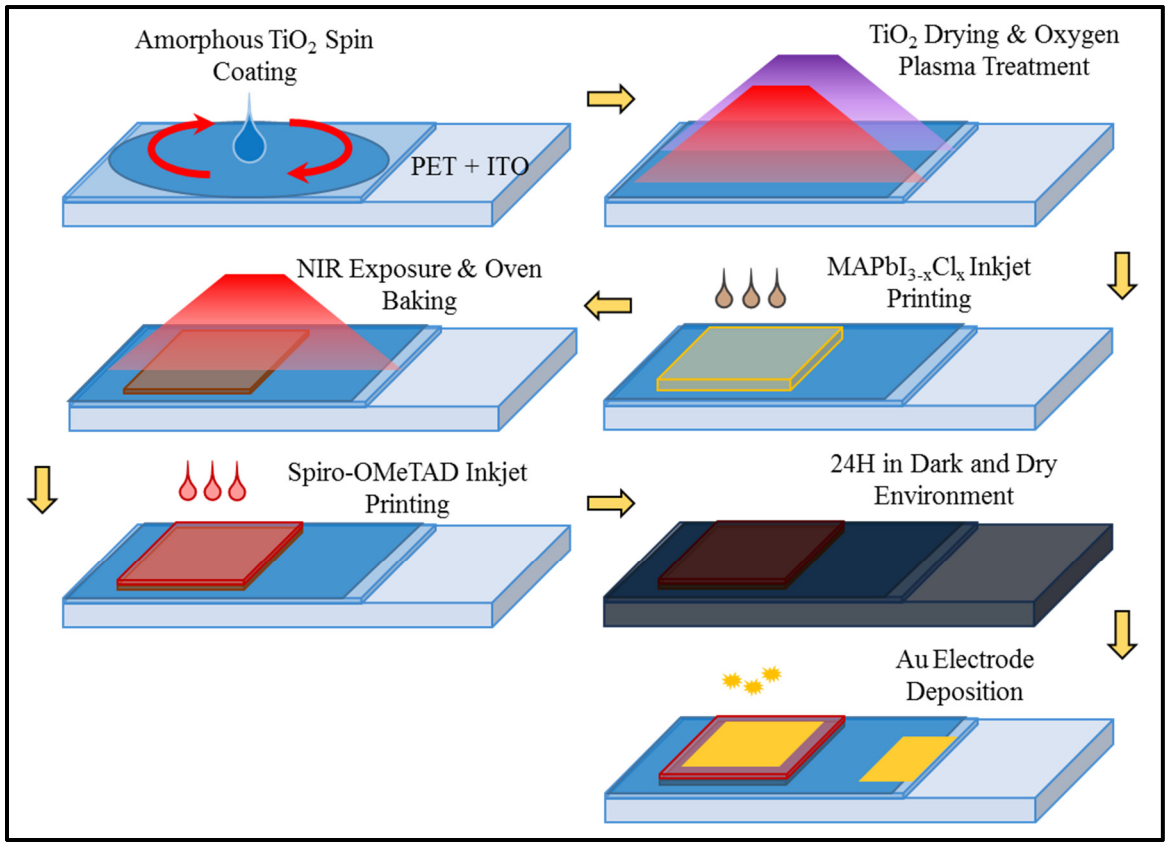

Figure 6.12 Schematic representation of the fabrication process for the proposed full architecture $MAPbI_{3-x}Cl_x$ optoelectronic devices on flexible PET substrate

Device Characterization

The I-V characteristics of the printed devices under 1 sun AM 1.5 illumination and under dark conditions are shown in Figure 6.13. These curves show working PV behavior with open circuit voltages of 0.87 V and 0.85 V, and short circuit currents of -5.1 $\mu A/cm^2$ and -3.68 $\mu A/cm^2$, for forward and reverse scanning modes respectively. An increase in both V_{oc} and I_{sc} is found when compared to the values of the devices printed on rigid glass substrates. FFs of

24 % and 26 % for forward and reverse scanning modes are calculated from the maximum power points, respectively. From these results an average PCE of 0.0037 % is calculated. The typical rectifying behavior is replaced by a linear behavior typical of high series-resistance devices. We speculate that this result stems from the amorphous nature of the TiO_2 which has lower charge carrier mobility and is more resistive than crystalline TiO_2 (Tang et al, 1994, p.2042-2047); (Shih et al., 2011, p.H609-H611).

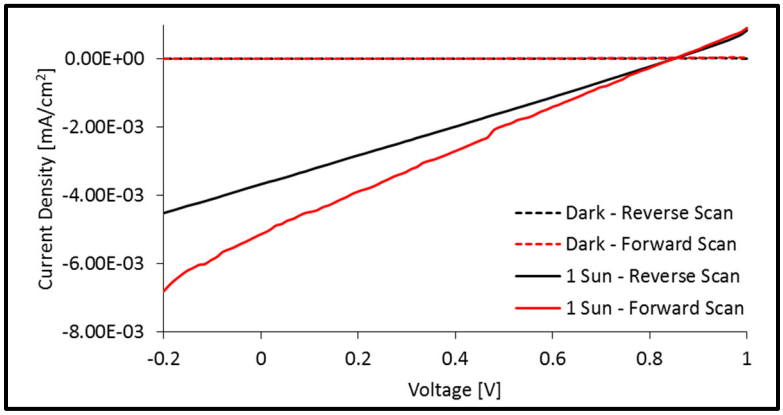

Figure 6.13 I-V characteristics of the flexible full architecture inkjet printed $MAPbI_{3-x}Cl_x$ PS based optoelectronic device under standard one (1) sun AM 1.5 illumination and under dark conditions

To characterize device dark current, photocurrent and response time, the one (1) sun AM 1.5 illumination is chopped at 0.12 Hz using a fan chopper and transient current behavior is recorded. The transient current behavior of the device is shown in Figure 6.14. Device dark current of - 30.5 ± 18 nA/cm^2 and photocurrent at 1 sun AM 1.5 illumination of – 4.1 ± 0.1 $\mu A/cm^2$ are measured, again showing a gain of two (2) orders of magnitude. Symmetrical on/off and off/on behavior is observed from the devices and a response time of 433 ± 76 ms is measured. Stable behavior showing no drift in device response after multiple on/off switching is observed.

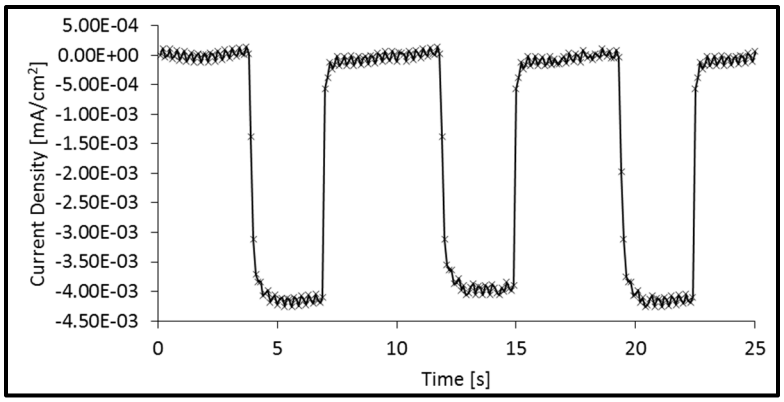

Figure 6.14 Transient current behavior of the flexible full architecture inkjet printed $MAPbI_{3-x}Cl_x$ PS based optoelectronic device under standard one (1) sun AM 1.5 illumination chopped at 0.12 Hz

The spectral responsivity of the device is characterized and is presented in Figure 6.15 a). A similar peak to the one found for the printed rigid devices is found towards the lower wavelengths, this is put in evidence in Figure 6.15 b) which compares the normalized spectral responsivity of both devices. This peak in responsivity is again associated to the charge generation effects at the TiO2/Spiro-OMeTAD junction where gaps in PS coverage are located. This time, it is much less pronounced and is indicative of reduced gaps in PS layer coverage. From 400 nm to 780 nm, the spectral responsivity decreases monotically, an average value of 0.008 mA/W is calculated.

The I-V device characteristics for both forward and reverse scan directions under one (1) sun AM 1.5 illumination and under dark conditions are summarized in Table 6.2 along with photodetector device performances including calculated NEP values.

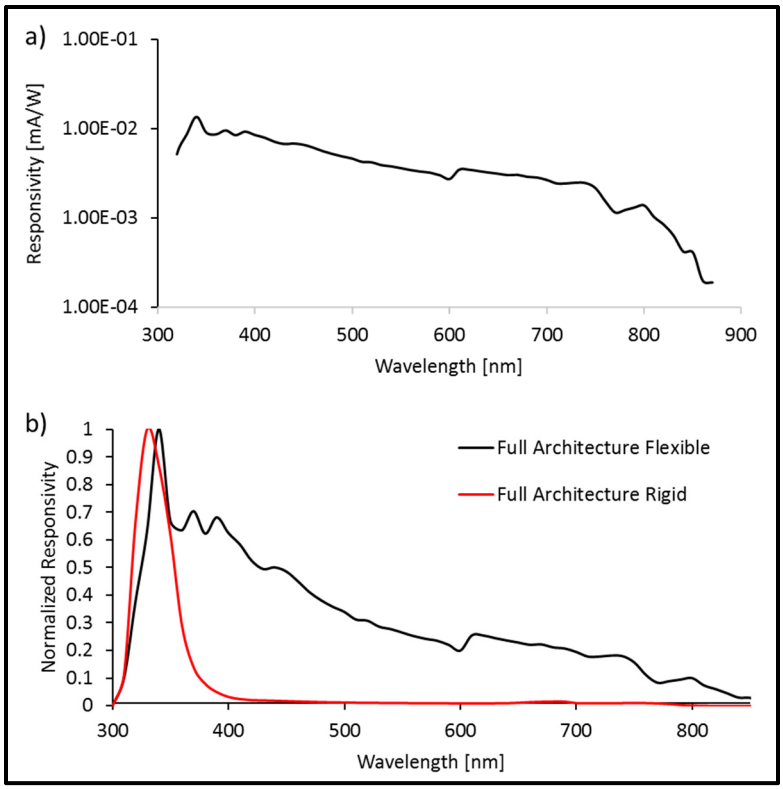

Figure 6.15 a) Spectral responsivity of flexible full architecture inkjet printed $MAPbI_{3-x}Cl_x$ PS based optoelectronic device. b) Normalized spectral responsivity of the flexible and rigid full architecture inkjet printed $MAPbI_{3-x}Cl_x$ PS based optoelectronic device

Table 6.2 Overview of flexible full architecture inkjet printed $MAPbI_{3-x}Cl_x$ PS based optoelectronic device performances

Device: TiO_2/$MAPbI_{3-x}Cl_x$/Spiro-OMeTAD on ITO/PET				
Scan Direction	**V_{OC} [V]**	**I_{SC} [mA/cm_2]**	**FF [%]**	**η [%]**
Forward	0.87	-5.1×10^{-3}	24	0.0044
Reverse	0.85	-3.68×10^{-3}	26	0.0031
Photocurrent [mA/cm^2]	**Dark Current [nA/cm^2]**	**Response Time [ms]**	**Average Responsivity [mA/W] (400-800nm)**	**NEP [$W/Hz^{0.5}$]**
$-4.1 \pm 0.1 \times 10^{-3}$	$- 30.5 \pm 18$	433 ± 76	0.008	7.2×10^{-4}

6.2.2 Architecture void of an ETL

Design

The design for the devices void of ETL compares to the design of the full architecture fabricated on flexible PET substrates but does not include the spin coated TiO2 ETL. A simplified band diagram of the designed architecture (void of ETL) is shown in Figure 6.16, along with a schematic representation of the device stack. Some of the results of the devices void of an ETL have been published previously (Trudeau, Bolduc, Beaupré, Ka, Asuo, & Cloutier, 2018, p.1-6).

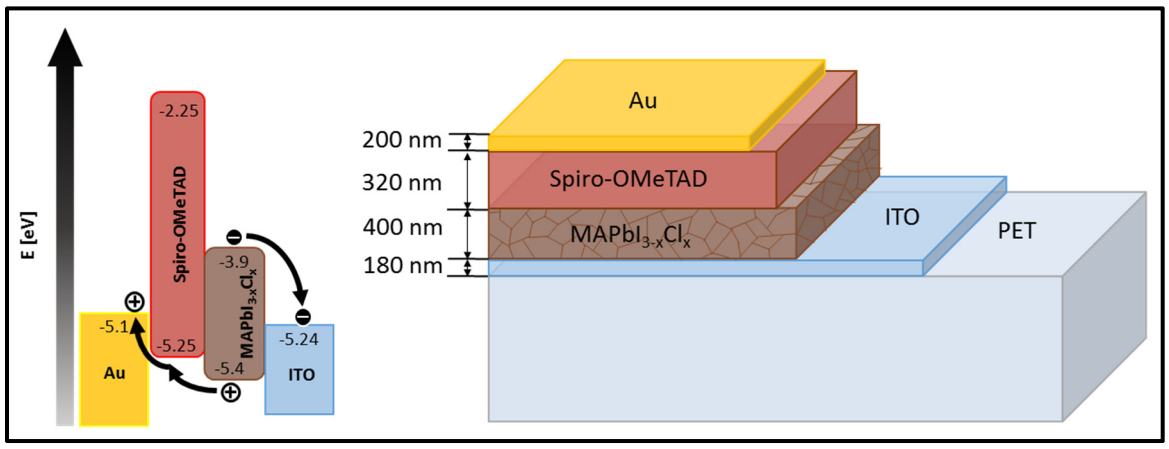

Figure 6.16 Schematic representation of the simplified band diagram and of the designed flexible TF $MAPbI_{3-x}Cl_x$ PS based optoelectronic device void of ETL

The removal of the TiO_2 ETL layer is expected to affect device performances in three (3) distinct ways. First, since there is no longer a Spiro-OMeTAD junction with TiO_2, the peak in responsivity around 330 nm due to this junction is expected to disappear (Bai, Shen & Tian, 2017, p.10543-10548). Secondly, V_{oc} values are expected to drop from the lack of an ETL layer (Wang et al., 2013, p.724-730), and finally, I_{sc} values are also expected to drop due to recombination of charges at the ITO interface as hole migration from the PS to the ITO electrode is theoretically no longer inhibited by an ETL. From a fabrication point of view,

removing the spin-coated TiO_2 layer is beneficial for two (2) reasons. The first, printing PS on ITO produces more homogeneous layers than printing on TiO_2, with a more homogenous layer printing, less gaps in material and thus higher shunt resistance devices are expected, counterbalancing drops in I_{sc} from charge recombination. Secondly, the removal of the spin coated TiO_2 layer brings the fabrication process a step closer to a complete inkjet-based fabrication process. For the remaining layers, the design of the device is not changed from the full device architecture design fabricated on rigid glass or flexible PET substrates.

Fabrication

The flexible MALH PS-based optoelectronic devices void of ETL are fabricated onto ITO-covered PET, where a hydrophilic oxygen plasma treatment is performed on the ITO surface. Prior to printing, the commercial Ossila I101 PS solution is heated to 70 °C for 120 minutes and allowed to cool down to room temperature for complete redissolution of the solutes. The PS solution is then printed in a square 5 mm x 5 mm pattern onto the substrate, using raster-mode printing. The printing parameters specificied in Section 4.3.5 for optimized printing on ITO surfaces are used for printing the PS layer. The PS layer is then subjected to an NIR preliminary annealing step using the in-situ NIR lamp operated at 5 % lamp power and a chuck displacement speed of 20 mm/s followed by oven annealing at 90 °C for 120 minutes. The Spiro-OMeTAD HTL and Au electrode are fabricated following the same procedure as for the full architecture devices. A schematic representation of the complete fabrication process of these devices, including pre- and post-printing treatments is depicted in Figure 6.18 and a photograph of a printed device is shown in Figure 6.17.

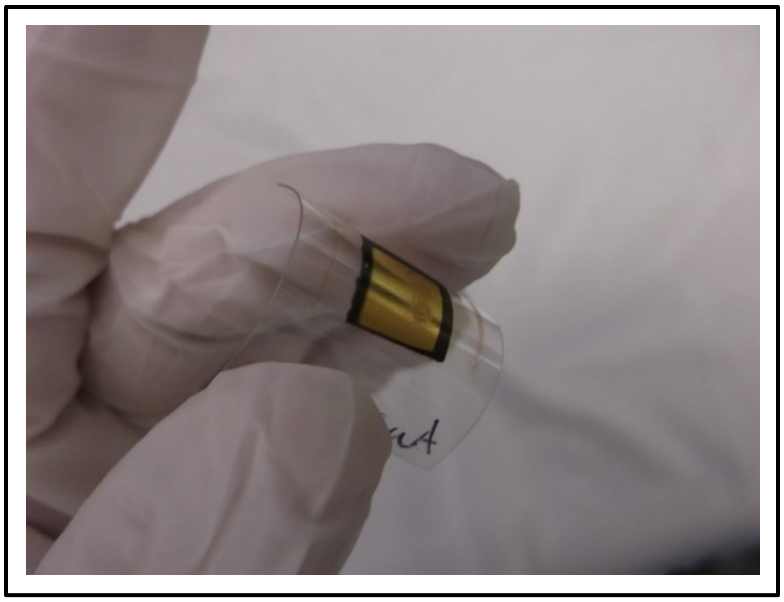

Figure 6.17 Photograph of a flexible inkjet printed $MAPbI_{3-x}Cl_x$ PS based optoelectronic device void of ETL

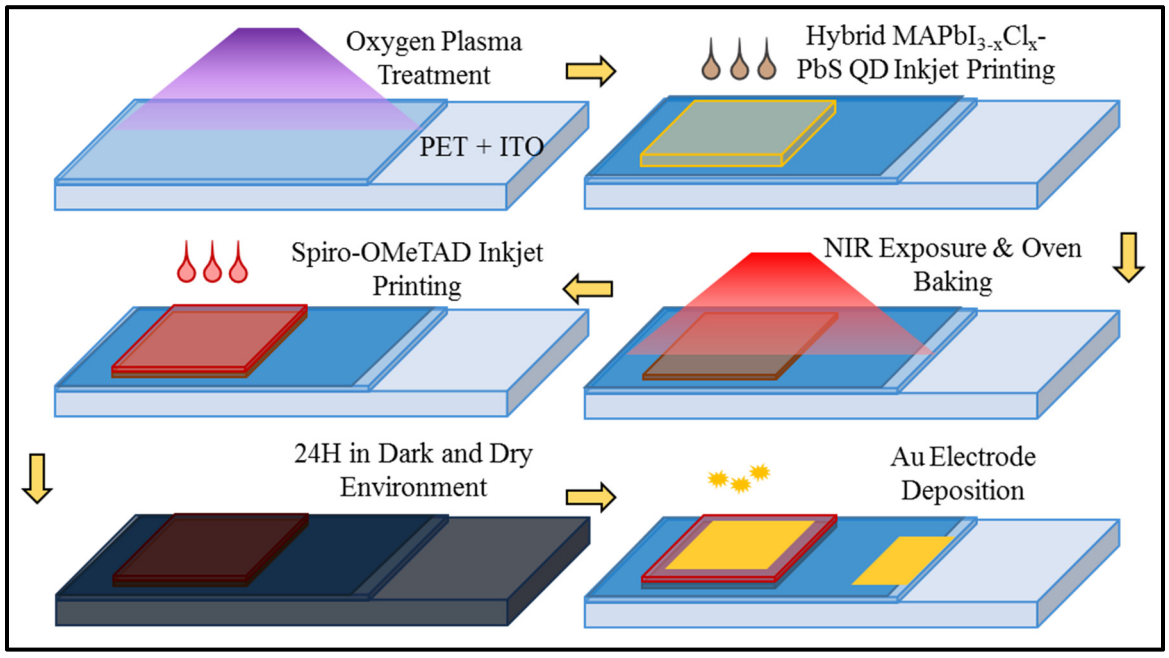

Figure 6.18 Schematic representation of the fabrication process for the proposed $MAPbI_{3-x}Cl_x$ PS based optoelectronic device architecture void of ETL on flexible PET substrate

Device Characterization

A 2-thetha XRD spectrum is taken of the printed PS layer after annealing but before the Spiro-OMeTAD is printed. The 2-thetha XRD spectrum shown in Figure 6.19, demonstrates near complete crystallization of the $MAPbI_{3-x}Cl_x$ PS to the tetragonal crystal phase, once more, traces of PbI_2 are present after annealing. The presence of the PbI_2 peak is less pronounced than in the corresponding XRD spectrum for the annealed PS layer used in the full architecture rigid device fabricated on glass. This can be attributed to the use of the NIR preliminary annealing step. The spectrum is dominated with a broad peak originating from the PET substrate and the presence of ITO peaks are also observed, both contributions are identified accordingly in red.

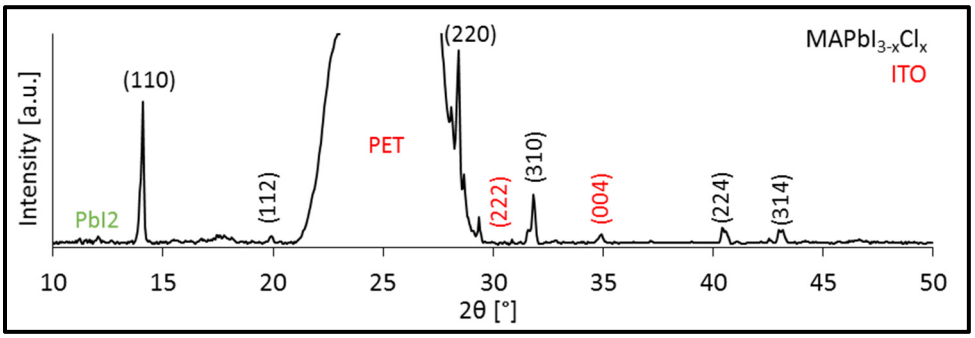

Figure 6.19 2-thetha XRD spectrum of printed $MAPbI_{3-x}Cl_x$ PS layer on ITO covered PET substrate after optical NIR treatment and oven annealing

The I-V characteristics of the printed devices under one (1) sun AM 1.5 illumination and under dark conditions are shown in Figure 6.20. These curves show working PV behavior with measure open circuit voltages of 0.033 V and 0.09 V and short circuit currents of -68.7 $\mu A/cm^2$ and -226 $\mu A/cm^2$ for forward and reverse scanning modes, respectively. FFs of 20 % and 27 % for forward and reverse scanning modes are calculated from the maximum power points, respectively. From these results an average PCE of 0.011 % is calculated.

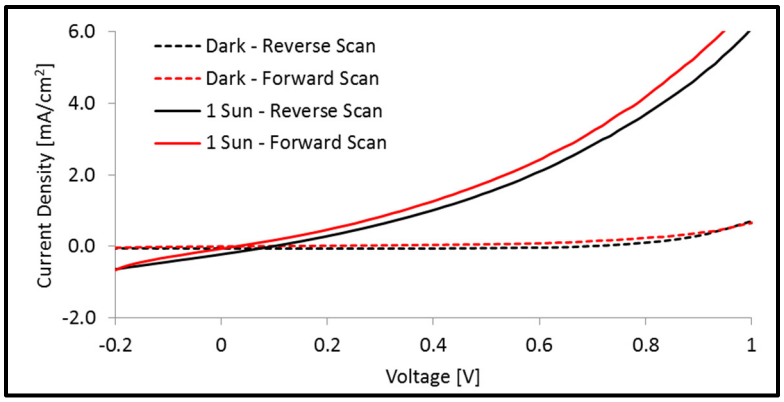

Figure 6.20 I-V characteristics of the flexible inkjet printed $MAPbI_{3-x}Cl_x$ PS based optoelectronic device void of ETL under standard one (1) sun AM 1.5 illumination and under dark conditions

As expected, lower V_{oc} values are observed from these devices and are attributed to the lack of ETL. However, much higher I_{sc} values are found when compared to the devices with a TiO_2 ETL. Even with much lower V_{oc} values, the increase in photo-generated current results in three (3) fold increased power efficiency when compared to devices with spin-coated TiO_2 ETL. From the I-V characterisation, these devices are deemed the best suited for optoelectronic applications out of the three (3) device architectures printed,. As such, more in depth characterisation of device performances is performed.

To characterize device dark current, and response time, the Torus 532 nm laser is operated with a laser power of 112.5 mW and chopped at 4 Hz using a fan chopper, the device is connected to a 5 MΩ load and transient current behavior is recorded. The transient current behavior of the device is shown in Figure 6.21. A device dark current of 62.1 ± 0.4 nA/cm^2 is measured, equating to a three (3) order of magnitude gain. Symmetrical on/off and off/on behavior is observed from the devices and a response time of 42 ± 11 ms is measured. A ~20-fold gain in current response is measured when the device is biased at 5 V when compared to device operation at 0 V bias. A stable behavior showing minimal drift in device response after multiple on/off switching is observed.

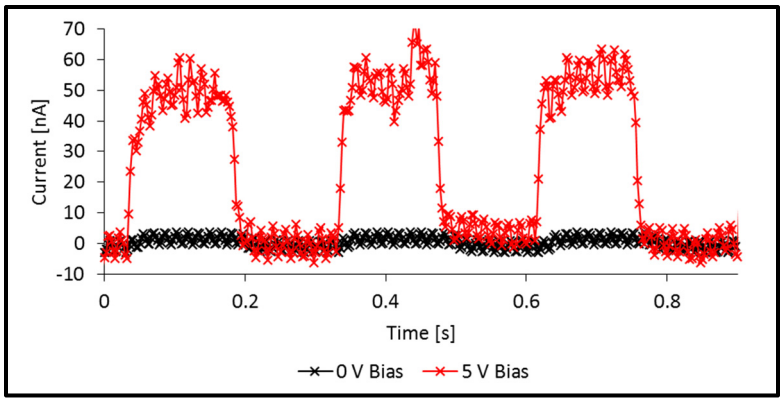

Figure 6.21 Transient current behavior of the flexible inkjet printed $MAPbI_{3-x}Cl_x$ PS based optoelectronic device void of ETL, under standard one (1) sun AM 1.5 illumination chopped at 4.0 Hz, under 0 V and 5 V bias

The power intensity of the incident 532 nm Torus laser is varied to characterise device responsivity with varying light intensities. Response of the device operated at 0 V bias is shown in Figure 6.22 and shows increasing current response as laser power is increased. The response is stable at all laser powers tested and shows no drift in response after multiple on/off switchings. Interestingly, for intermediate laser powers between 5.0 mW to 81.8 mW, a decrease in current is observed while the device is illuminated. This behavior is constant but does not seem to create a drift in the response for subsequent switching.

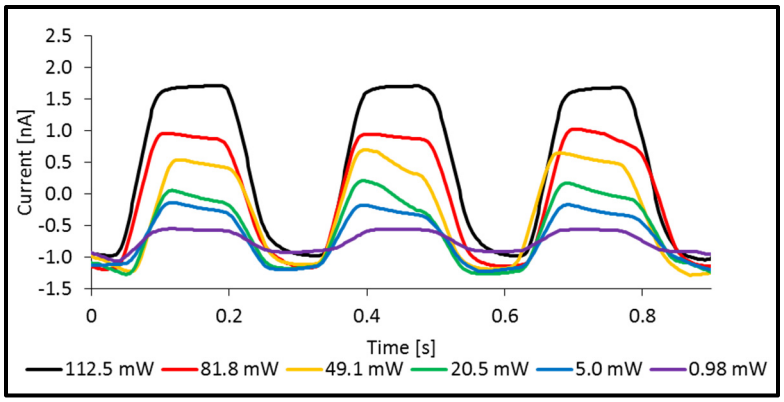

Figure 6.22 Transient current behavior of the flexible inkjet printed $MAPbI_{3-x}Cl_x$ PS based optoelectronic device void of ETL, under varying 532 nm incident laser power, chopped at 4.0 Hz

The transient current behavior with varying laser power for devices operated at 0 V and 5 V bias are used to calculate the responsivity of the devices over a range of laser power from 0.98 mW to 112.5 mW. The responsivity of the devices is shown in Figure 6.23. When operated at 0 V bias, the devices show an exponentially decrease in responsivity, starting at 6.12 $x10^{-7}$ A/W for a laser power of 0.98 mW and decreasing to 2.42 x 10^{-8} A/W for a laser power of 112.5 mW. When the device is operated at 5 V bias, an overall ~20-fold increase in responsivity is again observed, however, a decrease in the gain is observed at lower laser powers. A peak in responsivity of 4.0 x 10^{-6} A/W occurs at 5.0 mW laser power followed by an exponential decrease to 5.1 x 10^{-7} A/W at 112.5 mW laser power.

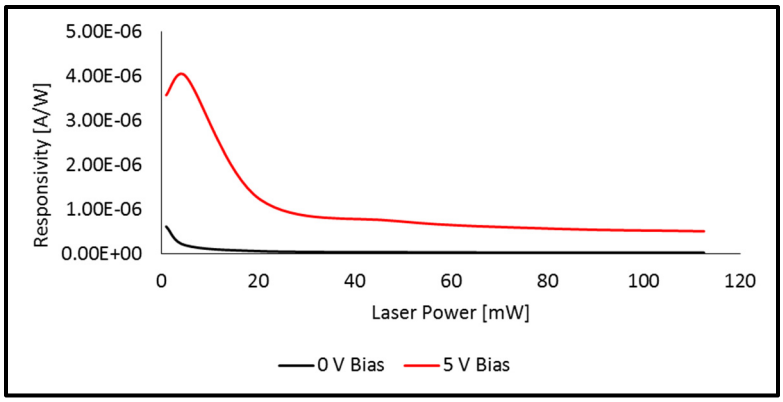

Figure 6.23 Printed $MAPbI_{3-x}Cl_x$ PS based optoelectronic device void of ETL responsivity curve with varying 532 nm incident laser power, devices biased at 0 V and 5 V

The spectral responsivity of the device is characterized using the setup specified at the start of this chapter and are presented in Figure 6.24. As expected, the device responsivity is no longer dominated by a peak at ~330 nm since the TiO_2 ETL is no longer present in the architecture of the device. From 400 nm to 780 nm, the responsivity is stable with an average value of 0.023 mA/W and 1.26 mA/W for devices operated at 0 V and 1 V bias, respectively. A sharp drop in responsivity after 780 nm is observed. The signal obtained from 400 nm to 780 nm indicates that the PS layer is working consistently, with stable responsivity over most of the visible spectrum. A ~55-fold increase in average responsivity is observed across the complete responsivity spectra when the device is operated with a 1 V bias, compared to 0 V bias. The higher measured responsivity and gain from applying a bias on the devices, taken with this setup, compared to the responsivity and gain measured using the 532 nm Torus laser can be attributable to device degradation between the two measurements. These two (2) measurements were taken approximatively 1 week apart (responsivity spectrum taken first) due to equipment limitations.

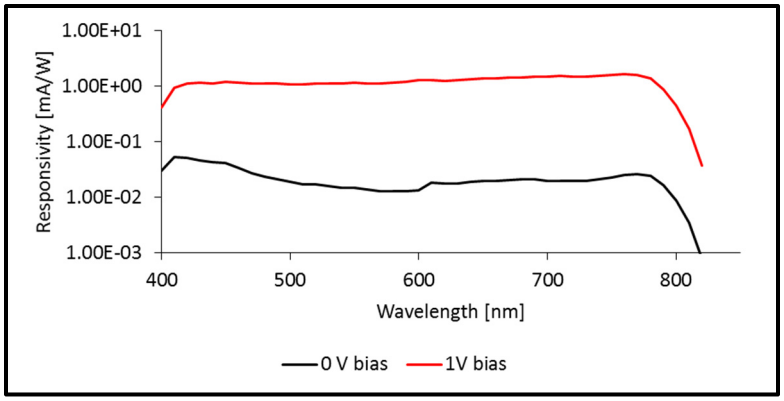

Figure 6.24 Spectral responsivity of flexible inkjet printed $MAPbI_{3-x}Cl_x$ PS based optoelectronic device void of ETL, devices biased at 0 V and 1 V

The I-V device characteristics for both forward and reverse scan directions under one (1) sun AM 1.5 illumination and under dark conditions are summarized in Table 6.3 along with photodetector device performances including calculated NEP values.

Table 6.3 Overview of the performances of the flexible inkjet printed $MAPbI_{3-x}Cl_x$ PS based optoelectronic devices void of ETL

Device: $MAPbI_{3-x}Cl_x$/Spiro-OMeTAD on ITO/PET				
Scan Direction	**V_{OC} [V]**	**I_{SC} [mA/cm$_2$]**	**FF [%]**	**η [%]**
Forward	0.033	-6.87×10^{-2}	20	0.0023
Reverse	0.09	-22.6×10^{-2}	27	0.0203
Photocurrent [mA/cm^2]	**Dark Current [nA/cm^2]**	**Response Time [ms]**	**Average Responsivity [mA/W] (400-800nm)**	**NEP [W/Hz$^{0.5}$]**
$2.2 \pm 0.2 \times 10^{-1}$	62.1 ± 0.4	42 ± 11	0.023	7.3×10^{-4}

6.2.3 Device Overview

The devices printed on flexible ITO covered PET substrates all showed working photodetector behavior, both architectures show comparable or enhanced performances to devices printed on rigid ITO covered glass substrates. The full architecture and the architecture void of ETL produced enhanced V_{oc} and enhanced I_{sc} respectively. The architecture void of a TiO_2 ETL is deemed best suited for printing arrays of devices on larger surfaces due to its ease in fabrication and enhanced photocurrent generation.

An overview of the device performances derived from I-V characterization under one (1) sun AM 1.5 illumination and under dark conditions is presented in Table 6.4, while an overview of device performances derived from transient current behavior and spectral responsivity is presented in Table 6.5

The amorphous TiO_2 ETL implemented in the full architecture flexible device is deemed a suitable replacement to the crystalline TiO_2 ETL and BL of the device fabricated on rigid glass. Indeed, an increase of V_{oc} to 0.87 V and 0.85 V is seen for forward and reverse scan directions, respectively. Due to the high series resistance of the device, lower FFs are found, although resulting PCE are increased to an average value of 3.75×10^{-3} %. Similar dark currents are found for the full architecture devices printed on flexible PET and rigid glass substrates. Response time is increased by a factor of ~1.7 to a value of 433 ± 76 ms for the flexible full architecture device when compared to the rigid device. The responsivity spectrum is similar to the one for the rigid device, showing a peak in responsivity in the lower wavelengths due to the TiO_2 spiro-OMeTAD junction.

For the flexible devices void of a TiO_2 ETL, a decrease in V_{oc}, from the lack of ETL, is seen. V_{oc} values of 0.033 V and 0.09 V are measured for forward and reverse scan directions, respectively. The largest increase in I_{sc} is seen for the devices void of ETL and originates once more from increased PS layer homogeneity. Indeed, a ~140-fold increase in I_{sc} is observed when compared to the full architecture device fabricated on rigid glass substrate. I_{sc} values of

-6.87 x10^{-2} mA/cm^2 and -22.6 x10^{-2} mA/cm^2 are measured for forward and reverse scan directions, respectively, FFs similar to the flexible full architecture devices are found, the high series resistance is therefore speculated to originate from the difference in ITO resistance of the covered rigid and flexible substrates (9-12 Ω/□ and 350-500 Ω/□, respectively). For the reverse scan direction, a ~10-fold increase in PCE to a value of 0.02 % is observed when compared to the rigid full architecture device. For forward scan directions, the PCE is similar to the flexible full architecture device, due to the lower V_{oc} measured. A slight increase in dark current is measured for the device void of ETL when compared to full architecture devices, while response time is reduced by a factor of ~ 10 to a value of 42 ± 11 ms. The responsivity spectra are constant throughout the visible region, from 400 nm to 780 nm, but do not show the same peak in responsivity in the lower wavelengths as the full architecture devices.

Table 6.4 Overview of the I-V characteristics and power conversion efficiencies of the inkjet printed $MAPbI_{3-x}Cl_x$ PS based optoelectronic devices

Device Architecture	**Substrate**	**Scan Direction**	**V_{OC} [V]**	**I_{SC} [mA/cm^2]**	**FF [%]**	**η [%]**
TiO_2/$MAPbI_{3-x}Cl_x$/ Spiro-OMeTAD	ITO/Glass (Rigid)	Forward	0.5	-1.5 x10^{-3}	30	0.0014
		Reverse	0.34	-1.6 x10^{-3}	61	0.0021
$MAPbI_{3-x}Cl_x$/ Spiro-OMeTAD	ITO/PET (Flexible)	Forward	0.033	-6.87 x10^{-2}	20	0.0023
		Reverse	0.09	-22.6 x10^{-2}	27	0.0203
TiO_2/$MAPbI_{3-x}Cl_x$/ Spiro-OMeTAD	ITO/PET (Flexible)	Forward	0.87	-5.1 x10^{-3}	24	0.0044
		Reverse	0.85	-3.68 x10^{-3}	26	0.0031

Table 6.5 Overview of photodetector performances of the inkjet printed $MAPbI_{3-x}Cl_x$ PS based optoelectronic devices

Device Architecture	**Substrate**	**Photo-current [mA/cm^2]**	**Dark Current [nA/cm^2]**	**Response Time [ms]**	**Average Responsivity [mA/W]**	**NEP [W/Hz$^{0.5}$]**
TiO_2 /$MAPbI_{3-x}Cl_x$/Spiro-OMeTAD	ITO/Glass (Rigid)	-1.4 ± 0.1 x10^{-3}	-43.8 ± 1.8	253 ± 147	0.519 (400-800nm)	3.3 x10^{-5}
$MAPbI_{3-x}Cl_x$/Spiro-OMeTAD	ITO/PET (Flexible)	-2.2 ± 0.2 x10^{-1}	-62.1 ± 0.4	42 ± 11	0.023 (400-800nm)	7.3 x10^{-4}
TiO_2/$MAPbI_{3-x}Cl_x$/Spiro-OMeTAD	ITO/PET (Flexible)	-4.1 ± 0.1 x10^{-3}	-30.5 ± 18	433 ± 76	0.008 (400-800nm)	7.2 x10^{-4}

6.3 Device Array Printing

6.3.1 Fabrication

The architecture void of ETL is chosen for device array printing due to its ease in fabrication and enhanced device performances, as transferring the TiO_2 spin coated layer to larger area flexible substrate poses additional challenges. The design of the device is kept the same, however, smaller 2 mm x 2 mm devices are printed for the array. A total of 10 devices are printed on each substrate, following the geometry of the printed isolated routing electrodes found in Chapter 5. Two sets of devices are printed, one set follows the same fabrication process explained in Section 6.2.3 and the other is fabricated without the NIR preliminary annealing step. This is done to evaluate if this step in the fabrication process is beneficial to device performances. A representative schematic of the fabrication process is shown in Figure 6.25.

After the fabrication of the device array, the isolated routing electrodes fabricated in Section 5.2.1 are attached to the device arrays using Kapton tape as an adhesive. Figure 6.26 a) and Figure 6.26 b) show a complete flexible device array with the isolated routing electrodes attached. Cu tape is then attached to the exposed Ag electrodes of the isolated routing

electrodes and to a section of exposed ITO to provide better contacts between the electrodes and the characterization equipment. Moreover, the device arrays are sandwiched between two glass slides to keep the devices in place for ease of manipulation. The device arrays ready for characterization are shown in Figure 6.26 c).

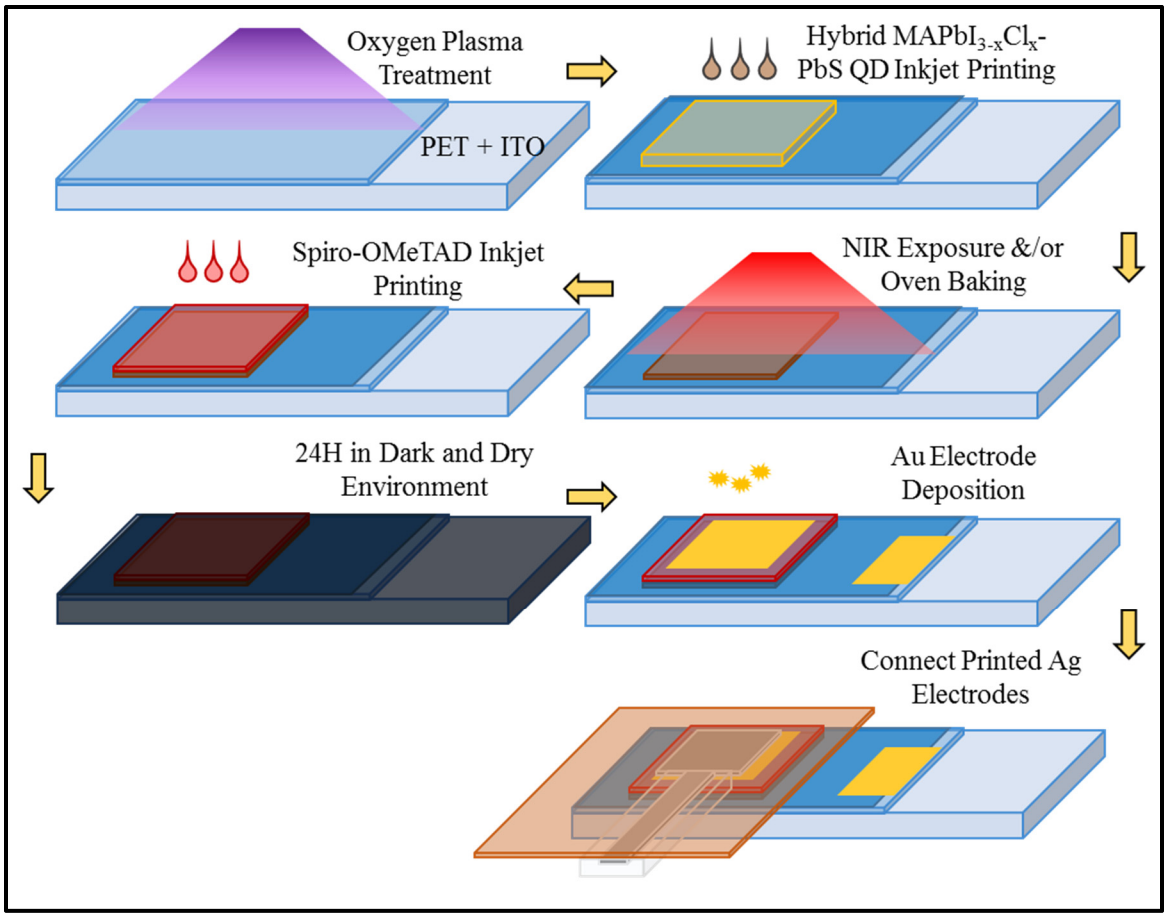

Figure 6.25 Schematic representation of the fabrication process for the proposed $MAPbI_{3-x}Cl_x$ PS based optoelectronic device arrays using the architecture void of ETL, printed on flexible PET substrate

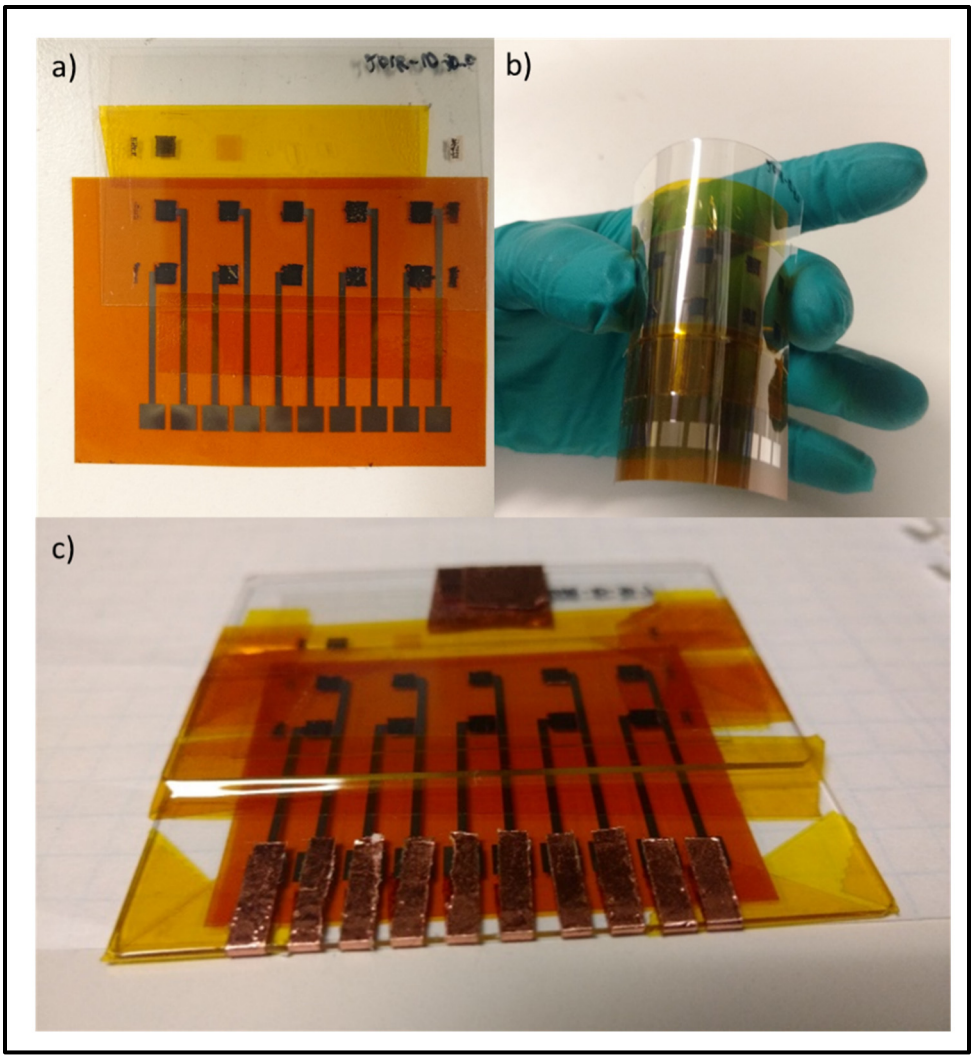

Figure 6.26 Inkjet printed flexible MAPbI3-xClx PS based optoelectronic device array, a) and b) showing the device array attached to the isolated routing electrodes and c) sandwiched between two glass slides, ready for device characterization and manipulation

6.3.2 Device Characterization and Statistical Analysis

Four device arrays are printed giving a total of 40 fabricated devices, 10 devices with the preliminary NIR annealing step and 30 devices without. Out of the 10 devices fabricated with the NIR preliminary annealing step, 6 devices showed working photodetector behavior and are included for characterization, giving a 60 % working device yield. Out of the 30 devices fabricated without the NIR preliminary annealing step, 25 devices showed working

photodetector behavior and are included for characterization, giving an 83 % working device yield.

Overall, both devices fabricated with and without the NIR preliminary annealing step showed similar I-V characteristics. Although, more variation is seen in device performances and slightly increased V_{oc} values are observed for devices fabricated with the preliminary NIR annealing step. Typical I-V characteristics of the printed devices under 1 sun AM 1.5 illumination and under dark conditions are shown in Figure 6.27. Typical V_{oc} and I_{sc} values of 0.010 V - 0.045 V and -0.02 mA/cm^2 - -0.09 mA/cm^2 are measured, respectively, for devices without the NIR preliminary annealing step. Whereas, typical V_{oc} and I_{sc} values of 0.024 V - 0.078 V and -0.02 mA/cm^2 - -0.16 mA/cm^2 are measured, respectively, for devices with the NIR preliminary annealing step. Both these ranges in I_{sc} and V_{oc} values are in agreement with the values found for printing single devices of larger area.

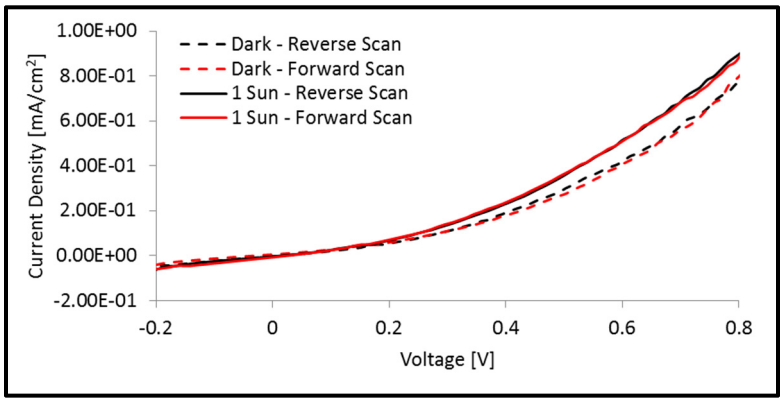

Figure 6.27 Typical I-V characteristics of the flexible inkjet printed $MAPbI_{3-x}Cl_x$ PS based optoelectronic device arrays using the architecture void of ETL, under standard 1 sun AM 1.5 illumination and under dark conditions

The champion device I-V behavior is shown in Figure 6.28 and belongs to a device fabricated using the NIR preliminary annealing step. The enhanced V_{oc} from the NIR preliminary annealing step is especially noticeable with the champion device. V_{oc} and I_{sc} values of 0.509 V and 0.515 V, and -0.662 mA/cm^2 and -0.536 mA/cm^2 are measured for forward and reverse

scanning directions, respectively. FFs of 19 % and 40 % are calculated from maximum power point tracking for forward and reverse scan directions, respectively. A maximum PCE of 0.11 % is calculated for the reverse scan direction.

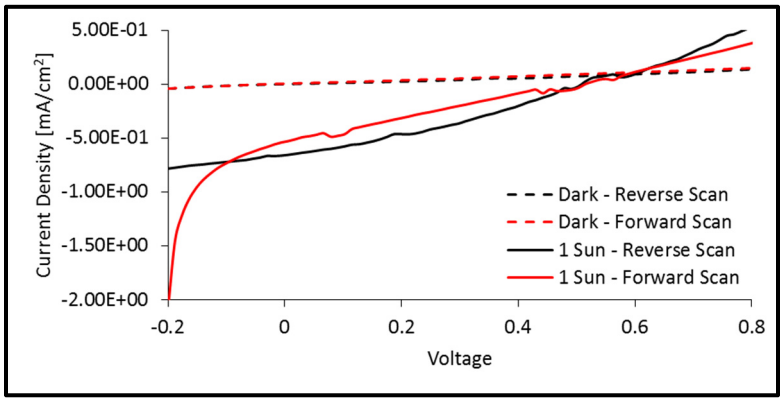

Figure 6.28 Champion device I-V characteristics of the flexible inkjet printed $MAPbI_{3-x}Cl_x$ PS based optoelectronic device arrays using the architecture void of ETL, under standard one (1) sun AM 1.5 illumination and under dark conditions

The spectral responsivity of the champion device is characterized using the setup specified at the start of this Chapter and are presented in Figure 6.29. The responsivity spectra is comparable to the one for the single printed device of larger area but is enhanced to an average value of 0.29 mA/W over a range of 400 nm – 780 nm. The responsivity is stable over this range and is followed by a sharp drop after 780 nm.

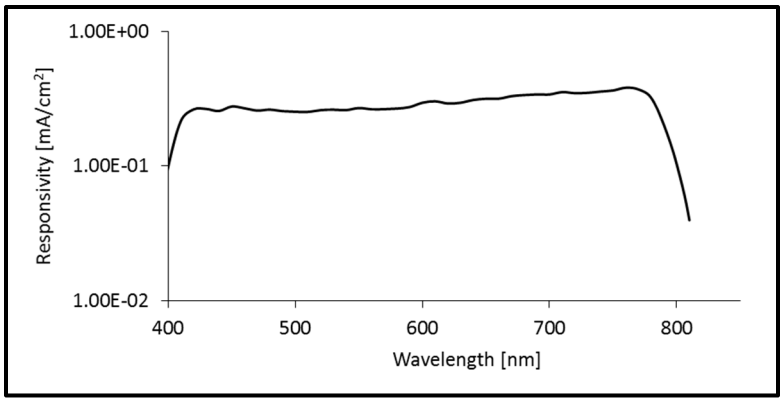

Figure 6.29 Spectral responsivity of the champion flexible inkjet printed $MAPbI_{3-x}Cl_x$ PS based optoelectronic device void of ETL

The responsivity of the champion device over a range of laser power from 0.98 mW to 112.5 mW is measured using varying Torus 532 nm laser power and is shown in Figure 6.30. The device shows the same curve as the single printed device of larger area when operated at 5 V bias, A peak in responsivity of 1.7 x 10^{-5} A/W occurs at 5.0 mW laser power followed by an exponential decrease to 4.1 x 10^{-6} A/W at 112.5 mW laser power.

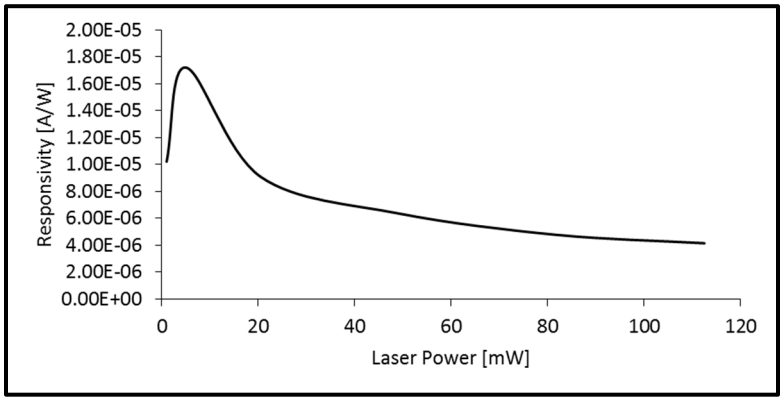

Figure 6.30 Printed $MAPbI_{3-x}Cl_x$ PS based optoelectronic champion device void of ETL responsivity curve with varying 532 nm incident laser power

Statistical analysis from the device I-V characteristics are performed and include the 6 devices fabricated with the NIR preliminary annealing step and the 25 devices fabricated without. Both V_{oc} and I_{sc} values for forward and reverse scan directions for the devices included in the statistical analysis are measured and the distribution are recorded in Figure 6.31 and Figure 6.32, respectively. Interestingly, a bimodal distribution is observed for the I_{sc} values with centers at -0.02 mA/cm^2 and -0.085 mA/cm^2, the distribution centered at -0.085 mA/cm^2 originates primarily from contributions of the reverse scan I_{sc} values. A similar but much less pronounced bimodal distribution is observed for V_{oc} values with centers at 0.005 V and 0.1 V.

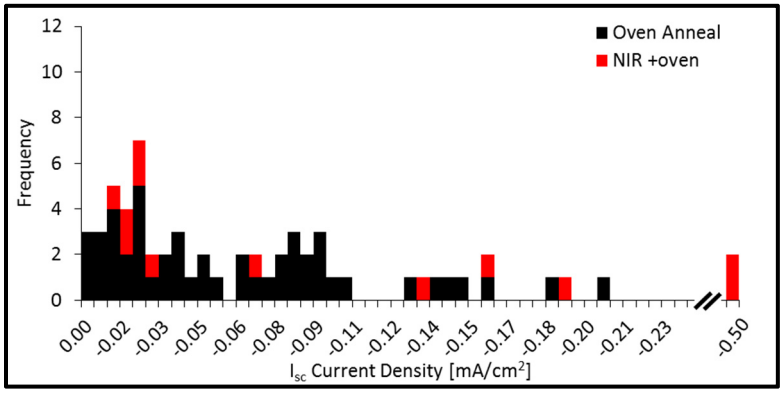

Figure 6.31 Distribution of measured I_{sc} values from the 31 inkjet printed flexible MAPbI3-xClx PS based optoelectronic devices fabricated in arrays

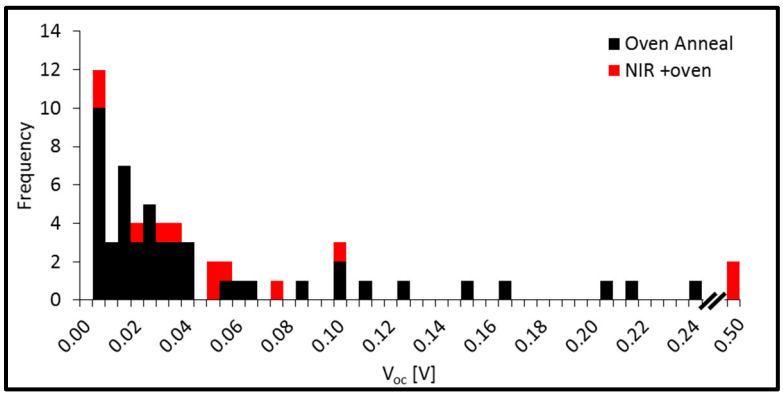

Figure 6.32 Distribution of measured V_{oc} values from the 31 inkjet printed flexible MAPbI3-xClx PS based optoelectronic devices fabricated in arrays

The values of I_{sc} and V_{oc} measured for the statistical analysis are presented in the form of box plots in Figure 6.33 a) and Figure 6.33 b), respectively, and compare the devices fabricated with and without the NIR preliminary annealing step. The minimum, Q1, median, Q3, maximum and average I_{sc} and V_{oc} values obtained from this statistical analysis are presented in Table 6.6. Overall the devices fabricated with the preliminary NIR annealing step showed a greater distribution towards higher I_{sc}. However, median and Q1 I_{sc} values are comparable with the values measured for the devices fabricated without the preliminary NIR annealing step. The devices fabricated with the preliminary NIR annealing step also showed consistently increased V_{oc} values with a smaller distribution of the Q1 to Q3 values when compared to the devices fabricated without.

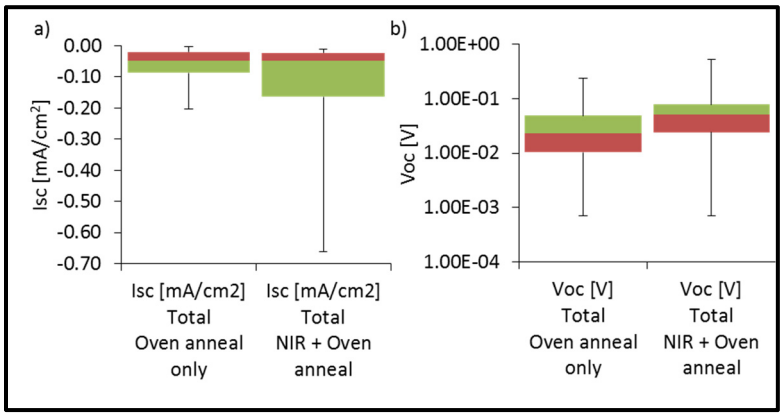

Figure 6.33 Statistical analysis of measured a) I_{sc} and b) V_{oc} values from the 31 inkjet printed flexible MAPbI3-xClx PS based optoelectronic devices fabricated in arrays, presented in the form of box plots

Table 6.6 Statistical analysis of measured Isc and Voc values from the 31 inket printed flexible MAPbI3-xClx PS based optoelectronic devices fabricated in arrays

	Devices w/o NIR Annealing		**Devices w/ NIR Annealing**	
Value	**I_{sc} [mA/cm^2]**	**V_{oc} [V]**	**I_{sc} [mA/cm^2]**	**V_{oc} [V]**
Minimum	-1.89×10^{-3}	0.001	-1.10×10^{-2}	0.001
Q1	-2.07×10^{-2}	0.010	-2.27×10^{-2}	0.024
Median	-4.77×10^{-2}	0.023	-4.73×10^{-2}	0.050
Q3	-8.78×10^{-2}	0.048	-1.64×10^{-1}	0.078
Maximum	-2.03×10^{-1}	0.239	-6.62×10^{-1}	0.515
Average	-6.08×10^{-2}	0.045	-1.56×10^{-1}	0.119

When considering which annealing method is best suited for device fabrication, both the yield of working devices and the device performances must be considered. The devices fabricated without the preliminary NIR annealing step showed a greater device yield (83 % vs 60 %) but suffered from decreased average device performances, when compared to the devices fabricated with the preliminary NIR annealing step. Nonetheless, the improved device performances from the devices fabricated with the preliminary NIR annealing step show that conventional annealing processes can be improved and adapted for device printing. Either of the annealing processes may be chosen for device fabrication depending on which aspect is deemed of most importance; device yield or average device performances.

A PCE of 0.11 % was found for the fabricated champion device. Although this may seem low, it can be comparable to power conversion efficiencies of fully printed single junction devices found from the literature, with typical maximum device efficiencies of 1 – 5 % (Eom et al., 2010, p.1516-1522); (Eggenhuisen et al., 2015, p.7255-7262); (Jung et al., 2014, p.1400432); (Peng et al., 2017, p.1703704); (Mitra et al., 2018, p.642).

6.4 Methylammonium Trihalide Based Bolometers

Smart-buildings, biomedical and wearable monitoring applications urgently need cheap and low-size, weight and power (SWAP) flexible temperature sensors. These critical applications often call for a limited temperature range sensing but require a high level of accuracy and precision. Temperature sensing ranges of 30 - 50 °C and 15 - 40 °C for applications in health care/human activity monitoring and smart building applications are typically targeted, respectively (Vaz et al., 2010, p.95-99); (Kokkoris et al., 1978, p.177-190); (Lim, Byrne & Lee, 2008, p.347); (Deng, Zhang, Ren & Liang, 2016, p.1-6); (Uribe, Martin, Garcia-Alegre, Santos & Guinea, 2015, p.27543-27568); (Moreno, Skarmeta, Venturi, Schmidt & Schuelke, 2015, p.705-710). Flexible substrates such as PET and PDMS can play a major role in device performances. These have been used and integrated in temperature, strain/stress and pressure sensors with success. (Bessonov & Kirikova, 2015, p.165-180); (Yu et al., 2010, p.675-678); (Yan, Wang & Lee, 2015, p.2130-2137); (Li, Samad & Liao, 2015, p.2181-2187); (Wang et al., 2015, p.2324-2331). Integration of light-sensing capabilities to the temperature-sensing capabilities is expected to be most beneficial for smart building applications. This dual sensing capability can be used for sensing day/night cycles or overcast conditions and for health care applications such as oximetry and UV overexposure prevention. In this chapter, the interdigitated Ag electrodes presented in Chapter 5 are shown to be effective PTC thermistors. With the addition of a printed MALH PS light absorbing layer to these PTC thermistors, bolometer structures capable of sensing light can effectively be fabricated.

Thermistor behavior of the all-inkjet printed devices are characterized using a 1487-1013-ND (Laird Technologies) thermoelectric cooler with a k-type thermocouple and a heat sink for temperature control. A Keithley 2400 source-measure unit is used for current-voltage (I-V) characterization, at different temperature, to measure thermistor behavior. The thermistor TCR values are calculated using Equation 3.7. MALH PS absorption spectra are calculated from transmission and reflection spectra acquired using a Carry 7000 spectrophotometer (Agilent). For photo-sensing behavior characterization, a solar simulator (Oriel Instruments 91160-1000) with a 1000 W Xenon lamp is used as 1 sun illumination source, with the same Keithley 2400

source-measure unit connected to the device for current-voltage (I-V) characterization in the dark and under 1 sun illumination.

6.4.1 Fabrication

Fabrication of the PS based thermistors starts with the fabrication of the interdigitated electrodes on Novele^{TM} IJ-220 PET, the fabrication process for these can be found in Section 5.2.2. Once the interdigitated electrodes are printed and annealed, two layers of Ossila I101 PS ink are printed in raster-mode to form an 8 mm x 8 mm active area over the interdigitated electrodes. The optimized jetting parameters for Ossila I101 PS ink found in Section 4.2.3 and the optimized printing parameters for printing PS on ITO found in Section 4.3.5 are used for printing the PS layer. The PS layer is then annealed using a preliminary NIR annealing step with an Adphos NIR lamp power of 5 % and a chuck displacement speed of 20 mm/s. After the optical annealing step, the PS is oven annealing at 90 °C for three (3) hours and rapidly cooled by placing the substrate on a heat sink. A schematic representation of the device fabrication process is depicted in Figure 6.34, while finished printed devices are pictured in Figure 6.35 a) and Figure 6.35 b).

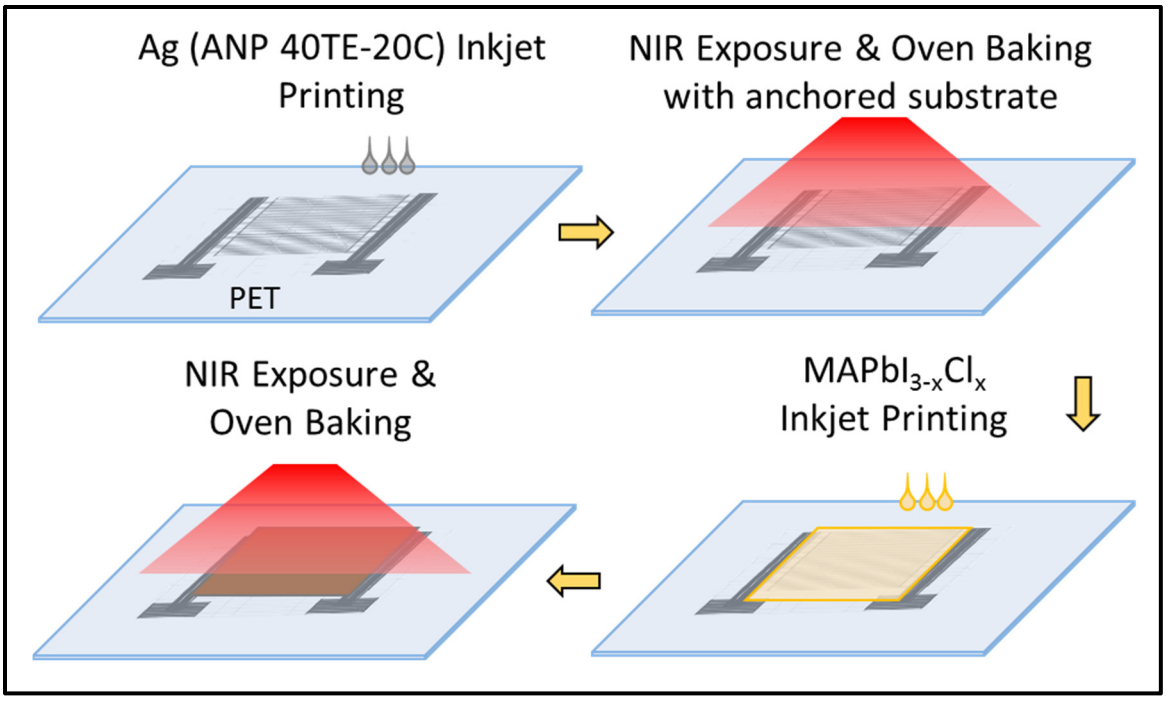

Figure 6.34 Schematic representation of the fabrication process for the proposed $MAPbI_{3-x}Cl_x$ PS bolometer based on the inkjet printed interdigitated electrodes

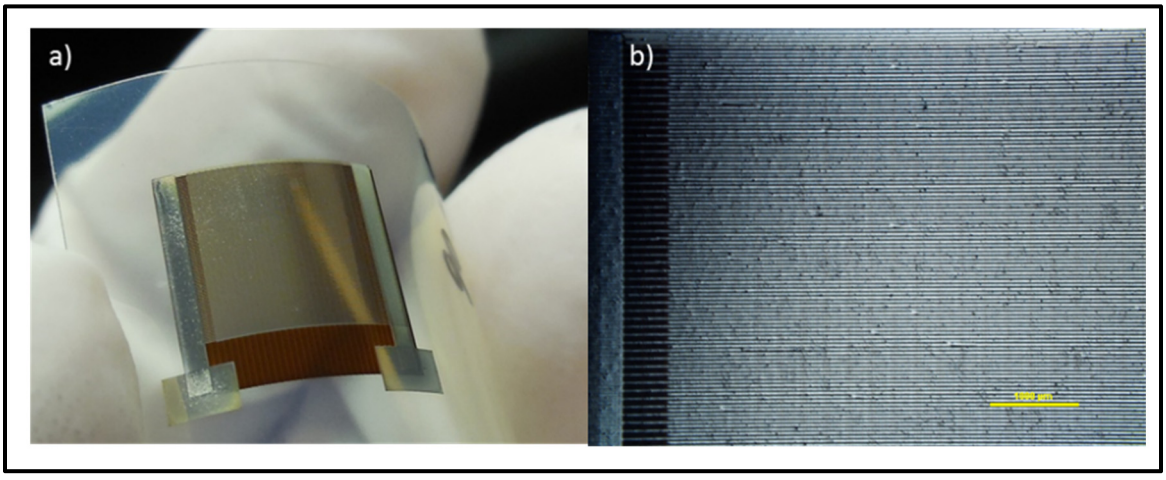

Figure 6.35 a) Photograph of an inkjet printed flexible $MAPbI_{3-x}Cl_x$ PS based bolometer, b) microscope image of the PS material deposited between the interdigitated electrodes

6.4.2 Device Characterization

The absorption of inkjet printed perovskite layers is tested to validate their implementation as light absorbing layers in bolometer structures. The absorption spectra of different number of printed perovskite layers are presented in Figure 6.36. From these results we observe that a single layer of printed perovskite offers near complete absorption of visible light up to 550 nm, while two (2) printed layers drastically improves absorption up to 750 nm. Further increasing the number of printed layers to three (3) marginally improves absorption at longer wavelengths, while four (4) printed layers offer almost no further improvement. We consider that two (2) layers of the printed perovskite absorber is enough for visible light sensing to validate bolometer behavior.

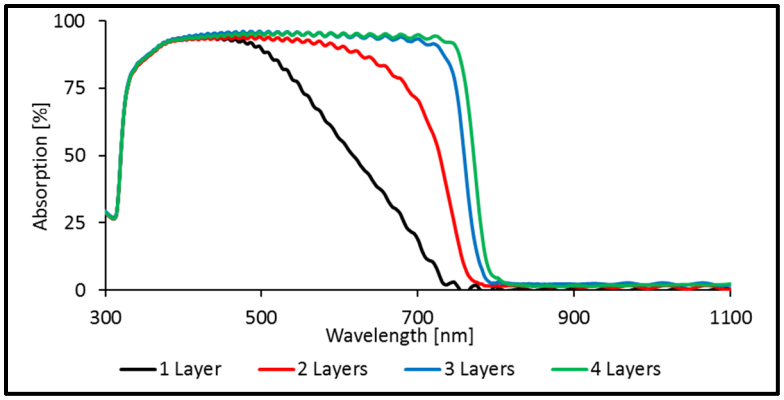

Figure 6.36 Absorption spectra of printed MAPbI3-xClx layers

The device's thermistor behavior is stable and repeatable for a temperature range of 17 °C - 36 °C. Below 17 °C, PS degradation starts to occur while the devices are under operation. This degradation is observed in the form of a gradual color evolution from dark brown to bright yellow as the device behavior becomes unstable. The PS degradation and color change is reversible only if the device is kept below 17 °C under operation for a short time (< 5 minutes), but the damage becomes irreversible if operated for longer periods. Above 36 °C the devices reach their maximum resistance, which no longer fluctuates with increasing temperatures. The

temperature-dependent I-V characteristics of the devices using D = 50 interdigitated electrodes, without (thermistor) and with the PS layer (bolometer) are shown in Figure 6.37 a) and Figure 6.37 b) respectively. Similar trends in the temperature dependence of the standalone thermistor and of the bolometer devices are observed. The resistances of the devices increase by six orders of magnitude from 17 °C to 36 °C. This behavior is reminiscent of polymer PTC thermistors, where conductive grains within a polymer medium form conductive pathways as the polymer is cooled (Zeng, Y., Wang, H., Du, J., Ying, Z., & Liu, C., 2014, p.6684) (Struempler, R. G.,1996, p. 377-382). The addition of the PS layer lowers the overall resistance, lowering the temperature-dependence but increasing the accuracy for higher temperatures (31 °C-36 °C). However, it also limits the operations of the device at lower temperatures (< 17 °C).

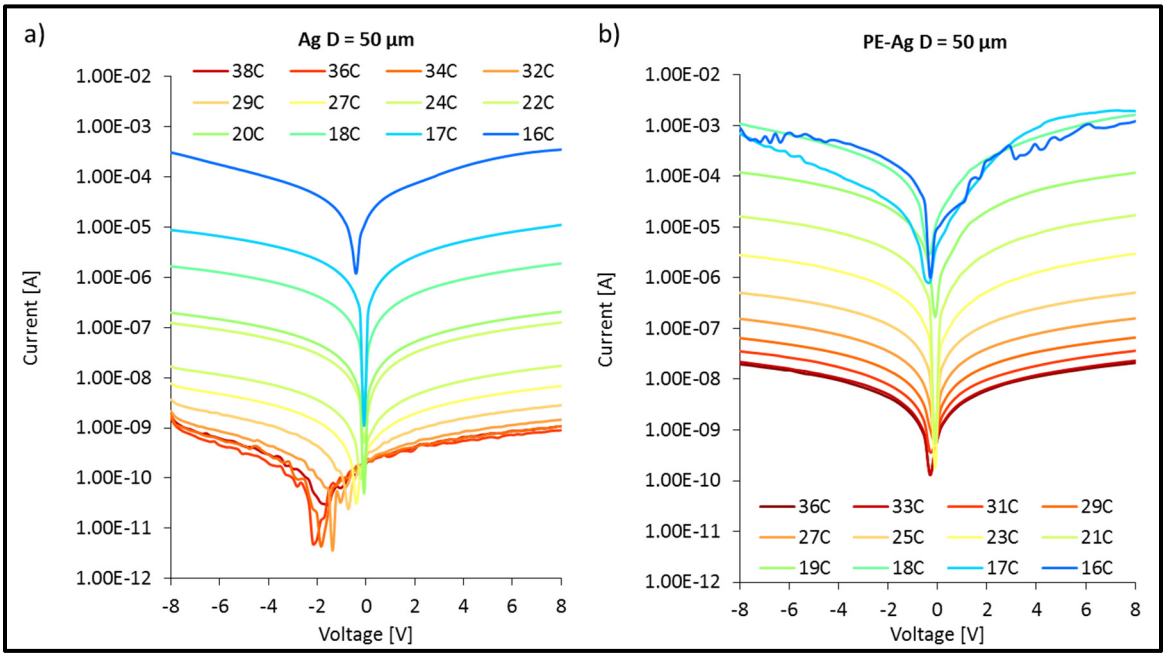

Figure 6.37 Temperature dependent I-V characteristics of
a) the interdigitated electrodes without the PS active layer and
b) the bolometers with the $MAPbI_{3-x}Cl_x$ PS active layer

The resistance and TCR of the devices are plotted as a function of the temperature in Figure 6.38. It is evident from these results that the silver interdigital electrodes on the flexible PET

substrate are responsible for the overall temperature dependence of the devices as both devices possess almost identical TCR values. We speculate that the micro splashing of the silver ink is responsible for the formation of increased conductive pathways as the devices are cooled and thus dictate their temperature-dependent behavior. Indeed, upon inspection we find evidence of Ag micro-spashing between the interdigital electrodes, this is presented in Figure 6.39.

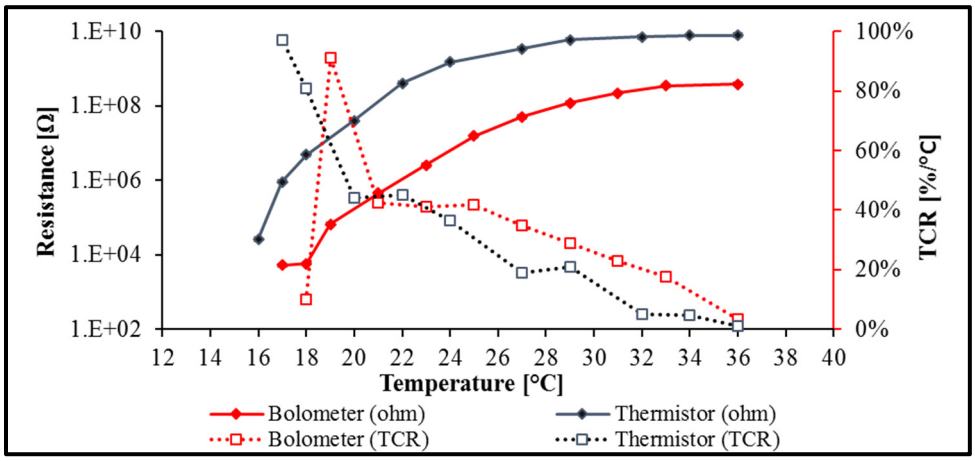

Figure 6.38 Pad-to-pad temperature dependent resistance and TCR of the inkjet printed thermistors and bolometers

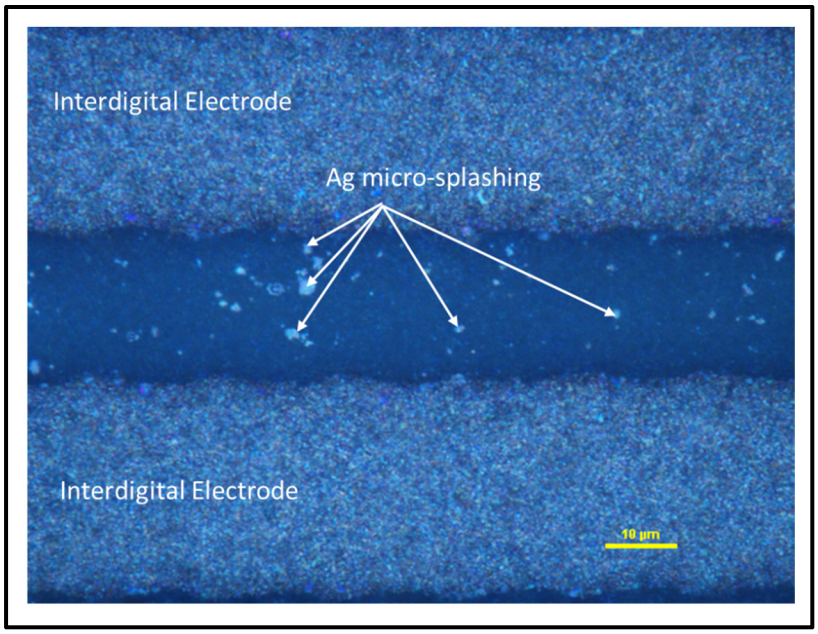

Figure 6.39 Photograph of interdigitated electrodes with evidence of Ag micro-splashing

To validate their use as bolometers the I-V characteristics of both device structures are measured in the dark and under one (1) sun illumination, the results are shown in Figure 6.40. While the thermistor structure shows only negligible change in I-V characteristics under illumination (with minor fluctuations due to light-induced heating), the bolometer structure shows clear photo-resistive switching behavior. We deduce that this photo-resistive behavior originates from light-induced heating effects as typical PS photo-resistive behavior shows inverse relations between resistance and incident light (Takshi, Bebeau & Rahimi, 2016, p.99440R); (Yang, Dou & Wang, 2018, p.9-17).

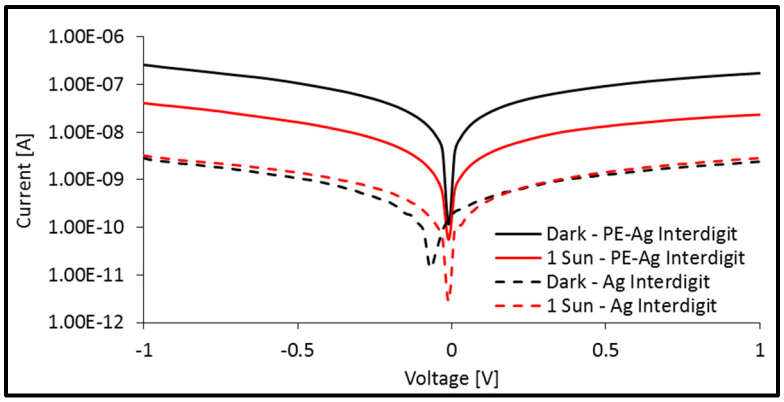

Figure 6.40 I-V characteristics of the inkjet printed $MAPbI_{3-x}Cl_x$ PS based bolometers and the standalone interdigitated electrodes under standard one (1) sun AM 1.5 illumination and under dark conditions

6.5 Conclusion

In this chapter, MALH PS based optoelectronic devices with varying architectures are fabricated. Printing processes using Ossila I101 PS ink, Spiro-OMeTAD solution and MicroChem SU-8 photoresist are used while conventional deposition processes for Au electrodes and TiO_2 materials are used for some architectures. Primary device fabrication is performed on rigid ITO covered glass substrates and consist of TiO_2 BL and ETL, a $MAPbI_{3-x}Cl_x$ active layer, a Spiro-OMeTAD HTL and an Au electrode with an SU-8 encapsulation. The devices showed working PV and photo-sensing behavior although suffered from poor performances. The device is shown to be responsive over the visible light spectrum, from 310 nm to 800 nm with a peak in responsivity around 330 nm.

The device fabrication is then transferred on flexible ITO covered PET substrates. From here, two different device architectures are tested and characterized. The first architecture tested mimics the architecture of the device fabricated on rigid glass substrates, however the TiO_2 ETL fabrication is adapted for deposition on flexible heat sensitive substrates. This device architecture showed overall improved PV performances when compared to the rigid devices, with increases in both V_{oc} and I_{sc} values, resulting in a two-fold increase in energy conversion

efficiencies. Device responsivity spectra behavior is shown to be similar to the rigid device responsivity.

In the second architecture, the TiO_2 ETL is removed entirely. This makes the fabrication process closer to an all-inkjet fabrication process and is the easiest architecture to translate for fabrication of device arrays on larger surfaces. This device architecture showed overall improved PV and photo-sensing performances. While V_{oc} values are reduced when compared to architectures with a TiO_2 ETL, a significant increase in I_{sc} values is observed, resulting in up to a ~5-fold increase in PCE when compared to the rigid device architecture. Spectral responsivity of the device architecture void of a TiO_2 ETL is limited to a range of 400 nm to 800 nm while no responsivity below 400 nm is measured contrary to device architectures with a TiO_2 ETL.

The device architectures and device performances of the two architectures are evaluated and the device architecture void of TiO_2 is identified as the most adequate architecture for moving forward to printing device arrays. Device sizes are reduced, and device arrays are designed and printed for easy connection with the routing electrodes detailed in Chapter 5. A total of 40 devices are tested for statistical analysis of their optoelectronic performances. Working device yields of up to 80 % are achieved with devices showing working PV behavior. Ranges and distribution in V_{oc} and I_{sc} values are presented and are consistent with single printed devices of the same architecture. However, champion device performances are well above any previously printed devices in this work, showing drastically increased I_{sc} values. A PCE up to 0.11 % is achieved, equating to a ~30-fold increase compared to the rigid device.

Finally, the interdigitated electrodes detailed in Chapter 5 are used as a basis for bolometer fabrication, $MAPbI_{3-x}Cl_x$ is printed onto the interdigitated electrodes to form an absorbing layer. The sensors are highly sensitive to temperature changes within a small temperature range (17 – 36 °C). While the interdigitated electrodes with the PET substrate are responsible for the basis of the temperature sensing capabilities, the addition of the PS active layer enhanced sensing accuracy in the upper temperature ranges and introduces light sensing capabilities. The

temperature sensing behavior resembles PTC thermistor behavior. We speculate that Ag ink micro-splashing introduces increased conduction pathways as the polymer substrate is cooled. The bolometer devices are shown to have light switching capabilities for high light intensities.

CHAPITRE 7

OPTICAL LASER SINTERING SIMULATIONS

Recently, research efforts have been made to explore highly-localized optical treatments for ink sintering purposes using IR and UV lamps (Denneulin et al., 2011, p.3815-3823); (Trudeau et al., 2017, p.1015-1020), high power flash lamps (Kim et al., 2009, p.791); (Chung et al., 2012, p.035202); (Eun et al., 2015, p.838-845); (Helgesen et al., 2012, p.2649-2655); (Peralaer et al., 2012, p.2620-2625), and continuous-wave laser irradiation (Ko et al., 2007, p.345202); (Laakso et al., 2009, p.1360-1366); (Zenou, Ermak, Saar & Kotler, 2013, p.025501); (Kumpulainen, 2011, p.570-576); (Kwon et al., 2014, p.1137-1145); (Yeo et al., 2014, p.562-568). These treatments have shown great promise for achieving control of the final ink properties. Some of these optical post-process treatments have been explored in early chapters of this work, more specifically, the optical annealing of PS and silver ink using NIR lamps and the cross-linking of SU-8 photoresist ink using UV lamps. While the optical annealing of the PS and silver inks provided interesting results in terms of silver conductivity and PS crystallization, controlling these post-processes to provide consistant results proved difficult. It has also been shown, recently, that microsecond-pulsed lasers allow for careful control of the irradiation to reach thermal equilibrium for the different materials present in ink solutions (Bolduc, Trudeau, Beaupre, Cloutier & Galarneau, 2018, p.1418); (Reinhold et al., 2013, p.476-478) This is seen as a critical aspect to provide more consistant and homogeneous optical annealing post-processes, since the heterogeneous nature of printable inks leads to complex heating dynamics and phase transitions, including the evaporation of different organic solvents and surfactants with the sintering of NPs. As such, microsecond-pulsed lasers can provide rapid and highly-localized sintering of the inks without thermal damage to the flexible polymer substrates (Kumpulainen, 2011, p.570-576); (Kwon et al., 2014, p.1137-1145); (Yeo et al., 2014, p.562-568); (Yeo et al., 2012, p.e42315). So far, pulsed laser technology has been used mostly with digital inkjet and aerosol-jet printing technologies, where local laser sintering paths can be adapted on the fly as quickly as the design layouts to allow rapid device prototyping (Lee et al., 2005, p.2436); (Hong et al., 2013, p.5024-5031). These techniques in

optical treatment are seen as pathways to replace lengthy conventional oven annealing processes and could prove beneficial for device fabrication using inkjet printing processes. Moreover, microsecond-pulsed laser sintering could provide additional benefits in terms of consistency and homogeneity when compared to large area optical annealing post-processes such as optical annealing using NIR lamps.

In this chapter, time-dependent finite element method (FEM) simulations using COMSOL 5.2 modeling software are performed to acquire a better understanding of the effects of time-domain pulse shaping on laser sintering of ANP DGP 40TE-20C Ag NP ink. The transient heating behavior of Ag ink traces induced by laser sintering using standard Gaussian shaped is compared to the heating behavior induced by modulated square pulses at different pulse train frequencies. The simulations are based on Institut National d'Optique (INO) proprietary Master Oscillator Pulsed Arbitrary Waveform (MOPAW) fiber laser system sintering experiments performed at INO (Bolduc et al., 2018, p.1418) and support the experimental data obtained.

7.1 Overview of MOPAW Laser Sintering Experiment

Laser sintering experiments are performed by Bolduc et al. using 16-µs laser pulse profiles at 1064nm wavelength, modulated in the time-domain in order to compare the effect of using square- and Gaussian-shaped laser pulses for the sintering of the solvent-based ANP DGP 40TE-20C Ag NP ink. The INO proprietary MOPAW fiber laser allows for such unique pulse-shaping modulation, while also allowing for precise control over the pulse energies (Deladurantaye et al., 2009, p.73860Q). In this study, the laser repetition rate is varied in the range of 0.5-10 kHz, while preserving a constant pulse energy of 0.35 ± 0.004 mJ/pulse and a laser travelling speed of 63 mm/s.

The resulting sheet resistivity from laser-treated Ag ink traces on Kapton substrate are presented in Figure 7.1 a) as a function of the total laser energy dose. Square-shaped laser pulses are compared with conventional Gaussian-shaped laser pulses. A benchmark sheet-

resistivity of 0.02 Ω/□ achieved using conventional oven-annealing is presented as a dashed line in Figure 7.1 a) for comparison. Optimal sintering conditions are achieved using square-shaped pulses with a total laser dose of 22mJ, resulting in sheet resistivities of ~0.027 Ω/□. At this maximum dose, the square-shaped pulses result in sheet resistivities as low as 0.027 Ω/□, compared with 0.055 Ω/□ when using Gaussian-shaped pulses. Images of the resulting sintered ink trances from the laser sintering experiment are presented in Figure 7.1 b) and visually show the difference in resulting sintered ink trace quality. From these images, it is observed that sintering using the non-modulated Gaussian-shaped pulses results in incomplete sintering with increased defects along incident laser pulse edges.

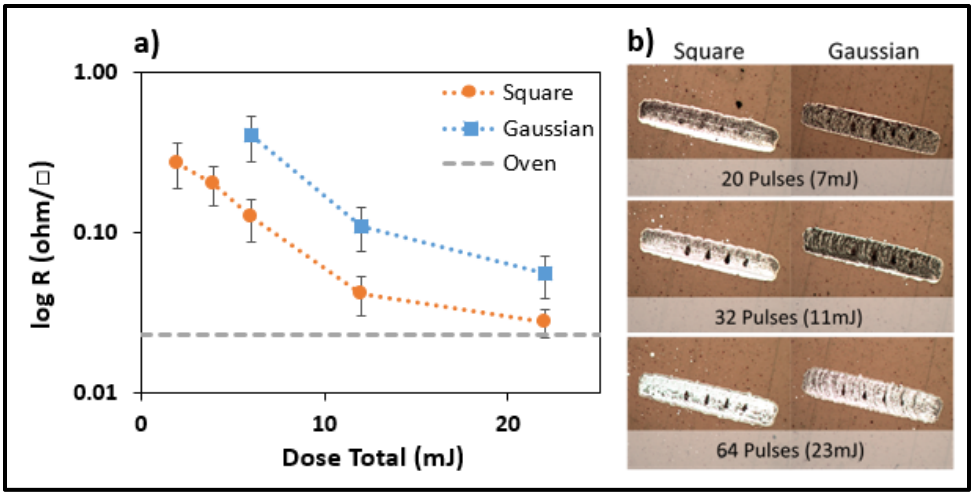

Figure 7.1 a) Sheet resistivity measurements and (b) printed solvent-based Ag ink traces on Kapton polyimide submitted to square- and Gaussian-shaped laser sintering pulses. The reference result achieved using standard oven-annealing process is shown as dashed line. The four black dots in each traces originate from the 4-point-probe resistivity measurements Taken from Bolduc et al. (2018, p.1418)

7.2 COMSOL Modeling

In this section, COMSOL 5.2 simulation software is used to simulate the MOPAW laser sintering experiment detailed in Section 7.1, to help explain the results obtain from the experiment and to acquire a better understanding of transient heating behavior from the laser-

matter interactions involved in laser sintering. The modelled geometrical, and physical properties of the materials are meant to mimic ANP DGP 40TE-20C Ag ink and DuPont™ Kapton® FPC polyimide substrate properties. Whereas, the incident sintering laser pulses are modelled to mimic MOPAW laser excitation pulse train parameters used in the laser sintering experiment. In short, the simulation consists of 350 μJ, 16 μs square- and Gaussian-shaped pulse trains of varying frequencies modelled as a translating heat source incident on a 500 nm-thick Ag ink trace supported by a Kapton substrate. Simulated transient temperature curves and transient heating rates are taken within the modelled ink and provide a better understanding of the experimental results. The simulations can further help to optimize or find limits to the laser sintering process. Moreover, the transient heating behavior of the substrate is simulated to gain an understanding of the heat penetration within the substrate volume.

7.2.1 Geometry, Meshing & Time Step

A printed 500 nm-thick trace with lateral dimensions of 1 mm (length) by 400 μm (width) is modelled as a bulk heterogeneous material. The modelled ink trace is supported by a 200 μm thick Kapton polyimide substrate with lateral dimensions of 3 mm x 2 mm and 0.4 mm thickness. The dimensions of the Kapton substrate are large enough to simulate an infinite substrate while minimizing simulation time. The ink trace and substrate are modelled to be surrounded by ambient atmospheric conditions by applying convection heat lose conditions to the outward facing planes.

The mesh size and time steps are important parameters in any time-dependent FEM simulations, they need to be small enough to simulate the physico-chemical interactions accurately, while keeping them large enough to minimize computation time. In our case, a refined mesh is used to accurately model the heat transfer from the laser to the ink within the studied ink volume. In contrast, a larger mesh size is used for the substrate since it is shown to sustain little temperature variation and thus, does not need to be spatially-resolved as finely (Niittynen, Kankkunen & Mantysalo, 2015, p.133-137). A top view image of the modelled geometry showing the different mesh sizes for the ink trace and the substrate is presented in Figure 7.2. Similarly, time-steps need to be adequate for the simulation purposes. In this case

the pulse width of 16 μs used in the simulation gives a good starting point to evaluate an adequate time-step. A time-step upper limit of 1.6μs or $1/10^{th}$ of pulse width is used to achieve an adequate precision regarding the laser pulses, while keeping the computation time to a minimum. Larger time-step limits are avoided since they may affect the accuracy of the modelled pulses, truncating the top-most sections of some pulses and/or affect the pulse shape, especially in the case of Guassian-shaped pulses.

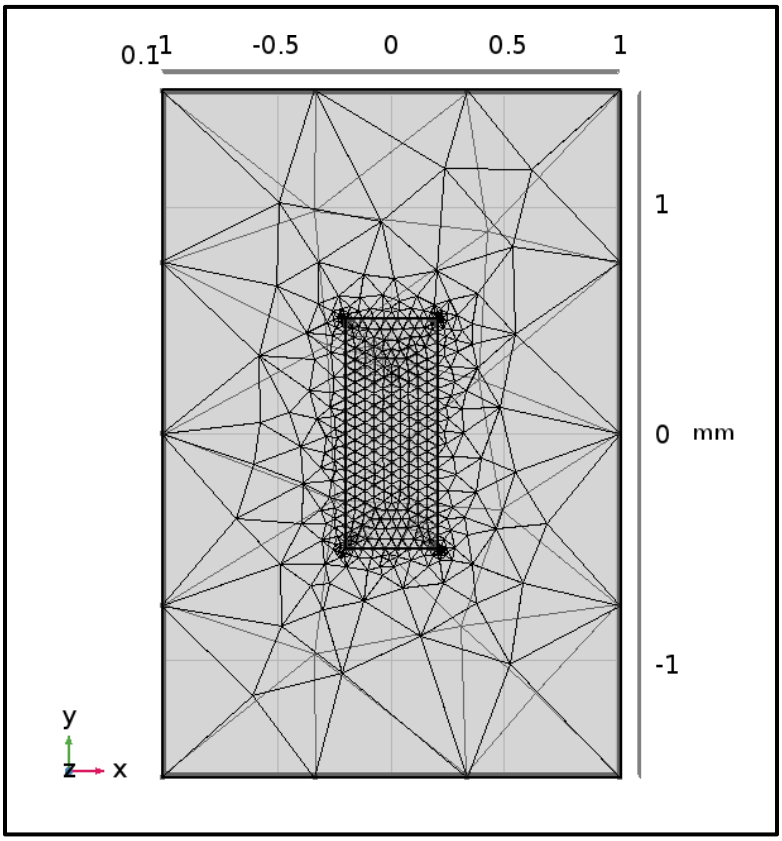

Figure 7.2 Top view of the modeled geometry showing the different mesh sizes used

7.2.2 Material Properties & Modelling Ink Interactions

The printed ink trace is modelled as a bulk heterogeneous material, where its temperature-dependent material properties are either estimated by a weighted average of the materials composition properties, acquired experimentally or by taking typical values from literature

examining similar ink material compositions (Powell, Ho & Liley, 1966, p.2-60); (Choi, Ryu, Park & Moon, 2015, p.904-909). The ink material is modeled after the TGME-solvent-based ANP DGP 40TE-20C ink with a Ag weight content of 30%. Two different phase transitions are integrated within the model due to the heterogeneous property of the material. First, a solid-liquid phase transition for the Ag content of the ink is estimated (from oven annealing results seen in Section 4.3.1) to happen at 200 °C. Secondly, a liquid-gaseous phase transition for the solvent content of the ink is estimated (from solvent boiling point) to occur at 255 °C.

The ink traces are supported by a flexible Kapton polyimide substrate large enough to simulate an infinite substrate but small enough to minimizing simulation time. The bottom surface of the substrate is modeled to have a constant temperature of 60 °C to mimic a printer chuck acting as a heat sink. The estimated or calculated material properties of the solvent-based Ag ink and the supporting Kapton polyimide substrate are presented in Table 7.1. Heat capacity, latent heat of melting and evaporation are taken as weighted averages of known bulk Ag and bulk ethylene glycol values. The thermal conductivity of the Ag ink is estimated from fitting thermal conductivity experimental data, found in the literature and acquired from similar composition inks (Choi et al., p.904-909), the experimental data and fit are shown in Figure 7.3. The remaining property values presented in Table 7.1 are taken from supplier's data sheets (Dupont, 2019); (Dupont, 2018) or typical values found in the literature (Powell et al., 1966, p.2-60).

Table 7.1 Overview of the material properties of the modeled solvent-based Ag ink and of the Kapton substrate

Property	**Solvent-based Ag Ink**	**Kapton Substrate**	**Units**
Thermal Conductivity	$0.036e^{(0.0153[1/K]\cdot T)}$ (0-327°C) 420 (≥327°C)	0.12	W/m K
Heat Capacity	2.09* (0-255°C) 0.24 (≥255°C)	1.09	J/Kg
Density	1560	1420	Kg/m^3
Latent heat of melting	26.4* (200°C)	-	KJ/Kg
Latent heat of evaporation	560* (255°C)	-	KJ/Kg
Initial temperature	60	60	°C

*Weighted average from bulk Ag and bulk ethylene glycol values

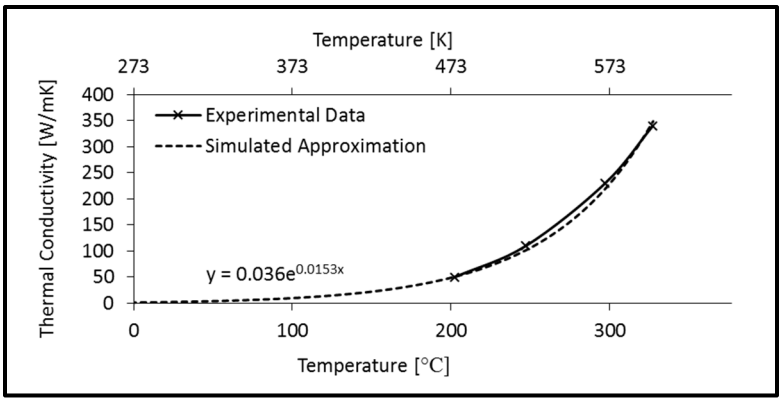

Figure 7.3 Thermal conductivity experimental data of the Ag ink and modeled approximation from exponential fit Adapted from Choi et al. (2015, p.904-909)

7.2.3 Modelling Laser Beam & Interactions

The pulsed laser is modelled as a heat flux on the surface of the Ag ink trace, as the non-reflected portion of the beam energy is assumed to be fully absorbed within the first few nanometers below the surface. The pulsed-laser heat flux equation is shown in Equation 7.1 and contains four (4) key components:

$$PulsedLaser(x, y, t, T) = P \cdot A(T) \cdot Beam(x, y, t) \cdot PulseTrain(t) \quad (7.1)$$

1. A constant tied to the laser power (P).
2. A temperature-dependent absorption coefficient (A(T)).
3. A spatial- and time-dependent beam parameter to account for the shape and displacement of the laser beam (Beam(x,y,t)).
4. A time-dependent pulse train parameter to account for the pulsed nature of the laser (PulseTrain(t)).

The absorption parameter is modelled as a piecewise function and has been assessed from experimental results obtained by means of spectrophotometry from optical reflectivity and transmission measurements of the solvent-based ink traces as a function of various oven

annealing temperatures ranging from 75-300 °C. The reflectivity and transmission measurements as well as the absorption coefficient as a function of temperature are shown in Figure 7.4.

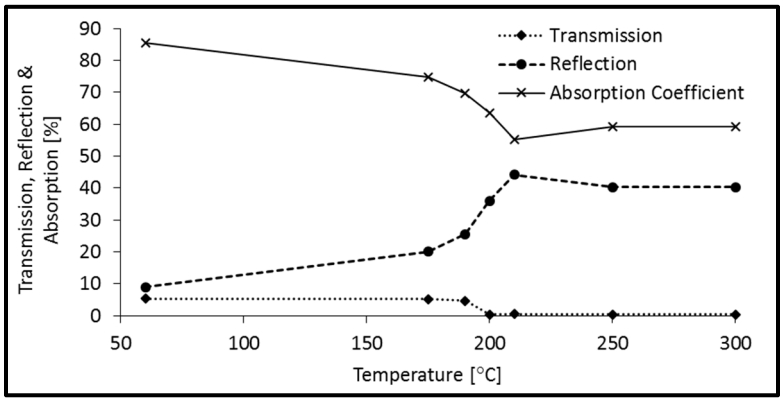

Figure 7.4 Solvent-based Ag ink temperature dependent transmission and reflection values and corresponding modeled absorption coefficient

The beam parameter is modelled as a moving square flat-top beam centered at x = 0 using Equation 7.2, where w_x and w_y are the half-width dimensions of the beam in the x and y directions, respectively. Meaning that for a beam of 400 µm x 400 µm, $w_x = w_y = 200$ µm. y_0 is the starting position of the beam, and V_y is the beam velocity in the y direction.

$$Beam(x,y,t) = e^{-\left(2\left(\frac{x}{w_x}\right)^{10}+2\left(\frac{y-(y_0+V_y\cdot t)}{w_y}\right)^{10}\right)} \tag{7.2}$$

The stationary beam centered at the origin ($V_y = 0$ mm/s and $y_0 = 0$ µm) and modelled using the beam parameter equation (Equation 7.2) is presented in Figure 7.5, showing the square shape of the beam and beam dimensions.

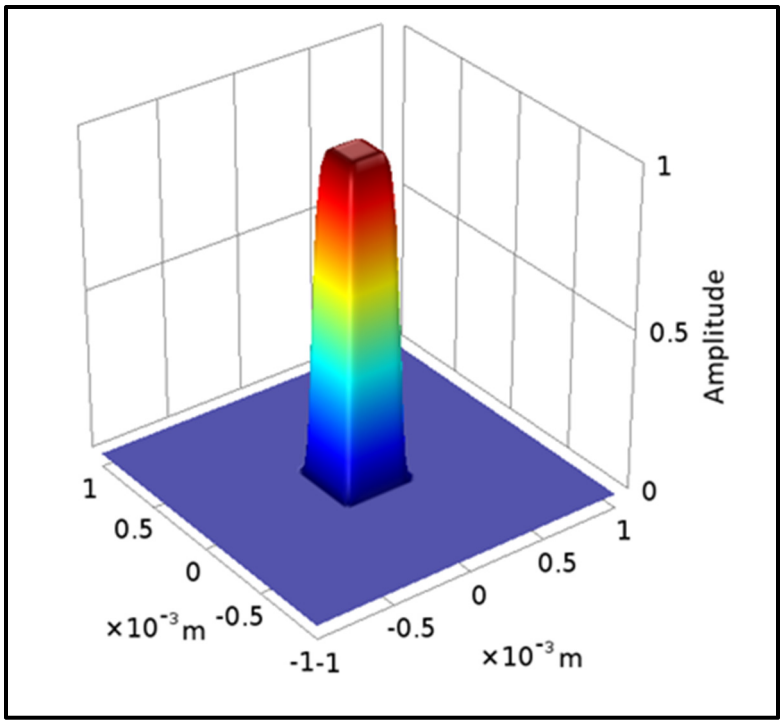

Figure 7.5 Modeled laser square shaped beam from the beam equation

The time-dependent pulse train parameter simulates the temporal square-shaped and Gaussian-shaped laser pulses, as well as the pulsed nature of a flat-top beam laser. For the Square pulse, the pulse train is modelled using the square waveform function in COMSOL. The Gaussian pulse train is produced by introducing a periodicity to the COMSOL Gaussian pulse function. The pulse width of 16 μs is taken as the full width at half maximum (FWHM) of the Square pulses and as the full width at a tenth maximum (FWTM) of the Gaussian pulses, mimicking the laser pulses produced by the MOPAW system used in the experiments. The laser power constant (P) varies depending on the pulse shape. For the COMSOL Gaussian pulse function, the integral of each pulse is equal to unity, meaning that the constant P is simply the value of the total pulse energy (350 μJ). On the other hand, it is the amplitude and not the integral of each pulse that is equal to unity for the square pulse train, therefore the constant P is calculated using the pulse energy divided by the pulse width (350 $\mu J/t_p$). The simulated 5 kHz Gaussian and square pulse trains are presented in Figure 7.6 and Figure 7.7, respectively.

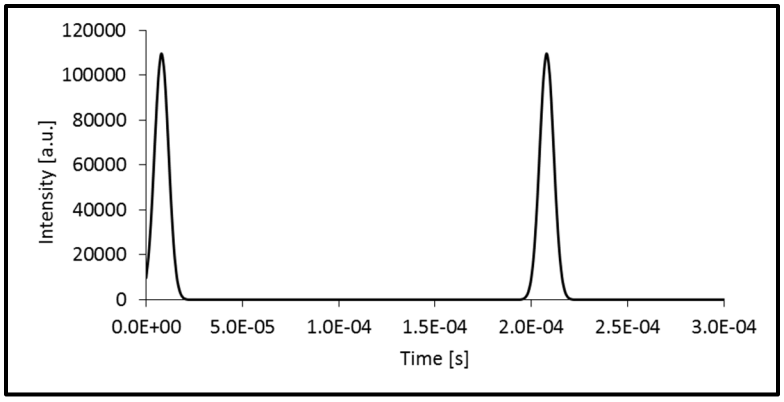

Figure 7.6 Gaussian-shaped pulse train

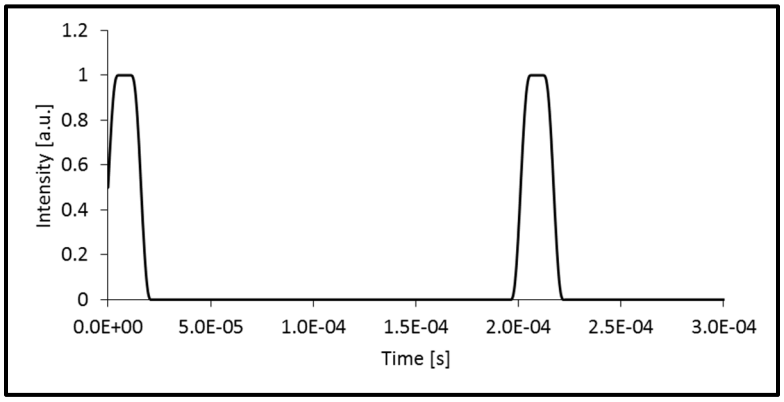

Figure 7.7 Square-shaped pulse train

To validate that the energy is kept constant between the square- and Gaussian-shaped pulses and to account for any change in pulse shape from time-step effects, the pulse trains simulated using the same time-step of 1.6 μs are integrated over a series of ten (10) pulses and the corresponding values of P are adjusted according to Equation 7.3.

$$P_G \int_0^{10/f} PulseTrain_G(t)\,dt \;=\; P_S \int_0^{10/f} PulseTrain_S(t)\,dt \;=\; 3500\ \mu\text{J} \tag{7.3}$$

Where P_G and P_S are the laser power constants for the Gaussian- and square-shaped pulse trains respectively, and $PulseTrain_G(t)$ and $PulseTrain_S(t)$ are the Gaussian- and square-shaped pulse train functions, respectively, of frequency *f*.

7.2.4 Simulation Results

Transient temperature curves calculated for up to 30ms of laser exposure with different operating frequencies (3 kHz, 5 kHz and 10 kHz), taken at the center position of the ink trace are presented in Figure 7.8 for modulated square-shaped and non-modulated Gaussian-shaped pulses. The complete sintering process time for 1 mm long traces equates to around 16 ms when trace displacement is performed at 63 mm/s. The transient temperature curves include 14 ms of relaxation time after completion of the sintering process.

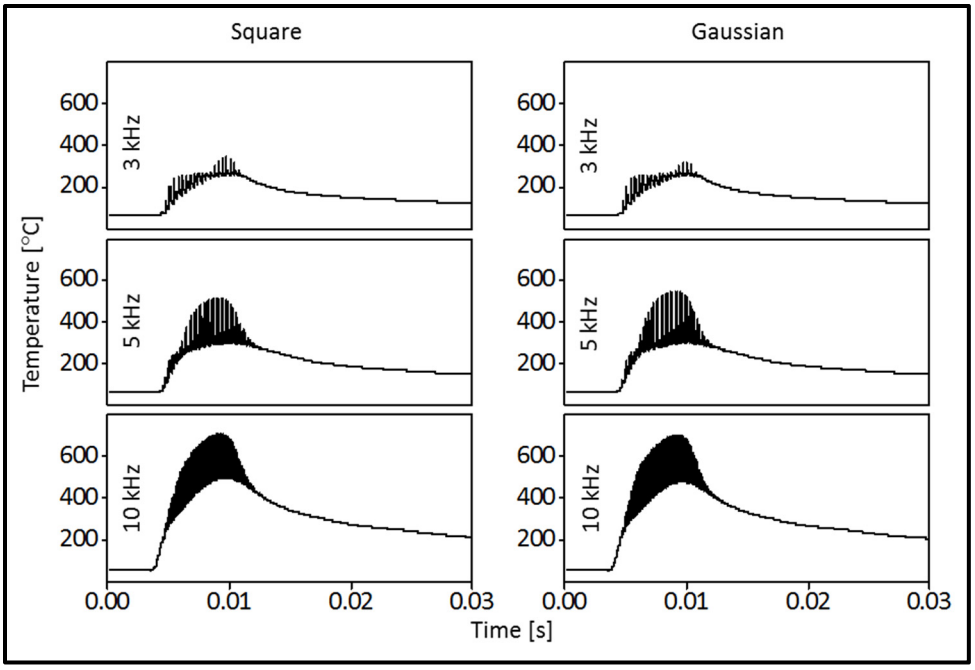

Figure 7.8 Simulated transient temperature curves of the modeled Ag ink traces from the square- and Gaussian-shaped laser pulse trains, taken at the center position of the ink traces, including 16 ms of sintering time and 14 ms of relaxation time

The temperature curves are highly similar for the square- and Gaussian-shaped pulses, although slight differences are observed in the maximum peak temperatures (T_{peak}), maximum residual temperatures ($T_{residual}$) and in the final temperatures after 30 ms. These values are represented in Table 7.2. Overall maximum T_{peak} and maximum $T_{residual}$ values obtained from the simulation are higher for square-shaped pulse trains than for their corresponding Gaussian-shaped pulse trains. However, the maximum T_{peak} for the 5 kHz Gaussian pulse train shows the greatest difference in corresponding temperatures and shows a 30 °C increase compared to the maximum T_{peak} of the 5 kHz square-shaped pulse train. The reason for this increase is yet unknown but can be observed in the transient temperature curves where the "hump" in the transient temperature curve of the 5 kHz Gaussian-shaped pulse train is more elongated when compared to the corresponding curve for the square-shaped pulse train. Nonetheless, all the simulated transient temperature curves result in maximum $T_{residual}$ temperatures at or above the minimum temperature needed to start Ag particle melting and to achieve optimal resistivity values (see Section 4.3.1 on ANP DGP 40TE-20C Post-Printing Process).

Table 7.2 Simulated transient temperature curve characteristics for the square- and Gaussian-shaped pulse trains

Pulse train Frequency	Square-Shaped Pulses			Gaussian-Shaped Pulses		
	Max. T_{peak}	**Max. $T_{residual}$**	**T (t=0.03s)**	**Max. T_{peak}**	**Max. $T_{residual}$**	**T (t=0.03s)**
3 kHz	335 °C	255 °C	122 °C	310 °C	252 °C	120 °C
5 kHz	517 °C	297 °C	153 °C	547 °C	297 °C	150 °C
10 Khz	716 °C	502 °C	215 °C	710 °C	483 °C	210 °C

In order to provide a deeper understanding of the experimental results, a single-pulse temperature curve is extracted from the simulations and is presented in Figure 7.9 a). A higher temperature over a shorter time is observed at the start of the Gaussian pulse, which then cools down faster and results in a lower $T_{residual}$ temperature compared with a corresponding square-shaped pulse excitation. However, the T_{peak} and $T_{residual}$ behavior alone does not explain the

significant difference in the sheet resistivity values found in the experiment performed by Bolduc et al. and detailed in Section 7.1. The heating rates for single-pulse excitations using square- and Gaussian-shaped and pulses are obtained from the time-derivative of the single-pulse temperature curves and are shown in Figure 7.9 b). These simulation results indicate that the maximum heating rate using Gaussian-shaped excitation pulses is almost twice that of square-shaped excitation pulses, with values of 3.15 x 10^7 °C/s and 1.74 x 10^7 °C/s, respectively. These results suggest a significantly-higher laser-induced thermal stress, when using Gaussian-shaped excitation pulses, due to both higher peak temperatures and heating rates. This effect may influence significantly the conductive properties of the sintered ink traces. It may induce some undesirable thermal stress, phase explosion or spallation phenomena, which are derived from the rapid heating and cooling rates from using very high laser intensities or when using Gaussian-shaped excitation pulses (Bulgakova & Bulgakov, 2001, p.199-208); (Zhigilei, Lin & Ivanov, 2009, p.11892-11906); (Thorslund, Kahlen & Kar, 2003, p.51-71). This is consistent with the higher peak temperatures, lower residual temperatures and higher peak heating rates observed from the Gaussian-shaped pulse train simulations. This is also consistent with the inclusion-initiated thermal explosion (TE) model, which predicts that the laser-induced damage temperature (LIDT) for Gaussian pulses is lower than for square-shaped pulses with the same pulse width (Manenkov, 2014, p.010901).

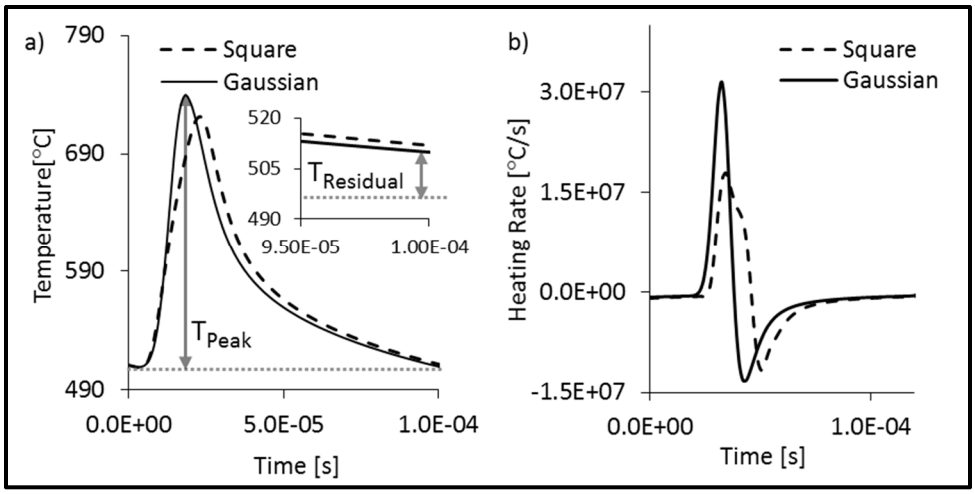

Figure 7.9 a) Single-pulse temperature curves extracted from the square- and Gaussian-shaped pulse train transient temperature curves, showing T_{peak} and $T_{residual}$ characteristics, b) single-pulse heating rates for the square- and Gaussian-shaped pulse trains, derived from the single-pulse temperature curves

A mix of peak and residual temperatures provides the necessary thermal energy to complete the sintering of the ink. Controlling these parameters as well as the induced transient heating rates is seen to be paramout for optimized pulsed laser sintering.

We next look at the effects of the pulse laser sintering on the substrates supporting the ink. The simulations results suggest that the temperature of the Kapton substrate at 10 μm beneath the surface (corresponding to 5 % of the total thickness of the substrate), follows closely the residual temperature of the sintered ink. More than 10 μm under the interface, the substrate temperature remains below the glass transition temperature of the Kapton (360-410 °C) (Dupont, 2018) during the entirety of sintering process. Top and cross-sectional views, showing internal thermal dynamics inside the ink and the substrate at t = 0.016 s, for the square-shaped pulse trains with frequencies of 3 kHz, 5 kHz and 10 kHz are presented in Figure 7.10, Figure 7.11 and Figure 7.12, respectively. Minimal differences in substrate temperature are seen between the square- and Gaussian-shaped pulsed excitation simulations. In all the simulation results, it is observed that the heat penetration into the substrate is limited to the top-most part of the substrate. From the experimental results, the integrity of the substrate and

the ink adhesion is observed to not be affected by this phenomenom (Bolduc et al., 2018, p.1418)

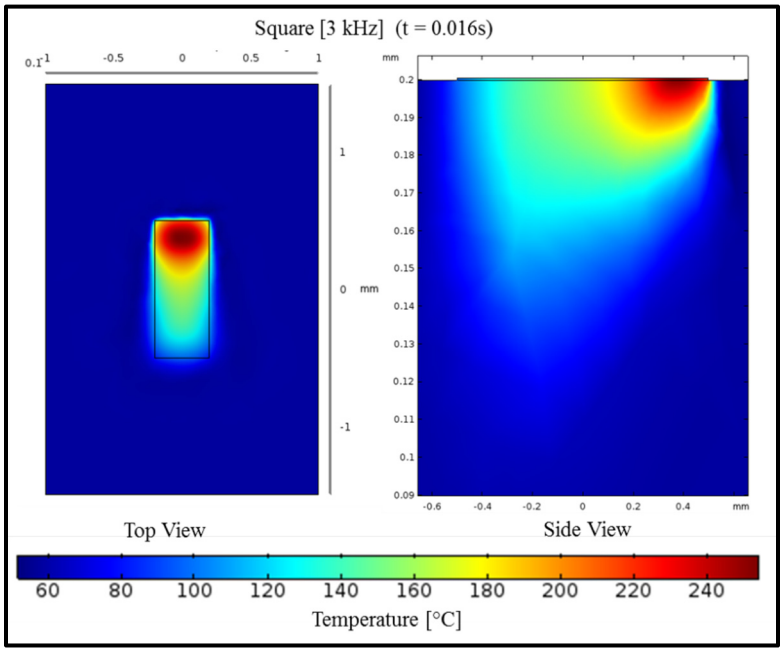

Figure 7.10 Top and cross-sectional views of the heating effects inside the modeled substrate at the end of the sintering process (t = 16 ms) for a 3 kHz square-shaped pulse train

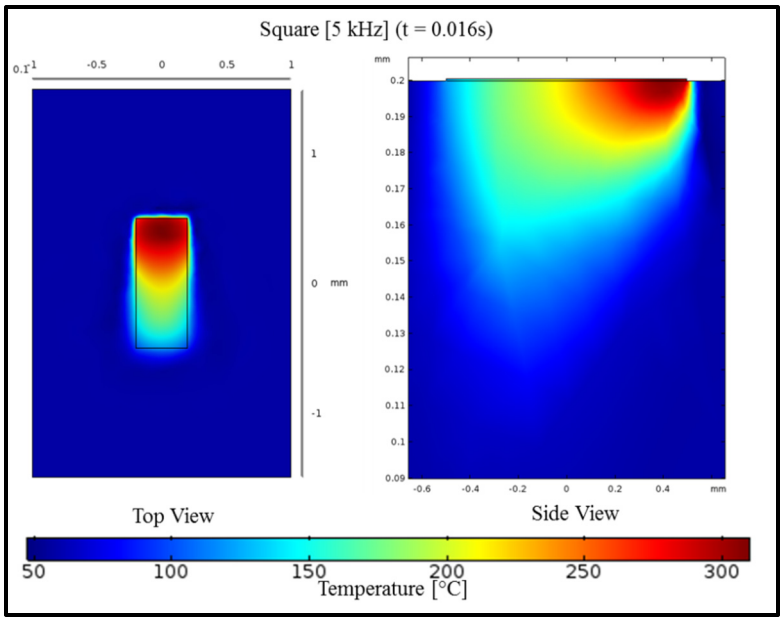

Figure 7.11 Top and cross-sectional views of the heating effects inside the modeled substrate at the end of the sintering process (t = 16 ms) for a 5 kHz square-shaped pulse train

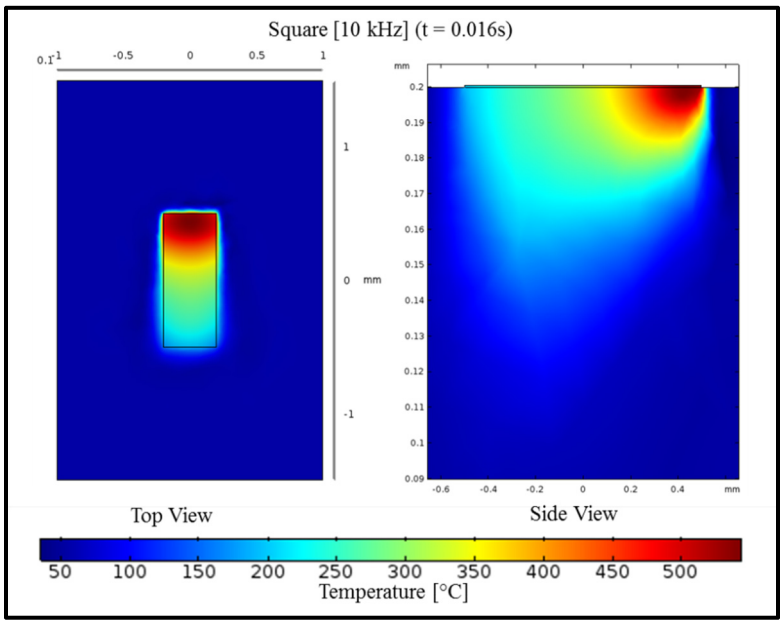

Figure 7.12 Top and cross-sectional views of the heating effects inside the modeled substrate at the end of the sintering process (t = 16 ms) for a 10 kHz square-shaped pulse train

7.3 Conclusion

In this chapter, COMSOL 5.2 simulation software is used to perform simulations of real-world laser sintering experiments on Ag ink traces to gain a deeper understanding of the laser-matter interactions and transient heating behavior of said ink trace. Excitation pulse trains consisting of 350 μJ, 16 μs square- and Gaussian-shaped pulses of varying frequencies are modelled as a translating heat source incident on a 500 nm-thick Ag ink trace supported by a Kapton substrate. Minimal differences in resulting transient heating behavior of the ink traces are found between square- and Gaussian-shaped excitation pulses. These differences do not explain the differences in resulting resistivities of the ink traces for the corresponding real-world experiments. However, large changes in the heating rates are found from the derivatives of the transient heating behaviors from square- and Gaussian-shaped excitation pulses. A two (~2) fold increased in heating rates is observed from Gaussian-shaped excitation pulses and may lead to structural damages from induced mechanical stresses. This phenomenom may explain the results of the real-world experiments. Moreover, from the transient heating behavior inside the supporting substrate volume, it is found that the heat penetration into the substrate is limited to the top-most part of the substrate. The simulations results suggest that the temperature of the Kapton substrate at up to 10 μm beneath the surface follows closely the residual temperature of the sintered ink. More than 10 μm under the interface, the substrate temperature remains below its glass transition temperature throughout the entirety of the sintering process.

CHAPITRE 8

FUTURE WORK

8.1 Perovskite Encapsulation

One of the main draw backs of PS materials is their ease of degradation. There are many pathways to PS degradation such as heat degradation, light exposure degradation and humidity degradation. (Divitini et al., 2016, p.15012); (Bryant et al., 2016, p.1655-1660); (Tong et al., 2015, p.3289-3295); (Wang, Shi, Li, Chen & Huang, 2017, p.1190-1212). PS degradation pathways are most affected by PS composition, and for $MAPbI_{3-x}Cl_x$ the main degradation pathway comes from exposure to high humidity environments. Throughout the work of this thesis, degradation of the PS active layer is one of the most problematic challenge for fabrication and characterization of the devices as these are often performed in two different geographical locations. Special considerations are taken while transporting samples, but degradation is still observed to affect the devices performances. A full study on PS active layer was not performed, but preliminary encapsulation experiments to reduce PS degradation have been performed and are intended to be expanded for future implementation in the printing fabrication process of the PS based devices.

The results of the preliminary encapsulation experiments are presented in Figure 8.1. Four (4) formulations are tested for PS encapsulation;

1. A toluene based poly(methyl methacrylate) (PMMA) solution.
2. A water-based PTFE solution.
3. A perfluorohexane based PTFE solution (AF1600 FC75).
4. A PTFE solution with no co-solvents (AF2400 FC75II).

300 µl of the solutions are deposited directly on printed and annealed Ossila I101 PS samples using a micropipette. The preliminary encapsulation experiment is run for 23 days in ambient room conditions with a RH range of 20% - 60%. Photographs of the samples are recorded daily

to evaluate the degradation in the samples. The $MAPbI_{3-x}Cl_x$ degradation state is evaluated visually by the change in color from dark brown/grey to a yellowish color (Wang et al., 2017, p.1190-1212).

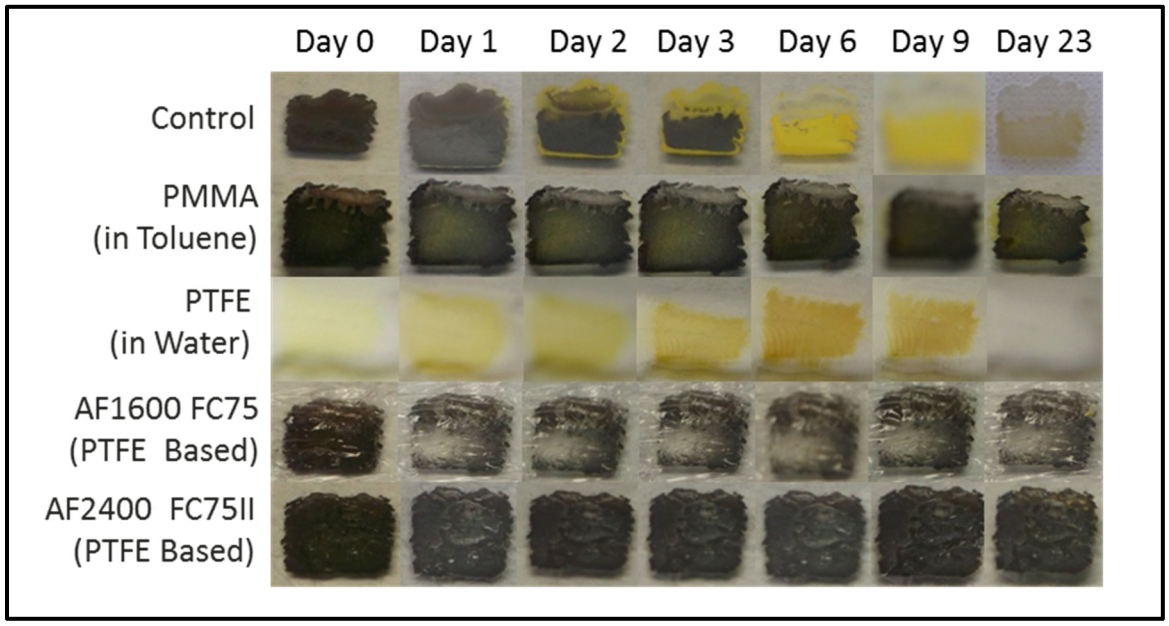

Figure 8.1 Preliminary results of 23-day $MAPbI_{3-x}Cl_x$ PS encapsulation in ambient conditions

Within 2 days the control samples start to show signs of degradation at the edges of the sample, while full degradation is observed from day 6 onwards. The PMMA solution provided some retardation in the degradation. However, some evidence of color change in the center and outside of the sample is still observed from day 1 onwards. This discoloration may be due to PMMA discoloration as yellowish hue is also found outside of the printed sample area. As is expected from a material which is readily degraded in high humidity environments, encapsulation using a water-based PTFE formulation resulted in accelerated degradation. Indeed, full degradation of the sample is seen seconds after the encapsulation is deposited. The two non-water-based PTFE solutions performed best, while the AF2400 FC75II solution outperforming all other solutions. The AF1600 FC75 solution resulted in some displacement of the PS material, but otherwise shows minimal discoloration of the PS sample. It is speculated

that the perfluorohexane used in the AF1600 FC75 solution interacts and may dissolve the PS solids. The PTFE solution with no co-solvent shows some discoloration at the time of deposition but this discoloration disappears on day 1 of the experiment, it is speculated that the discoloration originates from the solution and not the PS sample. Otherwise, no visible changes are seen up to the end of the experiment.

Further characterization of the samples needs to be performed to further evaluate and to quantify the effects of the solutions for encapsulation purposes. Furthermore, experiments to evaluate the degradation of complete PS-based printed devices encapsulated with these solutions are envisioned to test their compatibility with entire device architectures. Finally, once a formulation is identified as an adequate encapsulant, it needs to be adapted for ink jetting and printing to allow for a complete compatible printing process.

8.2 Understanding the Fundamental Connections Between Printing Parameters and Printed Material Properties

As we saw while optimizing printing paramaters in Chapter 5, printing parameters can have a large effect on the printed material properties. This is not fully understood and not much research as been performed on this subject. For example, an in-depth study on the effects of printing parameters on the PS crystal formation would be invaluable to PS-based device prototyping and optimization. This may offer novel pathways to printed device optimization and may offer insights to film formation mechanics from printing processes. This insight may help to bring printing process up to parity with more conventional deposition processes such as CVD, sputtering and evaporation in terms of understanding and industrial mastery.

8.3 All-Inkjet Printed Perovskite-Based Flexible Optoelectronic Device Arrays

As seen in this thesis, all-inkjet printed devices are very challenging to fabricate, especially when considering printing on flexible heat sensitive substrates. A few components of the PS based optoelectronic devices presented in this work are still fabricated using conventional processes. The three main components which are still fabricated using conventional processes

are, the ITO TCO electrode on the substrates, the Au electrodes evaporated on the HTL surface and the TiO_2 spin coated ETL. Printed devices void of the TiO_2 layer are demonstrated to achieve increased performances, therefore this conventionally fabricated layer can be ignored for the time being. The Au electrode evaporated on top of the HTL surface is fabricated using evaporation techniques due to the high temperatures needed to anneal such an electrode using Au inks. These high temperatures damage the PS active layer and thus render the devices obsolete.

One idea to circumvent the damage to the PS layer is to flip the architecture upside down and perform Au deposition before the PS active layer. However, this approach introduces new challenges. The ITO electrode which wasn't a problem before since ITO covered flexible substrates can be obtained commercially, now needs to be deposited after the PS layer. High conductivity PEDOT:PSS formulations could be used as ITO replacement, these formulations are compatible with inkjet printing processes. However, typical PEDOT:PSS ink solutions are formulated with a water solvent which is not compatible for deposition on $MAPbI_{3-x}Cl_x$ as it would induce degradation of the PS layer. More recently, formulation of PEDOT:PSS dispersed in EtOH have entered the market, these could be used for deposition directly on a PS layer as an ITO replacement, but may affect PS crystal structure (see Section 4.3.5). An envisioned device architecture compatible with all-inkjet printing processes is presented in Figure 8.2.

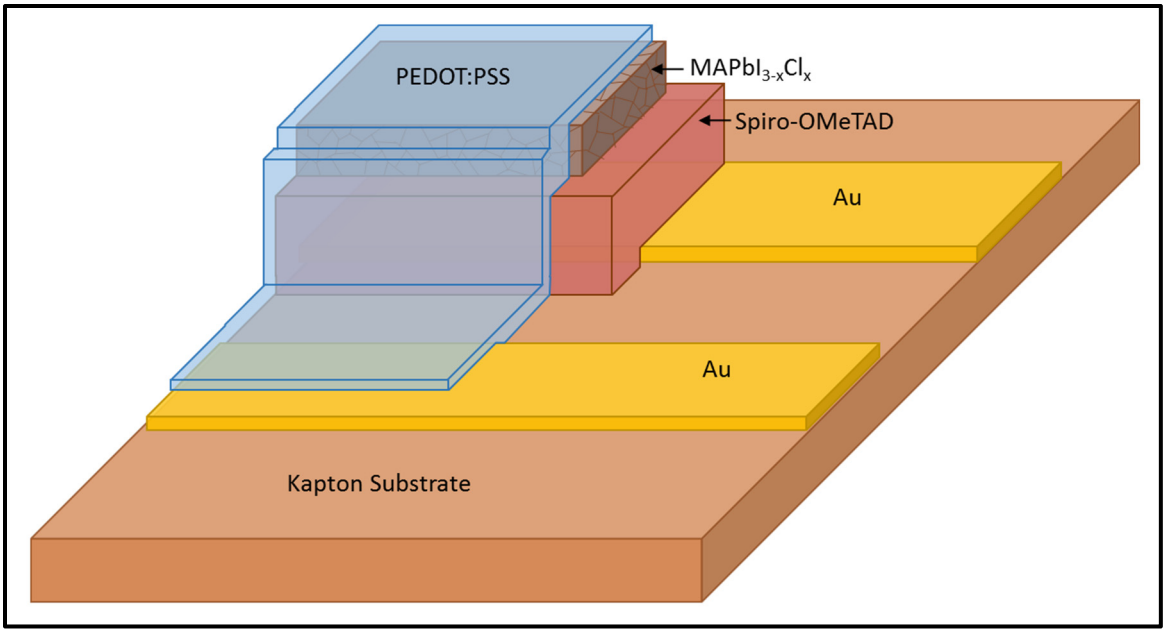

Figure 8.2 Proposed architecture for a fully inkjet printed flexible $MAPbI_{3-x}Cl_x$ PS based optoelectronic device

We have shown that simple readout circuits can be fabricated using all-inkjet printing processes and coupled to printed devices for device operation. However, hybrid approaches to systems fabrication can also be envisioned. In this hybrid approach, devices can be envisioned to be printed directly on conventional or flexible PCBs as a final step in the fabrication process. This has a few advantages when compared to typicall system and board assembly where pick-and-place, solder dispence and reflow equipments are used to position and attach device chips to the PCBs. These advantages may take the form of: reduced assembled PCB weights, more customizable designs and improved throughput. Moreover, some current processes such as solder dispence and reflow could be adapted to use inkjet-printing and optical sintering processes to further improve throughput and flexibility in PCB design.

With advances in AI and vision systems, we could also envision inkjet-printing being used for automated device repair, 2.5 D metamaterial fabrication and automated device design, fabrication and testing through rapid evolutive prototyping itterations.

CONCLUSION

In this thesis the feasibility of MALH PS based optoelectronic device fabrication using inkjet printing processes is established. A state-of-the-art chapter is dedicated to PE, more specifically, to the inkjet printing method. The equipment used and the processes associated with this printing method are viewed. Ink formulation for PE are in part driving the market for device printing, a section of the state-of-the-art is dedicated to these inks. An overview of the emerging PE markets is presented, and a few key players are identified. This state-of-the-art chapter is presented as general background for understanding printing processes and the advantages and disadvantages that these processes bring to device fabrication.

The objectives for the work in this thesis are presented in Chapter 2. The main objective put forward is to evaluate the feasibility of using inkjet printing process to fabricate PS based optoelectronic devices. This is performed through device prototype fabrication using optimized printing processes which are performed throughout this work. Other objectives such as enhancing device performances, adapting ink formulations for inkjet printing and optimizing printing parameters are also put forward, with varying results. Acquiring a deeper understanding of pre- and post- printing processes adapted to the inkjet printing process is also one of the goals of this work. This is performed in two ways, from using optical UV and NIR optical processes to adapt conventional annealing processes and through simulations of laser-matter interactions.

A literature review is performed to identify working PS based optoelectronic device architectures and to acquire an understanding for PS based device inner workings. A TF device structure containing a TiO_2 ETL, a PS active layer and a Spiro-OMeTAD HTL is identified as a suitable architecture for device fabrication using inkjet printing methods. The TiO_2 ETL is found to not be critical to device operations but may enhance device performances, similarly to the Spiro-OMeTAD HTL.

Ink materials and substrates necessary for device fabrication are identified and inkjet printing optimization is performed. Pre-printing treatments for substrate surface energy control are performed and their results are characterized. These treatments take the form of oxygen plasma processes and increase the wettability of the substrates. Optimization of this treatments concludes in a single set of treatment parameters used for all substrates prior to printing. The optimization of the jetting process using a Ceradrop F-series inkjet printing is then performed for the chosen inks and jetting parameters are established for each ink. The resulting ink jets are characterized in terms of stability. Ink manipulation and storage procedures are also established. The optimization of the printing process is performed, and printing test plan results are characterized in terms of printed layer thickness and homogeneity. Printing parameters are identified for each ink and are further optimized in some cases. Post-printing processes using UV and NIR lamps, and other conventional annealing processes are performed to achieve wanted final ink characteristics. Complete printing processes are found and presented for each ink. With this optimization process, the specific objectives pertaining to inkjet printing optimization are met (Section 2.1.1).

Non-PS based passive device are first fabricated to become familiar with the printing process and to evaluate challenges originating from printing multiple ink materials in stacks. Multilayer, generic TFT structures are fabricated, along with interdigitated electrodes, isolated routing electrodes and THz VPPs. While fabricating multilayered generic TFT structures, it is found that ink solvent content is important for printing multilayered structures. We find that inks with orthogonal solvents may be printed on top of each other without solvents interfering with each other. Similarly, for printing the isolated routing electrodes, no additional challenges are seen for printing the dielectric material on top of the conducting material. Interdigitated electrodes and the THz VPPs are printed to evaluate the minimal feature size achievable with the conductive Ag ink and to assess the challenges which arise for printing these small feature sizes. The smallest feature sizes recorded are on the order of 27 μm. Controlling the printing speed is found to be paramount to achieving continuous printing with these dimensions.

PS based optoelectronic devices are inkjet printed using the optimized printing parameters found in this work. First the PV devices are printed or rigid substrates following the identified architecture. This printing process is later adapted for printing on flexible substrates while the device architecture is changed to enhance device performances. The adapted printing process and architecture are used for printing arrays of PV devices which are attached to the isolated routing electrodes for characterization. Champion device energy conversion efficiency is measured at 0.11 %. While this value is low compared to conventionally fabricated devices using the same PS material (13 % - 14 %), it is more comparable to single junction PV devices fabricated using inkjet printing processes (1 % - 5 %). Working device fabrication yields of up to 80% are obtained when printing the PS based PV device arrays. Furthermore, PS based bolometers are printed using the interdigitated electrodes as a basis for fabrication. With the fabrication of these devices and the characterization of their performances, the main set of objectives pretaining to MALH PS-based optoelectronic device printing is met (Section 2.1.2).

Lastly, a simulation study on laser-matter interaction is performed to acquire a deeper understanding of the laser sintering process on printed ink traces. In this study, it is found that laser pulse temporal modulation can have a beneficial effect on the laser sintering process by offering a greater control over heating rates. By performing this study, the last set of objectives pertaining to laser sintering simulations is met (Section 2.1.3).

All in all, most of the objectives put forward at the start of this thesis are met and only a few sub-objectives could not be achieved. Finally, to answer the main question: “Is it feasible to inkjet print MALH based optoelectronic devices”, the answer is “yes”. However, further optimization, especially in terms of adapting the PS inks’ rheological properties to the inkjet printing process, is required to enhance device performances as these are seen to be lacking when compared to conventionally fabricated devices.

In terms of scientific contribution, this work has three major impacts. The first impact is on our understanding of the inkjet printing process, the myriads of pathways in which it can be optimized and used for the fabrication of various devices. In this work, a few of these

optimization pathways are explored in some depth while many more are identified. More specifically, the effects of multiple printing parameters on the thickness, homogeneity and, in some cases, crystalline parameters of the printed features are studied experimentally. The second impact relates to device fabrication. Although the photovoltaic devices fabricated in this work showed poor performances, other devices such as the VPPs, the thermistors and the bolometers showed very promising performances. On top of showing promising performances, these devices are fully inkjet printed, indeed, we believe that this work shows the first fully inkjet printed bolometer devices. The third impact relates to furthering our understanding of the mechanisms of optical sintering using a pulsed light source. Simulations and real-world pulsed laser sintering experiments showed that the heating rate of the scintered ink can be controlled by modulating laser pulse shapes and that this can have a major impact on scintered metallic ink conductivity.

APPENDIX I

CERADROP EJECTION REPORT

An example of a typical Ceradrop ejection report with its different sections is presented in this appendix.

Ejection Report

Ink name	MF-bleu
Operator	Admin
Date/time	Monday, May 16, 2016 4:01 PM

Ink information

mise en route tete 2

Ejection settings

Machine	MF150005Q
Ejection frequency (Hz)	20
Nozzles selected	P1_2-13
Meniscus vaccum (mbar)	10.000000
Lung vaccum (mbar)	600.000000
Pulses	1 : CARTRIDGE@Ag@20160516_C_22V-3us 2 : CARTRIDGE@Ag@20160516_C_22V-3us 3 : CARTRIDGE@Ag@20160516_C_22V-3us 4 : CARTRIDGE@Ag@20160516_C_22V-3us 5 : CARTRIDGE@Ag@20160516_C_22V-3us 6 : CARTRIDGE@Ag@20160516_C_22V-3us 7 : CARTRIDGE@Ag@20160516_C_22V-3us 8 : CARTRIDGE@Ag@20160516_C_22V-3us 9 : CARTRIDGE@Ag@20160516_C_22V-3us 10 : CARTRIDGE@Ag@20160516_C_22V-3us 11 : CARTRIDGE@Ag@20160516_C_22V-3us 12 : CARTRIDGE@Ag@20160516_C_22V-3us 13 : CARTRIDGE@Ag@20160516_C_22V-3us 14 : CARTRIDGE@Ag@20160516_C_22V-3us 15 : CARTRIDGE@Ag@20160516_C_22V-3us 16 : CARTRIDGE@Ag@20160516_C_22V-3us
Head model	CR
Head serial number	
Head position	HEAD1
Time acqusition (µs)	75
Temperature (°C)	Ambiant

Figure-A I-1 Ink information section of the Ceradrop ejection report

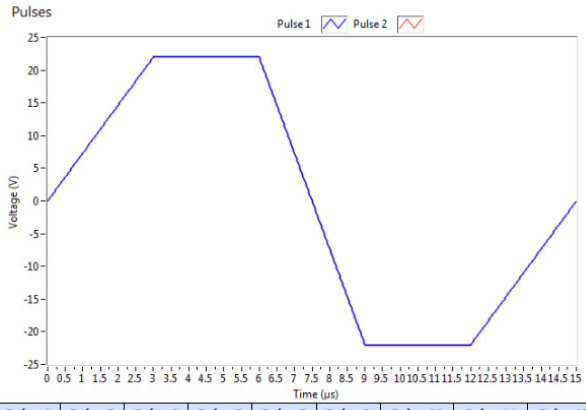

	Pulse 1	Pulse 2	Pulse 3	Pulse 4	Pulse 5	Pulse 6	Pulse 7	Pulse 8	Pulse 9	Pulse 10	Pulse 11	Pulse 12	Pulse 13	Pulse 14	Pulse 15	Pulse 16
Time_0	0.0	0.0	0.0	0.0	0.0	0.0	0.0	0.0	0.0	0.0	0.0	0.0	0.0	0.0	0.0	0.0
Voltage_0	0.0	0.0	0.0	0.0	0.0	0.0	0.0	0.0	0.0	0.0	0.0	0.0	0.0	0.0	0.0	0.0
Time_1	3.0	3.0	3.0	3.0	3.0	3.0	3.0	3.0	3.0	3.0	3.0	3.0	3.0	3.0	3.0	3.0
Voltage_1	22.0	22.0	22.0	22.0	22.0	22.0	22.0	22.0	22.0	22.0	22.0	22.0	22.0	22.0	22.0	22.0
Time_2	3.0	3.0	3.0	3.0	3.0	3.0	3.0	3.0	3.0	3.0	3.0	3.0	3.0	3.0	3.0	3.0
Voltage_2	22.0	22.0	22.0	22.0	22.0	22.0	22.0	22.0	22.0	22.0	22.0	22.0	22.0	22.0	22.0	22.0
Time_3	3.0	3.0	3.0	3.0	3.0	3.0	3.0	3.0	3.0	3.0	3.0	3.0	3.0	3.0	3.0	3.0
Voltage_3	-22.0	-22.0	-22.0	-22.0	-22.0	-22.0	-22.0	-22.0	-22.0	-22.0	-22.0	-22.0	-22.0	-22.0	-22.0	-22.0
Time_4	3.0	3.0	3.0	3.0	3.0	3.0	3.0	3.0	3.0	3.0	3.0	3.0	3.0	3.0	3.0	3.0
Voltage_4	-22.0	-22.0	-22.0	-22.0	-22.0	-22.0	-22.0	-22.0	-22.0	-22.0	-22.0	-22.0	-22.0	-22.0	-22.0	-22.0
Time_5	3.0	3.0	3.0	3.0	3.0	3.0	3.0	3.0	3.0	3.0	3.0	3.0	3.0	3.0	3.0	3.0
Voltage_5	0.0	0.0	0.0	0.0	0.0	0.0	0.0	0.0	0.0	0.0	0.0	0.0	0.0	0.0	0.0	0.0
Time_6	0.0	0.0	0.0	0.0	0.0	0.0	0.0	0.0	0.0	0.0	0.0	0.0	0.0	0.0	0.0	0.0
Voltage_6	0.0	0.0	0.0	0.0	0.0	0.0	0.0	0.0	0.0	0.0	0.0	0.0	0.0	0.0	0.0	0.0
Time_7	0.0	0.0	0.0	0.0	0.0	0.0	0.0	0.0	0.0	0.0	0.0	0.0	0.0	0.0	0.0	0.0
Voltage_7	0.0	0.0	0.0	0.0	0.0	0.0	0.0	0.0	0.0	0.0	0.0	0.0	0.0	0.0	0.0	0.0
Time_8	0.0	0.0	0.0	0.0	0.0	0.0	0.0	0.0	0.0	0.0	0.0	0.0	0.0	0.0	0.0	0.0
Voltage_8	0.0	0.0	0.0	0.0	0.0	0.0	0.0	0.0	0.0	0.0	0.0	0.0	0.0	0.0	0.0	0.0
Time_9	0.0	0.0	0.0	0.0	0.0	0.0	0.0	0.0	0.0	0.0	0.0	0.0	0.0	0.0	0.0	0.0
Voltage_9	0.0	0.0	0.0	0.0	0.0	0.0	0.0	0.0	0.0	0.0	0.0	0.0	0.0	0.0	0.0	0.0
Time_10	0.0	0.0	0.0	0.0	0.0	0.0	0.0	0.0	0.0	0.0	0.0	0.0	0.0	0.0	0.0	0.0
Voltage_10	0.0	0.0	0.0	0.0	0.0	0.0	0.0	0.0	0.0	0.0	0.0	0.0	0.0	0.0	0.0	0.0
Time_11	0.0	0.0	0.0	0.0	0.0	0.0	0.0	0.0	0.0	0.0	0.0	0.0	0.0	0.0	0.0	0.0
Voltage_11	0.0	0.0	0.0	0.0	0.0	0.0	0.0	0.0	0.0	0.0	0.0	0.0	0.0	0.0	0.0	0.0
Time_12	0.0	0.0	0.0	0.0	0.0	0.0	0.0	0.0	0.0	0.0	0.0	0.0	0.0	0.0	0.0	0.0
Voltage_12	0.0	0.0	0.0	0.0	0.0	0.0	0.0	0.0	0.0	0.0	0.0	0.0	0.0	0.0	0.0	0.0
Time_13	0.0	0.0	0.0	0.0	0.0	0.0	0.0	0.0	0.0	0.0	0.0	0.0	0.0	0.0	0.0	0.0
Voltage_13	0.0	0.0	0.0	0.0	0.0	0.0	0.0	0.0	0.0	0.0	0.0	0.0	0.0	0.0	0.0	0.0
Time_14	0.0	0.0	0.0	0.0	0.0	0.0	0.0	0.0	0.0	0.0	0.0	0.0	0.0	0.0	0.0	0.0
Voltage_14	0.0	0.0	0.0	0.0	0.0	0.0	0.0	0.0	0.0	0.0	0.0	0.0	0.0	0.0	0.0	0.0
Time_15	0.0	0.0	0.0	0.0	0.0	0.0	0.0	0.0	0.0	0.0	0.0	0.0	0.0	0.0	0.0	0.0
Voltage_15	0.0	0.0	0.0	0.0	0.0	0.0	0.0	0.0	0.0	0.0	0.0	0.0	0.0	0.0	0.0	0.0
Time_16	0.0	0.0	0.0	0.0	0.0	0.0	0.0	0.0	0.0	0.0	0.0	0.0	0.0	0.0	0.0	0.0
Voltage_16	0.0	0.0	0.0	0.0	0.0	0.0	0.0	0.0	0.0	0.0	0.0	0.0	0.0	0.0	0.0	0.0

Figure-A I-2 Pulse information section of the Ceradrop ejection report

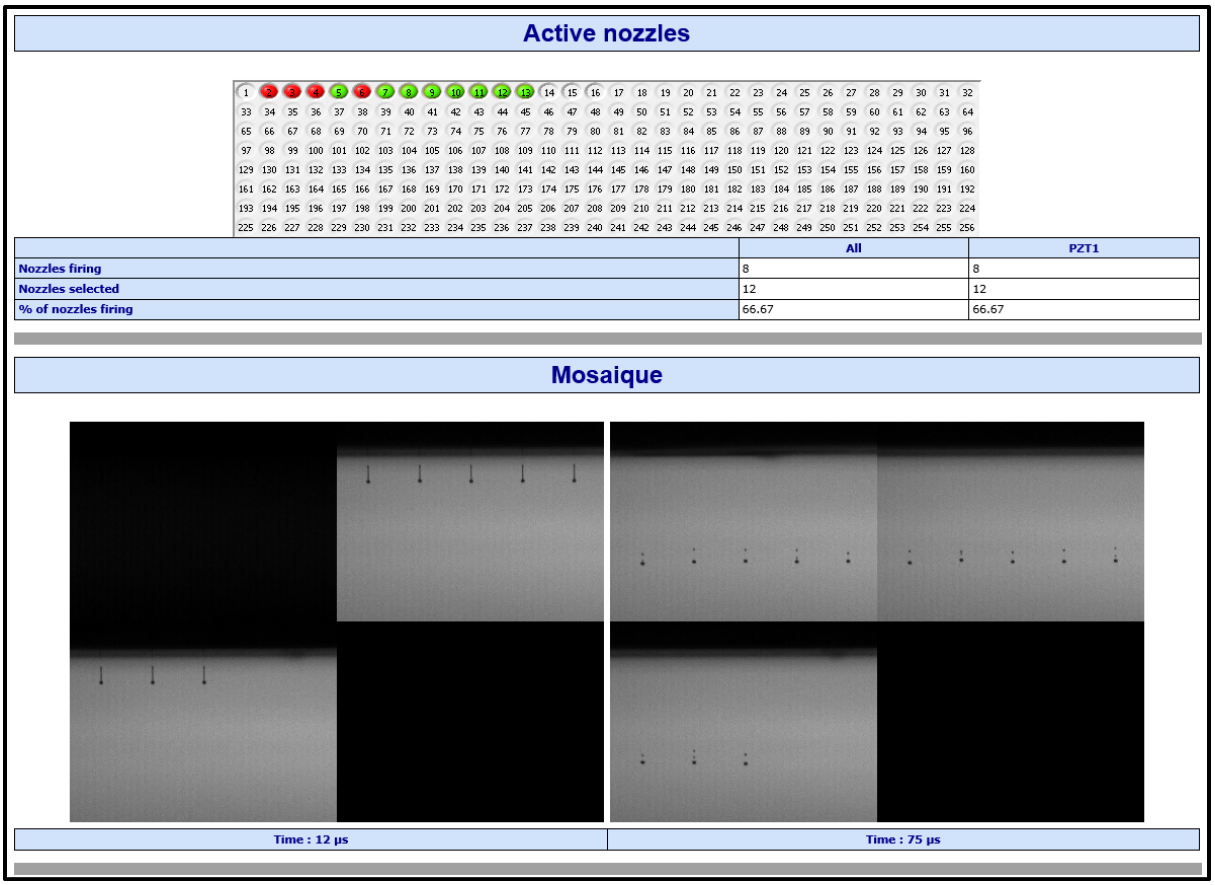

Figure-A I-3 Jetting statistical analysis section of the Ceradrop ejection report

Static analysis on the nozzle plate

	ALL	PZT1
Nozzles Analysed	11	11
Nozzles Selected	12	12
% of Nozzles Analysed	91.67	91.67

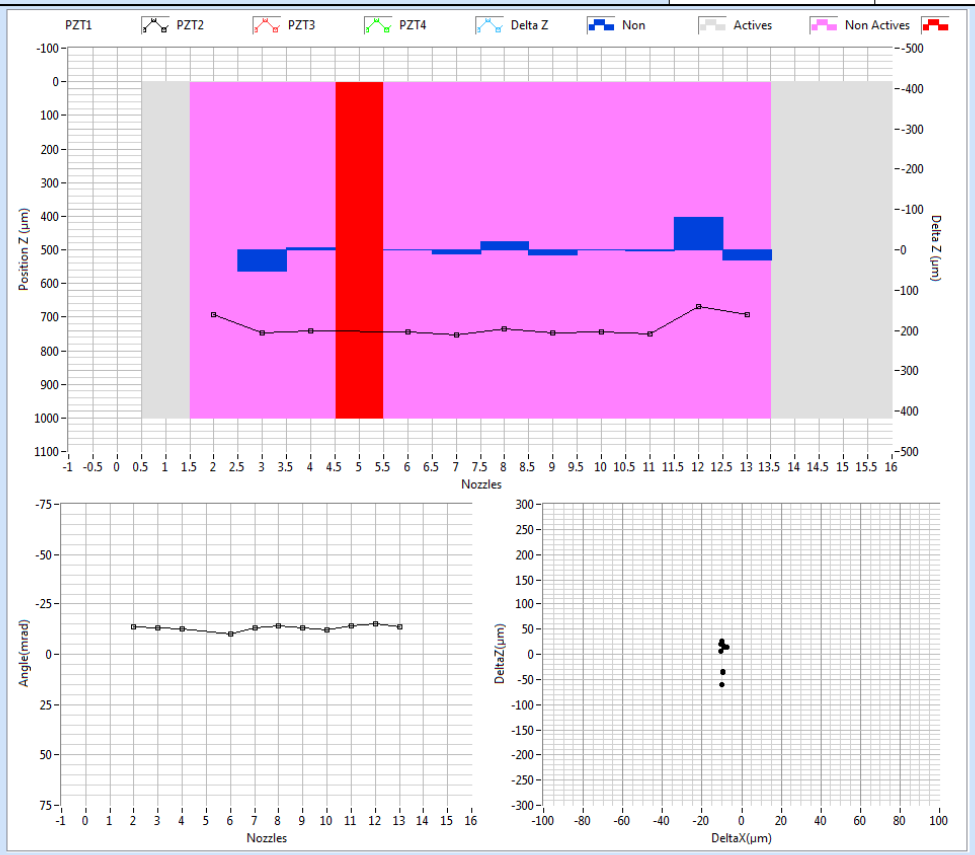

	ALL
POSITION Z (µm)	
Min	667.55
Max	754.05
Average	728.76
Standard deviation	29.31
Delta	86.50
VOLUME (pl)	
Min	1.67
Max	6.84
Average	4.15
Standard deviation	2.11
DELTA X (µm)	
Min	-10.57
Max	-7.62
Average	-9.29
Standard deviation	0.83
Angle (mrad)	
Min	-15.06
Max	-10.25
Average	-13.13
Standard deviation	1.27

Figure-A I-4 Cont. Jetting statistical analysis section of the Ceradrop ejection report

Local dynamic analysis

	Nozzle N°9	Nozzle N°10	Nozzle N°11	Nozzle N°12	Nozzle N°13
Formation distance(µm)	404.36	410.38	417.32	416.67	417.41
Average diameter (µm)	16.24	15.89	19.93	21.44	17.20
Average volume (pl)	2.24	2.11	4.50	5.47	2.79
Average velocity (m/s)	0.00	9.86	0.00	13.28	14.15
Average angle (mrad)	NaN	10.83	-53.89	15.82	9.80

Local static analysis

	Nozzle N°9	Nozzle N°10	Nozzle N°11	Nozzle N°12	Nozzle N°13
POSITION Z (µm)					
Min	649.91	657.24	644.90	647.20	659.46
Max	755.72	753.45	750.82	746.26	758.94
Average	715.77	718.31	702.70	709.56	715.05
Delta	105.81	96.22	105.92	99.06	99.48
Standard deviation	37.50	33.87	36.55	34.68	36.71
VOLUME (pl)					
Min	1.62	1.63	1.57	1.62	1.61
Max	6.74	6.68	6.73	6.55	6.82
Average	3.94	4.29	3.39	3.95	3.86
Ecart-type	2.03	2.05	1.92	2.05	2.20
DELTA X (µm)					
Min	-11.63	-11.17	-13.34	-11.01	-10.11
Max	-9.21	-9.45	-7.75	-8.44	-8.42
Delta	2.42	1.72	5.59	2.57	1.69
Average	-10.16	-10.19	-10.01	-9.51	-9.32
Standard deviation	0.59	0.48	0.97	0.56	0.51
Angle(mrad)					
Min	-16.36	-15.60	-17.95	-14.82	-14.67
Max	-12.92	-13.47	-10.35	-12.07	-12.16
Average	-14.20	-14.19	-14.25	-13.40	-13.04
Standard deviation	0.75	0.44	1.18	0.66	0.54

Figure-A I-5 Static and dynamic analysis section of the Ceradrop ejection report

APPENDIX II

ANP-DGP 40TE-20C PRINTING TEST PLAN

The printing test plans for ANP DGP 40TE-20C are performed on plasma treated FT Kapton-FPC 300 substrates using the jetting parameters specified in Section 4.2.3, the printing lattice, drop interpenetration and chuck temperature are controlled. Optical images of the single layered printed features are shown in Figure-A II-1, Figure-A II-2 and Figure-A II-3, for chuck temperatures of 25 °C, 40 °C and 60 °C respectively. The same test plan is performed using two printed layers instead of one, the overall trends are similar to single layer printed features and are not shown, characterization of both the single layered and two layered printed features are performed. From these figures, a few trends become evident;

1. Printing performed with a chuck temperature of 25 °C results in cleaner printed features although ink bleeding is more pronounced when using 50% drop interpenetration.
2. The coffee ring effect is apparent for printing performed at 40 °C and is more pronounced at 60 °C.
3. Lower ink coverage as chuck temperature increases, for 0% and 25% drop interpenetration,
4. Printing performed at 25% drop interpenetration results in visually better deposition. regardless of chuck temperature. With the exception of 50% drop interpenetration at 25 °C using a Hex Shift printing lattice.
5. Printing performed using a Hex Shift lattice results in visually cleaner printed features and reduced coffee ring effects when compared to the other printing lattices.

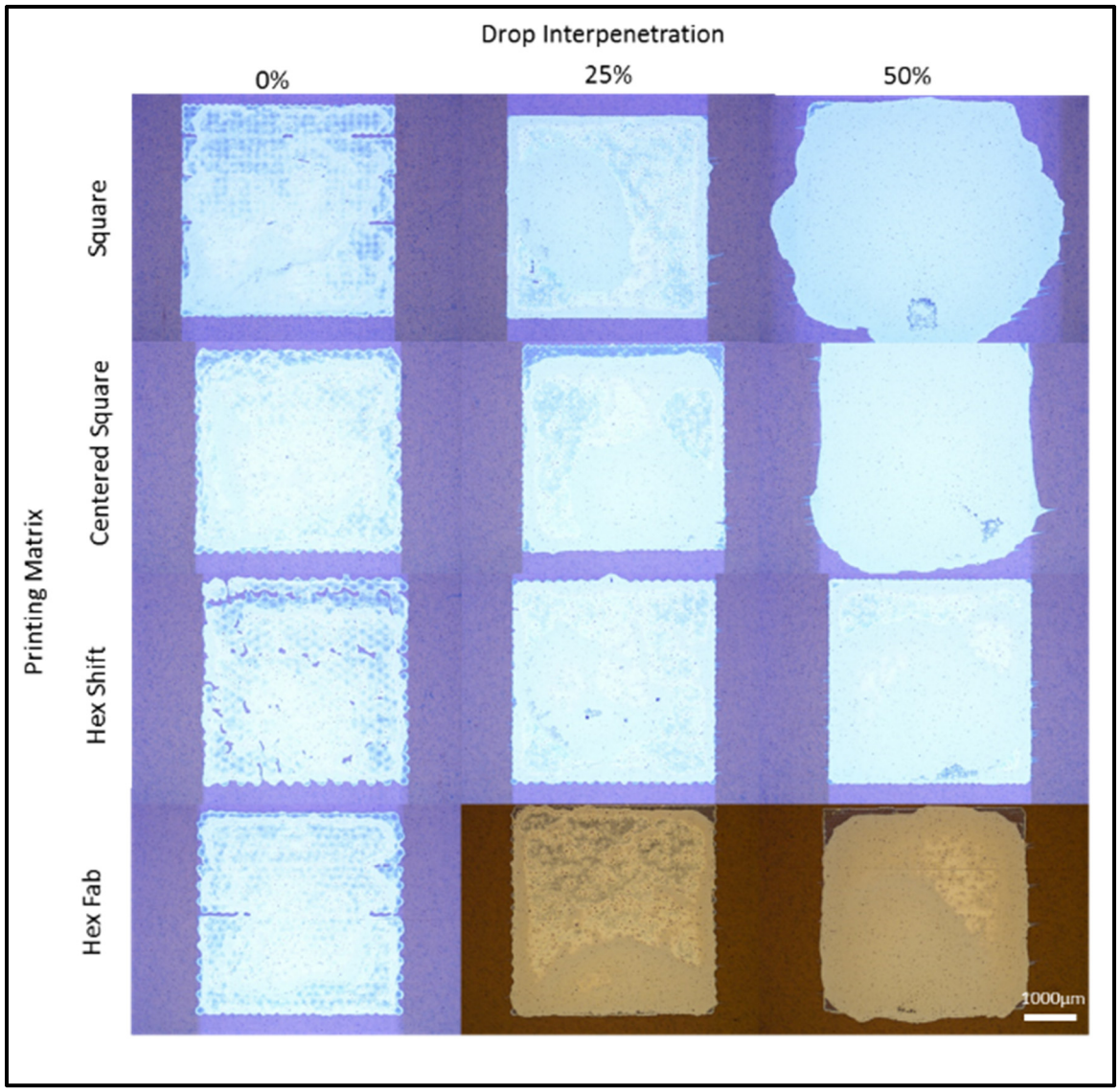

Figure-A II-1 Photographs of the printing test plans for ANP-DGP 40TE 20C Ag ink on a Kapton substrate with a chuck temperature of 25 °C

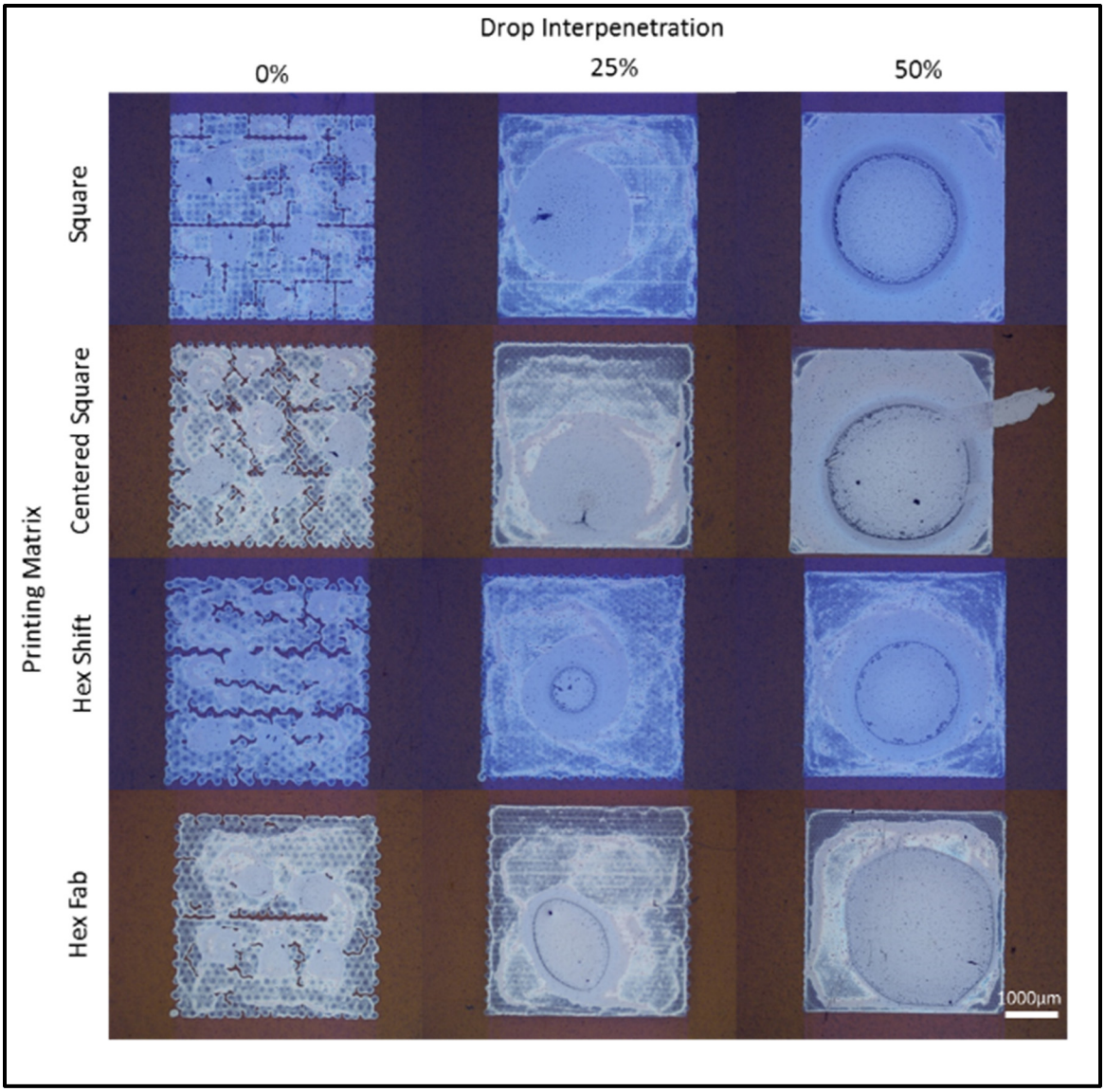

Figure-A II-2 Photographs of the printing test plans for ANP-DGP 40TE 20C Ag ink on a Kapton substrate with a chuck temperature of 40 °C

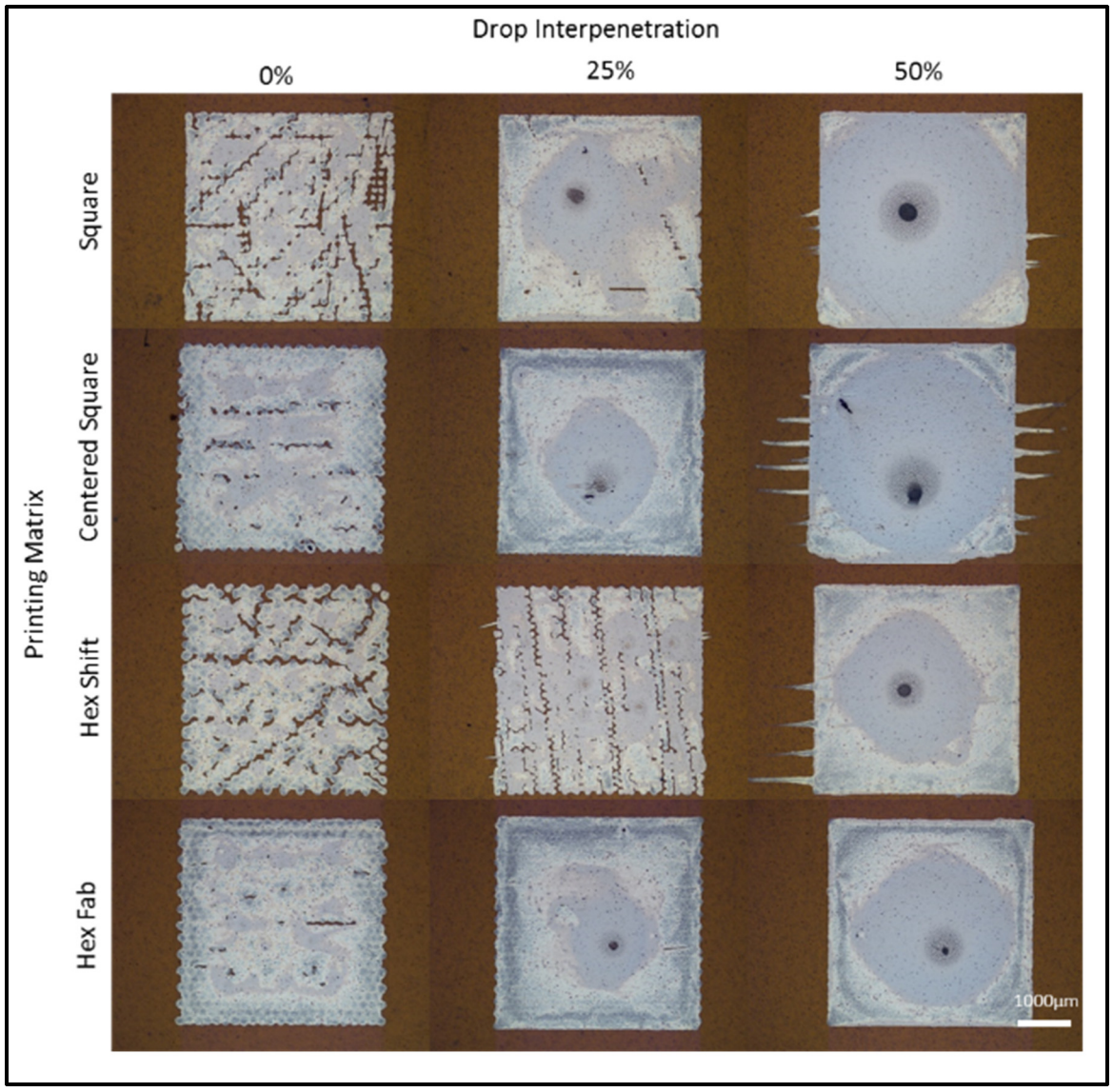

Figure-A II-3 Photographs of the printing test plans for ANP-DGP 40TE 20C Ag ink on a Kapton substrate with a chuck temperature of 60 °C

APPENDIX III

MICROCHEM SU-8 PHOTORESIT INK TEST PLAN

The printing test plans for MicroChem SU-8 photoresist ink are performed on plasma treated FT Kapton-FPC 300 substrates using the jetting parameters specified in section 4.2.3, the printing lattice, drop interpenetration and chuck temperature are controlled. Optical images of the single layered printed features are shown in Figure-A III-1, Figure-A III-2 and Figure-A III-3, for chuck temperatures of 25 °C, 40 °C and 60 °C respectively. The same test plan was performed using two printed layers instead of one, the overall trends are similar to single layer printed features and are not shown, characterization of both the single layered and two layered printed features are performed. From these figures, a few trends become evident;

1. Printing performed with a chuck temperature of 25 °C results in less clean edges of the printed features.
2. Printing performed with higher chuck temperatures and lower drop interpenetration results in ridges on the surface from non-coalescence of the drops jetted from adjacent nozzles.
3. Multiple printer parameters result in visually adequate printed features.

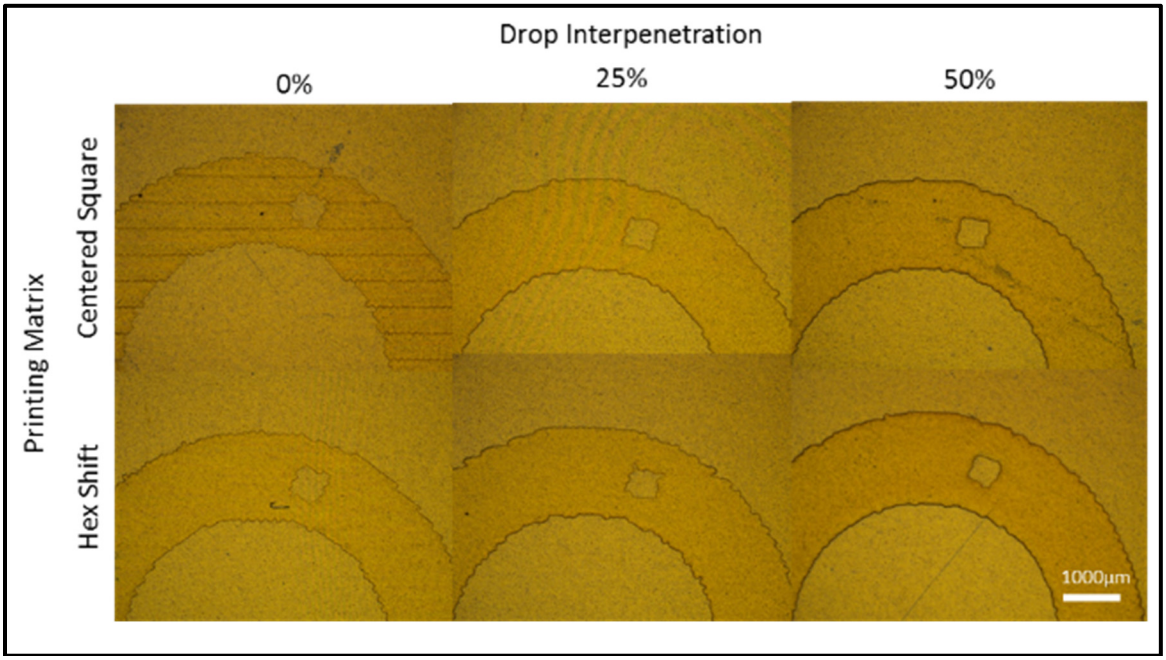

Figure-A III-1 Photographs of the printing test plans for MicroChem SU-8 ink on a Kapton substrate with a chuck temperature of 25 °C

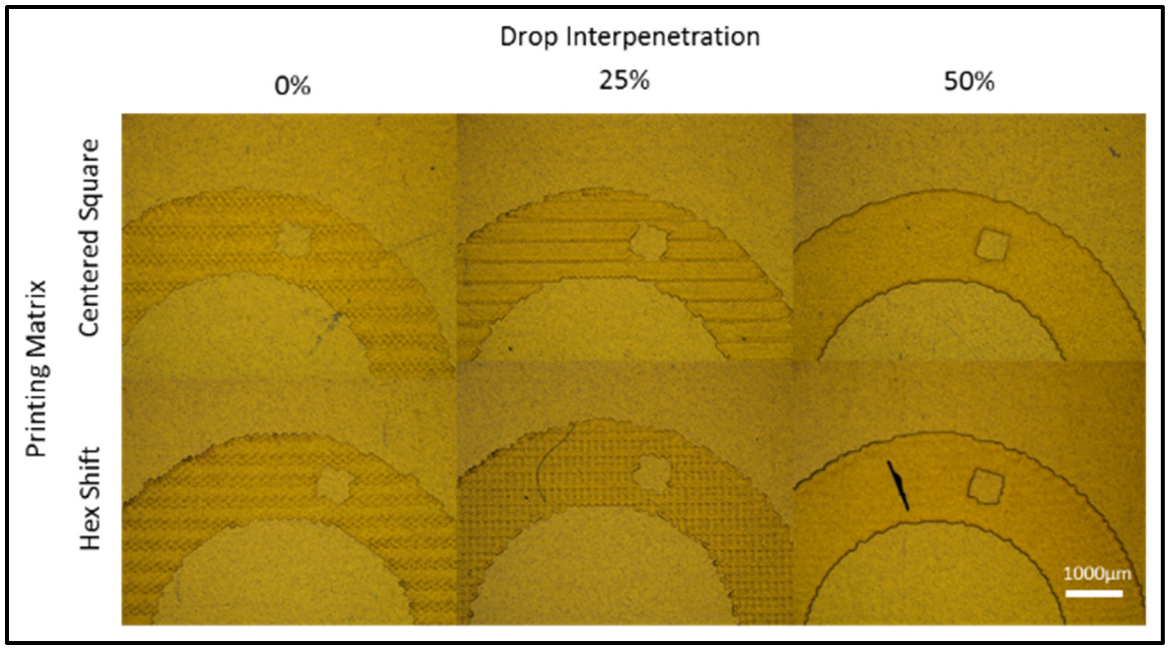

Figure-A III-2 Photographs of the printing test plans for MicroChem SU-8 ink on a Kapton substrate with a chuck temperature of 40 °C

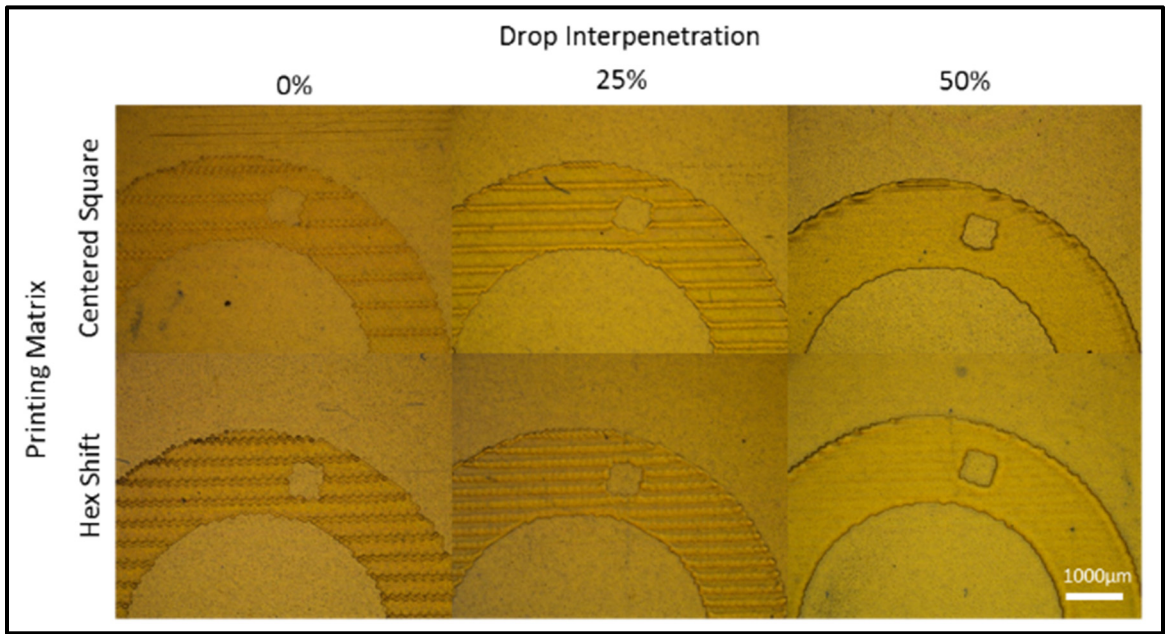

Figure-A III-3 Photographs of the printing test plans for MicroChem SU-8 ink on a Kapton substrate with a chuck temperature of 60 °C

APPENDIX IV

POLY INK HC PEDOT:PSS PRINTING TEST PLAN

The printing test plans for Poly Ink HC PEDOT:PSS semiconducting ink are performed on plasma treated FT Kapton-FPC 300 substrates using the jetting parameters specified in section 4.2.3, the printing lattice, drop interpenetration and chuck temperature are controlled. Optical images of the seven layered printed features are shown in Figure-A IV-1, Figure-A IV-2 andFigure-A IV-3, for chuck temperatures of 25 °C, 40 °C and 60 °C respectively. For this test plan, negative drop interpenetrations are chosen, as positive drop interpenetration results in beading of the ink on the surface due to the rheological properties of the ink. The tests plan are performed using seven and ten printed layers to counteract the negative drop interpenetration to achieve complete surface coverage and adequate thicknesses. Although the optical images of the 10 layered printed features are not shown, characterization of both the seven layered and ten layered printed features are performed. From these figures, a few trends become evident;

1. Gaps between raster tracks are prominent.
2. Printing performed at lower chuck temperatures results in better surface coverage.
3. Printing performed at higher drop interpenetration results in more prominent gaps between raster tracks.

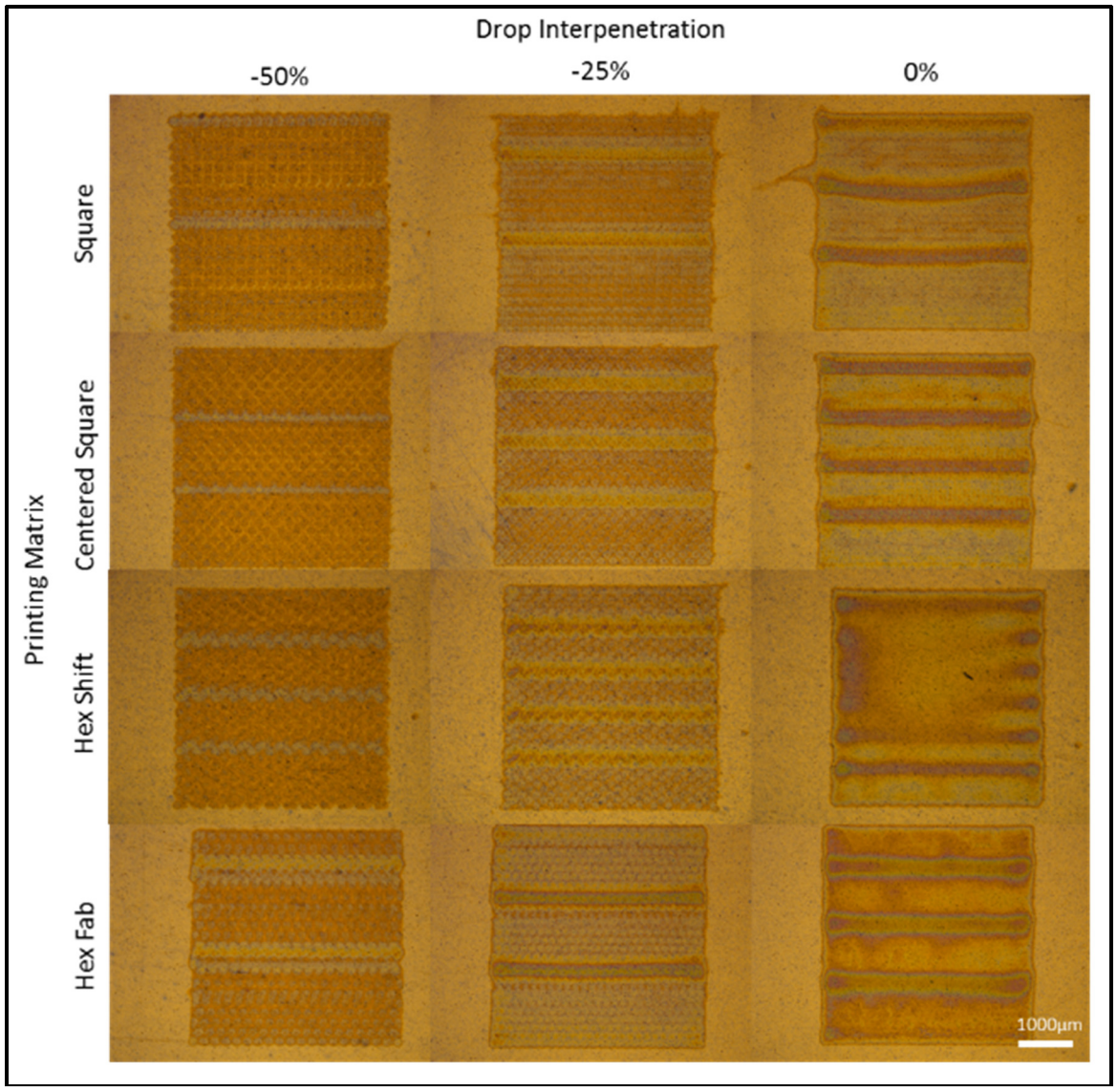

Figure-A IV-1 Photographs of the printing test plans for Poly Ink HC PEDOT:PSS ink on a Kapton substrate with a chuck temperature of 25 °C

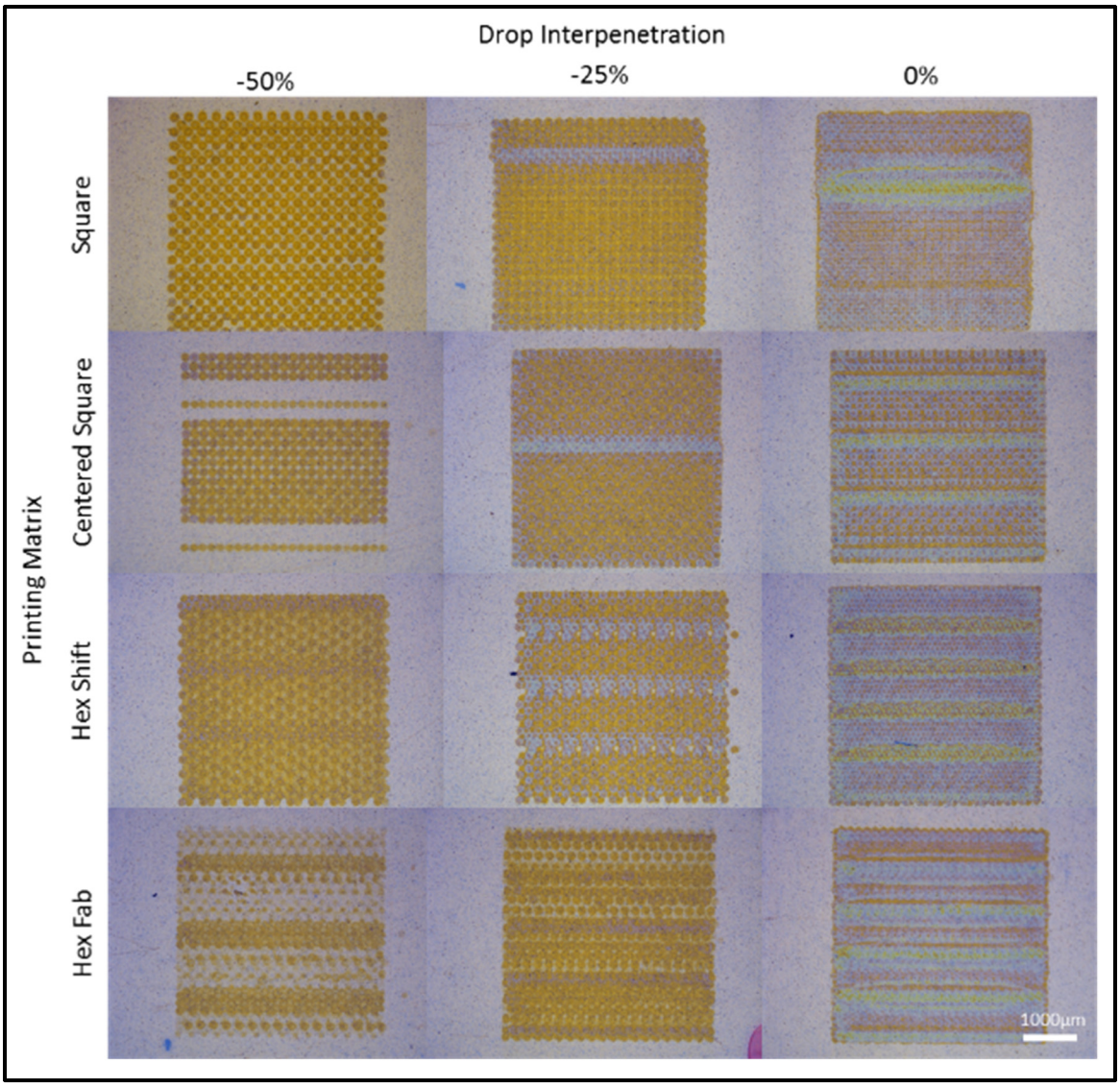

Figure-A IV-2 Photographs of the printing test plans for Poly Ink HC PEDOT:PSS ink on a Kapton substrate with a chuck temperature of 40 °C

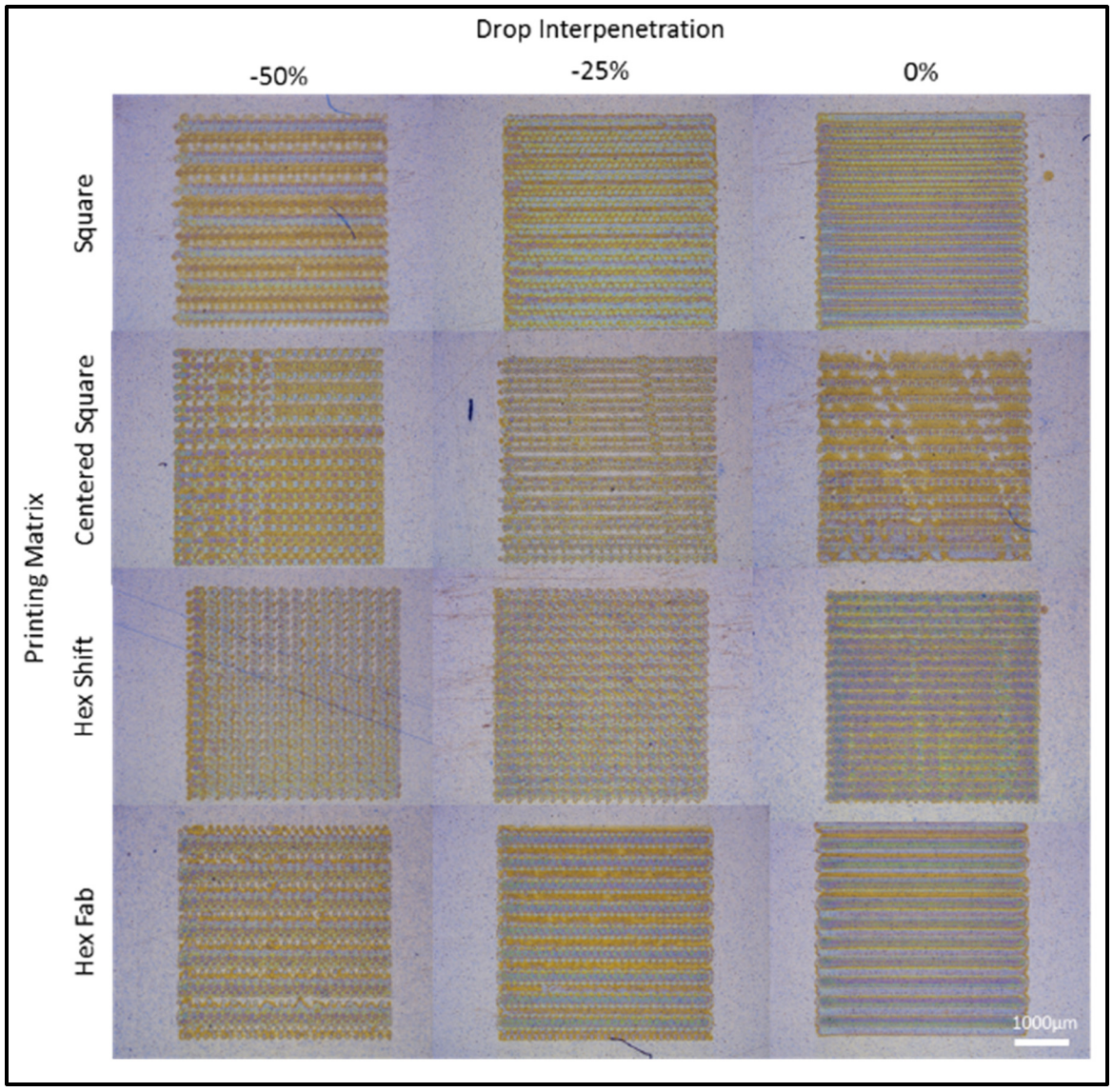

Figure-A IV-3 Photographs of the printing test plans for Poly Ink HC PEDOT:PSS ink on a Kapton substrate with a chuck temperature of 60 °C

APPENDIX V

SPIRO-OMETAD PRINTING TEST PLAN

The printing test plans for Spiro-OMeTAD formulation are performed on plasma treated FT Kapton-FPC 300 substrates using the jetting parameters specified in section 4.2.3, the printing lattice, drop interpenetration and chuck temperature are controlled. Test plans consisting of only single printed layer are performed as the targeted layer thickness is achieved with these conditions. From the State-of-the-Art and Literature Review sections, a layer thickness of 300 - 400 nm is targeted for the implementation of a Spiro-OMeTAD HTL for TF device applications in photo-sensing and energy harvesting. Although this is not an inkjet adapted commercial ink, it is found that this formulation of Spiro-OMeTAD results in the most homogeneous printed layers out of all the ink formulation used in this work. Optical images of the printed features are shown in Figure-A V-1, Figure-A V-2 and Figure-A V-3, for chuck temperatures of 30 °C, 40 °C and 60 °C, respectively.

From these figures, a few trends become evident;

1. Raster track ridges are present for most printing parameters tested, and raster overlap should be used for optimized printing.
2. Choice of printing lattice seems to affect the quality of deposition the most.
3. Visually clean deposition for most printing parameters with no ink bleeding outside of the printed area and very good coverage.

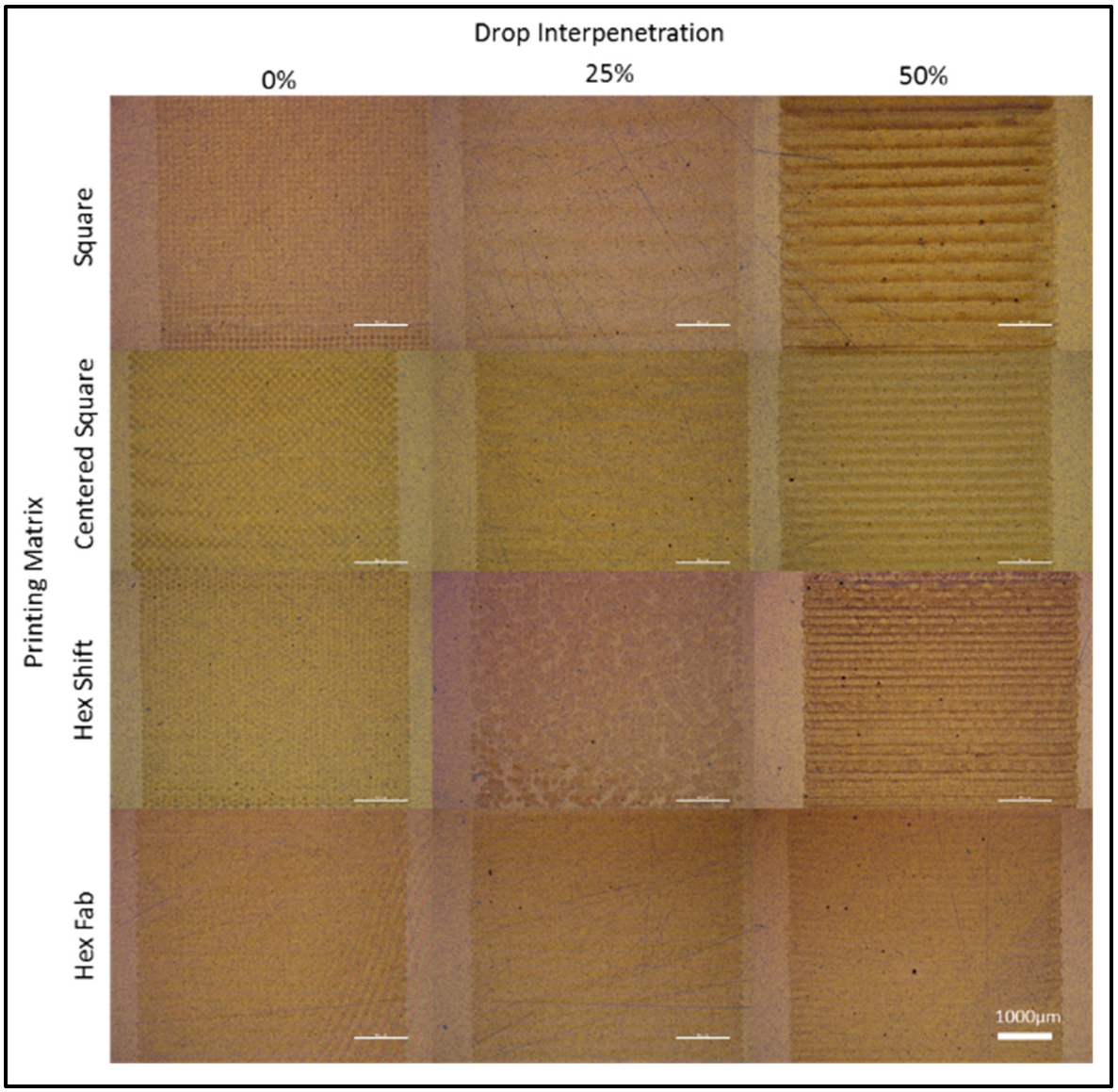

Figure-A V-1 Photographs of the printing test plans for spiro-OMeTAD ink on a Kapton substrate with a chuck temperature of 30 °C

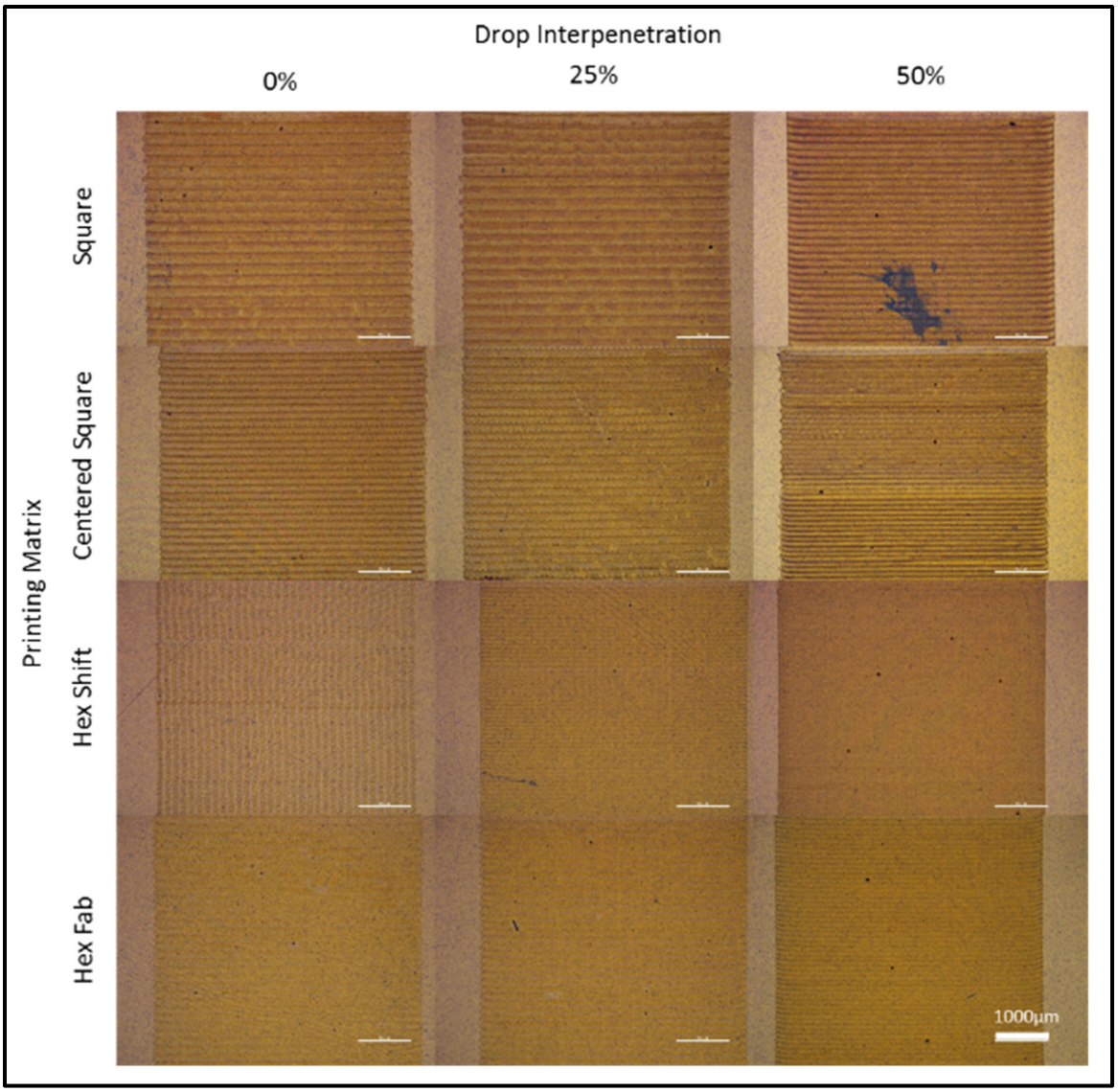

Figure-A V-2 Photographs of the printing test plans for spiro-OMeTAD ink on a Kapton substrate with a chuck temperature of 40 °C

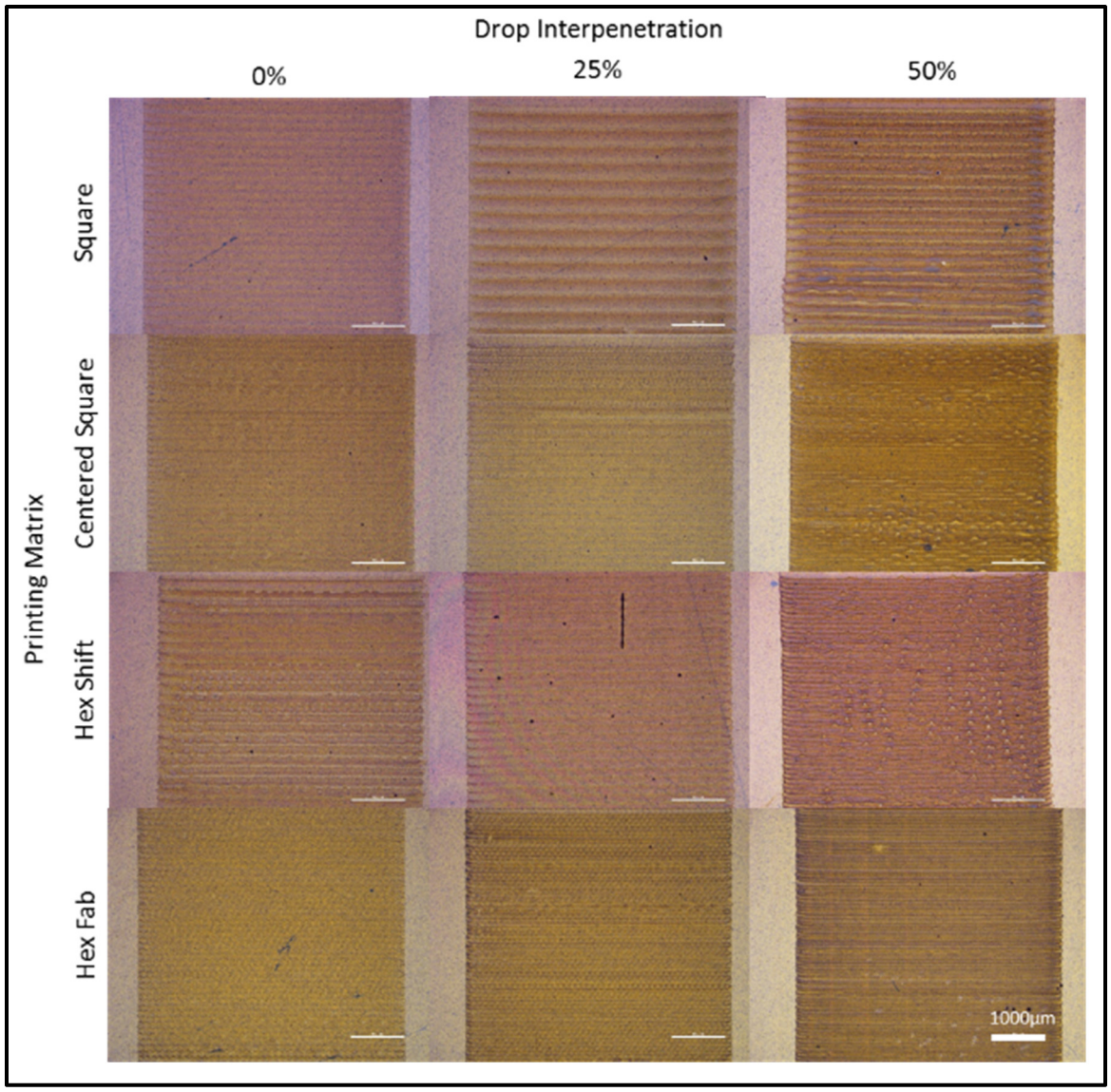

Figure-A V-3 Photographs of the printing test plans for spiro-OMeTAD ink on a Kapton substrate with a chuck temperature of 60 °C

APPENDIX VI

OSSILA I101 PRELIMINATY PRINTING TEST PLAN

The printing test plans for Ossila I101 PS formulation are performed on plasma treated FT Kapton-FPC 300 substrates using the jetting parameters specified in section 4.2.3, the printing lattice, drop interpenetration and chuck temperature are controlled. Test plans consisting of single and double printed layer are performed, the results after oven annealing at 90 °C for 2 hour (as stated by the manufacturer) are shown in Figure-A VI-1, Figure-A VI-2, Figure-A VI-3 and Figure-A VI-4. From the State-of-the-Art and Literature Review sections, a layer thickness of < 300 nm is targeted for the implementation of the MALH PS active layer for TF device applications in photo-sensing and energy harvesting. The test plans are performed using a chuck temperature of 30°C and 60°C.

From this test plan, a few trends become evident;

1. Raster tracks are present for most printing parameters tested, except when using a Hex Shift printing lattice.
2. Coverage is inadequate for most printing parameters.
3. Printing performed using 50 % drop interpenetration readily results in ink bleeding out of the printed feature area.
4. Crystallization of the PS is not controlled.

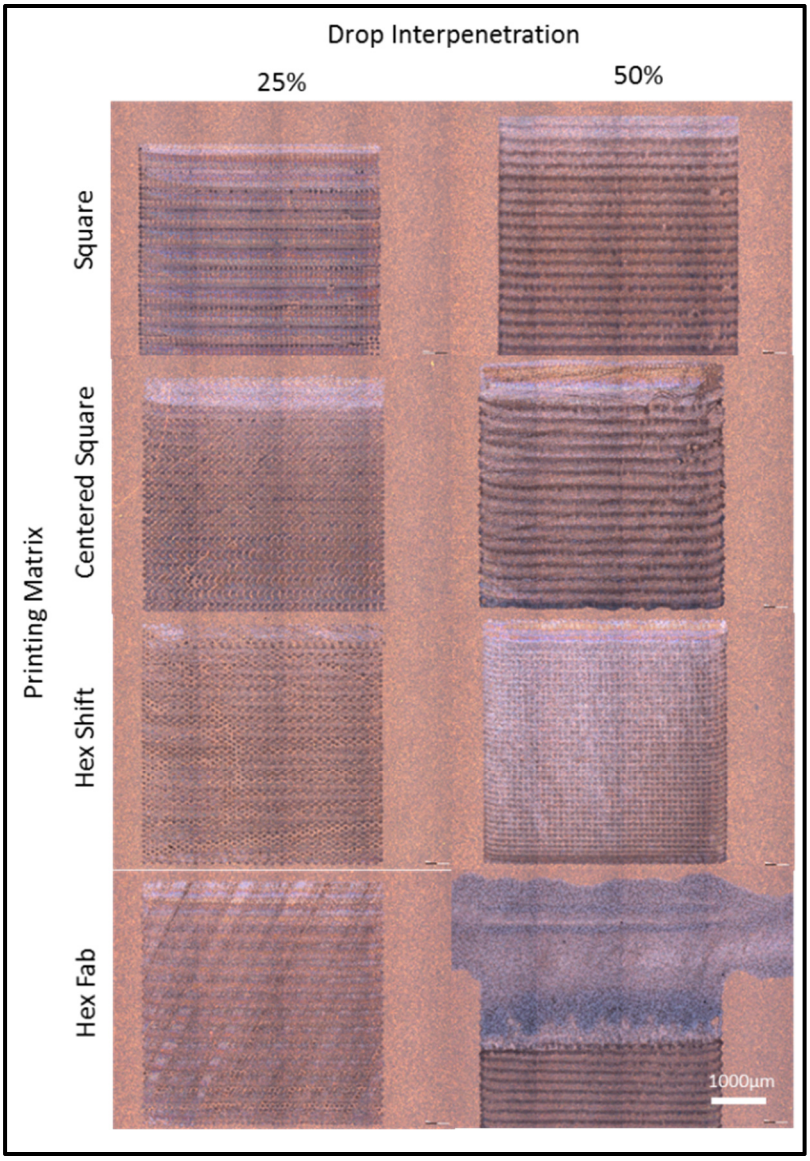

Figure-A VI-1 Photographs of the 1-layer printing test plans for Ossila I101 PS ink on a Kapton substrate with a chuck temperature of 30 °C

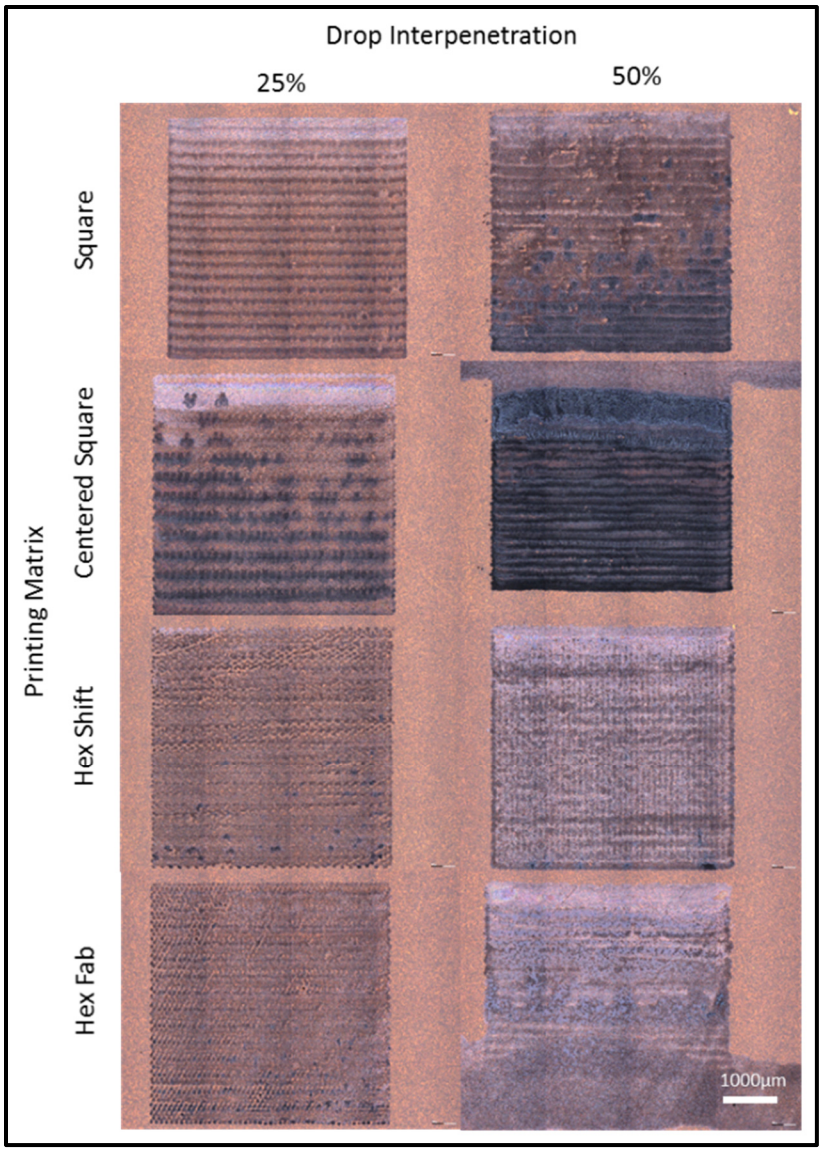

Figure-A VI-2 Photographs of the 2-layer printing test plans for Ossila I101 PS ink on a Kapton substrate with a chuck temperature of 30 °C

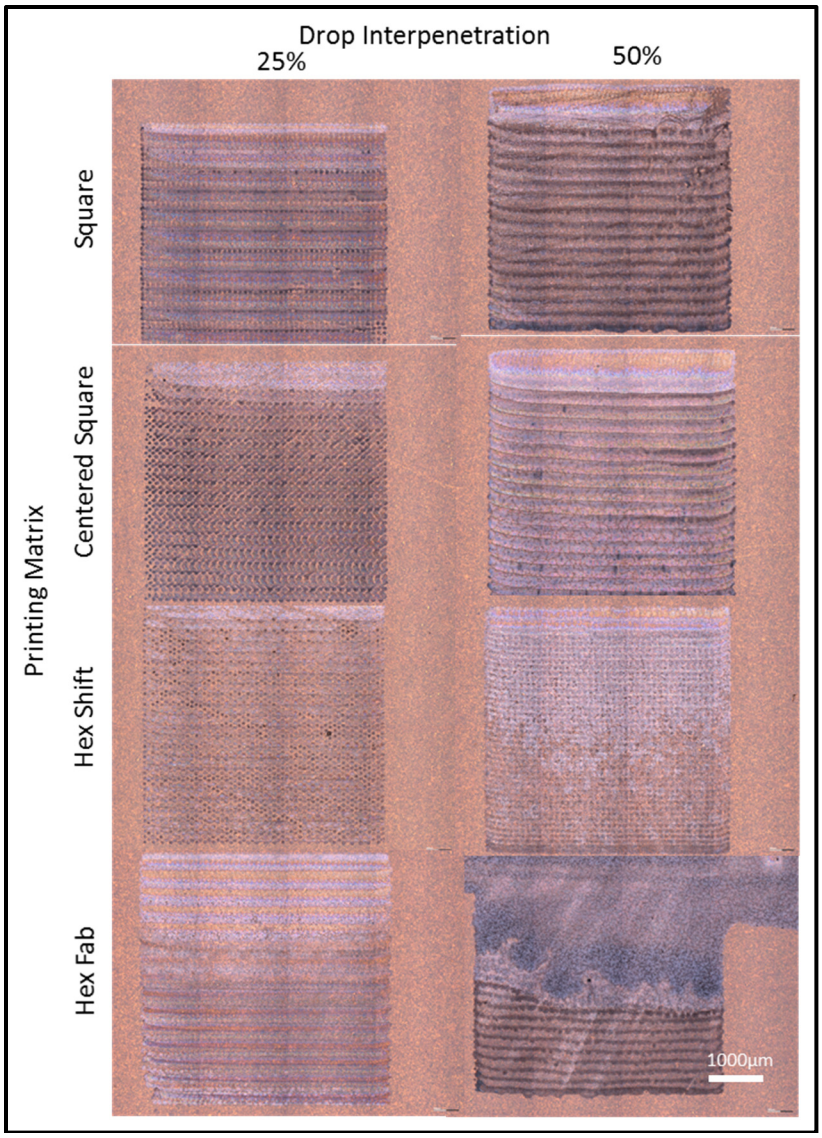

Figure-A VI-3 Photographs of the 1-layer printing test plans for Ossila I101 PS ink on a Kapton substrate with a chuck temperature of 60 °C

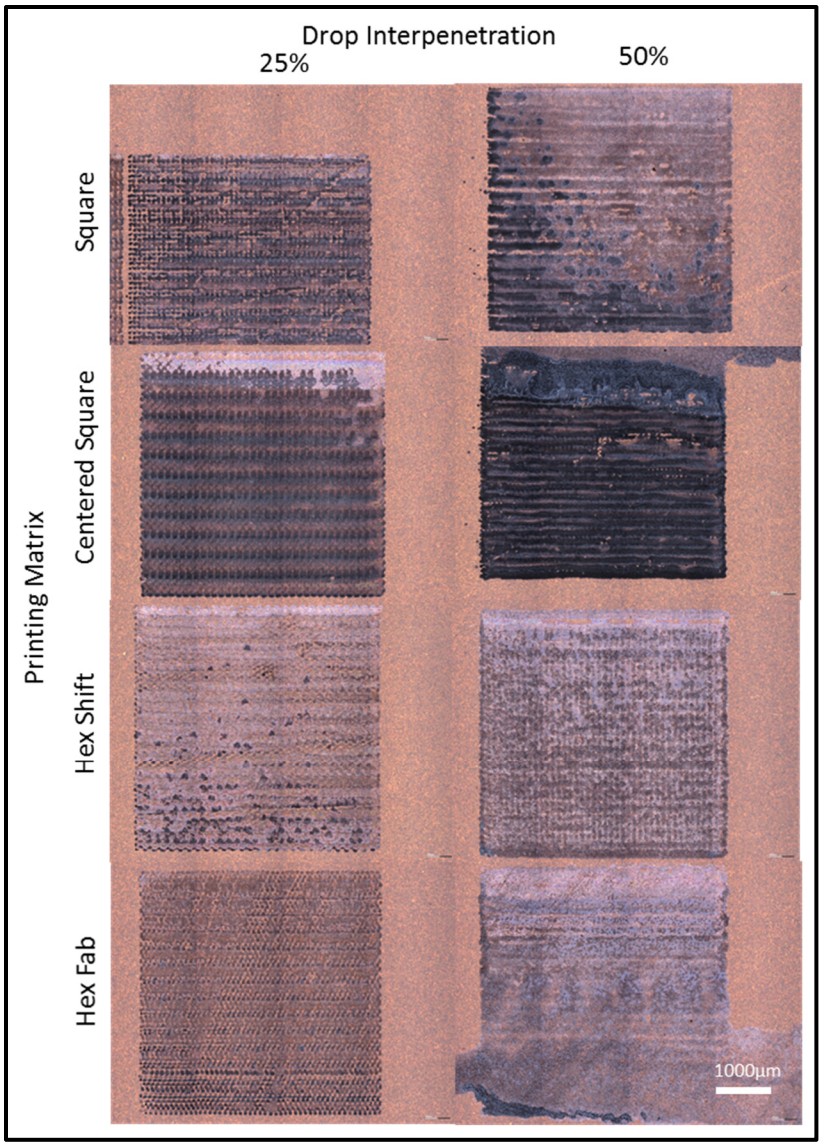

Figure-A VI-4 Photographs of the 2-layer printing test plans for Ossila I101 PS ink on a Kapton substrate with a chuck temperature of 60 °C

From the preliminary test plan, two sets of printing parameters are deemed best suited for Ossila I101 PS layer printing homogeneity and coverage: single layer printing performed with 50 % drop interpenetration, using a Square or a Hex Shift lattice and a chuck temperature of 30 °C.

Optimization of Crystallization and Layer Coverage

To increase coverage and to achieve better control of PS crystallization, three optimization pathways are explored. First, the effects of introducing raster overlaps while printing are tested to reduce raster tracks seen in the printed features. The results are illustrated in Figure-A VI-

5, showing the effects of positive and negative raster overlaps. It is found that introducing a slight positive raster overlap of 5 µm results in more homogeneous printing void of raster tracks. However, further increasing raster overlap to 20 µm reintroduces the raster track effect with lines of oscillating increases and decreases in material deposition. Negative raster overlaps result in gaps of material between rasters, as expected. Interestingly, further increasing the negative raster overlap to -20 µm is seen to result in smaller gaps of materials. A raster overlap of 5 µm is used from this point forward when printing Ossila I101 PS ink.

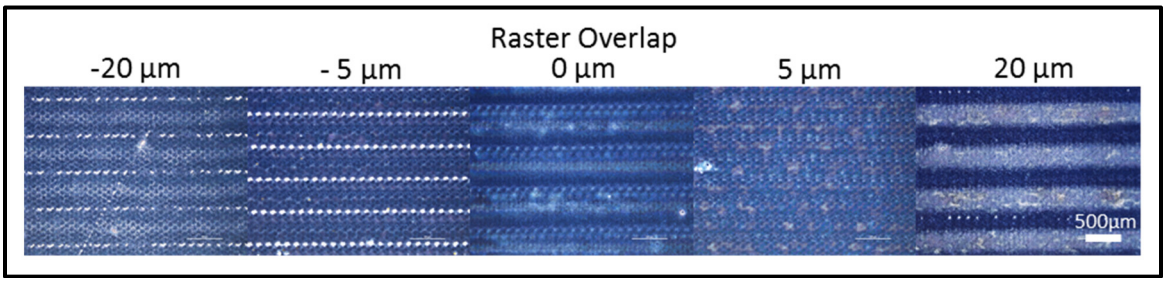

Figure-A VI-5 Results of the raster overlap optimization for printing Ossila I101 PS ink on Kapton substrate

Second, solvent assisted annealing of the PS is explored. From the literature, solvent addition during the annealing process is shown to homogenize PS crystal size, improve crystal packing, reduce number of pinholes and improve overall device performances (Xiao et al., 2014, p.6503-6509); (Liu et al., 2015, p.24008-24015); (Yu et al., 2016, p.321-326). The effects of different volume concentration combinations of EtOH and CB are tested. The solvent combinations are printed using an 80 µm diameter micro-fab single nozzle on the Ceradrop F-Series printer, optimized jetting parameters for these solvents are not achieved as solvent viscosities are not adequate for stable jetting. Semi-stable printing was achieved for all combination of solvents using the jetting and printing parameters found in Table-A VI-1

Table-A VI-1 EtOH :CB solvent printing and jetting parameters used for PS solvent annealing

Inkjet Nozzle	**Waveform [V- µs]**	**Nozzle & Chuck Temp. [°C]**	**Splat Diameter [µm]**	**Splat Overlap [%]**	**Printing Lattice**
80 µm MicroFab	150-15	30	100	35	Square

Prior to solvent printing, a preliminary NIR optical treatment is performed using a lamp power of 5 % with a chuck displacement speed of 20 mm/s to evaporate a portion of the DMF solvent present in the PS layer, this reduces bleeding effects considerably. Following solvent printing,

the PS is annealed at 90 °C for 2 hour in an oven, the effects of solvent annealing on the PS crystals is shown in Figure-A VI-6, EtOH:CB volume concentration of 100 %:0 % , 0 %:100 % , 25 %:75 % and 75 %:25 % are tested.

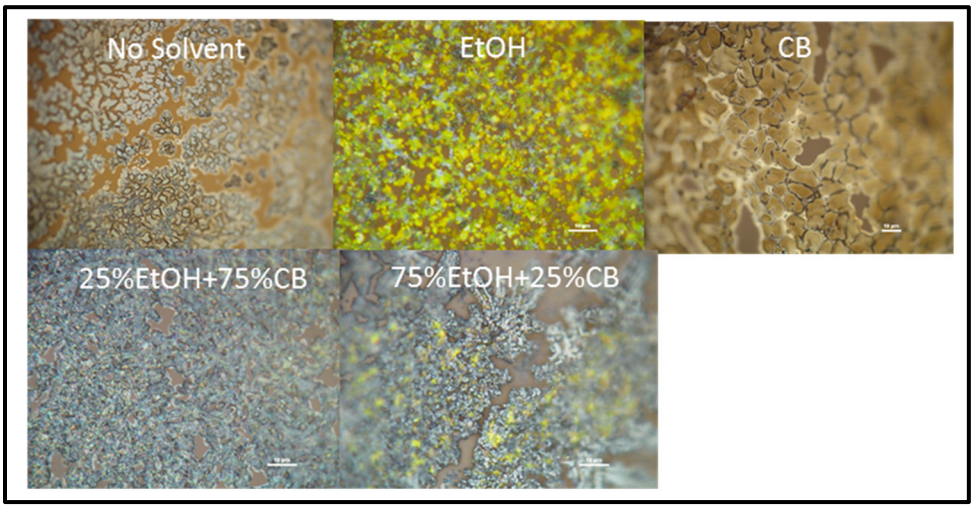

Figure-A VI-6 Overview of the effects of PS solvent annealing using varying volume ratios of EtOH and CB

Solvent annealing using pure EtOH results in smaller crystals and improve coverage of the PS, however PS degradation is seen to occur readily as is evidence from the color change to yellow. Using pure CB for PS solvent annealing results in larger crystals with improved crystal packing when compared to annealing performed without solvents. Moreover, the PS crystals are observed to be more transparent as the substrate color permeates through the crystals, this is expected to be detrimental to device operations as less light will be absorbed. Combinations of the two solvents results in overall better crystal homogeneity and coverage than when using either solvents alone or when no solvent annealing is performed. Performing the solvent annealing using a volume concentration of 75 % EtOH: 25 % CB results in degradation of the PS crystals, however, this effect is less pronounced than when using pure EtOH and is limited to few areas. The best results in terms of PS coverage and crystal homogeneity are achieved when using a solvent volume concentration of 25 % EtOH: 75 % CB, coverage is observed to be drastically improved over annealing without solvent while no PS crystal degradation is observed.

While increasing crystal uniformity and overall coverage, the process of printing solvents on top of the printed PS increases the ink bleeding out effect. Thus, a method of retaining the ink inside of the printed feature area is devised. Printing a SU-8 “pool”, of sufficient height, around the designed printed feature area, prior to printing the PS ink, is expected to retain the ink in the printed feature area and stop ink bleeding. As such, SU-8 square “pool” with an inner empty area of 5 x 5 mm and 2 mm width walls of ~20 µm height are fabricated by printing 8 layers of MicroChem SU-8 ink using the optimized jetting and printing parameters found in sections

4.2.3 and 4.3.2, respectively. Using these “pools”, more PS material can be printed and retained in the selected areas, either by increasing the number of printed layers or by increasing the drop interpenetration. This is expected to result in more coverage and thicker printed features. Printing test plans using the SU-8 “pools” are performed at different drop interpenetrations while using a square lattice and a chuck temperature of 30 °C, the results of which are shown in Figure-A VI-7. Further test plans using the SU-8 “pools” are performed using two values of drop interpenetration (13.4% and 66.4%) while varying the number of printed layers, a square lattice and a chuck temperature of 30 °C is used. The results of these test plans are are illustrated in Figure-A VI-8 and Figure-A VI-9, respectively. It is observed that the SU-8 “pools” perform as expected and stop the ink bleeding effects by creating a barrier around the printed feature area.

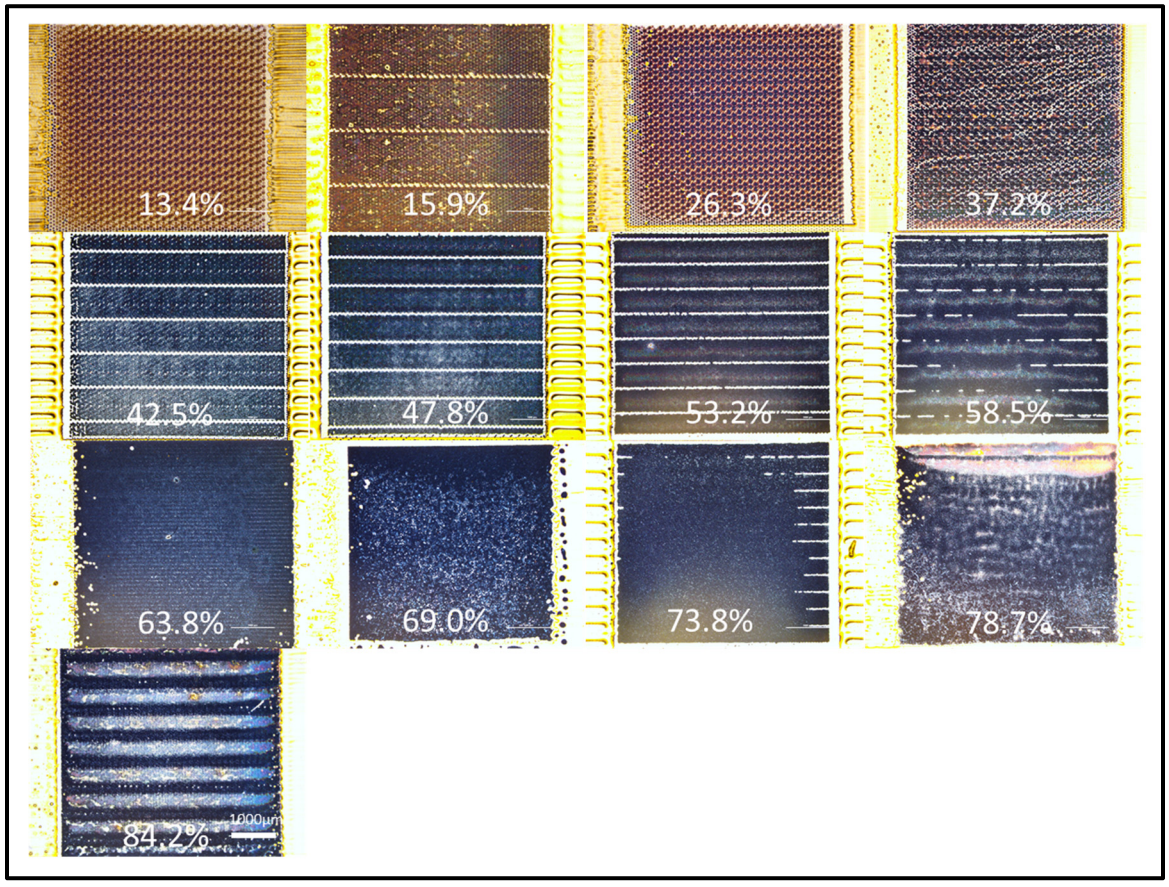

Figure-A VI-7 Optimization of drop interpenetration Ossila I101 PS ink using SU-8 “pools” and solvent annealing to avoid ink bleeding effects

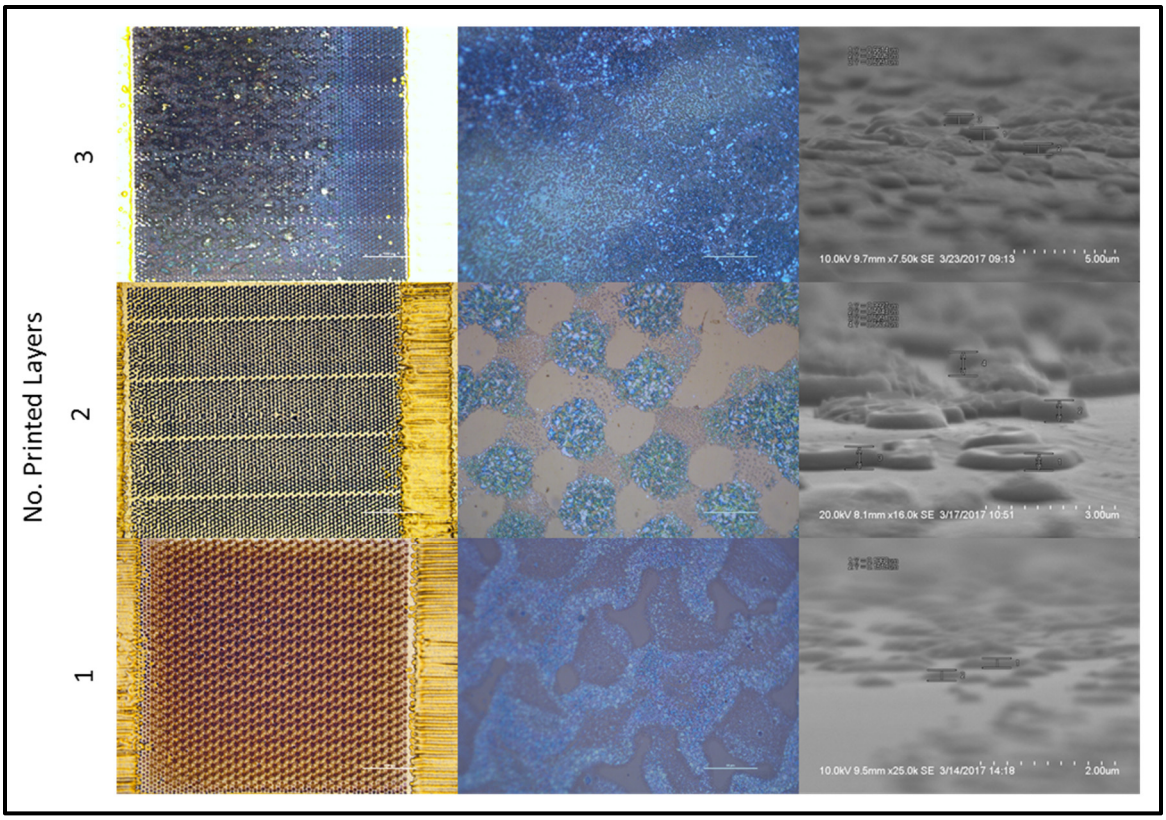

Figure-A VI-8 Optimization of number of printed layers for Ossila I101 PS ink with constant drop interpenetration of 13.4%, using SU-8 “pools” and solvent annealing to avoid ink bleeding effects

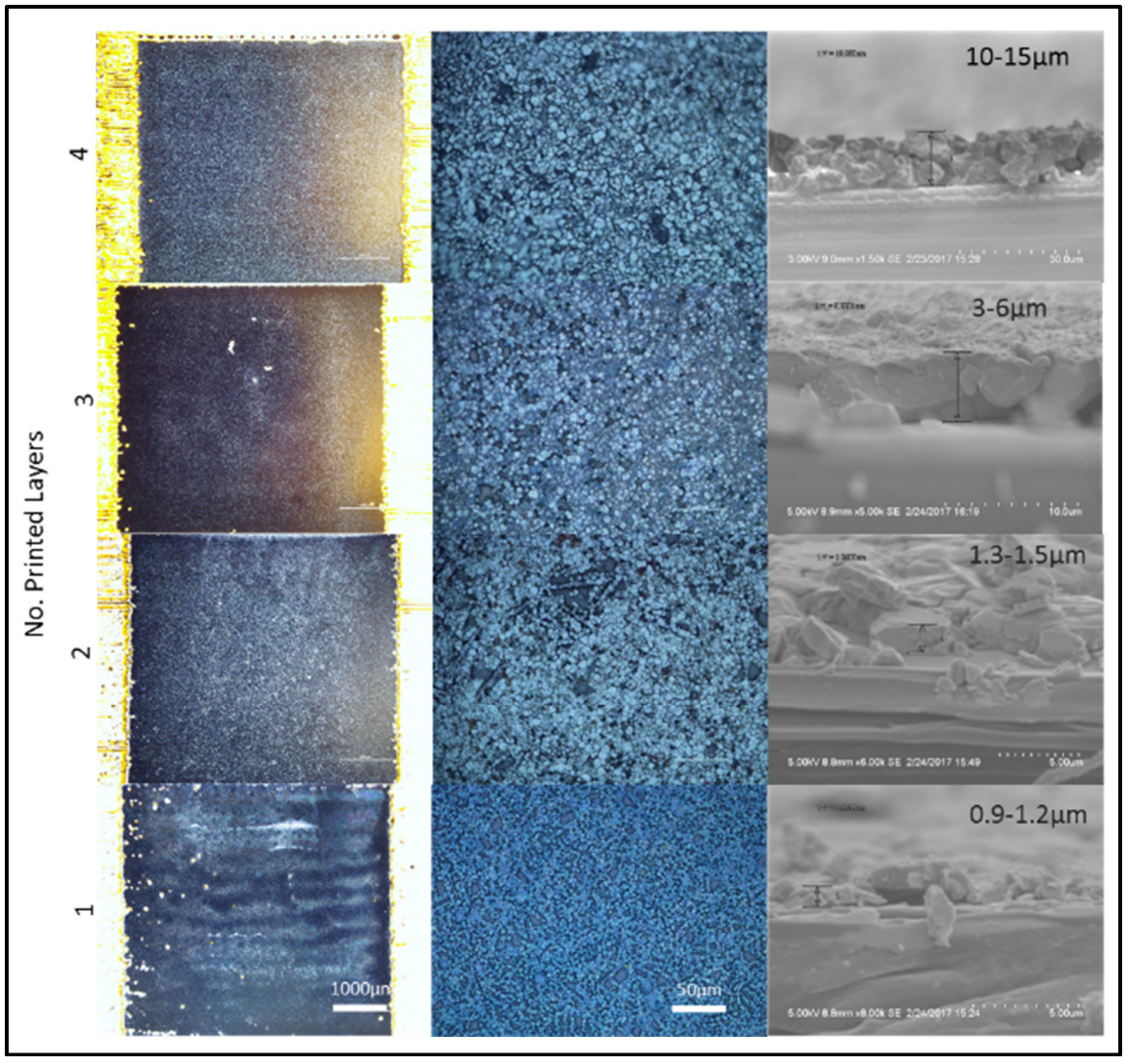

Figure-A VI-9 Optimization of number of printed layers for Ossila I101 PS ink with constant drop interpenetration of 66.4%, using SU-8 “pools” and solvent annealing to avoid ink bleeding effects

LIST OF BIBLIOGRAPHICAL REFERENCES

Abdelmageed, G., Mackeen, C., Hellier, K., Jewell, L., Seymour, L., Tingwald, M., . . . Carter, S. (2018). Effect of temperature on light induced degradation in methylammonium lead iodide perovskite thin films and solar cells. Solar Energy Materials and Solar Cells, 174, 566-571.

Alamán, J., Alicante, R., Peña, J., & Sánchez-Somolinos, C. (2016). Inkjet printing of functional materials for optical and photonic applications. Materials, 9(11), 910.

Ashraf, S., Mattsson, C. G., Fondell, M., Lindblad, A., & Thungström, G. (2015). Surface modification of SU-8 for metal/SU-8 adhesion using RF plasma treatment for application in thermopile detectors. Materials Research Express, 2(8), 086501.

Asuo, I. M., Ka, I., Gedamu, D., Pignolet, A., Nechache, R. & Cloutier, S. G. (2019) "Tunable thiocyanate-doped perovskite microstructure via water-ethanol additives for stable solar cells at ambient conditions." Solar Energy Materials and Solar Cells 200, 110029.

Bai, H., Shen, T., & Tian, J. (2017). An air-stable ultraviolet photodetector based on mesoporous TiO 2/spiro-OMeTAD. Journal of Materials Chemistry C, 5(40), 10543-10548.

Bale, M., Carter, J., Creighton, C., Gregory, H., Lyon, P., Ng, P., . . . Wehrum, A. (2006). Ink-jet printing: The route to production of full-color P-OLED displays. Journal of the Society for Information Display, 14(5), 453-459.

Ball, J. M., Lee, M. M., Hey, A., & Snaith, H. J. (2013). Low-temperature processed meso-superstructured to thin-film perovskite solar cells. Energy & Environmental Science, 6(6), 1739-1743.

Banyamin, Z. Y., Kelly, P. J., West, G., & Boardman, J. (2014). Electrical and optical properties of fluorine doped tin oxide thin films prepared by magnetron sputtering. Coatings, 4(4), 732-746.

Barnett, J. L., Cherrette, V. L., Hutcherson, C. J., & So, M. C. (2016). Effects of solution-based fabrication conditions on morphology of lead halide perovskite thin film solar cells. Advances in Materials Science and Engineering, 2016, p.1 -12.

Benayas, A., Ren, F., Carrasco, E., Marzal, V., del Rosal, B., Gonfa, B. A., . . . García-Solé, J. (2015). PbS/CdS/ZnS Quantum Dots: A Multifunctional Platform for In Vivo Near-Infrared Low-Dose Fluorescence Imaging. Advanced Functional Materials, 25(42), 6650-6659.

Bessonov, A., & Kirikova, M. (2015). Flexible and printable sensors. Nanotechnologies in Russia, 10(3-4), 165-180.

Bessonov, A. A., Allen, M., Liu, Y., Malik, S., Bottomley, J., Rushton, A., . . . Colli, A. (2017). Compound Quantum Dot–Perovskite Optical Absorbers on Graphene Enhancing Short-Wave Infrared Photodetection. ACS nano, 11(6), 5547-5557.

Bidoki, S. M., Nouri, J., & Heidari, A. (2010). Inkjet deposited circuit components. Journal of micromechanics and microengineering, 20(5), 055023.

Bodas, D., & Khan-Malek, C. (2006). Formation of more stable hydrophilic surfaces of PDMS by plasma and chemical treatments. Microelectronic engineering, 83(4-9), 1277-1279.

Bolduc, M., Trudeau, C., Beaupré, P., Cloutier, S., & Galarneau, P. (2018). Thermal dynamics effects using pulse-shaping laser sintering of printed silver inks. Scientific Reports, 8(1), 1418.

Bouzidi, K., Chegaar, M., & Bouhemadou, A. (2007). Solar cells parameters evaluation considering the series and shunt resistance. Solar Energy Materials and Solar Cells, 91(18), 1647-1651.

Bryant, D., Aristidou, N., Pont, S., Sanchez-Molina, I., Chotchunangatchaval, T., Wheeler, S., . . . Haque, S. A. (2016). Light and oxygen induced degradation limits the operational stability of methylammonium lead triiodide perovskite solar cells. Energy & Environmental Science, 9(5), 1655-1660.

Bulgakova, N., & Bulgakov, A. (2001). Pulsed laser ablation of solids: transition from normal vaporization to phase explosion. Applied Physics A, 73(2), 199-208.

Butler, K. T., Frost, J. M., & Walsh, A. (2015). Band alignment of the hybrid halide perovskites CH 3 NH 3 PbCl 3, CH 3 NH 3 PbBr 3 and CH 3 NH 3 PbI 3. Materials Horizons, 2(2), 228-231.

Cauchois, R., Saadaoui, M., Yakoub, A., Inal, K., Dubois-Bonvalot, B., & Fidalgo, J. C. (2012). Impact of variable frequency microwave and rapid thermal sintering on microstructure of inkjet-printed silver nanoparticles. Journal of Materials Science, 47(20), 7110-7116.

Chen, C. (2009). Evaluation of resistance–temperature calibration equations for NTC thermistors. Measurement, 42(7), 1103-1111.

Chen, F., Lin, Q., Wang, H., Wang, L., Zhang, F., Du, Z., . . . Li, L. S. (2016). Enhanced Performance of Quantum Dot-Based Light-Emitting Diodes with Gold Nanoparticle-Doped Hole Injection Layer. Nanoscale research letters, 11(1), 376.

Chen, T., Chen, W.L., Foley, B.J., Lee, J., Ruff, J.P., Ko, J.P., … & Yoon, M. (2017). Origin of long lifetime of band-edge charge carriers in organic-inorganic lead iodide perovskites. Proceedings of the National Academy of Sciences, 114(29), 7519-7524.

Cheng, G. G., Jiang, S. Y., Li, K., Zhang, Z. Q., Wang, Y., Yuan, N. Y., ... & Zhang, W. (2017). Effect of argon plasma treatment on the output performance of triboelectric nanogenerator. Applied Surface Science, 412, 350-356.

Cho, S.-J., Nguyen, T., & Boo, J.-H. (2011). Polyimide surface modification by using microwave plasma for adhesion enhancement of Cu electroless plating. Journal of nanoscience and nanotechnology, 11(6), 5328-5333.

Choi, J. H., Ryu, K., Park, K., & Moon, S.-J. (2015). Thermal conductivity estimation of inkjet-printed silver nanoparticle ink during continuous wave laser sintering. International Journal of Heat and Mass Transfer, 85, 904-909.

Chung, S., Kim, S. O., Kwon, S.-K., Lee, C., & Hong, Y. (2011). All-inkjet-printed organic thin-film transistor inverter on flexible plastic substrate. IEEE electron device letters, 32(8), 1134-1136.

Chung, W.-H., Hwang, H.-J., Lee, S.-H., & Kim, H.-S. (2012). In situ monitoring of a flash light sintering process using silver nano-ink for producing flexible electronics. Nanotechnology, 24(3), 035202.

Cook, B., Mariotti, C., Cooper, J., Revier, D., Tehrani, B., Aluigi, L., . . . Tentzeris, M. (2014). Inkjet-printed, vertically-integrated, high-performance inductors and transformers on flexible LCP substrate. Dans Microwave Symposium (IMS), 2014 IEEE MTT-S International (pp. 1-4). IEEE.

Das, R., Ghaffarzadeh, K., & HE, X. Printed, Organic & Flexible Electronics: Forecasts, Players & Opportunities 2013-2023. IDETECH.

Das, R., & Harrop, P. (2013). Printed, organic & flexible electronics: forecasts, players & opportunities 2013–2023. Cambridge: IDTechEx.

Dauskardt, R., Lane, M., Ma, Q., & Krishna, N. (1998). Adhesion and debonding of multi-layer thin film structures. Engineering Fracture Mechanics, 61(1), 141-162.

de Faro Orlando, A., Bellido, M. H., & Silva, R. N. D. (2012). Methodology for metrologieal evaluation of a PTC resettable thermistor. High Temperatures--High Pressures, 41(4).

Deladurantaye, P., Drolet, M., Desbiens, L., Taillon, Y., Labranche, B., Roy, V., & Laperle, P. (2009). 140-µJ, narrow-linewidth, robustly single-transverse mode nanosecond infrared fiber laser platform with fine pulse tailoring capability. Dans Photonics North 2009 (Vol. 7386, pp. 73860Q). International Society for Optics and Photonics.

Demirel, B., Yaraş, A., & Elçiçek, H. (2016). Crystallization behavior of PET materials. Balıkesir Üniversitesi Fen Bilimleri Enstitüsü Dergisi, 13(1), 26-35.

Deng, R., Zhang, Z., Ren, J., & Liang, H. (2016). Indoor temperature control of cost-effective smart buildings via real-time smart grid communications. Dans Global Communications Conference (GLOBECOM), 2016 IEEE (pp. 1-6). IEEE.

Denneulin, A., Blayo, A., Neuman, C., & Bras, J. (2011). Infra-red assisted sintering of inkjet printed silver tracks on paper substrates. Journal of Nanoparticle Research, 13(9), 3815-3823.

Derby, B. (2010). Inkjet printing of functional and structural materials: fluid property requirements, feature stability, and resolution. Annual Review of Materials Research, 40, 395-414.

Divitini, G., Cacovich, S., Matteocci, F., Cina, L., Di Carlo, A., & Ducati, C. (2016). In situ observation of heat-induced degradation of perovskite solar cells. Nature Energy, 1(2), 15012.

Docampo, P., Ball, J. M., Darwich, M., Eperon, G. E., & Snaith, H. J. (2013). Efficient organometal trihalide perovskite planar-heterojunction solar cells on flexible polymer substrates. Nature communications, 4, 2761.

Dostert, K. (1982). Applications of self-heated PTC-thermistors to flow and quantity of heat measurements. Sensors and Actuators, 3, 159-167.

Dubey, A., Kantack, N., Adhikari, N., Reza, K. M., Venkatesan, S., Kumar, M., . . . Qiao, Q. (2016). Room temperature, air crystallized perovskite film for high performance solar cells. Journal of Materials Chemistry A, 4(26), 10231-10240.

Dupont. (2018). DUPONT™ KAPTON® FPC - POLYIMIDE FILM. Accessed 03-08-2018 at http://www.dupont.com/content/dam/dupont/products-and-services/membranes-and-films/polyimde-films/documents/DEC-Kapton-FPC-datasheet.pdf

Dupont. (2019). PE827 Silver Composite Conductor Ink Data Sheet. Accessed 02-12-2019 at http://www.dupont.com/content/dam/dupont/products-and-services/electronic-and-electrical-materials/documents/prodlib/PE827.pdf

Eames, C., Frost, J. M., Barnes, P. R., O'regan, B. C., Walsh, A., & Islam, M. S. (2015). Ionic transport in hybrid lead iodide perovskite solar cells. Nature communications, 6, 7497.

Efimenko, K., Wallace, W. E., & Genzer, J. (2002). Surface modification of Sylgard-184 poly (dimethyl siloxane) networks by ultraviolet and ultraviolet/ozone treatment. Journal of colloid and interface science, 254(2), 306-315.

Eggenhuisen, T., Galagan, Y., Biezemans, A., Slaats, T., Voorthuijzen, W., Kommeren, S., . . . Verhees, W. (2015). High efficiency, fully inkjet printed organic solar cells with freedom of design. Journal of Materials Chemistry A, 3(14), 7255-7262.

Eom, S. H., Park, H., Mujawar, S., Yoon, S. C., Kim, S.-S., Na, S.-I., . . . Lee, S.-H. (2010). High efficiency polymer solar cells via sequential inkjet-printing of PEDOT: PSS and P3HT: PCBM inks with additives. Organic Electronics, 11(9), 1516-1522.

Etgar, L., Gao, P., Xue, Z., Peng, Q., Chandiran, A. K., Liu, B., . . . Grätzel, M. (2012). Mesoscopic CH3NH3PbI3/TiO2 heterojunction solar cells. Journal of the American Chemical Society, 134(42), 17396-17399.

Eperon, G. E., Burlakov, V. M., Docampo, P., Goriely, A., & Snaith, H. J. (2014). Morphological control for high performance, solution-processed planar heterojunction perovskite solar cells. Advanced Functional Materials, 24(1), 151-157.

Eun, K., Chon, M.-W., Yoo, T.-H., Song, Y.-W., & Choa, S.-H. (2015). Electromechanical properties of printed copper ink film using a white flash light annealing process for flexible electronics. Microelectronics Reliability, 55(5), 838-845.

Fang, Y., Dong, Q., Shao, Y., Yuan, Y., & Huang, J. (2015). Highly narrowband perovskite single-crystal photodetectors enabled by surface-charge recombination. Nature Photonics, 9(10), 679-686.

Fang, Y., Wang, X., Wang, Q., Huang, J., & Wu, T. (2014). Impact of annealing on spiro-OMeTAD and corresponding solid-state dye sensitized solar cells. physica status solidi (a), 211(12), 2809-2816.

Feteira, A. (2009). Negative temperature coefficient resistance (NTCR) ceramic thermistors: an industrial perspective. Journal of the American Ceramic Society, 92(5), 967-983.

Finer, J. T., Simmons, R. M., & Spudich, J. A. (1994). Single myosin molecule mechanics: piconewton forces and nanometre steps. Nature, 368(6467), 113.

Fujihara, K., Kumar, A., Jose, R., Ramakrishna, S., & Uchida, S. (2007). Spray deposition of electrospun TiO2 nanorods for dye-sensitized solar cell. Nanotechnology, 18(36), 365709.

Gamerith, S., Klug, A., Scheiber, H., Scherf, U., Moderegger, E., & List, E. J. (2007). Direct Ink-Jet Printing of Ag–Cu Nanoparticle and Ag-Precursor Based Electrodes for OFET Applications. Advanced Functional Materials, 17(16), 3111-3118.

Gedamu, D., Asuo, I. M., Benetti, D., Basti, M., Ka, I., Cloutier, S. G., . . . Nechache, R. (2018). Solvent-antisolvent ambient processed large grain size perovskite thin films for high-performance solar cells. Scientific Reports, 8(1), 12885.

Gevaerts, V., Biezemans, A., Passet, Q., Eggenhuisen, T., Willems, R., Veenstra, S., . . . Andriessen, R. (2016). Digitally printed photovoltaic devices with increasing stack complexity. Dans Photovoltaic Specialists Conference (PVSC), 2016 IEEE 43rd (pp. 1630-1631). IEEE.

Gibson, G., Courtial, J., Padgett, M. J., Vasnetsov, M., Pas'ko, V., Barnett, S. M., & Franke-Arnold, S. (2004). Free-space information transfer using light beams carrying orbital angular momentum. Optics express, 12(22), 5448-5456.

Gonzalez-Pedro, V., Juarez-Perez, E. J., Arsyad, W.-S., Barea, E. M., Fabregat-Santiago, F., Mora-Sero, I., & Bisquert, J. (2014). General working principles of CH3NH3PbX3 perovskite solar cells. Nano letters, 14(2), 888-893.

Gouda, L., Gottesman, R., Ginsburg, A., Keller, D. A., Haltzi, E., Hu, J., . . . Boix, P. P. (2015). Open circuit potential build-up in perovskite solar cells from dark conditions to 1 sun. The journal of physical chemistry letters, 6(22), 4640-4645.

Green, M. A., Emery, K., Hishikawa, Y., Warta, W., & Dunlop, E. D. (2015). Solar cell efficiency tables (version 46). Progress in Photovoltaics: Research and Applications, 23(7), 805-812.

Grouchko, M., Kamyshny, A., & Magdassi, S. (2009). Formation of air-stable copper–silver core–shell nanoparticles for inkjet printing. Journal of Materials Chemistry, 19(19), 3057-3062.

Guerrero, A., Juarez-Perez, E. J., Bisquert, J., Mora-Sero, I., & Garcia-Belmonte, G. (2014). Electrical field profile and doping in planar lead halide perovskite solar cells. Applied Physics Letters, 105(13), 133902.

Guo, L., Fei, C., Zhang, R., Li, B., Shen, T., Tian, J., & Cao, G. (2016). Impact of sol aging on TiO2 compact layer and photovoltaic performance of perovskite solar cell **胶体**陈化时间对 TiO2 **致密**层及钙钛矿太阳电池性能的影响探究. Science China Materials, 59(9), 710-718.

Ha, P. C., McKenzie, D., Bilek, M., Doyle, E., McCulloch, D., & Chu, P. (2006). Control of stress and delamination in single and multi-layer carbon thin films prepared by cathodic arc and RF plasma deposition and implantation. Surface and Coatings Technology, 200(22-23), 6405-6408.

Hammond, P., & Cumming, D. (2004). Encapsulation of a liquid-sensing microchip using SU-8 photoresist. Microelectronic engineering, 73, 893-897.

Hasan, M., Hamja, A., & Islam, M. K. (2015). Soft Lithography Based Printed Methyl Ammonium Iodide Hybrid Organo Metal Perovskite Solar Cell Without Hole Transporting Layer. Dans ICMERE2015 (pp. 26-29).

He, H., Friese, M., Heckenberg, N., & Rubinsztein-Dunlop, H. (1995). Direct observation of transfer of angular momentum to absorptive particles from a laser beam with a phase singularity. Physical Review Letters, 75(5), 826.

He, J., Wang, X., Hu, D., Ye, J., Feng, S., Kan, Q., & Zhang, Y. (2013). Generation and evolution of the terahertz vortex beam. Optics express, 21(17), 20230-20239.

Hedges, M., & Marin, A. B. (2012). 3d aerosol jet printing-adding electronics functionality to rp/rm. Dans DDMC 2012 conference (pp. 14-15).

Hejda, F., Solar, P., & Kousal, J. (2010). Surface free energy determination by contact angle measurements–a comparison of various approaches. Dans WDS (Vol. 10, pp. 25-30).

Helgesen, M., Carlé, J. E., Andreasen, B., Hösel, M., Norrman, K., Søndergaard, R., & Krebs, F. C. (2012). Rapid flash annealing of thermally reactive copolymers in a roll-to-roll process for polymer solar cells. Polymer Chemistry, 3(9), 2649-2655.

Hester, J. G., Tentzeris, M. M., & Fang, Y. (2015). Inkjet-printed, flexible, high performance, carbon nanomaterial based sensors for ammonia and DMMP gas detection. Dans Microwave Conference (EuMC), 2015 European (pp. 857-860). IEEE.

Ho, X., Nie Tey, J., Liu, W., Kweng Cheng, C., & Wei, J. (2013). Biaxially stretchable silver nanowire transparent conductors. Journal of Applied Physics, 113(4), 044311.

Hong, L., Le, N., Thuan, N., Thanh, N., Nghia, N., & Phuc, N. (2005). Observation of the phase formation in TiO2 nano thin film by Raman scattering. Journal of Raman Spectroscopy: An International Journal for Original Work in all Aspects of Raman Spectroscopy, Including Higher Order Processes, and also Brillouin and Rayleigh Scattering, 36(10), 946-949.

Hong, S., Yeo, J., Kim, G., Kim, D., Lee, H., Kwon, J., . . . Ko, S. H. (2013). Nonvacuum, maskless fabrication of a flexible metal grid transparent conductor by low-temperature selective laser sintering of nanoparticle ink. ACS nano, 7(6), 5024-5031.

Hooper, K., Smith, B., Baker, J., Greenwood, P., & Watson, T. (2015). Spray PEDOT: PSS coated perovskite with a transparent conducting electrode for low cost scalable photovoltaic devices. Materials Research Innovations, 19(7), 482-487.

Hu, L., Kim, H. S., Lee, J.-Y., Peumans, P., & Cui, Y. (2010). Scalable coating and properties of transparent, flexible, silver nanowire electrodes. ACS nano, 4(5), 2955-2963.

Hübler, A., Trnovec, B., Zillger, T., Ali, M., Wetzold, N., Mingebach, M., . . . Dyakonov, V. (2011). Printed paper photovoltaic cells. Advanced Energy Materials, 1(6), 1018-1022.

Jensen, N., Rau, U., Hausner, R., Uppal, S., Oberbeck, L., Bergmann, R., & Werner, J. (2000). Recombination mechanisms in amorphous silicon/crystalline silicon heterojunction solar cells. Journal of Applied Physics, 87(5), 2639-2645.

Jeon, N. J., Noh, J. H., Kim, Y. C., Yang, W. S., Ryu, S., & Seok, S. I. (2014). Solvent engineering for high-performance inorganic–organic hybrid perovskite solar cells. Nature materials, 13(9), 897.

Jeong, S., Woo, K., Kim, D., Lim, S., Kim, J. S., Shin, H., . . . Moon, J. (2008). Controlling the thickness of the surface oxide layer on Cu nanoparticles for the fabrication of conductive structures by ink-jet printing. Advanced Functional Materials, 18(5), 679-686.

Jiang, C.-S., Hasoon, F., Moutinho, H., Al-Thani, H., Romero, M., & Al-Jassim, M. (2003). Direct evidence of a buried homojunction in Cu (In, Ga) Se 2 solar cells. Applied Physics Letters, 82(1), 127-129.

Jiang, C.-S., Ptak, A., Yan, B., Moutinho, H., Li, J., & Al-Jassim, M. (2009). Microelectrical characterizations of junctions in solar cell devices by scanning Kelvin probe force microscopy. Ultramicroscopy, 109(8), 952-957.

Jiang, C.-S., Yang, M., Zhou, Y., To, B., Nanayakkara, S. U., Luther, J. M., . . . Padture, N. P. (2015). Carrier separation and transport in perovskite solar cells studied by nanometre-scale profiling of electrical potential. Nature communications, 6, 8397.

Jin, T., & Imamura, Y. (2016). Applications of highly bright pbs quantum dots to non-invasive near-infrared fluorescence imaging in the second optical window. ECS Journal of Solid State Science and Technology, 5(1), R3138-R3145.

Juárez-Moreno, J. A., Ávila-Ortega, A., Oliva, A. I., Avilés, F., & Cauich-Rodríguez, J. V. (2015). Effect of wettability and surface roughness on the adhesion properties of collagen on PDMS films treated by capacitively coupled oxygen plasma. Applied Surface Science, 349, 763-773.

Jokinen, V., Suvanto, P., & Franssila, S. (2012). Oxygen and nitrogen plasma hydrophilization and hydrophobic recovery of polymers. Biomicrofluidics, 6(1), 016501.

Ka, I., Gerlein, L. F., Nechache, R., & Cloutier, S. G. (2017). High-performance nanotube-enhanced perovskite photodetectors. Scientific Reports, 7, 45543.

Kamyshny, A., Steinke, J., & Magdassi, S. (2011). Metal-based inkjet inks for printed electronics. The Open Applied Physics Journal, 4(1).

Kawamura, Y., Mashiyama, H., & Hasebe, K. (2002). Structural study on cubic-tetragonal transition of CH 3 NH 3 PbI 3. Journal of the Physical Society of Japan, 71(7), 1694-1697.

Kim, D., Jeong, S., Moon, J., Han, S., & Chung, J. (2007). Organic thin film transistors with ink-jet printed metal nanoparticle electrodes of a reduced channel length by laser ablation. Applied Physics Letters, 91(7), 071114.

Kim, D., & Moon, J. (2005). Highly conductive ink jet printed films of nanosilver particles for printable electronics. Electrochemical and Solid-State Letters, 8(11), J30-J33.

Kim, H.-S., Dhage, S. R., Shim, D.-E., & Hahn, H. T. (2009). Intense pulsed light sintering of copper nanoink for printed electronics. Applied Physics A, 97(4), 791.

Ko, S. H., Chung, J., Pan, H., Grigoropoulos, C. P., & Poulikakos, D. (2007). Fabrication of multilayer passive and active electric components on polymer using inkjet printing and low temperature laser processing. Sensors and Actuators A: Physical, 134(1), 161-168.

Ko, S. H., Pan, H., Grigoropoulos, C. P., Luscombe, C. K., Fréchet, J. M., & Poulikakos, D. (2007). All-inkjet-printed flexible electronics fabrication on a polymer substrate by low-temperature high-resolution selective laser sintering of metal nanoparticles. Nanotechnology, 18(34), 345202.

Ko, S. H., Pan, H., Lee, D., Grigoropoulos, C. P., & Park, H. K. (2010). Nanoparticle selective laser processing for a flexible display fabrication. Japanese Journal of Applied Physics, 49(5S1), 05EC03.

Kojima, A., Teshima, K., Shirai, Y., Miyasaka, T. (2009). Organometal halide perovskites as visible-light sensitizers for photovoltaic cells. Journal of the American Chemical Society, 137(17), 6050-6051.

Kokkoris, C. P., Weitzman, E. D., Pollak, C. P., Spielman, A. J., Czeisler, C. A., & Bradlow, H. (1978). Long-term ambulatory temperature monitoring in a subject with a hypernychthemeral sleep-wake cycle disturbance. Sleep, 1(2), 177-190.

Krishna, A., Sabba, D., Li, H., Yin, J., Boix, P. P., Soci, C., . . . Grimsdale, A. C. (2014). Novel hole transporting materials based on triptycene core for high efficiency mesoscopic perovskite solar cells. Chemical Science, 5(7), 2702-2709.

Kumpulainen, T., Pekkanen, J., Valkama, J., Laakso, J., Tuokko, R., & Mäntysalo, M. (2011). Low temperature nanoparticle sintering with continuous wave and pulse lasers. Optics & Laser Technology, 43(3), 570-576.

Kwon, H., Choi, W., Lee, D., Lee, Y., Kwon, J., Yoo, B., . . . Kim, S. (2014). Selective and localized laser annealing effect for high-performance flexible multilayer MoS 2 thin-film transistors. Nano research, 7(8), 1137-1145.

Kwon, J., Trivedi, K., Krishnamurthy, N. V., Hu, W., Lee, J.-B., & Gimi, B. (2009). SU-8-based immunoisolative microcontainer with nanoslots defined by nanoimprint lithography. Journal of Vacuum Science & Technology B: Microelectronics and Nanometer Structures Processing, Measurement, and Phenomena, 27(6), 2795-2800.

Laakso, P., Ruotsalainen, S., Halonen, E., Mäntysalo, M., & Kemppainen, A. (2009). Sintering of printed nanoparticle structures using laser treatment. Dans Proc. ICALEO (pp. 1360-1366).

Lan, X., Voznyy, O., García de Arquer, F. P., Liu, M., Xu, J., Proppe, A. H., . . . Liu, M. (2016). 10.6% certified colloidal quantum dot solar cells via solvent-polarity-engineered halide passivation. Nano letters, 16(7), 4630-4634.

Langley, D., Giusti, G., Mayousse, C., Celle, C., Bellet, D., & Simonato, J.-P. (2013). Flexible transparent conductive materials based on silver nanowire networks: a review. Nanotechnology, 24(45), 452001.

Lee, H.-H., Chou, K.-S., & Huang, K.-C. (2005). Inkjet printing of nanosized silver colloids. Nanotechnology, 16(10), 2436.

Lee, M. M., Teuscher, J., Miyasaka, T., Murakami, T. N., & Snaith, H. J. (2012). Efficient hybrid solar cells based on meso-superstructured organometal halide perovskites. Science, 1228604.

Lee, S., Cho, I.-S., Lee, J. H., Kim, D. H., Kim, D. W., Kim, J. Y., . . . Park, N.-G. (2010). Two-step sol− gel method-based TiO2 nanoparticles with uniform morphology and size for efficient photo-energy conversion devices. Chemistry of Materials, 22(6), 1958-1965.

Lee, Y., Kwon, J., Hwang, E., Ra, C. H., Yoo, W. J., Ahn, J. H., . . . Cho, J. H. (2015). High-performance perovskite–graphene hybrid photodetector. Advanced materials, 27(1), 41-46.

Li, T., Albee, B., Alemayehu, M., Diaz, R., Ingham, L., Kamal, S., . . . Bishnoi, S. W. (2010). Comparative toxicity study of Ag, Au, and Ag–Au bimetallic nanoparticles on Daphnia magna. Analytical and bioanalytical chemistry, 398(2), 689-700.

Li, Y., Samad, Y. A., & Liao, K. (2015). From cotton to wearable pressure sensor. Journal of Materials Chemistry A, 3(5), 2181-2187.

Liang, C.-K., & Tsai, C.-C. (2005). Evaluation of a novel PTC thermistor for telecom overcurrent protection. Sensors and Actuators A: Physical, 121(2), 443-449.

Liang, P. W., Liao, C. Y., Chueh, C. C., Zuo, F., Williams, S. T., Xin, X. K., . . . Jen, A. K. Y. (2014). Additive enhanced crystallization of solution-processed perovskite for highly efficient planar-heterojunction solar cells. Advanced materials, 26(22), 3748-3754.

Lim, C. L., Byrne, C., & Lee, J. K. (2008). Human thermoregulation and measurement of body temperature in exercise and clinical settings. Annals Academy of Medicine Singapore, 37(4), 347.

Lin, K., Xing, J., Quan, L. N., de Arquer, F. P. G., Gong, X., Lu, J., Xie, L., Zhao, W., Zhang, D., Yan, C. & Li, W. (2018). Perovskite light-emitting diodes with external quantum efficiency exceeding 20 per cent. Nature, 562(7726), 245.

Liu, D., Gangishetty, M. K., & Kelly, T. L. (2014). Effect of CH 3 NH 3 PbI 3 thickness on device efficiency in planar heterojunction perovskite solar cells. Journal of Materials Chemistry A, 2(46), 19873-19881.

Liu, J., Gao, C., He, X., Ye, Q., Ouyang, L., Zhuang, D., . . . Lau, W. (2015). Improved crystallization of perovskite films by optimized solvent annealing for high efficiency solar cell. ACS applied materials & interfaces, 7(43), 24008-24015.

Liu, M., Johnston, M. B., & Snaith, H. J. (2013). Efficient planar heterojunction perovskite solar cells by vapour deposition. Nature, 501(7467), 395.

Liu, Y., Cui, T., & Varahramyan, K. (2003). All-polymer capacitor fabricated with inkjet printing technique. Solid-State Electronics, 47(9), 1543-1548.

Löbl, P., Huppertz, M., & Mergel, D. (1994). Nucleation and growth in TiO2 films prepared by sputtering and evaporation. Thin Solid Films, 251(1), 72-79.

Lorenz, H., Despont, M., Fahrni, N., LaBianca, N., Renaud, P., & Vettiger, P. (1997). SU-8: a low-cost negative resist for MEMS. Journal of micromechanics and microengineering, 7(3), 121.

Luo, S., & Daoud, W. (2016). Crystal structure formation of CH3NH3PbI3-xClx perovskite. Materials, 9(3), 123.

Luque, A., & Hegedus, S. (2011). Handbook of photovoltaic science and engineering. John Wiley & Sons.

Macklen, E. D. (1991). PTC Sensor Materials. In Concise Encyclopedia of Advanced Ceramic Materials (pp. 384-387). Pergamon.

Magdassi, S. (2010). Ink requirements and formulations guidelines. Dans The Chemistry of Inkjet Inks (pp. 19-41). World Scientific.

Manenkov, A. A. (2013). Fundamental mechanisms of laser-induced damage in optical materials: today's state of understanding and problems. Dans Pacific Rim Laser Damage 2013: Optical Materials for High Power Lasers (Vol. 8786, pp. 87861I). International Society for Optics and Photonics.

Manenkov, A. A. (2014). Fundamental mechanisms of laser-induced damage in optical materials: today's state of understanding and problems. Optical engineering, 53(1), 010901.

Martinez, V., Stauffer, F., Adagunodo, M. O., Forro, C., Vörös, J., & Larmagnac, A. (2015). Stretchable Silver Nanowire–Elastomer Composite Microelectrodes with Tailored Electrical Properties. ACS applied materials & interfaces, 7(24), 13467-13475.

Mathews, N., Morales, E. R., Cortés-Jacome, M., & Antonio, J. T. (2009). TiO2 thin films–Influence of annealing temperature on structural, optical and photocatalytic properties. Solar Energy, 83(9), 1499-1508.

Maynard, B., Long, Q., Schiff, E.A., Yang, M., Zhu, K., Kottokkaran, R., … & Dalal, V.L. (2016). Electron and hole drift mobility measurements on methylammonium lead iodide perovskite solar cells. Applied Physics Letters, 108(17), 173505.

McDonald, S. A., Konstantatos, G., Zhang, S., Cyr, P. W., Klem, E. J., Levina, L., & Sargent, E. H. (2005). Solution-processed PbS quantum dot infrared photodetectors and photovoltaics. Nature materials, 4(2), 138.

McKinley, G. H., & Renardy, M. (2011). Wolfgang von ohnesorge. Physics of Fluids, 23(12), 127101.

Memjet (2019). Versapass thermal inkjet printhead technical specifications datasheet. Accessed 09-20-2019 at https://www.memjet.com/wp-content/uploads/2017/08/VersaPass_Printhead_Datasheet-1.pdf

Mette, A., Richter, P., Hörteis, M., & Glunz, S. (2007). Metal aerosol jet printing for solar cell metallization. Progress in Photovoltaics: Research and Applications, 15(7), 621-627.

Michaelson, H. B. (1977). The work function of the elements and its periodicity. Journal of Applied Physics, 48(11), 4729-4733.

Miller, E. M., Kroupa, D. M., Zhang, J., Schulz, P., Marshall, A. R., Kahn, A., . . . Perkins, C. L. (2016). Revisiting the valence and conduction band size dependence of PbS quantum dot thin films. ACS nano, 10(3), 3302-3311.

MTI Corporation, (2019). ITO Coated Glass Substrate Accessed 12-02-2019 at https://www.mtixtl.com/ITO-101007-15C.aspx

Mitra, K. Y., Alalawe, A., Voigt, S., Boeffel, C., & Baumann, R. R. (2018). Manufacturing of All Inkjet-Printed Organic Photovoltaic Cell Arrays and Evaluating Their Suitability for Flexible Electronics. Micromachines, 9(12), 642.

Molesa, S., Redinger, D. R., Huang, D. C., & Subramanian, V. (2003). High-quality inkjet-printed multilevel interconnects and inductive components on plastic for ultra-low-cost RFID applications. MRS Online Proceedings Library Archive, 769.

Molina-Terriza, G., Torres, J. P., & Torner, L. (2001). Management of the angular momentum of light: preparation of photons in multidimensional vector states of angular momentum. Physical Review Letters, 88(1), 013601.

Moreels, I., Lambert, K., Smeets, D., De Muynck, D., Nollet, T., Martins, J. C., . . . Allan, G. (2009). Size-dependent optical properties of colloidal PbS quantum dots. ACS nano, 3(10), 3023-3030.

Moreno, M. V., Skarmeta, A. F., Venturi, A., Schmidt, M., & Schuelke, A. (2015). Context sensitive indoor temperature forecast for energy efficient operation of smart buildings. Dans Internet of Things (WF-IoT), 2015 IEEE 2nd World Forum on (pp. 705-710). IEEE.

Natu, R., Islam, M., Gilmore, J., & Martinez-Duarte, R. (2018). Shrinkage of SU-8 microstructures during carbonization. Journal of analytical and applied pyrolysis, 131, 17-27.

Navratil, J., Hamacek, A., Reboun, J., & Soukup, R. (2015). Perspective methods of creating conductive paths by aerosol jet printing technology. Dans Electronics Technology (ISSE), 2015 38th International Spring Seminar on (pp. 36-39). IEEE.

Nguyen, H. A. D., Lee, J., Kim, C. H., Shin, K.-H., & Lee, D. (2013). An approach for controlling printed line-width in high resolution roll-to-roll gravure printing. Journal of micromechanics and microengineering, 23(9), 095010.

Nie, W., Tsai, H., Asadpour, R., Blancon, J.-C., Neukirch, A. J., Gupta, G., . . . Alam, M. A. (2015). High-efficiency solution-processed perovskite solar cells with millimeter-scale grains. Science, 347(6221), 522-525.

Noh, J. H., Im, S. H., Heo, J. H., Mandal, T. N., & Seok, S. I. (2013). Chemical management for colorful, efficient, and stable inorganic–organic hybrid nanostructured solar cells. Nano letters, 13(4), 1764-1769.

Novacentrix. (2011). Novele™ IJ-220 - Printed Electronics Substrate - Inkjet Receptive. Accessed 12-02-2019 at https://store.novacentrix.com/v/vspfiles/assets/images/novele%20ij-220_2212.2.pdf

NREL. (2017). NREL - Best Research-Cell Efficiencies. Accessed 23-01-2017 at http://www.nrel.gov/pv/assets/images/efficiency-chart.png

Ohya, Y., Saiki, H., Tanaka, T., & Takahashi, Y. (1996). Microstructure of TiO2 and ZnO films fabricated by the sol-gel method. Journal of the American Ceramic Society, 79(4), 825-830.

Oku, T., Zushi, M., Imanishi, Y., Suzuki, A., & Suzuki, K. (2014). Microstructures and photovoltaic properties of perovskite-type CH3NH3PbI3 compounds. Applied Physics Express, 7(12), 121601.

Ossila. (2016). Perovskite Precursor Ink (for Air Processing). Accessed 17-12-2016 at https://www.ossila.com/products/perovskite-ink-air

Park, S.-J., Lee, E.-J., & Kwon, S.-H. (2007). Influence of surface treatment of polyimide film on adhesion enhancement between polyimide and metal films. Bulletin of the Korean Chemical Society, 28(2), 188-192.

Pech, D., Brunet, M., Taberna, P.-L., Simon, P., Fabre, N., Mesnilgrente, F., . . . Durou, H. (2010). Elaboration of a microstructured inkjet-printed carbon electrochemical capacitor. Journal of Power Sources, 195(4), 1266-1269.

Peng, X., Yuan, J., Shen, S., Gao, M., Chesman, A. S., Yin, H., . . . Angmo, D. (2017). Perovskite and organic solar cells fabricated by inkjet printing: progress and prospects. Advanced Functional Materials, 27(41), 1703704.

Perelaer, J., Abbel, R., Wünscher, S., Jani, R., van Lammeren, T., & Schubert, U. S. (2012). Roll-to-roll compatible sintering of inkjet printed features by photonic and microwave exposure: from non-conductive ink to 40% bulk silver conductivity in less than 15 seconds. Advanced materials, 24(19), 2620-2625.

Persano, L., Cardarelli, F., Arkadii, A., Uttiya, S., Zussman, E., Pisignano, D., & Camposeo, A. (2018). 3D printing of optical materials: an investigation of the microscopic properties. Dans Organic Photonic Materials and Devices XX (Vol. 10529, pp. 105290V). International Society for Optics and Photonics.

Pistor, P., Borchert, J., Fränzel, W., Csuk, R., & Scheer, R. (2014). Monitoring the phase formation of coevaporated lead halide perovskite thin films by in situ x-ray diffraction. The journal of physical chemistry letters, 5(19), 3308-3312.

Powell, R., Ho, C. Y., & Liley, P. E. (1966). Thermal conductivity of selected materials (Vol. 8). US Government Printing Office Washington, D. C.

Prasai, B., Cai, B., Underwood, M. K., Lewis, J. P., & Drabold, D. (2012). Properties of amorphous and crystalline titanium dioxide from first principles. Journal of materials science, 47(21), 7515-7521.

Preston, C., Xu, Y., Han, X., Munday, J. N., & Hu, L. (2013). Optical haze of transparent and conductive silver nanowire films. Nano research, 6(7), 461-468.

Qi, W., & Wang, M. (2004). Size and shape dependent melting temperature of metallic nanoparticles. Materials chemistry and physics, 88(2-3), 280-284.

Qiu, L., Ono, L. K., Jiang, Y., Leyden, M. R., Raga, S. R., Wang, S., & Qi, Y. (2017). Engineering interface structure to improve efficiency and stability of organometal halide perovskite solar cells. The Journal of Physical Chemistry B, 122(2), 511-520.

Radecka, M., Zakrzewska, K., Czternastek, H., Stapiński, T., & Debrus, S. (1993). The influence of thermal annealing on the structural, electrical and optical properties of TiO2-x thin films. Applied surface science, 65, 227-234.

Rajapaksha, R., Hashim, U., Gopinath, S., & Fernando, C. (2018). Sensitive pH detection on gold interdigitated electrodes as an electrochemical sensor. Microsystem Technologies, 24(4), 1965-1974.

Reinhold, I., Voit, W., Rawson, I., Martin, K., Pope, D., Farnsworth, S., . . . Munson, C. (2013). Novel developments in photonic sintering of inkjet printed functional inks. Dans NIP & Digital Fabrication Conference (Vol. 2013, pp. 476-478). Society for Imaging Science and Technology.

Reyes-Coronado, D., Rodríguez-Gattorno, G., Espinosa-Pesqueira, M., Cab, C., de Coss, R. d., & Oskam, G. (2008). Phase-pure TiO2 nanoparticles: anatase, brookite and rutile. Nanotechnology, 19(14), 145605.

Röhm, H., Leonhard, T., Schulz, A.D., Wagner, S., Hoffmann, M.J. & Colsmann, A. (2019). Ferroelectric properties of perovskite thin films and their implications for solar energy conversion. Advanced Materials, 31(26), 1806661.

Saidaminov, M. I., Adinolfi, V., Comin, R., Abdelhady, A. L., Peng, W., Dursun, I., . . . Bakr, O. M. (2015). Planar-integrated single-crystalline perovskite photodetectors. Nature communications, 6, 8724.

Saliba, M., Matsui, T., Seo, J.-Y., Domanski, K., Correa-Baena, J.-P., Nazeeruddin, M. K., . . . Hagfeldt, A. (2016). Cesium-containing triple cation perovskite solar cells: improved stability, reproducibility and high efficiency. Energy & Environmental Science, 9(6), 1989-1997.

Sanchez, R. S., & Mas-Marza, E. (2016). Light-induced effects on Spiro-OMeTAD films and hybrid lead halide perovskite solar cells. Solar Energy Materials and Solar Cells, 158, 189-194.

Scanlon, D. O., Dunnill, C. W., Buckeridge, J., Shevlin, S. A., Logsdail, A. J., Woodley, S. M., . . . Parkin, I. P. (2013). Band alignment of rutile and anatase TiO 2. Nature materials, 12(9), 798.

Schlaf, R., Murata, H., & Kafafi, Z. (2001). Work function measurements on indium tin oxide films. Journal of Electron Spectroscopy and Related Phenomena, 120(1-3), 149-154.

Seager, C. (1981). Grain boundary recombination: Theory and experiment in silicon. Journal of Applied Physics, 52(6), 3960-3968.

Seto, J. Y. (1975). The electrical properties of polycrystalline silicon films. Journal of Applied Physics, 46(12), 5247-5254.

Sette, D. (2014). Functional printing: from the study of printed layers to the prototyping of flexible devices (Université de Grenoble).

Sherkar, T. S., Momblona, C., Gil-Escrig, L. n., Ávila, J., Sessolo, M., Bolink, H. J., & Koster, L. J. A. (2017). Recombination in perovskite solar cells: significance of grain boundaries, interface traps, and defect ions. ACS energy letters, 2(5), 1214-1222.

Shih, W., Young, S., Ji, L., Water, W., & Shiu, H. (2011). TiO2-based thin film transistors with amorphous and anatase channel layer. Journal of The Electrochemical Society, 158(6), H609-H611.

Simpson, N., Dholakia, K., Allen, L., & Padgett, M. (1997). Mechanical equivalence of spin and orbital angular momentum of light: an optical spanner. Optics letters, 22(1), 52-54.

Snaith, H. J. (2013) "Perovskites: the emergence of a new era for low-cost, high-efficiency solar cells." The journal of physical chemistry letters 4(21), 3623-3630.

Snaith, H. J., Greenham, N. C., & Friend, R. H. (2004). The origin of collected charge and open-circuit voltage in blended polyfluorene photovoltaic devices. Advanced materials, 16(18), 1640-1645.

Soltman, D., & Subramanian, V. (2008). Inkjet-printed line morphologies and temperature control of the coffee ring effect. Langmuir, 24(5), 2224-2231.

Song, T.-B., Chen, Q., Zhou, H., Luo, S., Yang, Y. M., You, J., & Yang, Y. (2015). Unraveling film transformations and device performance of planar perovskite solar cells. Nano Energy, 12, 494-500.

Spina, M., Nafradi, B., Tóháti, H.-M., Kamarás, K., Bonvin, E., Gaal, R., . . . Horvath, E. (2016). Ultrasensitive 1D field-effect phototransistors: CH 3 NH 3 PbI 3 nanowire sensitized individual carbon nanotubes. Nanoscale, 8(9), 4888-4893.

Steubing, R. W., Cheng, S., Wright, W. H., Numajiri, Y., & Berns, M. W. (1991). Laser induced cell fusion in combination with optical tweezers: the laser cell fusion trap. Cytometry: The Journal of the International Society for Analytical Cytology, 12(6), 505-510.

Still, T., Yunker, P. J., & Yodh, A. G. (2012). Surfactant-induced Marangoni eddies alter the coffee-rings of evaporating colloidal drops. Langmuir, 28(11), 4984-4988.

Stoumpos, C. C., Malliakas, C. D., & Kanatzidis, M. G. (2013). Semiconducting tin and lead iodide perovskites with organic cations: phase transitions, high mobilities, and near-infrared photoluminescent properties. Inorganic chemistry, 52(15), 9019-9038.

Struempler, R. G. (1996). Polymer composites for temperature and current sensors. In 3rd International Conference on Intelligent Materials and 3rd European Conference on Smart Structures and Materials. International Society for Optics and Photonics, 2779, 377-382.

Suzuki, K., Yutani, K., Nakashima, M., Onodera, A., Mizukami, S., Kato, M., . . . Kameyama, K. (2009). A 200 ppi all-printed organic TFT backplane for flexible electrophoretic displays. Dans Proc. IDW (Vol. 9, pp. 1581-1584).

Suzuki, K., Yutani, K., Nakashima, M., Onodera, A., Mizukami, S., Kato, M., . . . KAMEYAMA, K. (2011). All-printed organic TFT backplanes for flexible electronic paper. NIHON GAZO GAKKAISHI (Journal of the Imaging Society of Japan), 50(2), 142-147.

Tai, Q., You, P., Sang, H., Liu, Z., Hu, C., Chan, H. L., & Yan, F. (2016). Efficient and stable perovskite solar cells prepared in ambient air irrespective of the humidity. Nature communications, 7, 11105.

Takshi, A., Bebeau, J., & Rahimi, F. (2016). Perovskite based photosensor for electrochemical studies. Dans Organic Sensors and Bioelectronics IX (Vol. 9944, pp. 99440R). International Society for Optics and Photonics.

Talapin, D. V., & Murray, C. B. (2005). PbSe nanocrystal solids for n-and p-channel thin film field-effect transistors. Science, 310(5745), 86-89.

Tang, H., Prasad, K., Sanjines, R., Schmid, P., & Levy, F. (1994). Electrical and optical properties of TiO2 anatase thin films. Journal of Applied Physics, 75(4), 2042-2047.

Tell, B., Shay, J., & Kasper, H. (1971). Electrical Properties, Optical Properties, and Band Structure of CuGa S 2 and CuIn S 2. Physical Review B, 4(8), 2463.

Tennyson, E.M., Doherty, T.A. & Stranks, S.D. (2019). Heterogeneity at multiple length scales in halide perovskite semiconductors. Nature Reviews Materials, 4(9), 573-587.

Thorlabs. (2019). ITO-Coated PET Film. Accessed 02-12-2019 at https://www.thorlabs.com/newgrouppage9.cfm?objectgroup_id=9535

Thorslund, T., Kahlen, F.-J., & Kar, A. (2003). Temperatures, pressures and stresses during laser shock processing. Optics and Lasers in Engineering, 39(1), 51-71.

Tobjörk, D., Aarnio, H., Pulkkinen, P., Bollström, R., Määttänen, A., Ihalainen, P., . . . Tenhu, H. (2012). IR-sintering of ink-jet printed metal-nanoparticles on paper. Thin Solid Films, 520(7), 2949-2955.

Tong, C.-J., Geng, W., Tang, Z.-K., Yam, C.-Y., Fan, X.-L., Liu, J., . . . Liu, L.-M. (2015). Uncovering the veil of the degradation in perovskite CH3NH3PbI3 upon humidity exposure: a first-principles study. The journal of physical chemistry letters, 6(16), 3289-3295.

Trudeau, C., Bolduc, M., Beaupré, P., Benavides-Guerrero, J., Tremblay, B. & Cloutier, S. G. (2018). Inkjet-printing of methylammonium lead trihalide perovskite as active layers for optoelectronic device. MRS Advances, 3(32), 1837-1842.

Trudeau, C., Bolduc, M., Beaupré, P., Ka, I., Asuo, I. M. & Cloutier, S. G. (2018). Inkjet-printing of methylammonium lead trihalide perovskite-based flexible optoelectronic device. International Electronics Technology Conference (IFETC), IEEE, 1-6.

Trudeau, C., Bolduc, M., Beaupré, P., Topart, P., Alain, C., & Cloutier, S. G. (2017). Inkjet-printed flexible active multilayered structures. MRS Advances, 2(18), 1015-1020.

Turner, L. W. (2013). Electronics engineer's reference book. Butterworth-Heinemann.

Uribe, O. H., Martin, J. P. S., Garcia-Alegre, M. C., Santos, M., & Guinea, D. (2015). Smart building: decision making architecture for thermal energy management. Sensors, 15(11), 27543-27568.

Van Gerwen, P., Laureyn, W., Laureys, W., Huyberechts, G., De Beeck, M. O., Baert, K., . . . Hermans, L. (1998). Nanoscaled interdigitated electrode arrays for biochemical sensors. Sensors and Actuators B: Chemical, 49(1-2), 73-80.

Vaz, A., Ubarretxena, A., Zalbide, I., Pardo, D., Solar, H., Garcia-Alonso, A., & Berenguer, R. (2010). Full passive UHF tag with a temperature sensor suitable for human body temperature monitoring. IEEE Transactions on Circuits and Systems II: Express Briefs, 57(2), 95-99.

Vaziri, A., Weihs, G., & Zeilinger, A. (2002). Experimental two-photon, three-dimensional entanglement for quantum communication. Physical Review Letters, 89(24), 240401.

Walther, F., Davydovskaya, P., Zürcher, S., Kaiser, M., Herberg, H., Gigler, A. M., & Stark, R. W. (2007). Stability of the hydrophilic behavior of oxygen plasma activated SU-8. Journal of micromechanics and microengineering, 17(3), 524.

Walther, F., Davydovskaya, P., Zürcher, S., Kaiser, M., Herberg, H., Gigler, A. M., & Stark, R. W. (2007). Stability of the hydrophilic behavior of oxygen plasma activated SU-8. Journal of micromechanics and microengineering, 17(3), 524.

Wang, D., Baral, J. K., Zhao, H., Gonfa, B. A., Truong, V. V., El Khakani, M. A., . . . Ma, D. (2011). Controlled Fabrication of PbS Quantum-Dot/Carbon-Nanotube Nanoarchitecture and its Significant Contribution to Near-Infrared Photon-to-Current Conversion. Advanced Functional Materials, 21(21), 4010-4018.

Wang, H.-H., Chen, Q., Zhou, H., Song, L., St Louis, Z., De Marco, N., . . . Chen, H. (2015). Improving the TiO 2 electron transport layer in perovskite solar cells using acetylacetonate-based additives. Journal of Materials Chemistry A, 3(17), 9108-9115.

Wang, J. T.-W., Ball, J. M., Barea, E. M., Abate, A., Alexander-Webber, J. A., Huang, J., . . . Snaith, H. J. (2013). Low-temperature processed electron collection layers of graphene/TiO2 nanocomposites in thin film perovskite solar cells. Nano letters, 14(2), 724-730.

Wang, S., Liu, X., Li, L., Ji, C., Sun, Z., Wu, Z., … & Luo, J. (2019). An unprecedented biaxial trilayered hybrid perobskite ferroelectric with directionally tunable photovoltaic effects. Journal of the American Chemical Society, 141(19), 7693-7697.

Wang, S., Yuan, W., & Meng, Y. S. (2015). Spectrum-dependent spiro-OMeTAD oxidization mechanism in perovskite solar cells. ACS applied materials & interfaces, 7(44), 24791-24798.

Wang, X., Zhang, H., Yu, R., Dong, L., Peng, D., Zhang, A., . . . Wang, Z. L. (2015). Dynamic pressure mapping of personalized handwriting by a flexible sensor matrix based on the mechanoluminescence process. Advanced materials, 27(14), 2324-2331.

Wang, Z., Shi, Z., Li, T., Chen, Y., & Huang, W. (2017). Stability of perovskite solar cells: a prospective on the substitution of the A cation and X anion. Angewandte Chemie International Edition, 56(5), 1190-1212.

Wassmer, M., Diel, W., & Krueger, K. (2010). Inkjet Printing of Fine-Line Thick-Film Inductors. Journal of Microelectronics and Electronic Packaging, 7(4), 205-213.

West, J., Carter, M., Smith, S., & Sears, J. (2012). Photonic sintering of silver nanoparticles: comparison of experiment and theory. Dans Sintering-Methods and Products. InTech.

White, D. (2017). Interpolation errors in thermistor calibration equations. International Journal of Thermophysics, 38(4), 59.

Wu, S.-H., & Chen, D.-H. (2004). Synthesis of high-concentration Cu nanoparticles in aqueous CTAB solutions. Journal of colloid and interface science, 273(1), 165-169.

Xiao, Z., Dong, Q., Bi, C., Shao, Y., Yuan, Y., & Huang, J. (2014). Solvent annealing of perovskite-induced crystal growth for photovoltaic-device efficiency enhancement. Advanced materials, 26(37), 6503-6509.

Xie, K., & Wei, B. (2016). Nanomaterials for Stretchable Energy Storage and Conversion Devices. Dans Nanomaterials for Sustainable Energy (pp. 159-191). Springer.

Xu, F., Benavides, J., Ma, X., & Cloutier, S. G. (2012). Interconnected TiO2 nanowire networks for PbS quantum dot solar cell applications. Journal of Nanotechnology, 2012.

Yan, C., Wang, J., & Lee, P. S. (2015). Stretchable graphene thermistor with tunable thermal index. ACS nano, 9(2), 2130-2137.

Yang, Z., Dou, J., & Wang, M. (2018). Graphene, Transition Metal Dichalcogenides, and Perovskite Photodetectors. Dans Two-dimensional Materials for Photodetector. InTech.

Yang, Z., Janmohamed, A., Lan, X., García de Arquer, F. P., Voznyy, O., Yassitepe, E., . . . Comin, R. (2015). Colloidal quantum dot photovoltaics enhanced by perovskite shelling. Nano letters, 15(11), 7539-7543.

Yantara, N., Yanan, F., Shi, C., Dewi, H. A., Boix, P. P., Mhaisalkar, S. G., & Mathews, N. (2015). Unravelling the effects of Cl addition in single step CH3NH3PbI3 perovskite solar cells. Chemistry of Materials, 27(7), 2309-2314.

Yassine, O., Shekhah, O., Assen, A. H., Belmabkhout, Y., Salama, K. N., & Eddaoudi, M. (2016). H2S Sensors: Fumarate-Based fcu-MOF Thin Film Grown on a Capacitive Interdigitated Electrode. Angewandte Chemie International Edition, 55(51), 15879-15883.

Yeo, J., Hong, S., Lee, D., Hotz, N., Lee, M.-T., Grigoropoulos, C. P., & Ko, S. H. (2012). Next generation non-vacuum, maskless, low temperature nanoparticle ink laser digital direct metal patterning for a large area flexible electronics. PLoS One, 7(8), e42315.

Yeo, J., Kim, G., Hong, S., Kim, M. S., Kim, D., Lee, J., . . . Kang, H. W. (2014). Flexible supercapacitor fabrication by room temperature rapid laser processing of roll-to-roll printed metal nanoparticle ink for wearable electronics application. Journal of Power Sources, 246, 562-568.

Yeshchenko, O. A., Dmitruk, I. M., Alexeenko, A. A., & Dmytruk, A. M. (2007). Size-dependent melting of spherical copper nanoparticles embedded in a silica matrix. Physical Review B, 75(8), 085434.

You, J., Hong, Z., Yang, Y., Chen, Q., Cai, M., Song, T.-B., . . . Zhou, H. (2014). Low-temperature solution-processed perovskite solar cells with high efficiency and flexibility. ACS nano, 8(2), 1674-1680.

Yu, C., Wang, Z., Zhu, J., Qiu, X., Jon, O., Yu, H., & Jiang, H. (2010). A mechanically stretchable temperature sensor based on buckled thin film devices on an elastomeric substrate. Dans Micro Electro Mechanical Systems (MEMS), 2010 IEEE 23rd International Conference on (pp. 675-678). IEEE.

Yu, H., Liu, X., Xia, Y., Dong, Q., Zhang, K., Wang, Z., . . . Li, Y. (2016). Room-temperature mixed-solvent-vapor annealing for high performance perovskite solar cells. Journal of Materials Chemistry A, 4(1), 321-326.

Yu, H.-H., & Hutchinson, J. W. (2002). Influence of substrate compliance on buckling delamination of thin films. International Journal of Fracture, 113(1), 39-55.

Yu, N., Genevet, P., Kats, M. A., Aieta, F., Tetienne, J.-P., Capasso, F., & Gaburro, Z. (2011). Light propagation with phase discontinuities: generalized laws of reflection and refraction. Science, 1210713.

Zeng, Y., Lu, G., Wang, H., Du, J., Ying, Z., & Liu, C. (2014). Positive temperature coefficient thermistors based on carbon nanotube/polymer composites. Scientific Reports, 4, 6684.

Zenou, M., Ermak, O., Saar, A., & Kotler, Z. (2013). Laser sintering of copper nanoparticles. Journal of physics D: Applied physics, 47(2), 025501.

Zhang, W., Saliba, M., Moore, D. T., Pathak, S. K., Hörantner, M. T., Stergiopoulos, T., . . . Abate, A. (2015). Ultrasmooth organic–inorganic perovskite thin-film formation and crystallization for efficient planar heterojunction solar cells. Nature communications, 6, 6142.

Zhang, X. W., Pan, Y., Zheng, Q., & Yi, X. S. (2000). A new polymer composite thermistor having double PTC transitions. Journal of applied polymer science, 78(2), 424-429.

Zhigilei, L. V., Lin, Z., & Ivanov, D. S. (2009). Atomistic modeling of short pulse laser ablation of metals: connections between melting, spallation, and phase explosion. The Journal of Physical Chemistry C, 113(27), 11892-11906.

Zhou, H., Chen, Q., Li, G., Luo, S., Song, T.-b., Duan, H.-S., . . . Yang, Y. (2014). Interface engineering of highly efficient perovskite solar cells. Science, 345(6196), 542-546.

Zhuldybina, M., Trudeau, C., Ropagnol, X., Bolduc, M., Zednik, R., & Blanchard, F. (2018). Terahertz vortex phase plate from a printed electronic device. Dans 2018 Photonics North (PN) (pp. 1-1). IEEE.

Zhuldybina, M., Ropagnol, X., Trudeau, C., Bolduc, M., Zednik, R. J., & Blanchard, F. (2019). Contactless in situ electrical characterization method of printed electronic devices with terahertz spectroscopy. Sensors, 19(3), 4